Stony Brook University

Characteristics of Aerosolized Ice Forming Marine Biogenic Particles

A dissertation Presented
by
Peter A. Alpert
to
The Graduate School
in Partial Fulfillment of the
Requirements
for the Degree of
Doctor of Philosophy
in
Marine and Atmospheric Science

Stony Brook University

August 2013

Stony Brook University

The Graduate School

Peter Aaron Alpert

We, the dissertation committee for the above candidate for the
Doctor of Philosophy degree, hereby recommend
acceptance of this dissertation.

Daniel A. Knopf - Dissertation Advisor
Associate Professor, School of Marine and Atmospheric Sciences/
Institute for Terrestrial and Planetary Atmospheres

Josephine Y. Aller - Dissertation Co-advisor
Professor, School of Marine and Atmospheric Sciences

Sultan Hameed - Chairperson of Defense
Professor, School of Marine and Atmospheric Sciences/
Institute for Terrestrial and Planetary Atmospheres
Director for the Institute for Terrestrial and Planetary Atmospheres

John E. Mak
Associate Professor, School of Marine and Atmospheric Sciences/
Institute for Terrestrial and Planetary Atmospheres

Thomas Koop
Professor, Bielefeld University
Department of Chemistry

This dissertation is accepted by the Graduate School

Charles Taber
Interim Dean of the Graduate School

Abstract of the Dissertation

Characteristics of Aerosolized Ice Forming Marine Biogenic Particles

by

Peter Aaron Alpert

Doctor of Philosophy

in

Marine and Atmospheric Science

Stony Brook University

2013

Ice particles are ubiquitous in the atmosphere existing as the sole constituents of glaciated cirrus clouds or coexisting with supercooled liquid droplets in mixed-phase clouds. Aerosol particles serving as heterogeneous ice nuclei for ice crystal formation impact the global radiative balance by modification of cloud radiative properties, and thus climate. Atmospheric ice formation is not a well understood process and represents great uncertainty for climate prediction. The oceans which cover the majority of the earths surface host nearly half the total global primary productivity and contribute to the greatest aerosol production by mass. However, the effect of biological activity on particle aerosolization, particle composition, and ice nucleation is not well established. This dissertation investigates the link between marine biological activity, aerosol particle production, physical/chemical particle characteristics, and ice nucleation under controlled laboratory conditions.

Dry and humidified aerosol size distributions of particles from bursting bubbles generated by plunging water jets and aeration through frits in a seawater mesocosm containing bacteria and/or phytoplankton cultures, were measured as a function of biological activity. Total particle production significantly increases primarily due to enhanced aerosolization of particles $\leq$ 100 nm in diameter attributable to the presence and growth of phytoplankton. Furthermore, hygroscopicity measurements indicate primary organic material associated with the sea salt particles, providing additional evidence for the importance of marine biological

activity for ocean derived aerosol composition. Ice nucleation experiments show that these organic rich particles nucleate ice efficiently in the immersion and deposition modes, which underscores their importance in mixed-phase and cirrus cloud formation processes. In separate ice nucleation experiments employing pure cultures of *Thalassiosira pseudonana*, *Nannochloris atomus* and *Emiliania huxleyi*, cells and cell fragments efficiently nucleate ice in the deposition mode, however, only *T. pseudonana* and *N. atomus* form ice in the immersion mode, presumably due to different cell wall compositions. This further corroborates the role of phytoplanktonic species for aerosolization of marine biogenic cloud active particles. Experimental data are used to parameterize marine biogenic particle fluxes and heterogeneous ice nucleation as a function of biological activity. The atmospheric implications of the results and their implementation into cloud and climate models are discussed.

Contents

List of Figures

List of Tables

Acknowledgements

The development of the body of work that made up my doctoral thesis would not have been possible without the help and support of many colleagues, friends, and family. I would like to thank all who directly participated and indirectly supported this thesis. First and foremost, I would like to thank Daniel Knopf for being a excellent mentor, supervisor and friend. In these years, you have helped me on countless occasions, struggled with me in tough situations, as well as celebrated with me in great academic achievement. Thank you very much for training me professionally and sharing your knowledge with me. I am fortunate to have someone like you that can push me in the right direction. It is without a doubt that you have shaped my professional path for years to come and will continue to have a significant impact on my life. You are a fantastic advisor and any other student would be so lucky. Second, I want to thank Josephine Aller who is also an excellent mentor and friend to me. Josie, thank you very much for standing by me all these years, for all your hard work correcting my writing while keeping me grounded, calm, and focused through hard times. You are kind and loving mentor, who is certainly tough when necessary. I appreciate your guidance. A special thanks goes to those collaborators for their support, Alex Laskin for hosting me at Pacific Northwest National Laboratory, and special thanks to Mary Gilles and Ryan Moffet for offering hours of time for free to train and work with me at the synchrotron light source at Lawrence Berkeley National Lab. I wish to thank the members of my Ph.D. committee including Sultan Hameed, John Mak, Thomas Koop, Josephine Aller and Daniel Knopf for helpful criticism and thoughtful advice. Thank you for your time and patience. I also thank members in the Knopf, Aller, and Mak group, Bingbing Wang, Yannick Rigg, Seanna Forrester, Jonathan Slade, Tracey Evans, Luping Su, Wendy Kilthau, and JoAnn Raday. Special thanks goes to Bingbing who was a role model student whom I learned much from. Special thanks also goes to JoAnn who made the biology thrive for this dissertation. I want to thank my family, my parents and sisters, for their love and support as I could not have gotten here without them. Finally, I thank my lovely wife, Sierra, who stood by me and supported me at every step. To her, I am most thankful for being my best friend. I could not have gotten through all of this without her encouragement and genuine love. Thank you all.

1 Introduction

1.1 Dissertation overview

The earth's atmosphere that extends from our planet's surface to free space, contains a mixture of gases and aerosol particles, which are solid or liquid matter suspended in air. The most abundant aerosol particle by mass in the atmosphere is sea spray consisting mostly of inorganic salts, a result of wave breaking in oceans which cover 70% of the earth's surface[24]. Organic material produced during the growth of photosynthetic algae or bacteria into oceanic waters may also become a part of sea spray released into the atmosphere where it may play an important role in various atmospheric processes. Here, it is hypothesized that biogenic material influences the amount and/or size of particles aerosolized and the way that liquid or ice clouds could form from these particles. Marine biogenic particles may possess different hygroscopicity than pure sea salt particles with subsequent effects on cloud microphysics including fog, cloud droplets and ice particle formation. This dissertation aims to determine unambiguously a link between marine biological activity, aerosolization and composition of marine particles, and how they impact ice nucleation in the atmosphere. The results will provide improved estimates of marine aerosol production, chemical composition, and hygroscopicity as well as an accurate physical representation of their ice nucleation ability for implementation in cloud and climate models.

1.2 Atmospheric aerosol particles

A tremendous diversity of particles are aerosolized directly from the surface of the earth from a variety of sources. From land they include, mineral dust, soil dust, volcanic particles, soot from biomass burning, and particles from fossil fuel combustion[41]. While particles are emitted from all water bodies, the oceans are the only source of salt containing sea spray particles[24,41]. Figure 1.1 shows examples of atmospheric particles and their corresponding size range. Aerosol particles $0.02 - 2.0$ μm in diameter are termed accumulation mode particles. They accumulate in the atmosphere because they are too small to settle significantly due to gravity and to large to coagulate efficiently with other particles (see Fig. 1.1)[41]. Accumulation mode particles are removed efficiently only by rainout, or wet deposition. Particles smaller than 0.02 μm are part of the Aitken mode and form in the atmosphere from condensing vapors, for example, sulfuric acid. Aitken particles grow

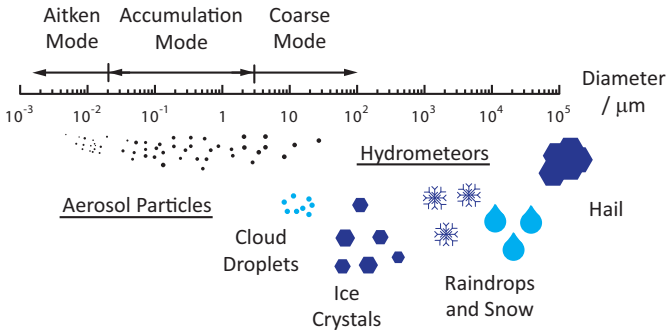

Figure 1.1: Typical sizes of atmospheric aerosol particles and hydrometeors.

quickly by condensation and coagulation and over a few hours can become part of the accumulation mode. Particles larger than 2 μm are termed coarse mode and are directly emitted into the atmosphere where they reside on the order of hours and are removed by gravitational settling and wet deposition[41]. Aerosol particles are at the center of fog and cloud droplets, as well as ice particles in the atmosphere. Figure 1.1 illustrates that these are much larger than aerosol particles, and therefore sediment more efficiently as a result of gravity, but are also carried and suspended by winds high above the earth's surface. When large enough, they may fall as precipitation. Accumulation mode particles remain in the atmosphere long enough to be transported to altitudes where clouds forms, thus their source strength and chemical and physical characteristics are important for estimating their impact on ice and liquid cloud formation and development.

1.3 Water vapor, aerosol particles and cloud formation

Water exists as a gas in the atmosphere, but also as a component of aerosol particles and hydrometeors in the form of liquid droplets or solid ice depending on thermodynamic conditions of temperature, T, and water partial pressure, p_{H_2O}, the total amount of water in the gas phase. Figure 1.2 illustrates air that moves

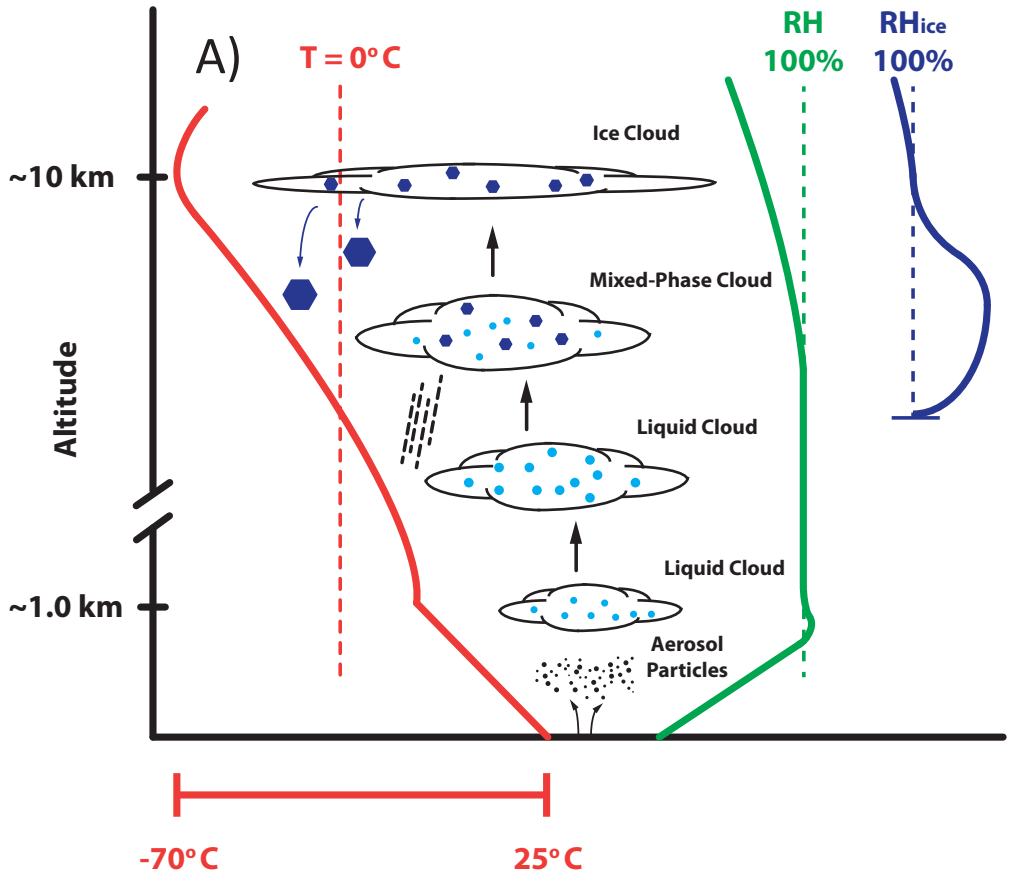

Figure 1.2: An illustration of rising air and subsequent liquid and ice cloud formation in the troposphere including vertical profile of temperature, relative humidity RH and relative humidity with respect to ice, RH_{ice}. Air temperature in red refers to the red axis located at the bottom of the figure.

through the troposphere characterized by decreasing T with increasing height starting at the earth's warm surface and rising until it reaches the cold tropopause, the top of the troposphere. At the surface, aerosol particles are released into the air and as the air rises, it cools due to adiabatic expansion. As temperature decreases, the water vapor pressure, $p^{\circ}_{H_2O}$, also decreases. Assuming that p_{H_2O} does not change significantly, the relative humidity, $RH = p_{H_2O}/p^{\circ}_{H_2O}$, will increase. Cloud formation requires aerosol particles to serve as cloud condensation nuclei (CCN) in a supersaturated environment when p_{H_2O} slightly exceeds $p^{\circ}_{H_2O}$, thus RH slightly exceeds 100% by fractions of a percent[41,42] as depicted in Fig. 1.2.

After a cloud forms, water droplets can exist as supercooled liquid when $T < 0^{\circ}$ C. When the saturation vapor pressure over a plane (flat) ice surface, $p^{ice}_{H_2O}$, is less than p_{H_2O}, the relative humidity with respect to ice, $RH_{ice} = p_{H_2O}/p^{ice}_{H_2O}$, can far exceed 100%, a condition required for ice to nucleate. Pure water droplets micrometers in size, can be supercooled until $\simeq$ 235 K is reached, corresponding to roughly $RH_{ice} \simeq 140\%$, at which point homogeneous ice nucleation occurs from supercooled droplets as illustrated in Fig. 1.3. Likewise, an aqueous solution droplet can be supercooled to lower temperatures than that for pure water before homogeneous ice nucleation occurs due to the solute effect causing a depression of the melting and freezing point[14,42–44]. Heterogeneous ice nucleation can occur when aerosol particles act as ice nuclei (IN) following various formation pathways as seen in Fig. 1.3. These include deposition freezing (ice forms on IN when supersaturated with respect to ice), immersion freezing (ice forms on IN immersed in aqueous supercooled droplets) and contact freezing (when IN collide with supercooled aqueous droplets)[42,45].

1.4 Ice formation pathways observed in cirrus and mixed-phase clouds

The various conditions of T, RH_{ice} and different formation pathways make ice nucleation in the atmosphere extremely difficult to quantify or represent in a model[46]. Homogeneous ice nucleation is a common ice formation mechanism in the atmosphere as inferred from ambient measurements of T, and RH[47–50] and generally taken as an upper limit of conditions for which ice forms, a notion supported by theoretical and laboratory studies (e. g. Pruppacher and Klett[42]). In addition to homogeneous ice nucleation, heterogeneous ice nucleation can play important roles in ice particle formation for cirrus clouds[47–53]. For example, Haag *et al.*[48] found that measurements of ambient in-cloud RH_{ice} from the Inter-hemispheric Differences in

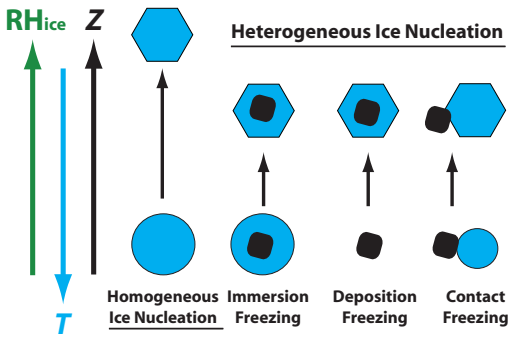

Figure 1.3: Homogeneous and heterogeneous ice nucleation modes. Increasing relative humidity with respect to ice, RH_{ice}, altitude, Z, and decreasing temperature, T, are indicated. Supercooled aqueous droplets, ice, and aerosol particles are shown as blue circles, blue hexagons and black squares, respectively.

Cirrus Properties From Anthropogenic Emissions (INCA) field experiment[54] could be reproduced in model simulations of ice nucleation in the mid-latitude northern hemisphere including both heterogeneous and homogeneous ice nucleation. Khvorostyanov *et al.*[53] modeled cirrus cloud formation and evolution during the Cirrus Regional Study of Tropical Anvils and Cirrus Layers - Florida Area Cirrus Experiment (CRYSTAL-FACE)[55] and could reproduce observations of ice supersaturation when homogeneous and heterogeneous ice nucleation were included. This is corroborated by observations of ice crystal residuals during the same campaign as both soluble and insoluble particles[49,52]. Immersion freezing is the dominant ice formation mechanism for mixed-phase clouds and responsible for the majority of global precipitation[56–60]. Meyers *et al.*[56], for example, show that immersion freezing dominates in precipitating clouds observed during the Sierra Cooperative Pilot Project (SCPP). Prenni *et al.*[61] show that immersion freezing dominates the ice formation mechanism over contact freezing from measurements of IN concentrations in mixed-phase clouds observed in the Mixed-Phase Arctic Cloud Experiment (M-PACE)[62] and the Surface Heat Budget of the Arctic (SHEBA)[63] campaigns. DeMott and Prenni[57] using model simulations and observations of IN concentrations for numerous field campaigns found that immersion mode freezing is also a dominant ice formation mechanism in mixed-phase clouds for temperatures between -5° C and -30° C. During the Ice in Clouds Experiment-Layer Clouds (ICE-L) campaign, Field *et al.*[60] tested the ability of all nucleation modes to reproduce observed IN concentrations in a model and also found that immersion freezing dominated ice nucleation to best simulate the mixed phase clouds they sampled from.

1.5 Aerosol, clouds and radiative balance

Aerosol particles, cloud droplets and ice crystals impact the radiative balance between the earth and sun, and a better understanding of their formation should improve predictions of future climate[1]. Energy from the sun which enters the atmosphere, must exactly equal that which leaves the atmosphere and is lost to space, thus establishing a radiative balance and setting the earth's temperature[64]. Understanding current and future climate depends on quantifying warming due to the variation of greenhouse gases, but also from understanding absorption, emission, reflection and scattering that occur due to the interaction of particles, cloud droplets, or ice crystals with short and longwave radiation[1]. Figure 1.4 shows the radiative forcing from greenhouse gases and aerosol particles and the natural solar forcing[1]. Although, there are other significant components of radiative forcing such as ozone, stratospheric water vapor, and land use, those included in Fig. 1.4 are only discussed here for simplicity. Radiative forcing is defined following Forster *et al.*[1] as the net change in irradiance from short and longwave radiation at the tropopause allowing for stratospheric temperatures to readjust keeping tropospheric and surface temperatures fixed. The radiative forcing can be directly related to the global mean surface temperature change at equilibrium. A positive radiative forcing indicates a global warming effect while a negative radiative forcing indicates a cooling effect. Aerosol particles, for example, can absorb solar radiation and to a lesser extent terrestrial radiation causing a net cooling effect on the earth's surface[65–69] as indicated in Fig. 1.4.

Aerosol particles can indirectly affect the radiative budget by acting as CCN and IN[1,70–75]. Liquid clouds, for example, can exhibit a high albedo, meaning they can reflect solar radiation back to space and prevent

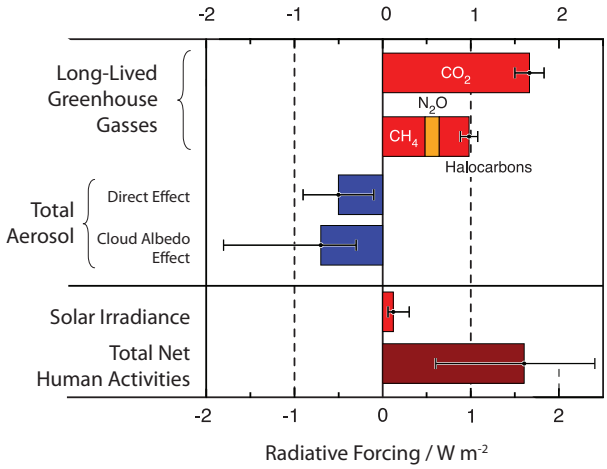

Figure 1.4: The difference in the globally averaged estimates of radiative forcing due to greenhouse gases, aerosols, and cloud albedo influenced by anthropogenic activities and the natural radiative forcing from increasing solar irradiance between the year 1750 and 2005[1]. The units of radiative forcing are energy in watts per square meter of the earth's surface, W m^{-2}.

sunlight from penetrating through the cloud resulting in a global cooling effect. However, different cloud types can have different radiative effects. Optically thin ice clouds at high altitudes may not significantly block solar radiation, however, they can be strong absorbers of outgoing infrared radiation from the earth's surface. Since high altitude ice clouds are much colder than the earth's surface they re-emit to space less radiation than they absorb, thus less energy leaves the earth resulting in a global warming[76]. This reflects a positive radiative forcing, as does warming from greenhouse gases (Fig. 1.4). Global estimates of future climate change do not, however, account for the influence of ice clouds on the radiative budget because their formation and radiative properties are uncertain[1]. The goal of the research described in this dissertation aims to better understand ice cloud formation due to aerosol particles, particularly marine biogenic particles, and provide physically based ice nucleation descpritions to be included in climate models.

1.6 Oceanic primary productivity and ocean particulate matter

Oceans and other water masses cover the majority of the Earth's surface. In addition to their ionic composition, oceans host significant biomass production predominately in the top most ocean layer, called the euphotic zone. Here, sunlight that penetrates the water and not yet attenuated allows for the growth of photosynthetic planktonic organisms. In spite of the fact that phytoplankton cells are on the order of micrometers in size, they contribute the vast majority of the net ocean primary productivity[77] due to their considerable densities ranging from thousands to millions of phytoplankton cells present in only milliliters of seawater at any given time. Organic exudates released from phytoplankton cells as a byproduct of photosynthesis, in turn support a multitude of bacteria and other microorganisms[78–83]. Phytoplankton exudates include proteins and polysaccharides which bind to divalent ions Ca^{2+} and Mg^{2+} in surface waters and agglomerate to form gel-like particles[83–85]. Figure 1.5 illustrates the fact that microgels can be nanometers to micrometers in size, while phytoplankton and bacteria can range in size from hundreds of nanometers to

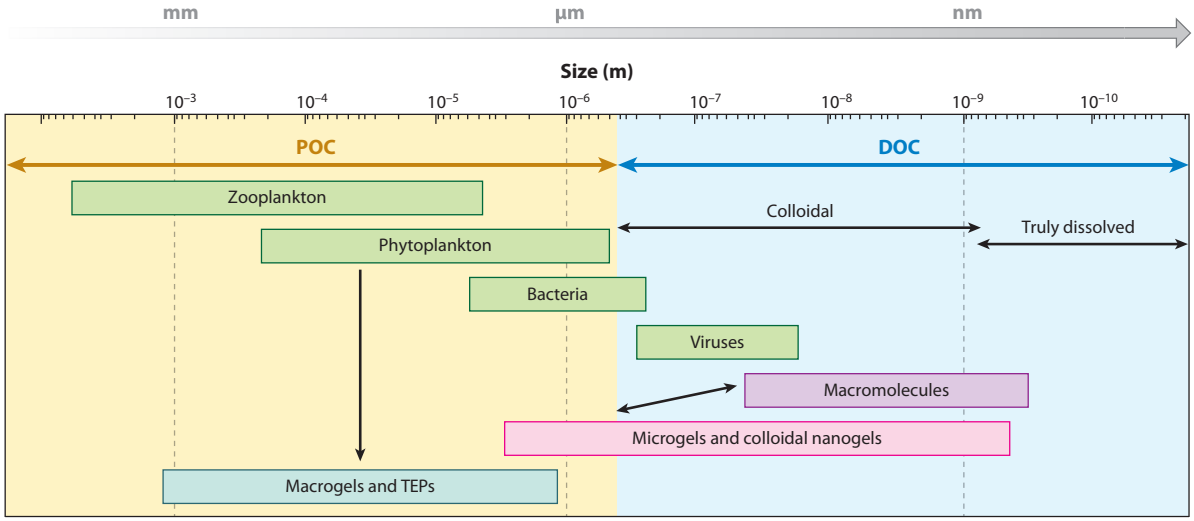

Figure 1.5: Types of particulate organic carbon (POC) and dissolved organic carbon (DOC) in seawater and their observed sizes adopted from Verdugo[2].

as large as hundreds of micrometers. These microgels agglomerate further over time to form transparent exopolymer particles (TEP) which are surface active and can concentrate at the interface between the ocean and atmosphere called the sea surface microlayer (SML)[86,87]. The SML which is on the order of tens to hundreds of micrometers in thickness is distinct from the underlying bulk water in terms of ionic and organic composition and in concentrations of bacteria, viruses and other cellular compounds[81,88–92]. Phytoplankton cells and other organic particulate are consumed by zooplankton and other marine organisms or settle out of the SML and either decompose or ultimately sediment onto the ocean floor. Alternatively, the organic material, microgels, TEP, phytoplankton, bacteria and cellular fragments in surface waters or in the SML become aerosolized though wind and wave breaking processes leading to a chemically and morphologically complex mix of airborne particles[24,93,94].

1.7 Generation of marine aerosol particles

Aerosol particles emitted from the ocean do so through bubble bursting and wave breaking processes. As a wave breaks, air is entrained into the water forming bubbles with diameters of centimeters to micrometers[24,93,94]. When bubbles rise to the air-water interface and burst, they can eject aerosol particles into the atmosphere in a size range similar to the accumulation and coarse mode. When a bubble film shatters, film drops micrometer and submicrometer in size are ejected into the air[24,95]. When the water surface rebounds after a bubble bursts, large coarse mode droplets, called jet drops, are ejected into the air[24,95]. In addition, waves can tear at their crest at wind speeds above about 10 m s^{-1} causing large coarse mode spume droplets to be released. Jet and spume droplets are not numerous and their sizes are > 2 μm in diameter generally leading to short lifetimes in the atmosphere due to sedimentation[24,95]. They may not, therefore, be important for liquid and ice cloud formation. Film droplets on the other hand, which are produced at much greater rates, up to thousands per bursting bubble, and are small enough to be lofted in to the atmosphere, do accumulate and potentially participate in cloud formation[24,95].

The flux of marine aerosol particles from the ocean surface into the atmosphere, termed the source function, describes the number of particles per volume of air emitted for a given time interval and ocean surface area as a function of particle diameter[24,95]. Marine aerosol source functions commonly relate higher wind speeds to more wave activity resulting in more white cap coverage and ultimately more aerosolized particles[24,95,96]. In laboratory experiments designed to understand processes observed in the field, bubbles can be generated using different techniques and the resulting aerosol particles quantified with respect to bubble coverage. A source function derived from bubble generation experiments can be determined from the measured particle concentrations as a function of particle diameter, also known as a size distribution, and then scaled with a fractional bubble or white cap coverage. Significant work relating bubble generation to aerosolization has been reported in recent literature. Keene *et al.*[27], for example, pumped seawater up from a depth of 5 m into a teflon tank holding 42 L while 9 L min^{-1} of air was passed through glass frits that produced bubbles with the diameters between $200 - 800$ μm. Particles that were generated resembled a lognormal distribution that peaked at 80 nm. Fuentes *et al.*[97] generated bubbles with impinging water jets, glass frits and diffuser stones and found that all produced aerosol size distributions that were dissimilar to each other. However, the plunging jet resembled most closely, ambient aerosol production measured in the North Atlantic with two dominant peaks at 48 nm and 124 nm[3,19]. Hultin *et al.*[98] also used a plunging water jet technique and saw two dominate peaks at particle diameters of 227 nm and 88 nm, larger diameters than what Fuentes *et al.*[97] observed. Prather *et al.*[99] generated a propagating breaking wave to produce bubbles in a 33 m long flume filled with Pacific Ocean seawater instead of a tank. They subsequently found the resulting size distribution peaked for particles 162 nm in diameter and was very broad with significant particle production from 20 nm to 2 μm[99]. Clearly, different techniques for generating bubbles result in dissimilar aerosolization and particle size distributions. Therefore, using a marine aerosol particle source function derived from bubble generation to describe actual ocean-atmosphere aerosol production will always be just an estimate. The most significant issue with any laboratory or field aerosolization experiment in which bubbles are artificially generated, is the applicability of representing an ocean bearing breaking wave in a scaled down enclosed system.

Despite the differences in particle aerosolization techniques, previous studies involving different bubble generation methods have served to explore differences in aerosolization as a result of changing water conditions including temperature, salinity and dissolved oxygen[19,25,93,100] or the abundance and diversity of microorganisms present in the seawater[99]. A recent study by Zábori *et al.*[101] found that marine particle aerosolization was unaffected for typical variations of salinity and dissolved oxygen found in Arctic oceans although decreasing water temperature from 10° C to 0° C resulted in an order of magnitude increase in total particle production. Ocean water organic composition can vary significantly depending on the activity and nature of the planktonic community. Because of differences in microorganisms and phytoplankton present in surface waters, it is therefore important to determine how biological activity, organic carbon content or the presence of particulate carbon, microgels, TEP, cellular material, and organic surfactants will affect the aerosolization of particles and the chemical nature of those particles compared with sea salt alone.

Bacteria are present in the SML at greater concentration per water volume than below the SML and can also become aerosolized at concentrations up to 10 fold higher than their concentration in underlying

waters[81]. Proteinaceous and carbohydrate particulate material is readily aerosolized from the SML[91]. A variety of surface active and organic compounds ubiquitous in the atmosphere are possibly linked to the organic material found at the SML[19,26,27,93,102,103]. Bigg and Leck[104] and Bigg[105] concluded that TEP, sea salt, and purely organic particles are frequently observed during multiple field campaigns in which marine particles in air were sampled. These authors find airborne fragments of diatoms and other marine microorganisms as well[104]. Fuentes *et al.*[106] added filtered phytoplankton exudates from various species to artificial sea water effectively increasing DOC and observed an increase in particle production that peaked at 35 nm, compared to the double peak observed for artificial seawater without exudates. Particles also decreased in their ability to take up water and in their ability to act as CCN[106]. However, this behavior was only observed for one species of diatom from the genus *Chaetoceros*, while other diatoms, green algae, and coccolithophorids had negligible effects in comparison[107]. Orellana *et al.*[108] provide direct evidence that marine microgels which are found in ocean water may be found in aerosol particles and cloud water, supporting the notion that organic material released into oceans does in fact become aerosolized. Most recently, Prather *et al.*[99] found that when bacteria grow up to concentrations of 8×10^6 cells mL^{-1}, aerosolized particles < 180 μm are dominated by organic matter. As particle sizes increased beyond 180 μm in diameter, increasing sea salt mass fractions were observed[99]. These studies clearly illustrate that differences in oceanic chemical and biological conditions and processes not only affect the size of aerosolized particles, but their chemical characteristics. The sum of biological activities, particularly in areas or during times of high biological activity and growth of phytoplankton, impacts the TEP, microgels and other organic compounds and which are released into surrounding waters where bacteria are present and the nature of the particles aerosolized. This "complete" complex marine system in which phytoplankton, bacteria, viruses, and other microorganisms grow simultaneously has not been included in bubble bursting studies.

1.8 Composition of field collected marine particles

As suggested by laboratory bubble generation experiments, field studies have found that marine aerosol particles are composed not only of sea salts, but also of organic material. Soluble and insoluble organic material in marine aerosol particles sampled from the air at Mace Head, Ireland was quantified by O'Dowd *et al.*[3]. O'Dowd and colleagues found that the organic fraction of submicrometer aerosol particle mass is highly correlated with chlorophyll concentrations in surface waters. Figure 1.6 shows that organic matter is highly enriched in submicrometer sized particles collected over waters in spring and fall months when chlorophyl concentrations are $\sim 1-10$ mg m^{-3} on average measured from the SeaWiFS instrument, suggesting that high biological activity may be linked to organic aerosol loading over the ocean. On the other hand, when chlorophyll concentrations and thus biological activity are low, Fig. 1.6 indicates that for all particle sizes, sea salt is the dominant component.

Using nuclear magnetic resonance (NMR) spectroscopy, similar chemical shifts marked by an enrichment of carbohydrates, lipids, and hydrophobic aliphatic carbon chains most notably derived from microbiological activity, were frequently observed for insoluble particulate organic material in the North Atlantic and in atmospheric aerosol particles that were simultaneously sampled[82]. The authors concluded that marine

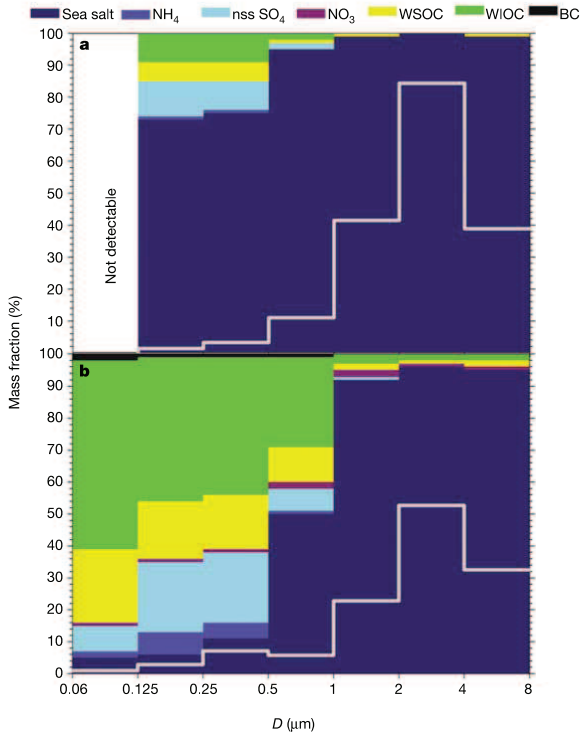

Figure 1.6: Size segregated marine aerosol particle composition adopted from O'Dowd *et al.*[3] observed for periods of low biological activity in panel (a) and for periods of high biological activity in panel (b) characterized by winter and spring through autumn seasons, respectively. Abbreviations are as follows, non sea salt sulfate (nss-SO_4), water soluble organic carbon (WSOC), water insoluble organic carbon (WIOC), and black carbon (BC).

microgels in ocean water must be aerosolized in order to observe similar NMR spectra of particles found in the water and those found in the air[82]. In a later study, Ovadnevaite *et al.*[109] concluded that high organic content in marine aerosol particles were directly emitted from wave breaking and bubble bursting consistent with a high correlation of oxidized and unoxidized hydrocarbon mass and an anti-correlation with non-sea salt sulfate in field collected aerosol particles. Russell *et al.*[110] examined field collected Arctic and Pacific marine aerosol particles with high resolution Fourier transform infrared spectroscopy (FTIR) and scanning transmission X-ray microscopy and near-edge X-ray absorption fine structure spectroscopy (STXM/NEXAFS), a technique used to determine the presence of unique carbon molecular bonding in aerosol particles such as the carboxyl functional group or carbon double bonding. The authors found that polysaccharides comprised 57% of the measured submicron organic particle mass on average[110].

Marine particles sampled from an aircraft at 1 km height between San Francisco and Sacramento by Laskin *et al.*[4] and subsequently analyzed with STXM/NEXAFS and with computer controlled scanning electron microscopy and energy dispersive X-ray analysis (CCSEM/EDX) providing morphological and elemental composition. Chemical information was obtained for thousands of particles achieving statistical significance for the aerosol particle populations. Particles from the air which traveled for $8 - 25$ hours were categorized as 1) sulfate, 2) sea salt coated by organic material, 3) internal mixtures of sulfate, sea salt, and organic material, and 4) carbonaceous only particles. Electron micrographs of the collected particles are shown in

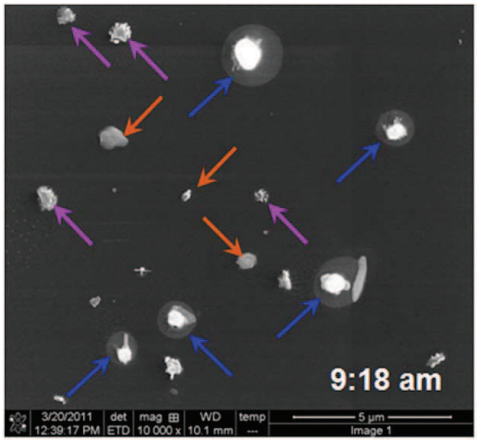

Figure 1.7: Scanning electron microscope image of particles taken from Laskin *et al.*[4] sampled from aircraft in the morning after atmospheric transport from the Pacific ocean and over San Francisco and Sacramento, CA. Blue arrows point to sea spray particles which are irregularly shaped, generally larger than 1 μm in diameter with sea salt cores and halos of organic material. Pink and orange arrows indicate internally mixed sulfate and sea spray particles and ammonium bisulfate/sulfate particles respectively.

Fig. 1.7. The authors found organic coated sea salt dominated with 50% of the total particles present[4]. Carbonaceous particles constituted less than 10% of the population at any given time[4]. It is important to note that the organic material associated with sea salt is commonly found as a coating. This is seen as a puddle of material surrounding the inorganic core in Fig. 1.7. Organic coated sea salt particles may play an important role in the chemistry occurring at the particle surface which can influence warm and ice cloud formation. Heterogeneous ice nucleation proceeds at the particle surface, and an organic coated sea salt particle is likely to have very different ice nucleation behavior than a particle without any coating.

In an effort to determine which particles in the ambient population were responsible for nucleating ice, airborne experiments have been employed to directly sample aerosol particles in the upper troposphere and collect individual ice crystals to observe their residue composition. In flights above the Pacific and Atlantic coast, particles containing sea salt were not found in significant numbers, totaling only 2% of the total particles[52,111]. However, sea salt was found in ice residues about 15% of the time off the Florida Atlantic coast and about 30% of the time thousands of kilometers west of Ecuador over the equatorial Pacific coast[52,111]. This suggests that depending of the prevailing wind direction, in the coastal oceans, marine particles may play a role in the formation of ice clouds. Over the open ocean where the influence of continental particles is expected to be minimal, the influence of marine particles may be much greater.

1.9 Ice forming marine biogenic particles

The studies mentioned above suggest that marine aerosol particles are i) primarily composed of both sea salt and organic material[3,82], ii) that the organic portion is primarily water insoluble and emitted by the same bubble bursting and wave breaking mechanism as for aerosolized sea salts[82,109], iii) that organic material is the result of biological processes in the ocean linked to phytoplankton productivity[3], and iv) that marine sea spray particles may have the ability to impact atmospheric ice formation[111]. If sea spray is

identified as consisting of sea salts and organic compounds, which are collected at high altitudes and found in ice crystal residues, then marine aerosol particles in general may play an important role in atmospheric ice formation affecting ice and mixed-phase cloud formation, their evolution and their radiative properties, and thus climate.

Few studies have suggested that marine biogenic particles may have the potential to nucleate ice[112–115]. Bigg[112] collected particles on filters from air sampled over the Arctic Ocean and found they nucleated ice heterogeneously. Subsequently, the greatest concentrations of IN measured by Bigg[112] were found around water mass convergence zones where upwelled nutrients are delivered to surface waters triggering phytoplanktonic blooms[113]. As a result, Schnell[113] suggested that airborne ocean-derived ice nuclei may be related to biological activity. Droplets made from some axenic, unialgal cultures of phytoplankton were observed to freeze heterogeneously, however, it could not be clearly determined if the IN were actually phytoplankton cells, exudates, or some other nucleating agent[113]. Surface sea water sampled from coastal regions of Vancouver, Nova Scotia, California, and the Bahamas contained IN associated with phytoplankton, yet the IN could not be unambiguously identified[114]. Some arctic aerosol particles suggested to have originated from the ocean were observed to be organic containing ice nucleating particles, however, no conclusive evidence was provided to specifically identify the organic ice nucleating agent[116].

In contrast to previous studies, Knopf *et al.*[34] and Alpert *et al.*[35],[117] used axenic, unialgal cultures of phytoplankton, and carefully controlled and accurate systems for ice nucleation studies. They were able to show unambiguously that whole phytoplankton cells and cell fragments are capable of nucleating ice in the immersion and deposition mode. Three phytoplankton species, *Thalassiosira pseudonana*, *Emiliania huxleyi*, and *Nannochloris atomus*, representative of three abundant marine algal groups, were used in ice nucleation experiments. Bacteria were not present in any culture or any ice nucleation experiment. Suspended in aqueous NaCl or pure water, *T. pseudonana* and *N. atomus* nucleated ice in the immersion mode at temperatures $10 - 30$ K warmer than temperatures for homogeneous ice nucleation[34,35,117]. Exposed to supersaturated water vapor, all three species nucleated ice in the deposition mode 25% to 40% lower in $\mathrm{RH_{ice}}$ than the homogeneous freezing threshold for temperatures $200 - 245$ K[34,117]. Marine biogenic particles have only recently been found to be ubiquitous in marine air from field studies and to nucleate ice with high efficiency from laboratory measurements, emphasizing their potential importance in atmospheric ice cloud formation.

1.10 Marine aerosol and their affect on clouds and climate

Marine aerosol particles may have significant impacts on climate as inferred from modeling studies investigating how particle number, composition and their ability to act as cloud condensation nuclei (CCN) impact radiative forcing by changing cloud albedo[118,119]. In particular, the influence of marine biogenic particles with various organic compositions and hygroscopicity on the top of the atmosphere radiative forcing estimates were investigated[118,119]. When modeling liquid cloud formation in the marine boundary layer, the error in radiative forcing remains small even when the organic volume fraction in marine aerosol particles is varied between 0.0 and 0.6 and an average hygroscopicity is employed for all organic particle types[119]. Despite different types of organic material having vastly different chemical compositions associated with

marine particles, Wang *et al.*[119] strongly suggests that the error in radiative forcing should remain below ± 0.2 W m^{-2}. If however, the volume fractions are larger than 0.6 then individual particle chemical characteristics must be accounted for. In contrast, the temporal and spatial flux of marine particles and their resulting concentration has shown to have significant impact on cloud albedo and the resulting radiative forcing. Employing an average marine particle source function, climate models result in a high variability and significant error in cloud radiative forcing at $\pm 0.5 - 0.7$ W m^{-2} on average and as high as ± 12.0 W m^{-2} locally[118]. This result implies that one single source function for marine particle aerosolization cannot be used for calculating cloud radiative forcing[118]. One aim of this dissertation research is to investigate how aerosol particle flux and hygroscopicity changes due to biological activity over time.

A recent modeling effort which included marine biogenic particles serving as IN, as inferred from field observations and laboratory experiments, found that they may contribute significantly to atmospheric ice crystal formation on regional to global scales, especially in air over the expanse of the Southern Ocean[120] where phytoplankton blooms are prevalent due to persistent upwelling and nutrient delivery to surface waters. Due to the ubiquity of sea spray, biogenic marine IN may impact cloud properties over the majority of the earth's surface, resulting in heretofore effects on cloud formation, evolution, precipitation distribution, and radiative balance. Clearly, the results of these modeling studies emphasize the need to study the link between marine biogenic particles and their aerosolization as a function of ocean biological activity, for a better understanding of their chemistry and their capability to efficiently nucleate ice.

1.11 Dissertation objectives

The overall goal of the research described in this dissertation is to assess the role of marine biogenic particles in ice cloud formation by establishing an unambiguous link between marine biological activity, particle aerosolization, and cloud formation potential of individual particles. To address this, the relationship between marine biogenic particle aerosolization, their composition, and ice nucleation ability is investigated in the laboratory. Here, the aim is to obtain a quantitative understanding of seawater composition, aerosol particle production, particle hygroscopicity, particle morphology, chemical composition, and ice nucleation as a function of marine biological activity. To achieve this, highly controlled measurements are made allowing quantification of particle aerosolization generated in a seawater mesocosm with a temporally evolving phytoplankton culture. The aerosol size distribution is measured precisely on nanometer scales as a function of phytoplankton bloom age. Biogenic aerosol particles are collected and probed for their ice nucleation ability using an optical microscope to observe freezing events in a cryogenic cold stage sample cell in which temperature and relative humidity are precisely controlled. State of the art instrumentation allows acquisition of chemical imaging of aerosol particle populations on an individual particle basis. A unique technique enabled identification of individual ice nucleating particles to detail their chemistry. This allowed unambiguous determination that marine biogenic particles are in fact the ice nucleators, thus linking biological activity to aerosolization and ice nucleation. These unique data sets allow for formulation of theoretical descriptions and physically based parametric approximations for prediction of marine particle flux and ice nucleation to be applied in atmospheric models and improve the representation of atmospheric aerosol particle loading,

CCN in liquid clouds and ice crystal production in cirrus and mixed-phase clouds.

2 Theory and background

2.1 Water vapor

When air is saturated with water vapor, the water partial pressure is equal to the pressure over a plane surface of pure water. According to the parameterization by Murphy and Koop[5], the vapor pressure of pure water, $p^{\circ}_{H_2O}$, can be obtained from

$$\begin{aligned}\ln\left(p^{\circ}_{H_2O}\right) = {} & 54.842763 - 6763.22/T - 4.210\ln\left(T\right) + 0.000367T \\ & + \tanh\left(0.0415(T - 218.8)\right)(53.8781331.22/T \\ & - 9.44523\ln\left(T\right) + 0.014025T)\end{aligned} \tag{1}$$

as a function of T. The vapor pressure of an aqueous solution droplet, $p^{sol}_{H_2O}$, for example an aqueous sea spray aerosol particle, is always less than $p^{\circ}_{H_2O}$. As an aqueous droplet comes into equilibrium with the surrounding water partial pressure, water will either condense on or evaporate from the droplet, thus increasing or decreasing its water vapor pressure, respectively, until $p^{sol}_{H_2O} = p_{H_2O}$. Once equilibrium is reached, the droplets water activity, a_w, will equal the RH[14] following the equation

$$a_w = \frac{p_{H_2O}}{p^{\circ}_{H_2O}}. \tag{2}$$

The vapor pressure for a plane ice surface is obtained from

$$\ln\left(p^{ice}_{H_2O}\right) = 9.550426 - 5723.265/T + 3.53068\ln\left(T\right) - 0.00728332T. \tag{3}$$

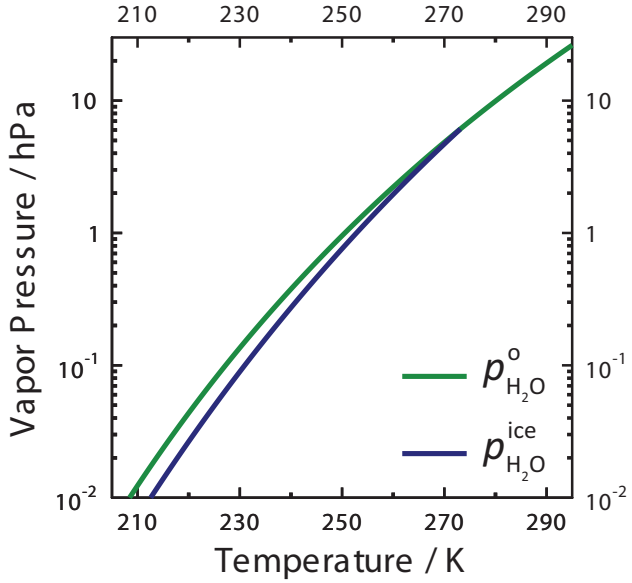

Figure 2.1: Water vapor pressure with respect to a plane surface a pure water, $p^{\circ}_{H_2O}$, and a plane surface of ice, $p^{ice}_{H_2O}$ [5]. Note that the ice melting temperature at 273.15 K occurs when $p^{\circ}_{H_2O} = p^{ice}_{H_2O}$.

Figure 2.1 shows that $p^{\circ}_{H_2O}$ and $p^{ice}_{H_2O}$ decreases with decreasing T. Notice that at the ice melting temperature of 273.15 K, $p^{ice}_{H_2O} = p^{\circ}_{H_2O}$ and below this temperature, $p^{ice}_{H_2O} < p^{\circ}_{H_2O}$. This means that aqueous solution or pure water droplets colder than their respective melting temperature, will always experience ice saturation. The ice saturation ratio, S_{ice}, is related to a droplets a_w in the supercooled temperature regime given by

$$S_{ice} = a_w \frac{p^{ice}_{H_2O}}{p^{\circ}_{H_2O}}. \tag{4}$$

From this equation is it clear that $S_{ice} = RH_{ice}/100$.

2.2 Deliquescence and efflorescence of NaCl particles and the NaCl phase diagram

Aerosol particles composed of crystallized salt are capable of taking up water vapor from their surrounding environment at a specific relative humidity termed the deliquescence relative humidity, DRH. The Gibb's free energy between the crystalline phase and the aqueous solution phase at the DRH are equal and at this point a crystalline salt particle spontaneously absorbs water to form a saturated salt solution[41,121]. When the ambient RH < DRH, a crystalline or pure phase is thermodynamically favorable due to its lower Gibbs free energy, than its aqueous solution phase. When the ambient RH $\geq$ DRH, the aqueous phase is thermodynamically favorable[41,121]. Imagine, for example, a crystaline sea salt particle at RH = 35% is exposed to increasing RH. Until it reaches its DRH $\simeq$ 75%, it will remain as a crystal as indicated in Fig. 2.2, following the path of the solid line. At the DRH, it will then take up water and follow the vertical trajectory

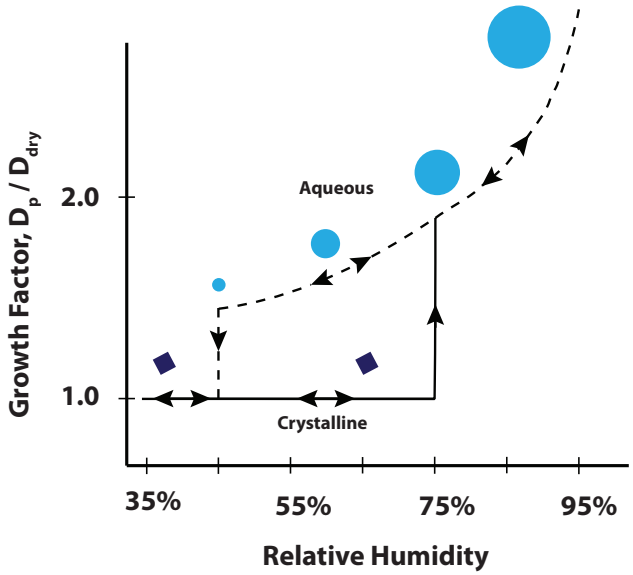

Figure 2.2: A humidogram of solid NaCl showing the growth factor as a function of relative humidity. The crystalline phase of NaCl is shown to follow the path of the solid line and the aqueous phase as the dashed line. Arrows denote respective paths that crystalline or aqueous NaCl can take when RH is increased or decreased. At RH = 75%, solid NaCl will deliquesce, experience growth from water uptake and then is fixed to the aqueous path. Only at RH $\simeq$ 45% will crystallization occur when sufficient supersaturation is reached.

on the solid line in Fig. 2.2 intersecting the dashed line which represents an aqueous solution. If an aqueous droplet then moves into a region with RH $< 75\%$ it will shrink in size due to evaporation, although it will remain a supersaturated aqueous solution. As RH decreases, an aqueous droplet will follow the dashed line only until it reaches a critical supersaturation point called the efflorescence relative humidity, ERH, where it will form a salt nuclei and quickly crystallize. Figure 2.2 shows that the ERH occurs around roughly at RH $= 45\%$, an estimate for micrometer sized droplets at room temperature[8,14].

The phase diagram of the binary mixture of NaCl and water is shown in Fig. 2.3, which is based on laboratory measurements of DRH and ERH, including ice melting and freezing points of aqueous NaCl and sea salt solutions[7–13]. The diagram is a tool to quickly determine the thermodynamically favorable phase state of a particle at any T and RH. If a particle lies the the liquid region, it will always be in a

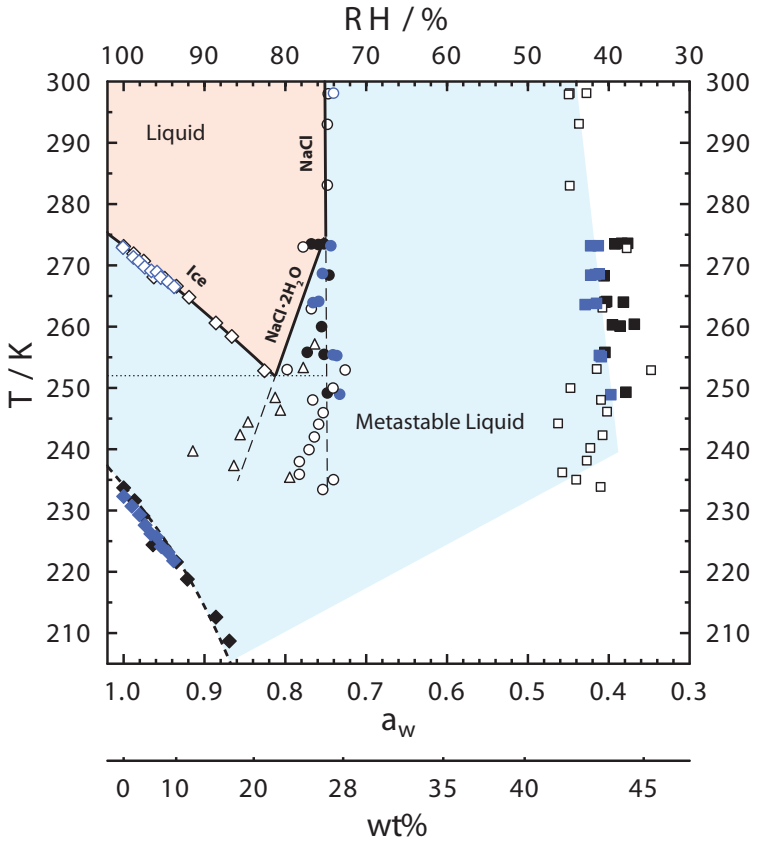

Figure 2.3: Phase diagram of the binary solution NaCl and water. The abscissa and ordinate are temperature, T, and water activity, a_w, respectively. The top ordinate is relative humidity, RH, and the lower ordinate is the corresponding NaCl solution weight percent in equilibrium with relative humidity derived from the E-AIM model[6]. Black and blue symbols represent NaCl and sea salt freezing (filled diamonds), ice melting (open diamonds), deliquescence relative humidity, DRH, (circles), and efflorescence relative humidity, ERH, (squares)[7]. Open circles and squares are compiled from various studies[8–13]. Open triangles are DRH points of sodium chloride dyhydrate ($NaCl{\cdot}2H_2O$)[8]. Solid lines indicate liquid-solid equilibrium between the aqueous phase and the crystalline phase labeled in bold letters. The dotted line is the eutectic temperature ~ 252 K and the dashed lines are extrapolations of the NaCl-solution, and $NaCl{\cdot}2H_2O$-solution equilibrium lines. The thick dashed line indicates theoretical predictions of homogeneous ice nucleation of micrometer sized aqueous solution droplets[14,15].

subsaturated aqueous solution. Even so a droplet may be in a metastable state, it can remain liquid although not thermodynamically favored. The data in Fig. 2.3 indicate at which position a phase change is likely to occur.

2.3 Hygroscopicity, growth factor, and cloud droplet activation

Measurements of DRH and ERH for both sea salt and NaCl occur similarly around 75% and 45% for $T > 245$ K. At room temperature and RH > DRH, sea salt will be completely dissolved in water as indicated by the red shaded region. For DRH > RH > ERH, an aqueous solution will be in the metastable regime, existing as a supersaturated aqueous solution. When a crystalline particle deliquesces and takes up water its size will increase as a result, growing to just under twice its dry diameter, if sufficient time is allowed for the aqueous droplet to come into equilibrium with its humidified environment. At RH = 80%, the growth factor, g, or the ratio between the droplet diameter and dry diameter, will be 2.0 and it will continue to grow along the aqueous trajectory seen in Fig. 2.2 if exposed to higher RH.

Over a highly curved pure water droplet, the vapor pressure is higher than over a flat surface according to the Kelvin equation[41,42] and thus, cloud droplet formation only involving the vapor phase would require supersaturation in excess of hundreds of percent. Aqueous aerosol particles, on the other hand will grow in size to maintain equilibrium with their surroundings, thus, reducing the supersaturation required to nucleate a cloud droplet following Köhler's theory[41]. When a critical supersaturation is reached, liquid cloud droplets can form and grow to sizes on the order of 10 μm in diameter. The larger or more hygroscopic an initial crystalline aerosol particle is, the larger it will become due to water uptake and the less supersaturation is required to form a cloud droplet. Conversely, less hygroscopic particles may be less efficient to act as CCN. Thus, hygroscopicity is an important characteristic of aerosol particles allowing one to understand their ability to convert vapor to liquid, grow in size and to act as CCN for liquid cloud formation.

Sea spray particles can consist of organic material in addition to inorganic sea salts which may affect their hygroscopicity and their ability to act as CCN[41,97,99,122–124] For example, Fuentes *et al.*[106] showed that g for laboratory generated sea spray particles from seawater enriched in organic carbon material dissolved organic carbon (DOC), defined as organic material < 0.2 μm in size, was less than for pure sea salt. This may be because organic material can be less hygroscopic than sea salt alone and a mixed sea salt/organic particle will not take up as much water resulting in a smaller particle than if it were composed entirely of sea salt. The Zdanovskii-Stokes-Robinson mixing rule[125] describes g for a two-component aerosol particle (sea salt and organic material) as the contribution of particle growth from each component following the equation,

$$g = ((1 - \epsilon_{\text{org}})g_{\text{inorg}}^3 + \epsilon_{\text{org}}g_{\text{org}}^3)^{1/3}, \tag{5}$$

where g_{inorg} and g_{org} are the growth factors of the inorganic and organic material, respectively. The organic volume fraction of the particle is ϵ_{org}. In other words, if a sea spray particle is 50 % sea salt with $g_{\text{NaCl}} = 2.0$ and 50 % organic with $g_{\text{org}} = 1.2$, then using Eq. 5 would predict $g = 1.7$ for the mixed particle. Data from McFiggans *et al.*[123] concludes that for aerosol particles sampled from remote marine air with particle sizes

between $50 - 150$ nm in diameter, $g = 1.42 - 1.78$, possibly consisting of sea salt, organics or sulfate. At high wind speeds and for much larger particles, growth factors corresponding to pure sea salt are observed, although infrequently[123].

Organic materials in sea spray aerosol particles may also change the surface tension between the liquid and air, $\sigma_{l/g}$, resulting in a change of the Kelvin effect and CCN activation[41,123,124,126]. Moore *et al.*[126] measured the surface tension of seawater and the CCN activation of atomized seawater from the Atlantic coast. The authors found that direct measurements of $\sigma_{l/g}$ agreed with those calculations for observation of CCN formation, and conclude that the organic compounds in seawater act to depress $\sigma_{l/g}$ and decrease the critical supersaturation for cloud droplet activation[126] following the Köehler theory[41]. Direct measurement of nanometer sized aerosol particle surface tension in the atmosphere is not currently possible. Thus, only inferences from measurements of critical supersaturation for cloud droplet activation due to organic containing particles can be made[41,123,124,126].

2.4 Aerosol particle size distributions

In order to describe aerosol particle production, a size distribution can be defined as the concentration of particles per volume of air in a specific size interval normalized to the difference between upper and lower interval limits. Due to the fact that aerosol particle diameters can span orders of magnitude, the size distribution is conveniently expressed as on the decadal logarithmic scale of the particle diameter. The particle size distribution is calculated according to

$$\frac{dN}{d\log D_p} = \frac{dN}{\log(D_{p,i}) - \log(D_{p,i-1})}, \tag{6}$$

where dN is the concentration of particles per volume of air in a single size bin having an upper interval diameter $D_{p,i}$ and a lower interval diameter $D_{p,i-1}$, where $D_{p,i} > D_{p,i-1}$[41]. On a decadal log scale, the concentration is normalized to the difference in the log of the diameters, $d\log D_p$. On a linear scale the difference of diameters, dD_p, is used. This normalization is necessary for comparing size distributions measured with different bin widths. It is also common in laboratory studies to compare only the shape of the size distribution, accomplished by dividing Eq. 6 by the observed total particle concentration, N_{tot}, so that upon integrating, the result is equal to unity. The same mathematical description for aerosol particles can also be applied to quantify the amount of bubbles at a particular size in water. The bubble size distribution $dN_b/d\log D_b$ is substituted in Eq. 6, where dN_b is the concentration of bubbles in a single bubble diameter size bin normalized to the diameter bin width, $d\log D_b$.

Although useful for comparing laboratory observations, $dN/d\log D_p$ is, however, cumbersome for use in models because the data based on experimental results can be discontinuous in particle diameter. It is therefore, customary to fit the size distribution to a superposition of lognormal distributions having the form

$$\frac{dN}{dD_p} \simeq n_N(D_p) = \sum_{i=0}^{M} \frac{N_{\mathrm{tot}}^i}{(2\pi)^{1/2} D_p \ln \sigma_g^i} \exp\left(-\frac{(\ln D_p - \ln \overline{D}_{pg}^i)^2}{2\ln^2 \sigma_g^i}\right), \tag{7}$$

where dN/dD_p is the discontinuous particle size distribution on a linear diameter scale, $n_N(D_p)$ is the continuous fitted size distribution on a linear scale, M is the number of lognormal modes and N^i_{tot} is a fitting parameter that describes the total amount of particles contributing to N_{tot} only from the i^{th} mode. The lognormal fitting parameters for each mode, σ^i_g and $\overline{D}^i_{pg}$, are the geometric standard deviation and the median diameter of the particle population, respectively[41]. A simple conversion is required to obtain the fitted continuous size distribution on the decadal log scale, $n^\circ_N(d\log D_p) = 2.303 D_p n_N(D_p)$.

2.5 Classical nucleation theory

2.5.1 Homogeneous Ice Nucleation

Homogeneous ice nucleation is a kinetic process as there exists a probability for ice to form at water partial pressures supersaturated with respect to ice, or $\text{RH}_{\text{ice}} > 100\%$. The kinetic ice nucleation process can be described by classical nucleation theory (CNT)[42] in terms of a time-dependent homogeneous ice nucleation rate coefficient, J_{hom}, in units of $\text{cm}^{-3}\ \text{s}^{-1}$. Analogous to a rate constant for chemical reactions, J_{hom} describes the rate of ice nucleation and scales with the aqueous volume of a supercooled liquid droplet. That is to say for larger liquid volumes, ice nucleation is more probable. Also, as the length of time that a single supercooled droplet remains at a constant temperature increases, the freezing probability increases following a exponential probability distribution function. It is important to note that J_{hom} is independent of aqueous volume and time, and only depends on thermodynamic parameters such as T and RH_{ice}. J_{hom} is related to the formation and growth of water molecule clusters in the bulk volume of a droplet to become the center of a critical ice embryo[42,127]. Figure 2.4 depicts the energy of a cluster as it grows and reaches a critical size to form an ice embryo and thus, trigger ice nucleation, commonly referred to as the Gibb's free

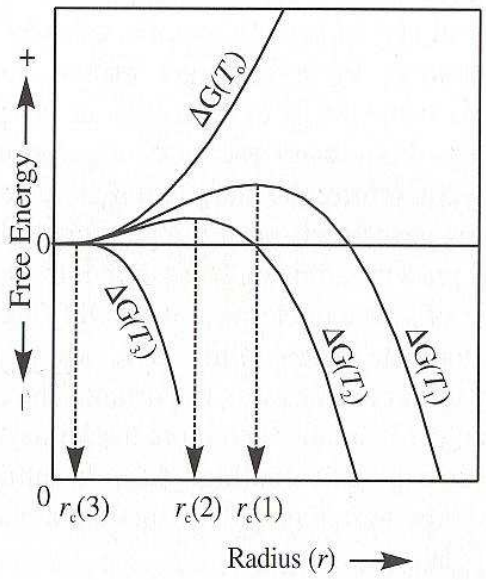

Figure 2.4: The Gibb's free energy of formation for a cluster of H_2O molecules as a function of cluster radius, r_c, taken from Nesse[16]. The temperature, T_0, is warmer than the ice-liquid equilibrium temperature, T_m, and other temperatures indicate higher levels of supercooling, i. e. $T_m > T_1 > T_2 > T_3$.

energy, ΔG[16,42].

At the ice melting temperature, T_m, formation of a critical ice embryo is impossible and thus, ΔG approaches infinity with increasing cluster size. However, at any supercooling for temperatures below T_m, there exists a critical cluster radius at which point the water molecular cluster is in an unstable equilibrium characterized by a local maximum in ΔG. When the critical cluster radius is surpassed, ice nucleation occurs followed by a cascading decrease of $\Delta G$and bulk crystallization. Figure 2.5 illustrates water molecules experiencing cluster formation and growth followed by the formation of the critical embryo in supercooled water. J_{hom} is the rate at which ice embryos form and governed by the equation,

$$J_{\text{hom}}(T) = \frac{k_{\text{b}}T}{h}\exp\left(-\frac{\Delta F(T)}{k_{\text{b}}T}\right) n_v \exp\left(-\frac{\Delta G(T)}{k_{\text{b}}T}\right), \tag{8}$$

where k_{b} is the Boltzmann constant, h is Planck's constant and n_v is the number density of water molecules in the aqueous volume[42]. Parameterization of thermodynamic variables involved in Eq. 8 are found collectively in Zobrist *et al.*[128]. $\Delta F(T)$ is the diffusion activation energy calculated from

$$\Delta F(T) = \frac{d\ln\left[D_{\text{H}_2\text{O}}(T)\right]}{dT} k_{\text{b}}T^2, \tag{9}$$

where $D_{\text{H}_2\text{O}}$ is the diffusivity of, e. g. water in aqueous solution[129]. $\Delta G(T)$ is referred to in the remainder of this dissertation as the Gibb's free energy of formation of a critical ice embryo for homogeneous ice nucleation and can be described by

$$\Delta G(T) = \frac{16\pi}{3}\frac{\nu^2(T)\sigma_{i/l}^3(T)}{\left[k_{\text{b}}T\ln S_{\text{ice}}(T)\right]^2}, \tag{10}$$

where ν and $\sigma_{i/l}$ are the volume of a water molecule in ice and the interfacial energy as a function of T

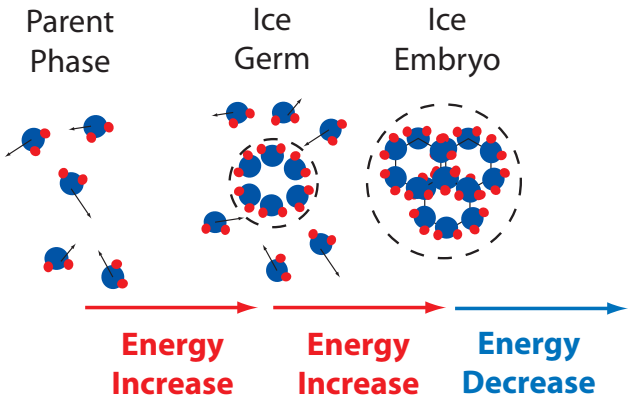

Figure 2.5: Illustration of the formation of the critical ice embryo for homogeneous ice nucleation is shown. Water molecular clusters increase in size corresponding to an increase in Gibbs free energy, ΔG. Ice supersaturation also increases until a critical ice embryo is formed.

between ice and the surrounding parent phase, respectively[41]. The volume of a water molecule in ice is,

$$\nu = \frac{M_w}{N_A \rho_0}(1 - 0.05294T_r - 0.05637T_r^2 - 0.002913T_r^3)^{-1}, \tag{11}$$

where the reduced temperature, T_r, is given as $(T - T_m)/T_m$, M_w is the molar mass of water, ρ_0 is the density of ice at T_m and N_A is Avogadro's constant[128]. The liquid-ice interfacial energy is,

$$\sigma_{i/l} = 3.298 \times 10^{-6} + \left(1.2048 \times 10^{-6}\right) T_r - \left(4.6705 \times 10^{-5}\right) T_r^2, \tag{12}$$

as parameterized by Zobrist *et al.*[128] for pure water. Parameterization of water diffusivity in pure water is given in Smith and Kay[130] as,

$$D_{\mathrm{H_2O}}(T) = D_0 \exp\left(-\frac{E}{T - T_0}\right), \tag{13}$$

where $E = 892$ K, $T_0 = 118$ K, and $D_0 = 3.06 \times 10^{-3}$ cm^2 s^{-1} for pure water following the Vogel-Fulcher-Tammann equation[130].

An outstanding issue of CNT for homogeneous ice nucleation is the unknown dependency of these parameters on solute concentration especially at supercooled temperatures. Only a few studies have investigated $\sigma_{i/l}$ and $D_{\mathrm{H_2O}}(T)$ in aqueous solution. Jones and Chadwick[131], for example, were able to estimate the interfacial energy from the contact angle between ice planes in aqueous solutions at thermodynamic equilibrium in the solution melt which occurs at temperatures warmer than the eutectic and colder than the melting temperature. The authors calculated that $\sigma_{i/l}$ increases as the concentration of NaCl increases. Molecular dynamic studies have investigated $D_{\mathrm{H_2O}}(T)$ for multiple solutions and concentrations[36,132]. Kim and Yethiraj[36] for example found that at room temperature, $D_{\mathrm{H_2O}}(T)$ in aqueous NaCl solution was less than that for pure water for all concentrations. However, as temperature decreases, $D_{\mathrm{H_2O}}(T)$ can be greater than that of pure water, for example at 260 K and for NaCl concentrations up to 5 M, $D_{\mathrm{H_2O}}(T)$ is up to 1.5 times greater than for pure water and peaks at a concentration of about 1.5 M[36]. Despite advances in models and experiments to determine these thermodynamic parameters, values of $\sigma_{i/l}$ and $D_{\mathrm{H_2O}}(T)$ still remain elusive for many solutes and especially at highly supercooled temperatures when homogeneous ice nucleation takes place.

2.5.2 Heterogeneous ice nucleation: Immersion and deposition freezing

The conceptual framework for heterogeneous ice nucleation via immersion freezing follows closely to that of homogeneous ice nucleation except that the presence of a foreign substrate acts to reduce $\Delta G(T)$, thus a critical ice embryo is formed on the surface of an ice nucleus more favorably than in the bulk aqueous phase. On the surface of an insoluble particle, certain characteristics make an efficient ice nucleus, such has having a similar crystallographic molecular structure as that of ice or having a surface chemistry capable of influencing the hydrogen bonding network of water molecules similar to ice. Additionally, surface inhomogeneities such as cracks, edges, pores, or cavities, in addition to possible chemical impurities may nucleate ice preferentially

in some cases[42]. Heterogeneous ice nucleation rates, J_{het}, with units of cm^{-2} s^{-1} scale with the IN surface area and describe the rate of ice embryo formation on the surface of IN. J_{het} is derived by

$$J_{\text{het}}(T) = \frac{k_{\text{b}}T}{h} \exp\left(-\frac{\Delta F(T)}{k_{\text{b}}T}\right) n_s \exp\left(-\frac{\Delta G(T)}{k_{\text{b}}T} f_{\text{het}}\right), \tag{14}$$

where n_s is the number density of water molecules at an ice nucleus surface and f_{het} is the fractional reduction in $\Delta G(T)$ due to the IN, i. e. $0 \leq f_{\text{het}} \leq 1$. All other thermodynamic variables are the same as in Eq. 8. The fractional reduction of $\Delta G(T)$, commonly referred to as the compatibility factor, depends on the contact angle, α, and is described by

$$f_{\text{het}}(m) = \frac{m^3 - 3m + 2}{4}, \tag{15}$$

where $m = \cos(\alpha)$. The contact angle is a useful parameter which holds information on the interplay of energy between three interfaces: the ice nucleus, the ice embryo, and the surrounding parent phase which can be aqueous solution or supersaturated water vapor.[42,133]. Figure 2.6 illustrates the contact angle of an ice embryo on an ice nucleus surface as a spherical cap. Note that the curvature of the ice nucleus surface is assumed to be much larger than that of the ice embryo, an assumption used in Eq. 15. Values of α can be between 0° indicating complete compatibility, i. e. $f_{\text{het}} = 0$ and no Gibb's free energy of formation exists, and 180° indicating complete incompatibility, i. e. Gibb's free energy is not reduced compared with homogeneous ice nucleation.

In the deposition mode, α characterizes the interfacial energies between the ice nucleus, the ice embryo, and the supersaturated water vapor phase. As a result, Eq. 14 is modified to

$$J_{\text{het}}(T) = A \cdot \exp\left(-\frac{\Delta G(T)}{k_{\text{b}}T} f_{\text{het}}\right), \tag{16}$$

where $A = 10^{25}$ cm^{-2} s^{-1} is the kinetic coefficient defined as the rate at which a critical ice embryo gains one molecule from the vapor phase[134–136]. $\Delta G(T)$ for deposition freezing depends on the interfacial energy between the ice embryo and supersaturated water vapor phase, $\sigma_{i/v} = 106$ mJ m^{-2}, taken from previous literature[42,136].

CNT can provide a physical understanding of the underlying kinetics of the ice nucleation mechanism from thermodynamic variables involved in the formation of the solid phase such as $D_{\text{H}_2\text{O}}$ and $\sigma_{i/v}$. The application of CNT for homogeneous and heterogeneous ice nucleation is, however challenging due the lack

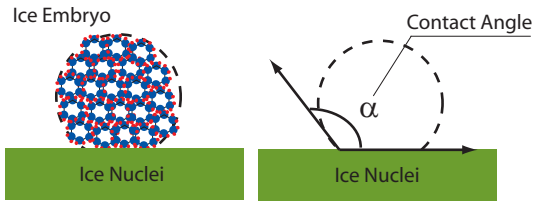

Figure 2.6: The critical ice embryo that forms on the surface of an ice nucleus is depicted and exhibits a contact angle, α, with the ice nucleus surface.

of thermodynamic data. Additionally, the unknown relationship between an ice nucleus surface and aqueous solution adds further complexity to understanding heterogeneous ice nucleation. There is also concern when employing CNT to describe ice nucleation due to the inherent assumption that bulk thermodynamic parameters can describe molecular dynamic interactions, known as the capillary approximation[41]. Despite these limitation, CNT has proven to be useful for a better understanding of and the only physical model for ice nucleation in the atmosphere.

2.5.3 Models of heterogeneous ice nucleation

Experimental studies of heterogeneous ice nucleation conducted in laboratory settings typically measure the frozen fraction, f, of droplets or particles[35,42,137–141]. Various descriptions of heterogeneous freezing using CNT are used to fit f and evaluated on their ability to reproduce f in ice nucleation experiments. The common approach of these models is to statistically represent ice nucleating properties of a particles' surface with probability density functions or randomly sampled values of α in a particle population[42,117,128,137,139,141,142]. The first model called single-α, sets one value of α for the entire particle population. The second model, α-PDF, assumes that values of α are distributed with a lognormal distribution, with each particle having one value of α. The active site model assumes that multiple surface sites are distributed over the particle following a Poisson distribution with areas equivalent to the ice embryo size and having different values of α. A fourth model is time-independent called the deterministic model. It is assumed that each nucleation event is triggered by an active site at a characteristic temperature, and thus f is a function of temperature only and neglects the time dependence predicted by CNT. An underlying assumption for these models is that the interactions of the particle surface with aqueous solution, pure water, or water vapor does not change with differences in T, a_{w}, or $\mathrm{RH_{ice}}$.

This concept of fitting to and reproducing the same experimental data set, as done in these models, does not provide a fundamental proof of any underlying ice nucleation mechanism, a weakness in their construct. Additionally, f is dependent not only on T and $\mathrm{RH_{ice}}$, but also on the range of particle surface area and experimental time constrained in the laboratory, and any empirical parameterization fitted to f can only be strictly applied within the range of parameters investigated in the laboratory[141].

These four models were evaluated by Rigg *et al.*[141] employing immersion freezing data from surrogates of humic soils in pure water and in aqueous solutions of $(NH_4)_2SO_4$. The authors found that the single-α model could not reproduce the experimental data, but for an individual aqueous $(NH_4)_2SO_4$ concentration, the other three models perform equally well. Unfortunately, no model could account for the entire range of solution concentrations investigated by the authors[141]. This suggests that any underlying ice nucleation mechanisms cannot as of yet, be uncovered by fitting to and reproducing f employing statistical interpretations of α. In a modeling study by Ervens and Feingold[143], the performance of the different statistical models in an ice cloud parcel model was investigated. The authors concluded that these parameterizations formulated from data collected in laboratory experiments could not be applied to the atmosphere due to their high sensitivity of ice particle production on T, time, or surface area outside of the range that they were investigated[143]. Rigg *et al.*[141] suggested that the same conclusion should also hold for different solute concentrations. This

is in contrast to derivations of J_{het} from CNT, which are independent of surface area or time.

Laboratory studies can derive J_{het} directly from experimental data as long as particle surface area, T, and the time it takes for ice nucleation to occur, referred to as nucleation time, t_{nuc}, are known. This involved CNT to derive nucleation kinetics without any fitting procedure. In this way Eq. 14 and Eq 16 can be used to calculate α for various particle types as done for ice nucleation of aqueous droplets[35,117,128,140,141,144] and for deposition freezing[145–150]. These studies have all shown that α calculated from experimentally derived J_{het} shows a strong dependence on T and solute concentration for immersion freezing, and on $\mathrm{RH_{ice}}$ for deposition freezing. This implies that the interfacial energies between the ice embryo, ice nucleus, and the surrounding parent phase may be altered by thermodynamic variables in such a way to vary the contact angle. This is in contrast to the suggestion from statistical models mentioned above, that assume that α is a fixed property of a particle surface.

2.6 A water activity based description of ice nucleation

2.6.1 Homogeneous ice nucleation

The process of homogeneous ice nucleation scales with the volume of the aqueous solution and t_{nuc} for $S_{\mathrm{ice}} > 1.0$[33,42,127,151]. Koop *et al.*[14] introduced the parameter a_{w} to describe homogeneous ice nucleation by predicting freezing temperatures and J_{hom} for pure water and aqueous solutions droplets without knowledge of solute composition. Koop *et al.*[14] has shown that homogeneous freezing temperatures for different types of aqueous solutions and concentrations as a function of a_{w} all fall along one freezing curve constructed from the thermodynamically defined ice melting curve as a function of a_{w}[14]. A positive horizontal shift in the ice melting curve by the defined quantity Δa_{w} toward values of higher a_{w} completely represents the homogeneous freezing curve[14,15]. The equation used to calculate Δa_{w} is

$$\Delta a_{\mathrm{w}} = a_{\mathrm{w}} - a_{\mathrm{w}}^{\mathrm{ice}}(T), \tag{17}$$

where $a_{\mathrm{w}}^{\mathrm{ice}}(T)$ is the thermodynamic ice melting curve in the water activity - temperature space[5,15]. Since the ice melting curve is fixed, Δa_{w} represents pairs of T and a_{w} for any freezing point. This concept is demonstrated by the example in Fig. 2.7 adapted from Knopf and Alpert[17].

Furthermore, each constructed freezing point curve representing a specific Δa_{w} value describes a single J_{hom} value. A decrease in Δa_{w} translates into increased freezing temperatures and a decreased J_{hom} value with J_{hom} converging to zero as T approaches the ice melting point. Figure 2.7 shows that the homogeneous freezing curve (shown as a grey dashed line) is determined for $\Delta a_{\mathrm{w}} = 0.313$ and corresponds to a J_{hom} value on the order of 10^9 cm^{-3} s^{-1}. The a_{w} based description of homogeneous ice nucleation kinetics has been found to be generally valid experimentally[14,33–35,152–154] and when used in cloud parcel and climate models[155–159]. However, a drawback of the water activity based homogeneous ice nucleation theory is, that for many aqueous solutions, a_{w} is inferred at or above the ice melting point having been obtained by extrapolation at supercooled temperatures using thermodynamic models[160–165]. If no data or model are available, it is assumed that a_{w} does not vary significantly with decreasing temperature, as is the case for

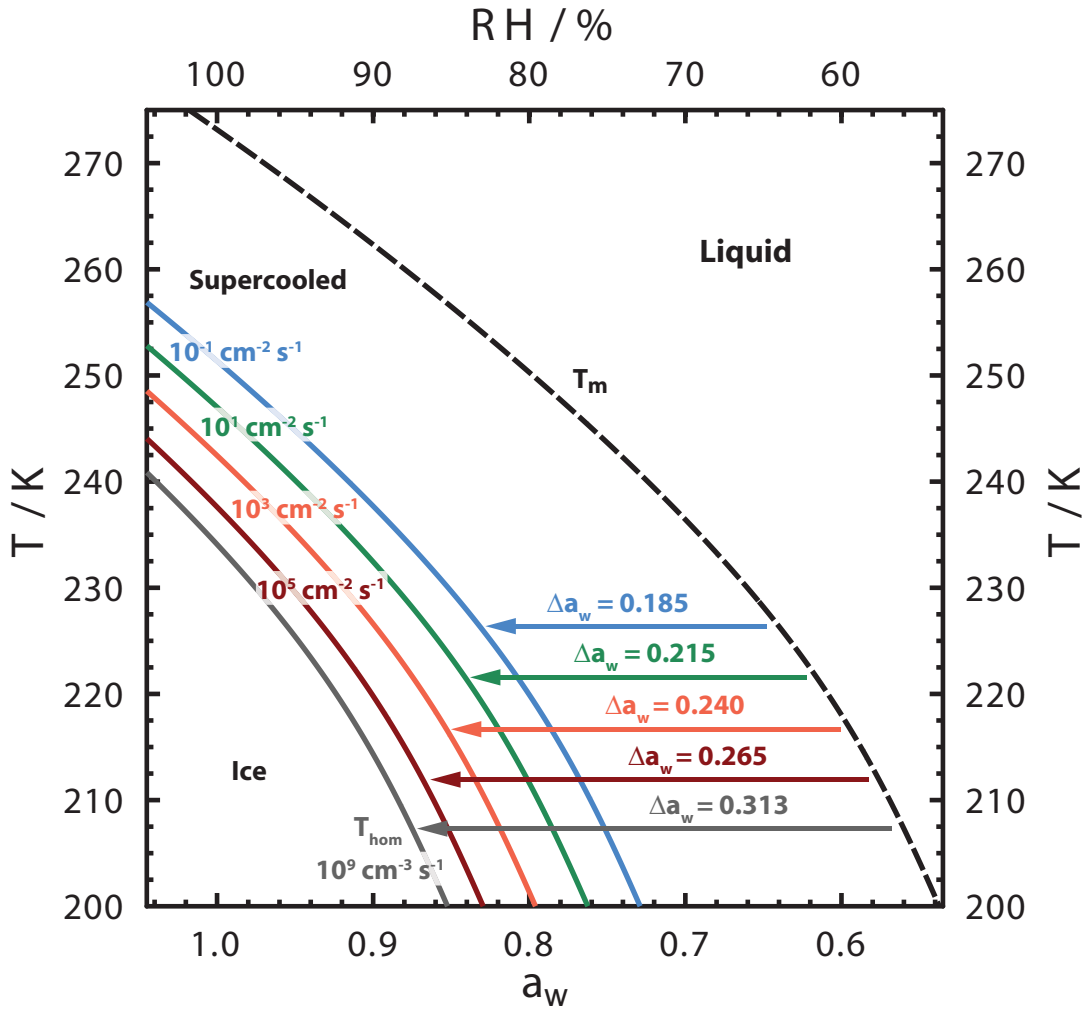

Figure 2.7: Summary of the conceptual framework of the water activity based homogeneous ice nucleation description[14] and water activity based immersion freezing description adapted from Knopf and Alpert[17]. The dependency of homogeneous and heterogeneous freezing temperatures and homogeneous and heterogeneous ice nucleation rate coefficients in units cm^{-3} s^{-1} and cm^{-2} s^{-1}, respectively, on the water activity criterion, Δa_{w},, are shown. Homogeneous and heterogeneous ice nucleation temperatures and rates are given as gray and colored lines, respectively. This criterion implicitly accounts for changes in nucleation time and available ice nuclei surface area. Numbers for the ice nucleation rate coefficients have only an exemplary purpose.

many, but not all inorganic and inorganic/organic aqueous solutions[14,15,33,34,144,152,153,166]. In general, using a_{w} greatly simplifies the prediction of homogeneous freezing temperatures and kinetics for aqueous solution droplets.

2.6.2 Immersion freezing

Laboratory studies have shown that immersion freezing temperatures of many different types of IN follow a freezing curve generated by Δa_{w} independent of the nature of the surrounding aqueous solu-

tions[15,34,35,117,141,144,166–169] as conceptually shown in Fig. 2.7. Prediction of J_{het} using Δa_w, similar to homogeneous ice nucleation, is termed the water activity based immersion freezing model (ABIFM), introduced by Knopf and Alpert[17]. For decreasing Δa_w values, freezing temperatures increase and J_{het} values decrease as shown in Fig. 2.7. It should be noted that J_{het} is a coefficient and independent of IN surface areas or nucleation times, but dependent only on T and a_w. The ABIFM can be used to predict freezing temperatures and nucleation kinetics accounting for all possible changes in the parameters controlling the nucleation process. It therefore represents a holistic model of immersion freezing. For example, in the studies of Knopf and Forrester[144], the median freezing temperatures of 1-nonadecanol coated aqueous solution droplets were found to follow a freezing curve parameterized only by Δa_w like those seen in Fig. 2.7. Knopf and Forrester[144] also found that a parameterization of J_{het} only as a function of Δa_w for pure water, could also describe J_{het} for droplet freezing of NaCl solutions. This is remarkable due to the fact that aqueous solution data was not used to describe $J_{het}(\Delta a_w)$. Later, Knopf and Alpert[17] found that median freezing temperatures and heterogeneous ice nucleation kinetics of phytoplankton cells and cell fragments[17,35,117], Humic like substances[141], fungal spores[170] and the mineral dusts illite[17,171,172], kaolinite[172,173], aluminum oxides and iron oxides[168] could also be described by Δa_w. For every particle type, a single J_{het} value can be calculated from knowing only Δa_w independent of the nature of the aqueous solution that particle is immersed in[17]. This implies that Δa_w is the determinant of the ice nucleation process similar to the homogeneous ice nucleation case.

Kärcher and Lohmann[174] described immersion freezing as a function of a_w in a cloud resolving model by parameterization of the water activity based homogeneous ice nucleation theory[14]. Due to a lack of a physical model and experimental data, J_{hom} values were shifted with respect to a_w to yield J_{het} assuming a nucleation rate of 1 s^{-1} at $S_{ice} = 1.2$. In other words, heterogeneous freezing rates are tied to homogeneous freezing rates resulting in similar dependencies on water activity and exactly the same temperature dependency despite their different underlying nucleation mechanisms. Thus, homogeneous and heterogeneous ice nucleation are not independent of each other in the parameterization by Kärcher and Lohmann[174]. A physical model of heterogeneous ice nucleation should be decoupled from homogeneous ice nucleation.

The ABIFM offers a physically based alternative approach for calculating J_{het} because only the single parameter Δa_w is needed, thus circumventing the capillary approximation in CNT and any need for bulk thermodynamic parameters (Eqs. 8-15). Furthermore, it is independent of homogeneous ice nucleation. This physically based model is rooted in CNT, however, does not require an extensive collection of bulk thermodynamic data to implement. Thus, the ABIFM more easily provides J_{het} for application in parcel, cloud resolving, or climate models to predict ice nucleation.

3 Experimental

3.1 Aerosolization of marine biogenic particles

3.1.1 Mesocosm tank, bubble generation, aerosolization and impaction

Experiments were carried out in a 1000 L mesocosm which allowed for controlled growth of microbial communities. Quantitative measurements of bubble production were made, aerosol particle size distributions under dry and humidified conditions were determined, and aerosol particles for chemical characterization and ice nucleation experiments were collected. The mesocosm contained either artificial seawater (ASW) or natural seawater (NSW) which was temperature controlled and had illumination optimized for sustaining phytoplankton growth for a 2 week period. Figure 3.1 shows a schematic of the mesocosm tank modeled after previous experimental setups[19,82,97,175–179]. Sea spray aerosols are generated via bursting of bubbles produced by glass frit aeration[25–27,27,180,181] and plunging water impingement jets[19,82,97,98,175] in the seawater filled mesocosm. At $\sim$ 1.5 m in height, the enclosed tank incorporates a system of eight identical high speed ($\sim$ 1.5 m s^{-1}), high volume (1 L min^{-1}) water jets and 4 bottom-mounted 90 mm diameter glass aerators with a pore size of $10 - 16$ μm to produce bubble plumes. At the surface the dispersed plumes burst, producing aerosol particles. Compressed filtered and particle free air is injected into the head space at 10.0 L min^{-1} above the water surface to transport freshly generated aerosol particles out of the tank

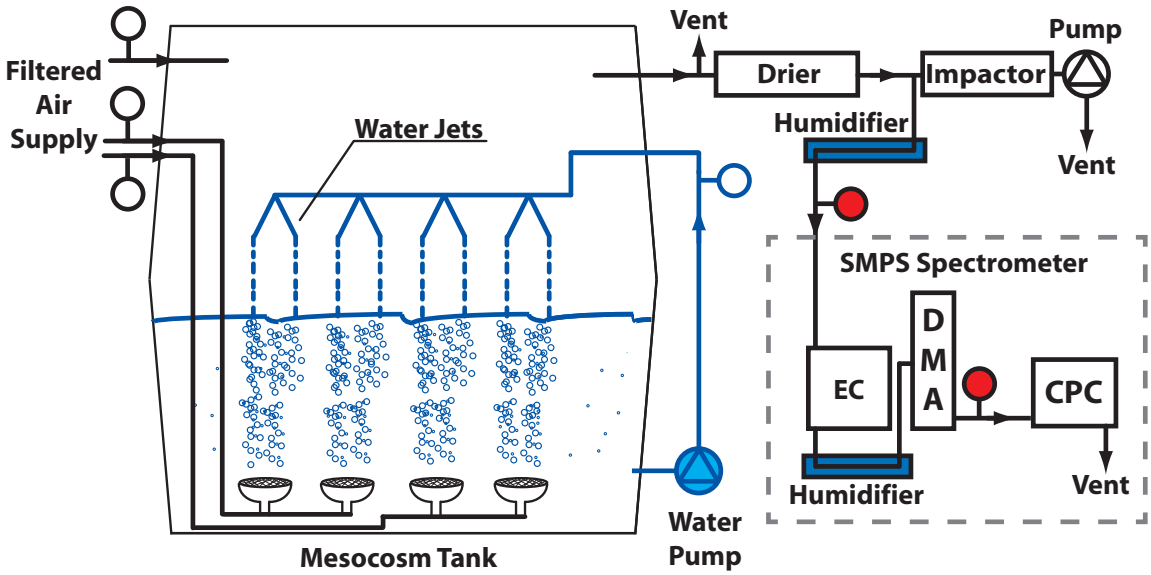

Figure 3.1: Schematic of the mesocosm system for generation of marine particles by bubble bursting from impinging water jets and aeration through glass frits. Blue lines indicate water flow and black lines show air flow. Blue and black circles indicate the position of a water or air valve and flow meter, respectively. Particles are first dried in a diffusion drier, and then are either collected utilizing an impactor or their size distribution is measured with a scanning mobility particle sizer spectrometer (SMPS) comprised of an electrostatic classifier (EC), differential mobility analyzer (DMA), and condensation particle counter (CPC). Humidifiers are placed in series with the air flow indicated by the blue rectangles when a humidified size spectrum is measured. When measuring a dry particle size spectrum, the humidifiers are removed. Humidity probes are indicated by red circles.

through individual ports after first passing through a diffusion dryer to obtain a dry particle flow. Next the particles are either collected on sample substrates with an impactor for concurrent physical and chemical characterization or the particle size distribution is measured. The size distribution of aerosol particles in the polydispersed aerosol flow is measured using a scanning mobility particle sizer spectrometer (SMPS, TSI Mo. 3936) shown in Fig. 3.1 composed of an electrostatic classifier (EC, TSI Mo. 3080) and a long differential mobility analyzer (DMA, TSI Mo. 3081) coupled to a condensation particle counter (CPC, TSI Mo. 3775). A humidified size spectrum is also measured employing two inline humidifiers, one before the inlet of the SMPS (PermaPure MH-070-12) and another used to humidify a particle free air recirculating flow (sheath flow) in the DMA (PermaPure MH-070-12). When a dry aerosol size spectrum is desired, the humidifiers are easily removed. The humidity is continuously monitored using hand held humidity probes (Vaisala HMP75).

3.1.2 Aerosol size distribution measurements

The SMPS is capable of separating particles by diameter for high nanometer resolution measurements of the particle size distribution in the range of $10-1000$ nm. Particles sampled by the SMPS are given an equal charge by the EC, then enter into the DMA where they are separated by their electrical mobility, and finally counted optically by the CPC. The CPC has the ability to detect particles as small as 4 nm in diameter and particle concentrations up to 10^7 cm^{-3} in air. Dry and humidified particle size distributions are measured for RH $< 20\%$ and $80\% \pm 4.0\%$, respectively. The humidifier for the sheath flow of the DMA is necessary to keep aqueous particles from evaporating which would change their size. The two humidifiers shown in Fig. 3.1 use temperature controlled and recirculated distilled and deionized water to supply humidity to the air.

3.1.3 Aerosol particle collection

Particles were collected by impaction on a variety of substrates using a SKC Sioutas Cascade Impactor with an air flow rate of 9 L min^{-1}. Sample substrates were taped to the final stage of the impactor with a 50% collection efficiency, d_{50}, at a particle diameter of 0.25 μm. The polydispersed aerosol flow first passes through 3 other stages with $d_{50} = 0.5$ μm, 1.0 μm and 2.5 μm prior to passing through the last stage. The top three particle collection plates were coated with high vacuum grease preventing as many particles as possible larger than about 0.5 μm, to move to the final stage. Four substrates were used for particle collection, hydrophobically coated glass discs 11 mm in diameter, 2 mm silicon wafer squares, 1 mm square silicon nitride windows 100 nm thick supported on 5 mm square silicon wafers, and $15-25$ nm thick carbon coated copper grids. Prior to particle collection, the substrate surfaces were cleaned and confirmed to be particle free using optical microscopy at 500x magnification. After particle collection, the substrates are placed into a petri dish, flushed with dry, particle free N_2 gas and sealed from ambient air. The particles on substrates were used for examining ice nucleation and chemical imaging described later.

3.1.4 Bubble lifetime and size distribution measurements

Bubble plumes generated with the water jets penetrate the bulk water to a depth of ~ 15 cm although the smallest bubbles < 1 mm in diameter can penetrate toward the bottom of the tank (~ 50 cm) where they are

thoroughly mixed. When generated by bottom-mounted aerators set $\sim$ 10 cm from the tank bottom, bubbles rise the remaining 40 cm to the water surface at a total air flow rate of about 0.5 L min^{-1}, 0.125 L min^{-1} per each aerator. For various bubble diameters from plumes produced by the jet or the frit, the lifetime of a bubble, τ_b, is largely dependent on bubble terminal rise velocity, path length and turbulent motion due to the water or wake effects from the bubble itself or neighboring bubbles[97,178,182–187]. The tank was designed to represent realistic values of τ_b found in the ocean[19,82,97,175–179]. Calculations of τ_b for a representative range of bubble diameters, D_b, experienced in our mesocosm tank equal to 2.0 mm and 0.2 mm, yields $\tau_b = 24$ s and $\tau_b = 177$ s, respectively, using the jets. Bubbles generated by the frit move directly toward the water surface in contrast to the jet generated bubbles which initially move toward the tank floor, turn around and head to the surface. Thus, τ_b for frit generated bubbles is slightly less than for the jet, $\tau_b = 10$ s and 70 s for $D_b = 2.0$ and 0.2 mm, respectively. These lifetimes are similar to those observed in the open ocean in which bubble swarms can exist for τ_b on the order of seconds to minutes for a similar size range[24,97,176,177,188–190].

Measurements of the bubble size distribution were made from a single impinging jet and aerating frit from digital images taken with a Cannon 60D digital single lens reflex camera with a MP-E 65 mm super macro 1-5x lens positioned against a window in the side of a glass tank filled with Instant Ocean ASW at 16.5° C and a salinity of 35 ppt. Bubble diameters were measured at 1 cm and 11 cm away from the water jet center, 5 cm and 11 cm away from the glass aerator center, and 3 cm below the water surface in a sample volume with a field of view of 4 mm x 5 mm and depth of field of 1 mm using image analysis software. The measurement locations were chosen so as to not overcrowd the viewing area while obtaining the nascent bubble spectra. About 2000 individually sized bubbles were counted. Figure 3.2 gives examples of photographs of bubbles rising in the water. A millimeter ruler was submerged in the tank in the same location as the measurements and imaged for length calibration. After removal, bubble counts were taken without moving the SLR camera to maintain the calibration. Bubbles in focus with dark rings and bright centers were counted.

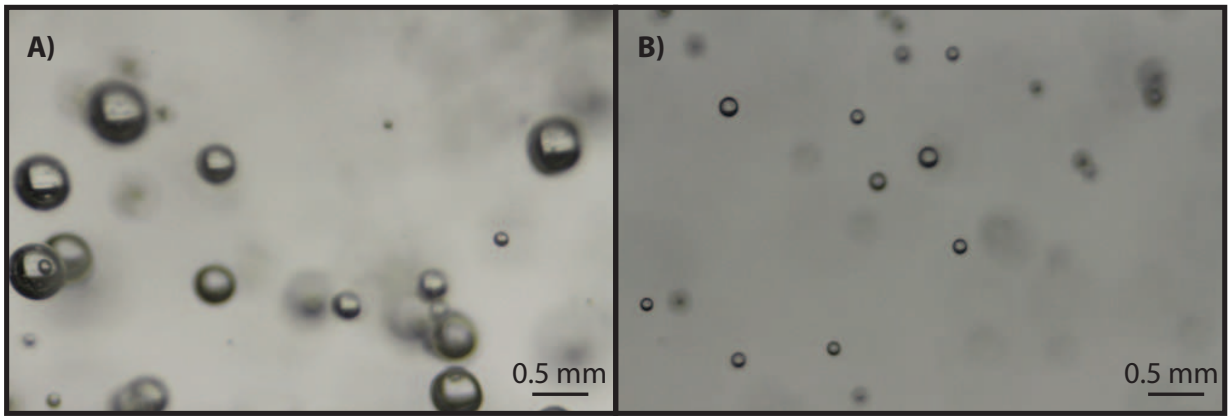

Figure 3.2: Example photographs of bubbles produced from A) a single water jet and B) aeration through a single glass frit.

3.1.5 Sea water analysis: Bacteria and phytoplankton concentration, dissolved organic carbon and particulate carbon

Aliquots of sea water were taken from the mesocosm intermittently for counting bacteria and phytoplankton, and quantification of dissolved organic carbon (DOC) and particulate carbon (PC). Two identical seawater samples 20 mL in volume are removed from the mesocosm, and immediately fixed either with lugols iodine for preservation of phytoplankton including diatoms and dinoflagellates or preserved with neutralized sodium borate treated formaldehyde solution at 4% final concentration for bacteria and nanoplankton. Samples were refrigerated and kept in the dark until examined. Identification, enumeration and classification into broad groups of algae were made using light microscopy and bacterial and phytoplankton abundances assessed by epifluorescence microscopy after staining with the fluorescent dye 4-, 6-diamidino-2-phenylindole (DAPI) after Porter and Feig[191] with a precision better than 5.0%.

Measurements of PC and DOC were taken simultaneously from a seawater sample 40 mL in volume. Seawater was filtered through a quartz-fiber filter retaining particulate matter above 0.1 μm and stored in a septum bottle. The resulting supernatant was acidified to a pH of 1.5 with roughly 3 drops of pure sulfuric acid to react inorganic carbon, such as CO_3^{2-}, to CO_2 prior to analysis in the DOC analyzer (Shimadzu TOC-L, $\pm$1% precision). The particulate remaining on the filter was then analyzed for carbon content using an elemental carbon combustion gas analyzer (Interscience Flash EA 1112, $\pm$2% precision). Contamination of DOC samples was carefully avoided by using only acid washed glassware and filter apparatus, and by pre-combusting the quartz fiber filters at 550° C.

3.1.6 Seawater and phytoplankton growth experiments

Measurements of the dry and humidified aerosol particle size distribution, particle collection by impaction and the seawater analyses outlined above were done as a function of the concentration of algal cells in the mesocosm tank. Eight independent growth experiments were conducted. First, control runs were performed twice where ASW was employed without any added nutrients, phytoplankton or bacteria. Experiments referred to as ASW-1 and ASW-2 represent the first day of adding ASW at the start of each control run. After experiment ASW-2, the seawater remained for 14 days in the mesocosm and particles in the air and water composition were quantified in a third experiment referred to as LowBact. A fourth experiment used a mixed bacterial culture obtained by enrichment of Great South Bay seawater and the addition of peptone and yeast extract (referred to as ASW-GSBBact). In three separate experiments, ASW was inoculated with a single phytoplankton species, *Thalassiosira pseudonana*, *Emiliania huxleyi* and *Nannochloris atomus* (referred to as Tpseu, Ehux, and Natom, respectively). *T. pseudonana* is a representative diatom averaging ~ 5 μm in size with a siliceous cell wall. Diatoms are cosmopolitan in the oceans and the dominant phytoplanktonic organism in polar regions[192,193]. *E. huxleyi* is a coccolithophorid with cells averaging 4 μm in diameter. These cells are covered by an array of ~ 30 interlocking calcium carbonate platelets or coccoliths[194] but with very little associated organic material compared to diatoms or other unarmored picoplankton. This species is widespread and abundant both at high latitudes[195,196] and low latitudes in oligotrophic and upwelled coastal waters[197,198] typically forming massive blooms with 10^8 cells mL^{-1} covering $> 100,000$ km^2[199]. The

microalga *N. atomus* has a cell wall of cellulose, and is among the smallest photosynthetic organisms reaching concentrations of 10^6 cells mL^{-1} in virtually all oceanic euphotic zones[200]. It is also capable of exponential growth forming widespread blooms and known to be a dominate species in the North Atlantic contributing to total phytoplankton concentrations reaching 10^8 mL^{-1} during the fall bloom[201]. The final mesocosm experiment employed natural seawater with added nutrients to grow a natural phytoplankton community. Roughly 800 L of seawater was collected off the south eastern shore of Long Island, NY at the Shinnecock inlet during incoming tide, and transported back to the lab to fill the mesocosm.

Water temperature was kept at 16° C at all times for all experiments. High output florescent lighting supplied 30 μE m^{-2} s^{-1} (micro-Einsteins per meter squared per second) of light where 1 E is equivalent to 6.022×10^{23} photosynthetically active photons. Algae were grown using a 14 hr light : 10 hr dark cycle. Due to the relatively heavy silica frustules of the diatom *T. pseudonana* compared with the other two phytoplankters, the seawater which contained *T. pseudonana* was mixed with a submersible pump set on the tank bottom to suspend the cells. A test to determine if mixing affected aerosolization found that the particle size distribution did not change whether or not the water was mixed, therefore mixing is assumed to not have an effect on aerosol flux.

Prior to mesocosm experiments, the head space in the tank was flushed with particle free air at 30 L min^{-1} for about 2 hours until the particle concentrations fell to around 5 cm^{-3} (air) prior to bubble production for the jet and frit, as shown in Fig. 3.3. Bubble production began after flushing was completed thus, the aerosolized particles in the head space were entirely due to the primary production from bubble bursting.

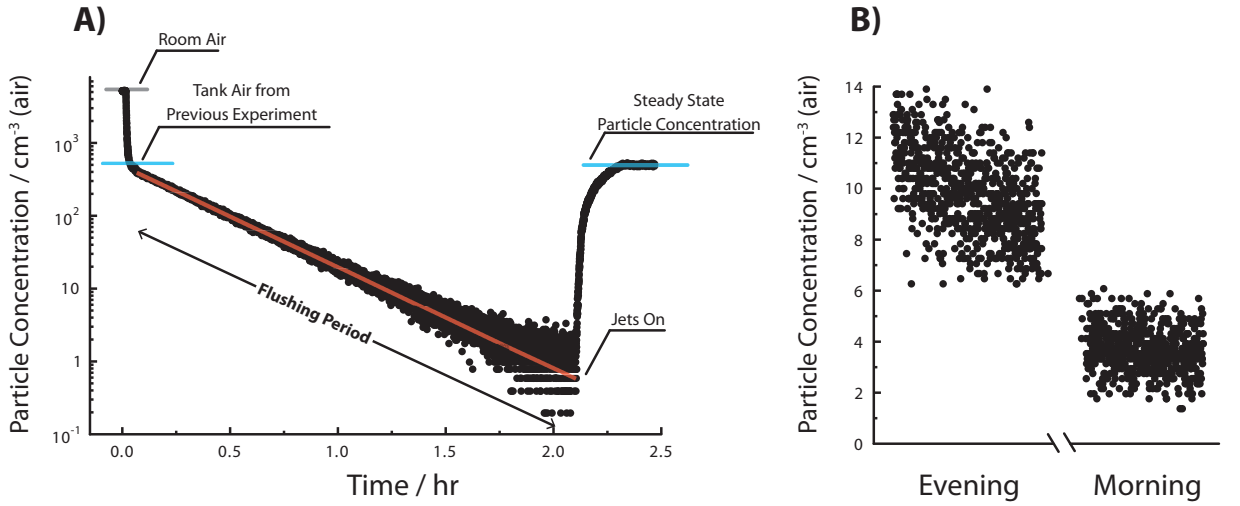

Figure 3.3: A: Measurements of particle concentrations in the mesocosm tank during a flushing procedure as a function of time. The particle concentration in the ambient air was initially measured for time, $t = 0$ hr. After a few minutes, particle concentrations from the tank were measured. The concentration of particles at $t = 0.1$ hr indicated by the blue horizontal line stem from a previous experiment employing jet generated aerosol particles. After tank flushing, the particle concentration falls to about 1 cm^{-3} on average at which point the water flow for jet impingement began. A sharp rise is seen from $2.1 - 2.25$ hr at which point a steady state particle concentration is obtained. Note that the final concentration for jet generated particles after steady state is reached, is the same as the initial concentration of particles prior to flushing. B: Measurements of particle concentration in the tank after flushing to 10 cm^{-3} in the evening and 12 hr later the next morning.

Figure 3.3 shows a time series of the total particle concentration through the course of a tank flushing procedure and the resultant particle production after the jets were turned on. To ensure that no particulate contamination entered the tank, the tank headspace was flushed at the end of the day to a particle concentration of about 10 cm^{-3} and kept overnight sealed against the ambient air. The next morning (after 12 hours) the particle concentration typically fell to about 3 cm^{-3} as indicated in Fig. 3.3. This implies that ambient room air (which had a concentration of particles > 7000 cm^{-3} determined from the CPC) did not enter the tank headspace. The decreasing particle concentration is likely due to wall loss and loss by coagulation and gravitational settling.

After a steady state particle concentration was reached, measurement of the aerosol size distribution was performed by scanning the particle sizes from $\sim 16 - 1000$ nm and counting the number of particles in size bin. The scan time was 6 min and the wait time between scans was 1.5 min. Therefore, a single scan corresponded to an aerosol size distribution averaged over 7.5 min. Subsequent scans were averaged together over the course of about 1 hour to achieve sufficient counting statistics in each particle size bin. As an example, individual scans taken from one mesocosm experiment are shown in Fig. 3.4 for a total time of 67.5 min. Clearly, the shape of the size distribution and the total number of particles did not change significantly over the course of 1 hour, implying that the flux of particles reached steady state. The uncertainty of each value of $dN/d\log D_p$ for a size bin is determined from the counting error, $\sqrt{N^i}$, where N^i is the total counts in the i^{th} size bin for a single scan. When averaging each bin from consecutive scans the total counts are additive and therefore, the final percent error for the average distribution is smaller than for a single scan. For a total particle concentration on the order of 10^3 cm^{-3}, as was observed for conditions using the jets, it was necessary to include multiple scans to ensure the error in $dN/d\log D_p$ remained well below 10%. The resulting spectrum is shown in the lower right panel of Fig. 3.4. When using the frits, particle concentrations were observed to be about 2 orders of magnitude higher and so fewer scans were needed. Nevertheless

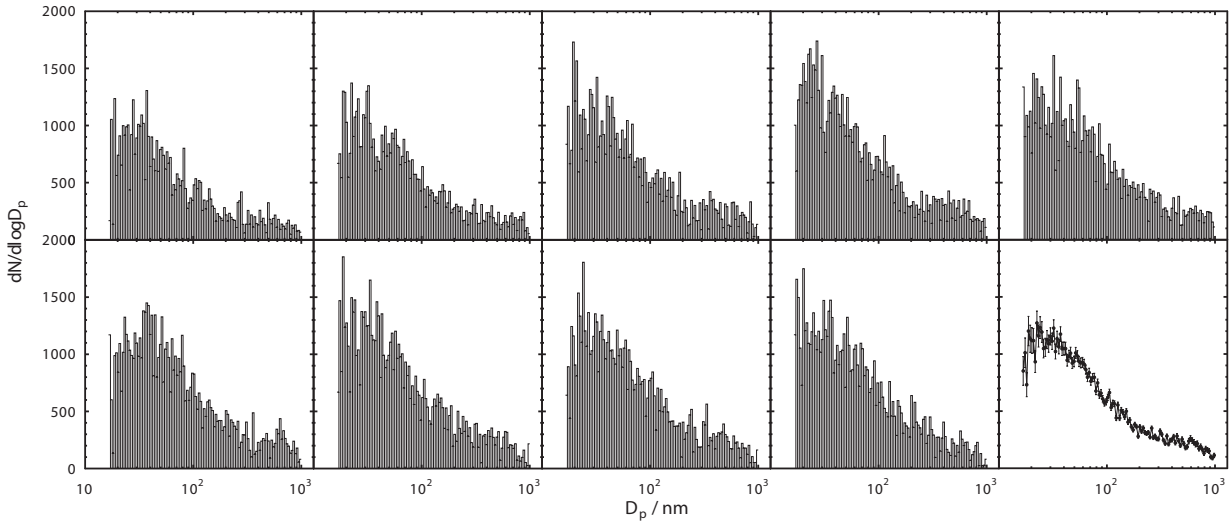

Figure 3.4: Consecutive aerosol size distributions from jet generated particles measured over the course of ~ 1 hour are shown as bar graphs where each distribution in a panel took 7.5 minutes to complete. A single size spectrum shown in the bottom right panel and the corresponding uncertainty is determined from averaging together the individual distributions and summing the particle counts, respectively.

it was also confirmed that particle production using frits reached steady state and that the shape of the distributions did not change over time with a similar procedure.

Prior to filling the mesocosm with seawater, the entire tank and plumping system was thoroughly cleaned to minimize the presence of contaminating particles. The tank was washed with a solution of 50% bleach/water and allowed to sit for an hour, followed by two sequential washes with water. All water tubing, pump and flow meters were washed with a bleach/water solution. The presence of contaminating particles, including foreign bacteria or other organic particles on the surfaces of the tank or in tubing was checked with epifluorescence microscopic examination of stained swabs. No detectable contamination was present prior to any experiments. Seawater used in the growth experiments was added sooner than 24 hours after cleaning. ASW was made from a solution of Instant Ocean salts mixed with tap water. Because the tap water used may initially contain impurities, the presence of bacteria or other foreign organic particles were investigated using epifluorescence microscopy. No detectable bacteria or particulate material was observed in the mesocosm seawater at the start any of the growth experiments. The seawater was initially mixed in 20 L carboys at a high salt concentration, added to the tank, and diluted with water to a salinity of 35 ppt. The seawater stock solution was visually slightly cloudy initially and salts quickly settled on the bottom of the tank. The water was thoroughly mixed overnight using a submersible pump to dissolve as much of the salt as possible. It is clear however, that in spite of extensive mixing, that not all of the Instant Ocean mix, dissolves even at a standard salinity of 35 ppt. The water in the tank became visibly clear after mixing and the inorganic particulate that remained were larger in size than the range of diameters investigated for aerosol size distributions. It is therefore expected that the aerosolization of sub-micrometer sized particles is not affected as a result of impurities in the Instant Ocean.

3.2 Ice nucleation experiments

Two distinct types of ice nucleation experiments taking advantage of customized apparati are used to determine the ice nucleation capability of aerosolized particles and phytoplankton cells. One experiment investigated immersion freezing of aqueous solution droplets micrometers in diameter deposited onto hydrophobically coated glass discs[34,35,117,153,154]. A second experiment employed dry aerosol particles or phytoplankton cells deposited on hydrophobically coated glass slides, silicon wafers, and silicon nitride window substrates for observation of deposition freezing following procedures used in previous studies[34,37,117,202–204].

3.2.1 Droplet sample preparation

Suspensions of pure water or aqueous solution droplets containing cells and cell fragments of only one phytoplankton species per droplet, *N. atomus*, *T. pseudonana* or *E. huxleyi* were prepared. Axenic, i. e. bacteria free unialgal cultures verified by staining an aliquot and epifluorescence microscopic observation, are grown for one week in a 14 hr light : 10 hr dark cycle in 300 mL volumes with a nutrient supply. Cells are washed and resuspended in either pure water or an aqueous solution with a known amount of NaCl. Micrometer sized droplets are generated using a piezo-electric single drop on demand dispenser[34,35,117,141] to create $30-60$ monodisperse droplets with diameters of $40-70$ μm typically containing 3 cells and fragments

of cells on a hydrophobic coated glass plate[34,35,117]. Surface area per droplet was determined by observation of cell numbers per droplet by optical microscopy and known surface area per cell[34,35,117].

3.2.2 Droplet water activity conditioning

The a_w of micrometer-sized aqueous solution droplets was preset using an aerosol conditioning cell (ACC) that allowed droplets to equilibrate with a controlled RH[35,117,141,144,153]. Droplets are exposed to a humidified flow of N_2 gas with known dew point temperature, T_d. The uncertainty of T_d is $< \pm 0.15$ K. The droplet temperature, T_{drop}, is controlled within $\pm$ 0.2 K. Droplet samples are allowed to come into equilibrium with RH and thus, a_w = RH is set. The error in a_w derived from the error in T_d and T_{drop} is $\pm$ 0.01. RH calibration is achieved by determination of the ice melting point and DRH of various inorganic salts such as K_2CO_3, K_2SO_4, LiCl, $(NH_4)2SO_4$ and NaCl[35,117,141,144,153,205,206]. Droplet samples are sealed against the environment using a second hydrophobically coated glass slide cover and a tin foil spacer coated with high vacuum grease.

3.2.3 Droplet freezing via immersion ice nucleation

The ice nucleation experimental setup for droplet freezing consisted of a cryogenic cooling stage coupled to an optical microscope and equipped with digital imaging capabilities used to investigate immersion freezing of micrometer sized droplets[34,35,117,141,153,154,206]. This setup allowed controlled cooling and heating of droplets in the temperature range of about $150 - 350$ K. A magnification of 100x is used to view the 1.5 mm sample area for micrometer droplets[153]. Ice nucleation is investigated for a cooling rate of 10 K min^{-1} until all droplets freeze. Heating rates of 0.5 K min^{-1} are used to determine the melting temperatures. Temperature calibration is conducted by measuring known melting points of ice and various organic species such as heptane (182.60 K), octane (216.33 K), decane (243.55 K), dodecane (263.58 K) and ice (273.15 K) covering the investigated freezing temperatures[144,153,206] resulting in a temperature uncertainty of $< \pm 0.1$ K. During the freezing and melting cycles, images are recorded at 0.2 K intervals that contain experimental time and temperature. Thus, 0.2 K is the experimental uncertainty in determining temperature. At least three independently prepared droplet samples are applied for each investigated a_w, and each droplet sample is used for maximum of three cooling and melting cycles. After completion of an experiment, the images are reviewed and droplet freezing and melting temperatures are recorded.

3.2.4 Deposition ice nucleation

Observations of deposition freezing are based on techniques described in Dymarska *et al.*[207], Parsons *et al.*[208] and detailed in Wang and Knopf[37]. The onset of ice nucleation (the first observed instance of ice nucleation) was determined using an ice nucleation system which consisted of an optical microscope coupled to an ice nucleation cell 1 mm in diameter having a volume < 0.8 cm^3 allowing control of the particle temperature, T_p, and RH_{ice}. Particles deposited on either silicon wafer substrates, hydrophobically coated glass discs, or silicon nitride windows are exposed to humidified nitrogen with a flow $\sim$ 1 L min^{-1} at a constant T_d. The particles are cooled at a rate of 0.1 K min^{-1} until ice nucleation is observed. The cooling

rate is chosen to mimic relevant rates reported for mid- and low-latitude cirrus and mixed phase clouds. RH_{ice} and RH are derived from T_p and T_{dew} using Eqs. 1 and 3. Digital images are recorded every 0.02 K ($\sim$ 12 s between images) and the image sequences are reviewed to determine the onset conditions of ice nucleation or water uptake. This system allows observation of individual ice formation events, and very fine visual distinction between ice nucleation modes and water uptake. Water uptake and ice nucleation can be detected if the particle size increases by 0.2 μm in diameter using 100x magnification.

Calibration of T_p was performed after the occurrence of ice nucleation following the procedure of Dymarska *et al.*[207]. Ice crystals are exposed for only a few seconds to $RH_{ice} \simeq 90\%$ by warming T_p by about ~ 0.5 K above T_d resulting in the ice crystal slowly decreasing in size due to sublimation. Immediately, the ice crystal is cooled at the same rate as used to observe ice nucleation and imaged to observe ice deposition as RH_{ice} ramps from 90% to 110% RH_{ice}. The change in the 2-D projected ice crystal surface area due to vapor deposition or sublimation is measured with imaging software. The instance when the ice crystal does not change size, equilibrium conditions between ice and water vapor are established and thus $T_p = T_d$. The particle temperature is calibrated against the dew point temperature, by calculating a temperature offset to correct T_p. An increase in vapor pressure over an ice surface due to the Kelvin effect is significant only for ice crystals on the order of 100 nm in diameter. Ice crystals used for calibration runs are on the order of 10 μm in size thus, curvature can be neglected. Timescales for water gas phase diffusion are on the order of 2×10^{-6} s and negligible for the ice crystal to establish an equilibrium with the ice saturated air. Observations of ice nucleation and temperature calibration are repeated up 3 times per sample and T_d. Prior to initiating ice nucleation, particle samples are first exposed to temperatures above 273 K to ensure complete sublimation of ice from any prior experiment.

3.3 Particle morphological and chemical investigation

3.3.1 Computer controlled scanning electron microscopy and energy dispersive X-ray analysis (CCSEM/EDX)

Scanning electron microscopy (SEM) and energy dispersive X-ray analysis (EDX) was used to obtain morphological and elemental composition of individual particles and additionally, computer controlled scanning electron microscopy coupled with energy dispersive X-ray analysis (CCSEM/EDX) was used to provide individual particle elemental composition for a statistically significant number of particles[29,209]. The principle of SEM and EDX is based off of the detection of scattered electrons by a particle surface to produce an image, and the detection of a single energy X-ray photon released when an electron is kicked out of its ground state molecular orbital by the incoming beam and another electron takes its place. When using CCSEM/EDX, an image is taken of a particular sample area, a threshold is applied by computer software to locate individual parties on the sample area, and finally EDX spectra are taken at these locations over the entire particle. The elemental composition of a representative number of particles[203] (typically > 1000) is determined and can be used to infer the elemental composition of the entire particle population.

Particles collected during mesocosm experiments on copper grids were imaged with a scanning transmission electron microscopy (STEM) detector at Pacific Northwest National Laboratory (PNNL) located

in Richland, WA. Images with STEM give valuable morphological characterization of the particles as well information on mixing state. Using STEM, a known area of the sample is imaged and the location of each particle in a single field of view identified with computer software. EDX spectra are recorded only where the threshold indicates a particle. A new particle is then imaged and a new EDX spectrum is acquired. The stage is automatically moved to a different field of view when all particles in the current field have been exhausted. Copper is not quantified in elemental analysis. The elemental composition of a particle is measured with atomic percentages, AP, a fractional composition of a particular element. Uncertainty in AP is determined from the relative statistical error for the elemental peak intensity expressed as one standard deviation. The number of X-ray photons that are counted using EDX should remain above 100 cps (counts per second) in order to obtain sufficient counting statistics and thus acceptable error in AP. Larger particles give rise to greater CPS and particles, typically, having diameters < 200 nm do not produce sufficient photon counts. Additionally, EDX is prone to irradiation damage of aerosol particles, in particular for elements with low atomic ratios such as C, N, and O. Therefore, determination of total C, N, or O is not accurate for small particles (< 200 nm in diameter), due to the fact that the vaporization of these elements is sufficient to deplete the mass and cause error in any quantifiable measure. As a result, < 200 nm sized particles are not examined using CCSEM/EDX. The electron beam dwell time over a single particle for recording a EDX spectrum was short (10 s) to keep the beam damage at a minimum for a beam current of 0.43 nA and accelerating voltage of 20 keV.

3.3.2 Scanning transmission X-ray microscopy coupled with near edge X-ray absorption fine structure spetroscopy (STXM/NEXAFS)

Examination of individual particles on silicon nitride windows identified experimentally as having ice nucleating potential were investigated with scanning transmission X-ray microscopy coupled with near edge X-ray absorption fine structure spectroscopy (STXM/NEXAFS)[38,210] operated at beamline 5.3.2.2 of the synchrotron light source at Lawrence Berkeley National Laboratory (LBNL) located in Berkeley, CA. Chemical composition and mixing state, in addition to carbon bonding information is investigated with STXM/NEXAFS. With 40 nm resolution, single particle maps of individual carbon functional groups, such as a carboxyl group (COOH), were generated. Carbon bonding morphology was also quantified.

Particle analysis by STXM/NEXAFS proceeds by first focusing a high brightness, low energy X-ray beam on a 40 nm spot size on the sample. The beam raster scans the sample at a single energy across a know field of view and the transmitted intensity through the sample substrate is detected, I_0, and compared with the intensity transmitted through a single particle and the sample substrate, $I(d)$, as a function of the particle thickness, d, at that spot. Thus, the X-ray intensity is attenuated by the particle compared with a particle free surface. The Beer-Lambert's law then gives the optical density, OD, of the 40 nm spot size on the particle that attenuated the X-ray beam as

$$\mathrm{OD} = -\ln\left(\frac{I(d)}{I_0}\right) = \rho\mu d = \sigma d, \tag{18}$$

where ρ is the particle density, μ is the mass absorption coefficient, and σ is the absorption cross section. For a particle composed of multiple chemical compounds, the total OD is given by the sum of the OD contribution for each compound. The beam is then raster scanned at a single energy across the sample by moving the sample stage. Using Eq 18, and an appropriate value of I_0, an OD is calculated at each 40 nm pixel in the field of view. After a single OD image is complete, the beam increases in energy by fractions of an eV and takes another OD image. Typically 120 individual OD images at different X-ray energy points are taken to form a stack. An image stack is then aligned spatially for beam drift and analyzed for the corresponding particle spectrum and carbon functional group mapping. An example of a carbon NEXAFS spectrum is shown in Fig. 3.5 and described below.

Investigation of carbon bonding information is done by measuring carbon near-edge X-ray fine structure spectra, containing X-ray absorption features dependent on bonding and unoccupied molecular orbitals. An X-ray with energy between $\sim 278 - 320$ eV is absorbed by a ground state energy level (1s) electron, also known as K-edge absorption. Sharp absorptions are observed at narrow energy bandwidths from electronic resonance transitions of different carbon functional groups. For example, a C 1s $\rightarrow$ $\pi^*_{\mathrm{R(C^*{=}O)OH}}$ transition occurs for incident X-ray energy only between $288.4 - 290$ eV. Peak absorption can be observed at 288.5 eV. An example of a STXM/NEXAFS spectrum is shown in Fig. 3.5 for a particle having carbon double bonds, carboxylic bonds, and potassium[18]. The individual peaks show unambiguously the unique carbon bonding present in this particle. Table 1 details the range of K-edge absorption of carbon[38,39]. The chemical composition of marine biogenic particles are revealed by their carbon spectrum and any peak found to be present in the absorption spectrum is a positive identification of unique carbon bonding. Thus, the nature of organic, internal carbon bonding structure and organic carbon composition of individual particles can be quantified and mapped with high spatial resolution using STXM/NEXAFS.

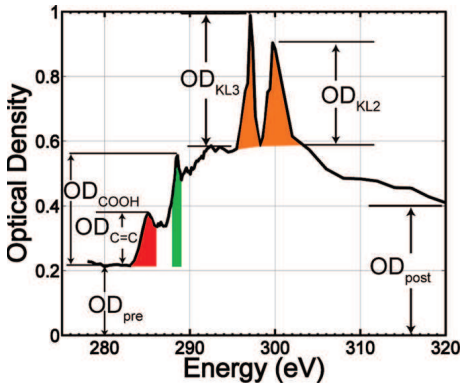

Figure 3.5: Example of a single particle carbon K-edge near edge X-ray absorption fine structure (NEXAFS) adapted from Moffet *et al.*[18]. Spectral features include carbon pre-edge absorption, $\mathrm{OD_{pre}}$, carbon post-edge absorption, $\mathrm{OD_{post}}$, carbon double bonding, $\mathrm{OD_{C=C}}$, carboxyl function group, $\mathrm{OD_{COOH}}$, and potassium L_2 and L_3 edges, $\mathrm{OD_{KL2}}$ and $\mathrm{OD_{KL3}}$, respectively.

Table 1: Peak absorption energies for various carbon functional groups and chemical compounds found in the carbon K-edge absorption fine structure[29,38–40].

Functional Group/Compound		Peak Energy / eV
Double Bond	R(C=C)R	285.1
Phenolic-Hydroxyl	phenolic(C-OH)	286.5
Hydroxyl	R(C-OH)	287.0
Aliphatic	C-H	287.7
Carboxyl	R(C=O)OH	288.5
Carbonyl	R(C=O)R	289.1-289.8
Carbonate	CO_3	290.4
Potassium	K L-Edge	299.7 & 297.1
Calcium	Ca L-Edge	346.2 & 349.7

3.3.3 Ice nuclei identification

The ice nucleation apparatus in combination with STXM/NEXAFS and CCSEM/EDX was used to physically and chemically characterize the ice nucleating particles and the total particle population. The experiment for deposition freezing essentially probed the particles resting on a silicon nitrite window substrate for the one, or few, particles that have the ability to nucleate ice. Once a particle nucleated ice, its location was recorded for identification and chemical investigation for subsequent investigation using STXM/NEXAFS. The following describes the procedure for unambiguously identifying ice nucleating particles using optical microscopy and re-locating the particle with STXM/NEXAFS. Thus, chemical characterization of and comparison between ice nucleating particles and non-ice nucleating particles using STXM/NEXAFS was quantitatively investigated. In subsaturated conditions with respect to ice, an ice crystal will shrink due to sublimation toward the ice nucleating particle. The residual particle can be clearly identified after complete sublimation using optical microscopy. Immediately after calibration of T_p is completed, the ice crystal is warmed at a rate of 0.5 K min^{-1} and images are taken every 0.1 K until the ice crystal completely sublimates. The sublimation and ice nucleation image sequences are reviewed together to unambiguously identify which particle is responsible for nucleating ice. When ice nucleation experiments are completed for a particle sample, it is removed from the ice nucleation cell and placed in a petri dish flushed with dry, particle free N_2 gas and sealed from ambient air. Figure 3.6 shows optical microscope images of two ice crystals after ice nucleation was observed. After sublimation, the ice nucleating particles are clearly visible. At LBNL, an optical microscope is equipped with digital micrometer stages which are calibrated to match the XY coordinates of the STXM/NEXAFS sample stage. Thus, IN can be identified offline and their coordinates programed into the automatic STXM stage control to immediately locate a specific particle. A raw intensity STXM image of roughly the same sample area as observed with optical microscopy is shown in Fig. 3.6. Finally, high spatial resolution images of a single ice nucleating particle at 3 different X-ray energies are shown for an example of the baseline capabilities of STXM/NEXAFS.

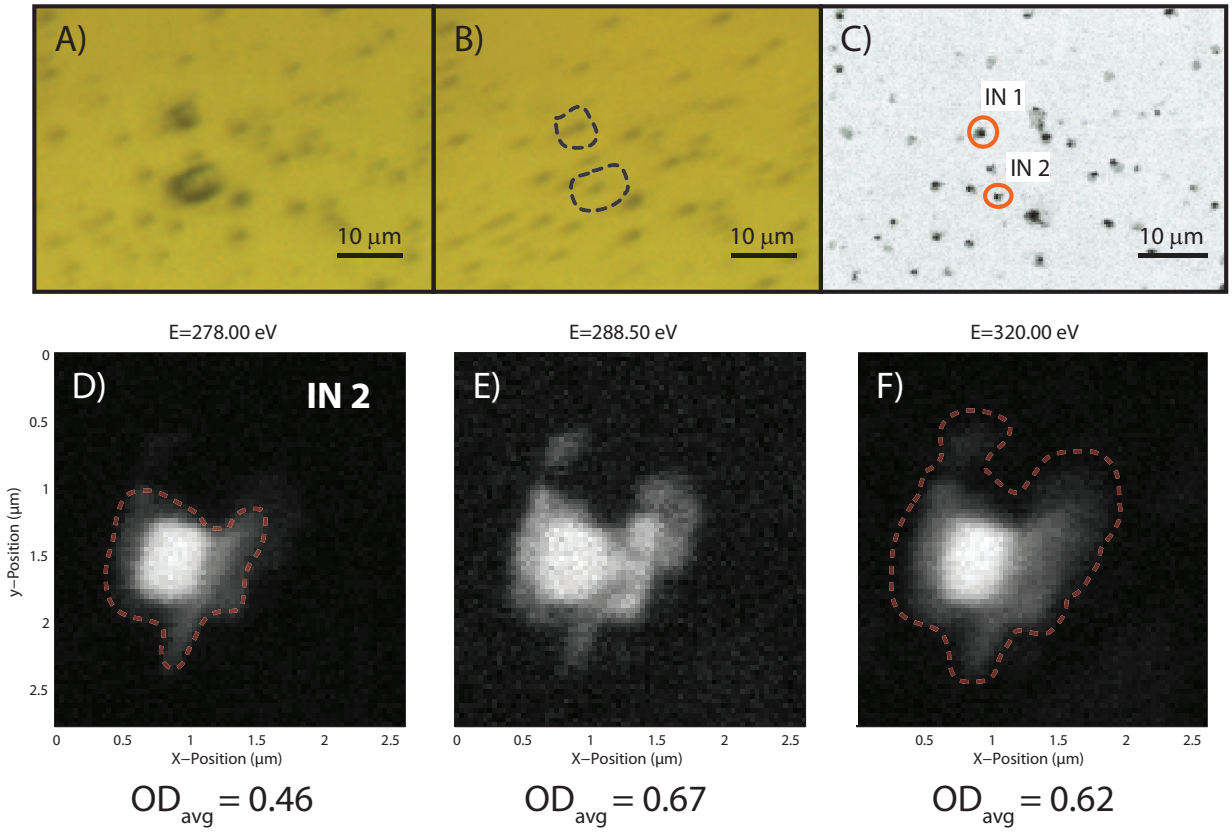

Figure 3.6: A) Optical microscope image taken at the end of an ice nucleation experiment where two ice crystals formed. B) After sublimation, residual particles responsible for nucleating ice can be clearly identified. The dashed lines outline the extent of the ice crystal. The apparent non-focus of the image is due to the temperature change during warming. Playback of all images taken during warming the ice crystals are used to determine the ice nucleating particle. C) A raw intensity image of roughly the same field of view as panel A and B taken with scanning transmission X-ray microscopy (STXM). D) A high spatial resolution optical density (OD) image at 278.0 eV indicating X-ray absorption from elements other than carbon. E) OD image at 288.5 eV, indicating the absorption contribution from the carboxyl functional group. F) An OD image at 320.0 eV indicates absorption from all carbon atoms.

3.3.4 Chemical analysis and quantification using STXM/NEXAFS

Stacks of STXM images at various energies were used to construct the absorption spectrum of a particle which could then be chemically mapped for carbon functional groups or calculations of total carbon. Carbon pre-edge absorption occurs at 278.00 eV due to the attenuation of X-rays from compounds that do not contain carbon. The carboxyl function group peak absorption occurs at 288.5 eV, indicating for example, carboxylic acids or amino acids. Notice that the particle in Fig. 3.6 appears significantly brighter and thicker. Additionally, pieces of the particle that were not seen in Fig. 3.6D are visible in E and F, indicating the strong presence of the carboxyl function groups at these locations and coating of the particle core. Total carbon absorption occurs at 320.00 eV. The average optical density, OD_{avg}, for the entire area indicated in Fig. 3.6F is about 26% higher than in Fig. 3.6D, which indicates that this ice nucleating particle is composed of a significant amount of carbon. Particle morphology inferred from STXM images also gives

important information. It can be seen that the carboxyl functional group imaged in Fig. 3.6E tends to be entirely surrounding the inner core which is cubic, indicating an organic carbon coating an inorganic sea salt particle.

4 Results: Aerosolization and characterization of marine particles

Several mesocosm experiments were conducted to investigate the relationship between biological activity, aerosol particle generation, and cloud formation potential. Table 2 describes the conditions used for the experiments including water type and microbial community composition. Growth of each community and other measures of biological activity were followed over time from inoculation of cells at low concentrations to simulated bloom conditions at concentrations several orders of magnitude higher. Particles aerosolized from mesocosms were exposed to controlled humidity in order to observe changes in their growth factor due to water condensation. Additionally, aerosolized particles were collected and probed for their ability to nucleate ice in immersion and deposition modes. Finally the particle population and individual ice nucleating particles were physically and chemically characterized. Listed below are the main findings of the series of experiments described in table 2; Detailed results follow.

1. Different bubble generation methods employing either water jet impingement or aeration through a glass frit were compared. These methods produced dissimilar bubble size distributions and significant differences in total bubble production.

2. Aerosolization of particles using the water jets were significantly different from particles produced with glass frits both in terms of the shapes of the size distributions and the total number of particles generated. These differences are likely related to the difference in bubble production between the jet and frit.

3. When only bacteria were present in an experiment, the aerosol particle size distributions using both jets or frits changed as a function of bacterial concentrations. Furthermore, even when bacterial concentrations stabilized, distributions continued to change as a function of time. This may reflect changes in species composition, nutritional status, or turnover.

4. When bacteria and phytoplankton were grown simultaneously, the changes in particle aerosolization were similar in terms of the shape of the particle size distributions and total production to when bacteria was grown without phytoplankton.

5. Hygroscopicity of the aerosolized particles, in general, could not be distinguished from that of pure sea salt within the experimental uncertainties. This allowed the determination of the possible limits of average particle organic volume fraction and organic hygroscopicity.

6. Despite differences in aerosolization methods or the biological activity occurring in different phytoplankton mesocosm experiments, all particles were found to nucleate ice heterogeneously. Furthermore, the efficiency at which ice nucleation occurred was remarkably similar.

7. Electron and X-ray spectromicroscopic techniques confirmed that aerosolized particles contained mixtures of sea salt and organic material. Additionally, individual ice nucleating particles were found to have a significant amount of organic material and sea salt associated with them.

Table 2: Names and descriptions of the various mesocosm experiments investigated in this study.

Name	Water Type	Duration	Nutrient Supply	Inoculation
ASW-1	ASW[a]	1 day	None	None
ASW-2	ASW	1 day	None	None
LowBac	ASW[b]	14 days	None	None
GBac	ASW	13 days	50 mg L^{-1} peptone, 10 mg L^{-1} yeast extract	Bacteria[c]
Tpseu	ASW	12 days	F/2+Si	*T. pseudonana*
Ehux	ASW	12 days	F/50	*E. huxleyi*
Natom	ASW	12 days	F/2	*N. atomus*
NatSW	NSW[d]	11 days	F/2[e]	None

[a]Artificial seawater
[b]ASW-2 continued for 14 days
[c]A mixed natural bacteria culture from seawater obtained at Great South Bay
[d]Natural seawater obtained from Shinnecock Inlet
[e]F/2 and F/50 are standard nutrients described in Guillard[211]

4.1 Bubble generation

Size distributions of bubble plumes generated using a single water impingement jet and by aeration through a single glass frit in artificial seawater, are shown in Fig. 4.1 along with distributions from previous laboratory studies and ambient ocean measurements. Individual bubbles rising with the main bubble plume near its center (red circles) were larger than those at a distance away from the plume (red squares) which tended to mix in the whole water volume rather than rise quickly and directly to the surface. Bubbles having $D_b \sim 100$ μm were the most abundant for both the frit and jet consistent with their greater production and longer lifetime in the water ($\sim$ minutes). The total integrated bubble numbers for the frit were, $N_b = 1.1 \times 10^9$ and 4.4×10^8 m^{-3} at 5 and 11 cm away from the frit center, respectively. Bubble concentrations for the frit at 100 μm are especially high and peak 1 order of magnitude higher than for the jet. As a result, bubble production for the jet was an order of magnitude less than the frit at $N_b = 3.2 \times 10^8$ and 3.6×10^7 m^{-3} at 5 and 11 cm away from the jet center, respectively.

For $D_b > 100$ μm, bubble concentrations decreased with increasing D_b likely due to their decreased generation and their dramatically increasing terminal rise velocity (5 cm s^{-1} for $D_b = 1000$ μm). The decline in bubble concentration with increasing D_b can be described by a power law, $dN/dD_b \sim D_b^{\beta}$, where β is referred to as the scaling factor. Jet generated bubbles have two β values for measurements 1 cm away ($\beta = -0.80$ and -4.91) and for measurements 11 cm away ($\beta = -1.27$ and -4.01) from the plume center. Frit generated bubbles have a single β value for measurements 5 cm away ($\beta = -2.4$) and 11 cm away ($\beta = -6.19$).

Figure 4.1A and B clearly show that bubble size distributions for both the jet and frit vary significantly between our studies and those of other investigators, by about 2 to 4 orders of magnitude at a single D_b for the jet and frit. It is important to note that direct inter-comparisons are difficult due to the use of various water or air flow parameters, including water velocity, jet diameter and nozzle height for the impingement

method, and air flow rate, pore size, and frit diameter for the aeration method. Additionally, bubble sizes in any given study, may have been measured at different locations within the water column. This may explain the variability in bubble size distributions between the data presented here and previous studies.

Figures 4.1B and D compare jet and frit generated bubble size distributions from this study to measurements done $25 - 30$ cm under a breaking wave in the ocean[21–23] (green symbols) and from artificially

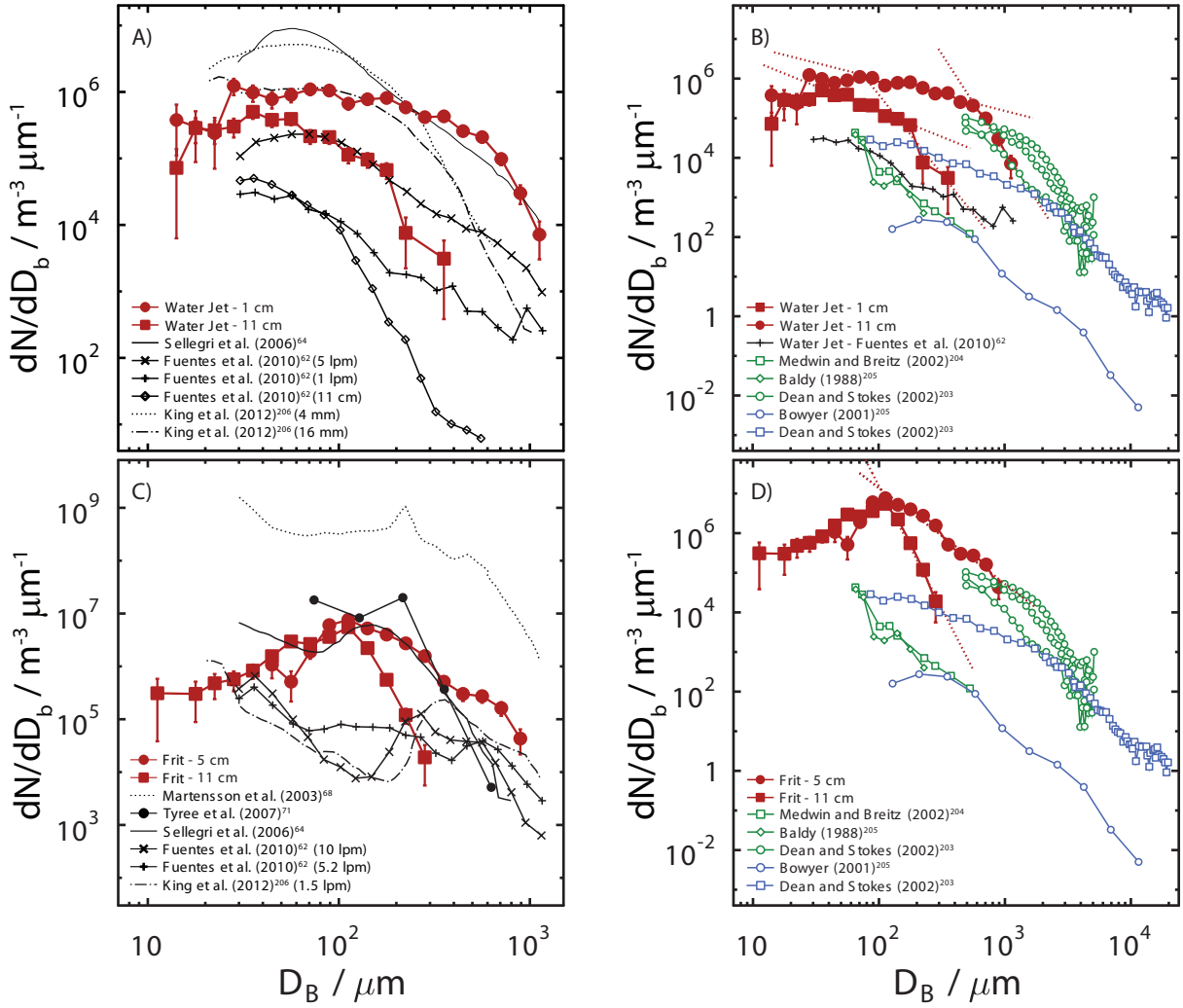

Figure 4.1: Bubble size distributions measured as a function of bubble diameter for plumes generated by water jet impingement (A and B) and air flow through a glass aerator (C and D) in artificial seawater (ASW). Data presented here are shown as red symbols, lines and vertical error bars as standard counting error. The red dotted line are fits to a power law, $dN/dD_b \sim D_b^{\beta}$, where β is the scaling factor. Centimeter lengths indicate distances from jet or aerator center. Previous laboratory studies who generate bubbles in ASW are shown as black symbols and lines. Millimeter lengths indicate jet nozzle inner diameter. Liter per minute flows (lpm) indicate water or air flow for the jets and frits, respectively. Sellegri *et al.*[19] did not report total bubble concentrations and so their data is scaled with a concentration of ~ 1000 m^{-3}. Bubble measurements in a wave flume were measured from a wind[20] and paddle[21] generated wave. Ambient bubble size distributions were measured 25 cm below breaking waves as green symbols and lines[21–23].

generated waves in laboratory seawater flumes about 30 m long[20,21] (blue symbols). The bubble size distribution of breaking waves between laboratory and field measurements vary by as much as 3 orders of magnitude. The bubble size distributions measured in the ocean by Deane and Stokes[21] from three separate breaking events observed off the coast of Southern California during the winter of 2000, are actually in closer agreement to data obtained here for both jet and frit generation.

Based on the data shown in Fig. 4.1, it is impossible to claim that a water jet or glass frit accurately represents bubble formation for a breaking wave. Measurements of bubble size spectra using any kind of tank in a laboratory setting with different bubble generation techniques, or in the ocean under breaking waves tend to be highly variable as shown in all previous studies. This is not unreasonable given that bubble generation in laboratory systems is a chaotic processes with dissimilar turbulence and shattering of air pockets to be expected. In the ocean, differences wind speeds, as well as wave and surf height, would be expected to result in variable bubble spectra. It is highly unlikely that a single measurement of a bubble size spectrum for artificially generated bubbles either in the laboratory or naturally generated by ocean waves is representative for oceanic conditions under all circumstances in all locales.

As shown in this dissertation, spectra for bubbles by both jets and frits, near or far away from the bubble plume center, fall within a range of values found in previous laboratory and ocean data sets. Clearly the method of bubble generation, tank design, nature of the water used in the laboratory or location of ocean bubble size measurements, produce variability in size spectra. In this study the jets produced far fewer bubbles than the frits and had a broader bubble size distribution. Because of these differences, there is every reason to expect that the aerosolized particles from these two generation methods would be different. Since consistent bubble generation methods were used in all experiments and bubble size spectra are reproducible under controlled conditions using artificial seawater, we are confident that variation in the particles aerosolized can be attributed to differences in tank experimental conditions.

4.2 ASW-1 and ASW-2 mesocosm experiments: Initial state of artificial seawater

Aerosol particle size spectra for mesocosm experiments ASW-1 and ASW-2 for dry (RH<20%) and humidified, or wet (RH=80%), conditions for both jets and frits normalized to their total particle concentration, i.e. scaled by dividing the particle spectra by the integrated particle concentration, N_{tot}, are shown in Fig. 4.2. Two independent jet generated particle size distributions from different mesocosm experiments produce reproducible spectra with similar shape and position of dominant particle production around a particle diameter, $D_p = 100$ nm. The distribution for ASW-1 and ASW-2 has a primary modes at 101 nm and 77 nm, respectively and secondary modes at 588 nm and 572 nm, respectively. For both ASW-1 and ASW-2, a third mode centered at 25 nm can be used in the fit to better reproduce the spectra, however, this mode is small and does not significantly contribute to the total particle production, $N_{\mathrm{tot}} = 1.1 \times 10^3$ cm^{-3}.

The aerosol particle size distributions of Fuentes *et al.*[97], Sellegri *et al.*[19], and those presented here show that the majority of production occurs around $D_p = 100$ nm. There are however differences in peak locations and relative peak heights, in general among all studies shown in Fig. 4.2A. Sellegri *et al.*[19] and Fuentes

et al.[97] both argue that the appearance of multiple modes may be due to the forced bursting of bubbles at the water surface induced by splashing from water impingement. Despite the differences, the general feature of the aerosol particle size spectrum for jet generated particles, are reproducible and consistent with previous

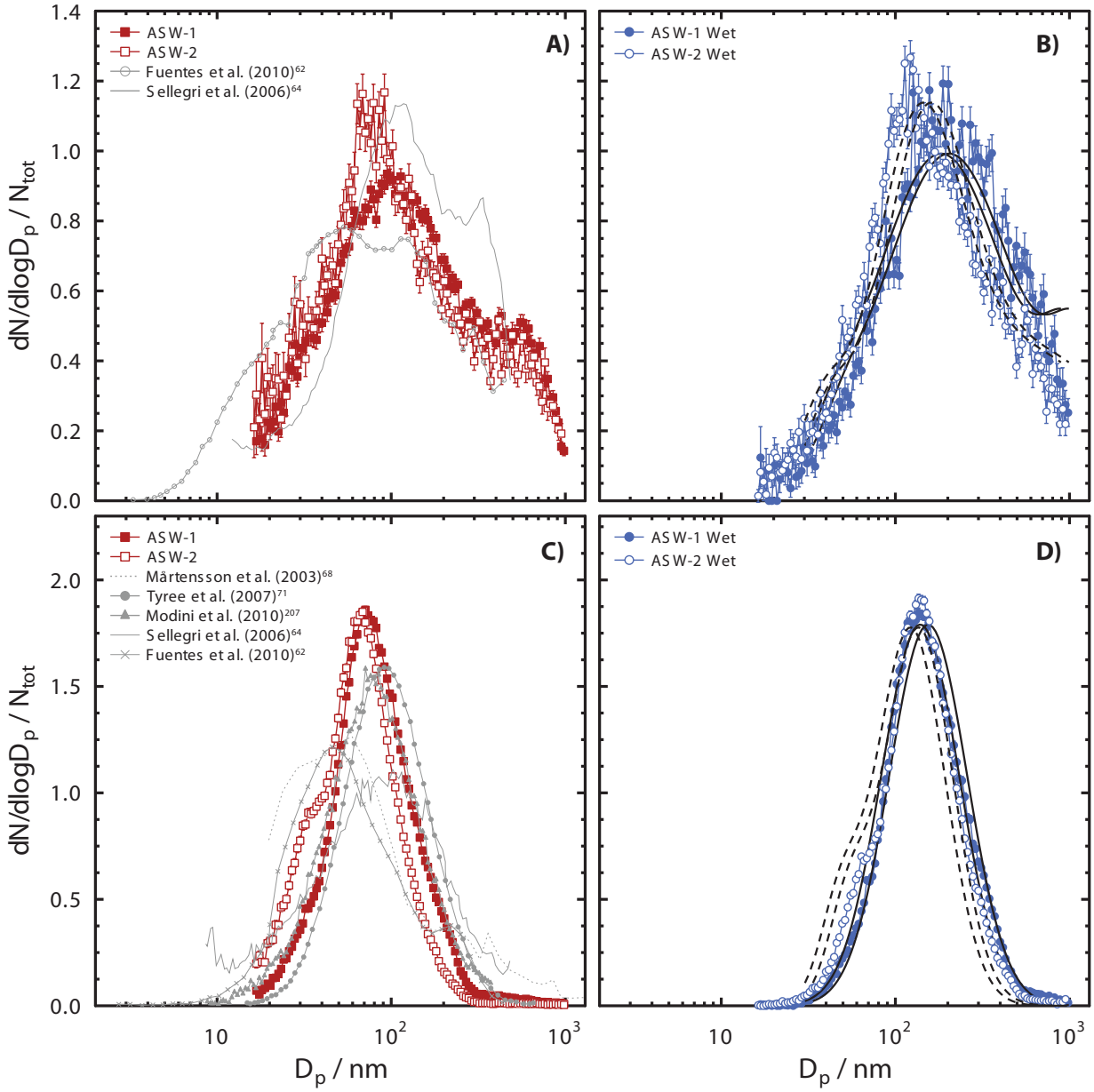

Figure 4.2: Aerosol particle size distributions in the mesocosm experiments ASW-1 and ASW-2 normalized to total particle concentration, N_{tot}, generated in artificial seawater (ASW) by plunging water jets (A and B) and frits (C and D). Dry and wet in B and C, refer to particles exposed to RH $< 20\%$ and RH $= 80\%$, respectively. Dry particle size distributions are compared with previous studies in A and C. In B and D, solid and dotted black lines are the dry particle spectra of ASW-1 and ASW-2, respectively, fitted to a multimodal lognormal distribution with the dry particle diameter multiplied by a factor of 1.8 and 2.

laboratory setups[19,97].

The size distribution of jet generated particles exposed to RH = 80% is shown in Fig. 4.2B. The uncertainty in controlling RH is ±4% corresponding to an uncertainty of about ±0.1 in the growth factor, g, which would be due only to the theoretical growth curve of NaCl. Taking into consideration the scatter in the data, possible variability in aerosolization from water temperature of ±1.0° C and salinity of ±2%, an error in g inferred from the measurements of size distributions is conservatively estimated at ±0.2. Therefore, if wet particle size distributions shift toward larger D_p by a factor less than $g = 1.8$, then this may be attributable to an average decrease in particle hygroscopicity compared to pure sea salt. Figure 4.2B shows the corresponding dry jet generated size distribution shifted by a factor of $g = 1.8$ and $g = 2.0$. We do find that at RH = 80% within the scatter in the data, dominant modes for jet generated particles double suggesting $g = 2.0$ in agreement with literature values for NaCl and observed for sea salt aerosol particles[97].

The aerosol size distributions obtained with the frits are shown in Fig. 4.2C. For both ASW-1 and ASW-2, the spectra almost replicated exact lognormal distributions centered at 75 nm with both having a similar distribution width. In all cases, a single dominant mode is observed between $70 - 100$ nm in diameter, in agreement with previous investigations[19,25,26,97,212]. For the frits, $N_{\text{tot}} = 3.2 \times 10^4$ cm^{-3}, significantly more that for the jets. This may be due to the more numerous amount of bubbles produced by the frit (Fig. 4.1). At RH = 80%, the particle size distributions generated with the frit suggest that $g = 2.0$.

Subtle differences are observed in the size spectra between ASW-1 and ASW-2 for both the jet and frit generated particles. For example, in the ASW-2 distributions shown in Fig. 4.2C, a secondary mode at 28 nm is much more distinct than for ASW-1. Size distributions measured using the jet and the frit for ASW-1 and ASW-2 are noticeably different and may imply there was a difference in the composition of the Instant Ocean used in each of these experiments. While assumed to be a standard product, Arnold *et al.*[213] investigated the dissolved organic carbon (DOC) content of 5 different batches of Instant Ocean and found that 3 had DOC concentrations below detectable levels, i. e. DOC < 0.2 mg L^{-1} (water), while 2 batches had concentrations of 0.2 and 0.3 mg L^{-1}. Background DOC concentrations in the ocean, typically between $\sim 0.5 - 1.0$ mg L^{-1}, are considered to be refractory[214]. Although the Instant Ocean ASW used in this study has very low DOC concentrations compared to what is found in the ocean, small differences in DOC even at low concentration may result in differences in aerosolization mechanisms. This variability may explain the small differences observed in the size distributions measured here and shown in Fig. 4.2A and C. Many previous studies use reagent grade salts to make home-made sea salt solutions to avoid this complication. However, these studies also exhibit variations between themselves for aerosolization using the frit, and especially the jets. Therefore, a small variability in the DOC concentration in ASW as observed by Arnold *et al.*[213] for different batches of Instant Ocean likely does not explain the variability in aerosol particle size distributions measurements made in this study compared to others.

In conclusion, the particle size distributions generated by the jets and frits measured here (Figs. 4.2A and C) using Instant Ocean ASW are different from each other. However, they are reproducible and within the range of measurements made in previous investigations using similar bubble/aerosol generation methods. The production of particles in a mesocosm tank for each bubble generation method are, of course, not the same as those which would be generated in the open ocean with immense wave heights, wind, and turbulence

among other chaotic effects that cause great variability. However, the characterization of bubble and particle size distributions are at a minimum internally consistent and do allow for the investigation of aerosol particle production as a function of biological activity. Using Fig. 4.2 as a reference for low or no biological activity, this allows a point by point comparison of any changes in the resulting particle size distributions due to phytoplankton or bacterial growth in the mesocosm.

4.3 Mesocosm experiments: Mixed bacteria growth in artificial seawater (LowBac)

4.3.1 Jet generated aerosol particles

The mesocosm was filled with ASW for a 14 day experiment designed to observe particle aerosolization due to bubble bursting without any added nutrients and without inoculation of phytoplankton or bacteria. In this mesocosm experiment called LowBac, changing water conditions were investigated over time and aerosol particle size spectra were measured as the seawater in the tank evolved with the growth of background concentrations of bacteria. Figure 4.3A shows that the dry aerosol particle spectra varies over the two week experimental period. Peak particle production shifts from 70 to 50 nm. The overall shape of the particle size distributions shifted toward smaller sizes compared with ASW-1 and ASW-2 jet generated particles (Fig. 4.2A). Averaged for the entire growth period, N_{tot} remains within 10% of 1.1×10^3 with no clear trend of either increasing or decreasing over the sampling times. The wet aerosol particle spectra on day 1 and day

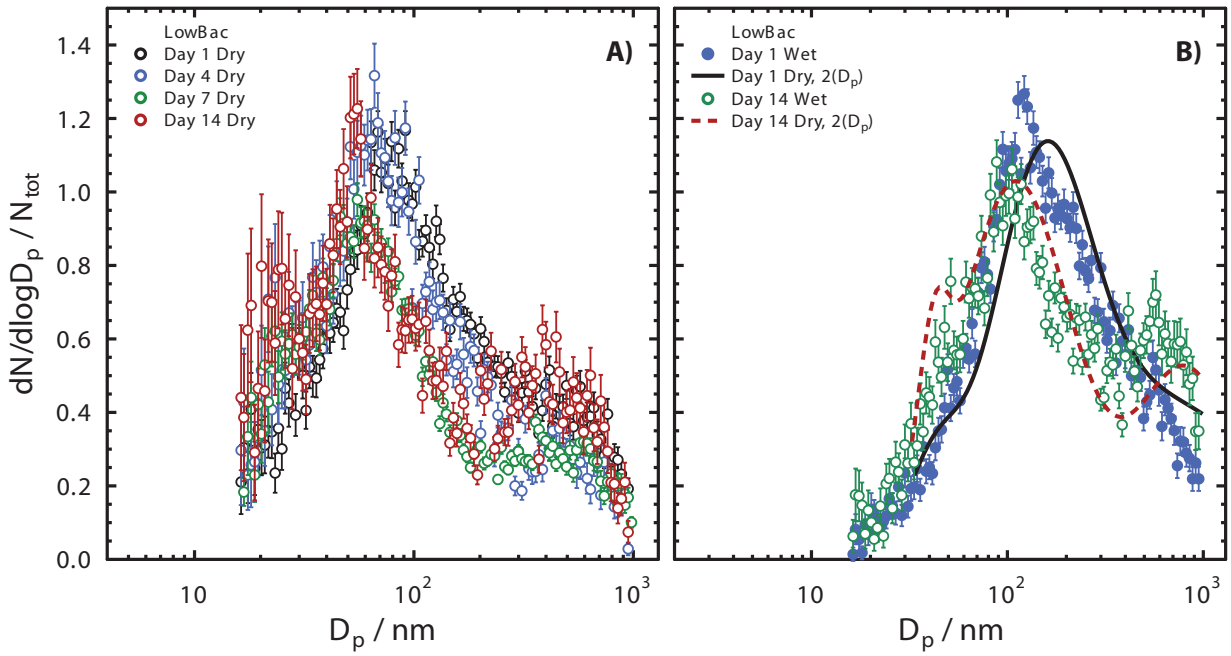

Figure 4.3: Changes in the normalized aerosol particle size distributions in the experiment LowBac produced by plunging water jets in artificial seawater as a function of seawater age. Dry aerosol spectra are shown in A and humidified spectra in B. Solid lines in panel B correspond to the dry spectra fitted to a multimodal lognormal distribution with twice the dry particle diameter. The days after the start of the experiment are indicated.

14 are compared in Fig. 4.3B with corresponding dry particle spectra shifted by $g = 2.0$. In general, the humidified particle size distributions are in agreement with water uptake of pure sea salt particles. Thus it can be concluded that there is no apparent change hygroscopicity occurred during the entire experimental time period.

4.3.2 Frit generated aerosol particles

Figure 4.4A shows clearly that the dry aerosol particle spectra for frit produced particles does not change over time. Peak particle production occurs around 70 nm and $N_{\text{tot}} = 3.1 \times 10^4$ and remains the same with 10% for the entire time period. The wet aerosol particle spectra for the frits on day 1 and day 14 in Fig. 4.4B indicates $g = 2.0$. There is little change in the size distributions or hygroscopicity for frit generated particles during the experimental period.

4.3.3 Water composition

Bacteria in fact were present in the mesocosm water with concentrations over time shown in Fig. 4.5. Initially, bacteria concentrations in the tank were undetectable. Bacterial concentrations rose to 1×10^4 mL^{-1} after the first day. Over the course of 7 days, bacteria concentrations increased exponentially reaching $\sim 3 \times 10^6$ mL^{-1}. Notice that when bacterial cell concentrations rose, the dry jet generated aerosol particle size spectra (Fig. 4.3A) experienced a small shift toward smaller sized particles.

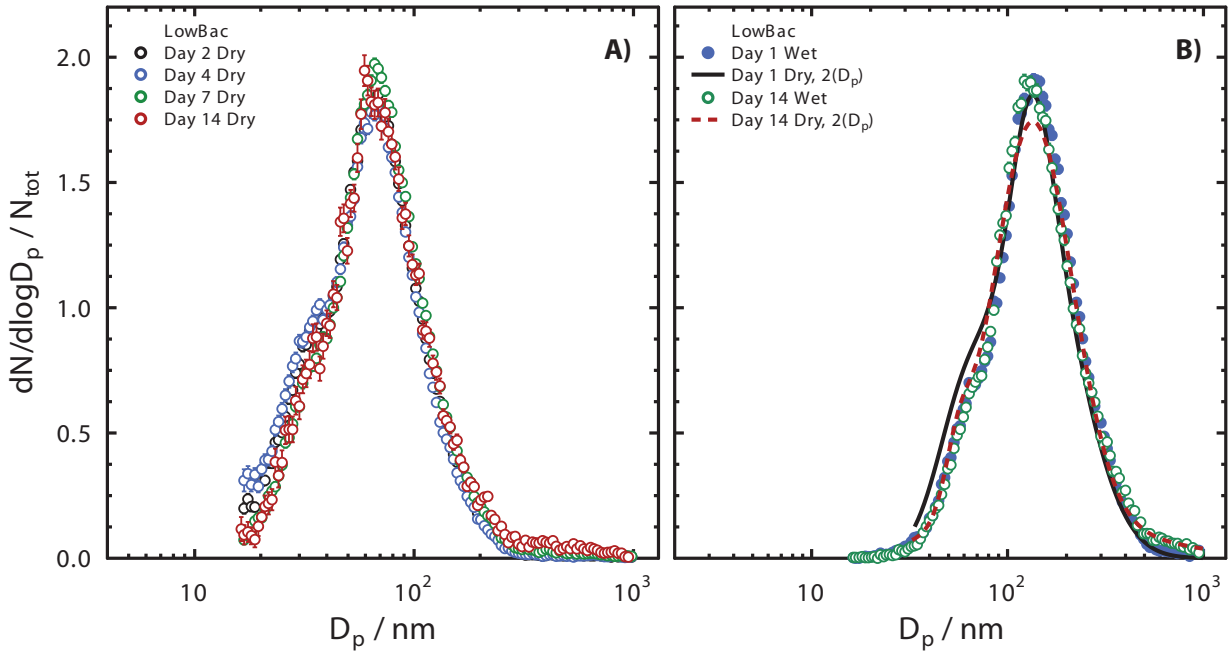

Figure 4.4: Changes in the normalized aerosol particle size distributions in the experiment LowBac produced by aeration through glass frits in artificial seawater as a function of seawater age. Dry aerosol spectra are shown in A and humidified spectra in B. Solid lines in panel B correspond to the dry spectra fitted to a multimodal lognormal distribution with twice the dry particle diameter. The days after the start of the experiment are indicated.

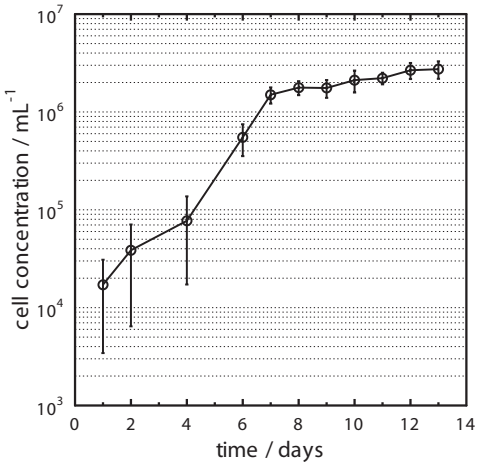

Figure 4.5: Bacteria cell concentrations in artificial seawater as a function of seawater age in the experiment LowBac.

4.3.4 Summary of experiment LowBac

When bacteria are present in seawater, changes are detected in the jet generated particles from measurements of the size distribution for bacterial concentrations from $< 4 \times 10^4$ mL^{-1} up to 3×10^6 mL^{-1}. Despite these changes, hygroscopicity is not observed to be different than sea salt as determined from the humidified particle size distributions within the experimental uncertainty and the scatter of the data. The change in particle spectra with bacterial growth has been investigated by Prather *et al.*[99] using a propagating wave with natural seawater and bacteria cell concentrations ranging from 5×10^5 to 8×10^6 mL^{-1}. In these experiments, the authors reported no difference in the size distribution with changing bacteria concentrations, in contrast to the measurements made during the experiment LowBac. One explanation may be that the range of bacterial cell concentration over a 4 day growth experiment is too small to see any significant effect on particle aerosolization. Another explanation may be that may be that the size distribution measured by Prather *et al.*[99] had low particle concentrations, $N_{\mathrm{tot}} \sim 145$ cm^{-3}, which would certainly cause low counting statistics and high variability. It is also likely that the use of natural seawater in their experiments already had a background concentrations of algal or bacterial cell fragments possibly aerosolized from the water, which were initially not present in the experiments presented here, but increased in concentration over time.

4.4 Mesocosm experiments: Great South Bay natural bacterial community in artificial seawater (GBac)

For comparison with experiment LowBac, ASW was inoculated with a mixed bacteria culture prepared from water collected in Great South Bay, Long Island, NY to which nutrient broth consisting of peptone and yeast extract was added to stimulate bacterial growth. In this experiment named GBac, bacterial concentrations reached 10^9 mL^{-1} within 4 days. The bacteria were found to be doubling in concentration every 2.5 hours and so aerosol particle size spectra were measured continuously for 84 hours in order to resolve aerosolized particle sizes during exponential and stationary growth. Changes in the particle size distributions were then measured on a daily basis for 14 days.

4.4.1 Week 1: Jet generated particles

Figure 4.6 shows dry and humidified aerosol spectra for jet generated particles during the GBac experiment. Initially, the dry jet generated particle spectra was different from spectra observed in LowBac, ASW-1, and ASW-2. This was most likely due to the initial nutrient addition. Just after 16 hours, the dry size distribution changed dramatically as seen in Fig. 4.6A. Peak production shifted from 93 nm to 59 nm and the distribution widths increased significantly. Within 72 hours, N_{tot} increased by a factor of 2, from 594 to 1103 cm^{-3} in the submicometer size range.

The humidified spectra taken at the beginning and end of GBac are shown in Fig. 4.6B and compared with the dry spectra taken a few hours earlier with twice the dry diameter. Every effort was made to keep the time delay between measuring the dry and wet particle size spectra to a minimum given the rapid growth of the bacteria cells. Within the scatter of the data, the humidified spectra at 18 hours indicates $g = 2.0$, and thus a similar hygroscopicity to sea salt.

4.4.2 Week 1: Frit generated particles

Figure 4.7A shows that the dry aerosol particle spectra for the frit generated particles does not change shape over time. Peak particle production occurs around 64 nm and N_{tot} rises from about 1.1×10^4 to 1.5×10^4 cm^{-3}. The humidified aerosol particle spectra for hour 12 through hour 82 in Fig. 4.7B indicate that $g = 2.0$ thus, no change in particle hygroscopicity occurred.

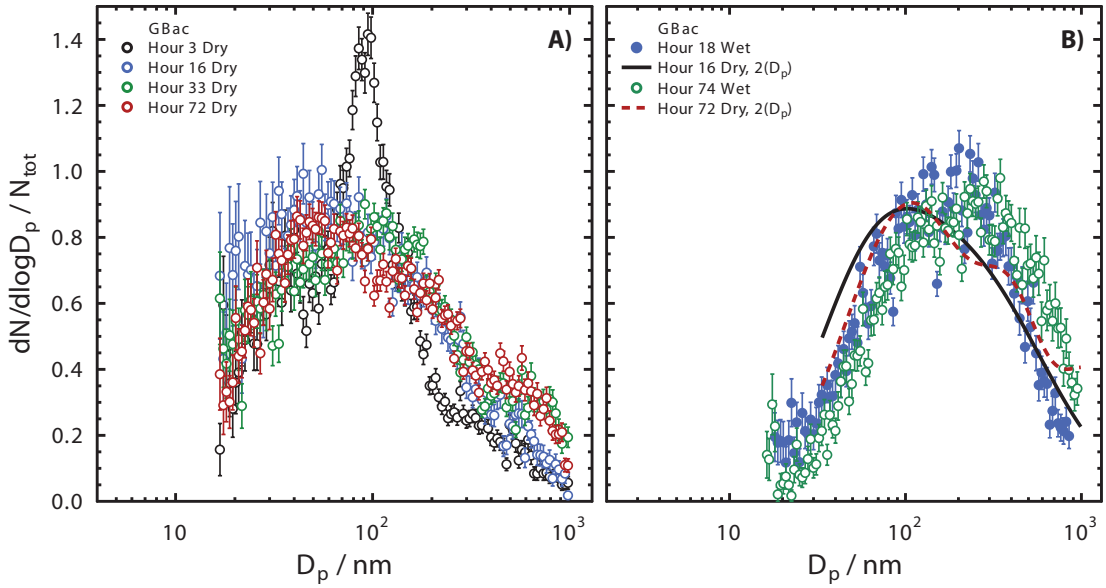

Figure 4.6: Changes over 84 hours in the normalized aerosol particle size distributions in mesocosm experiment GBac produced by plunging water jets in artificial seawater inoculated with a mixed bacteria culture from Great South Bay and added nutrients. Dry aerosol spectra are shown in A and humidified spectra in B. Solid lines in panel B correspond to the dry spectra fitted to a multimodal lognormal distribution with twice the dry particle diameter. The hours after inoculation of the mesocosm are indicated.

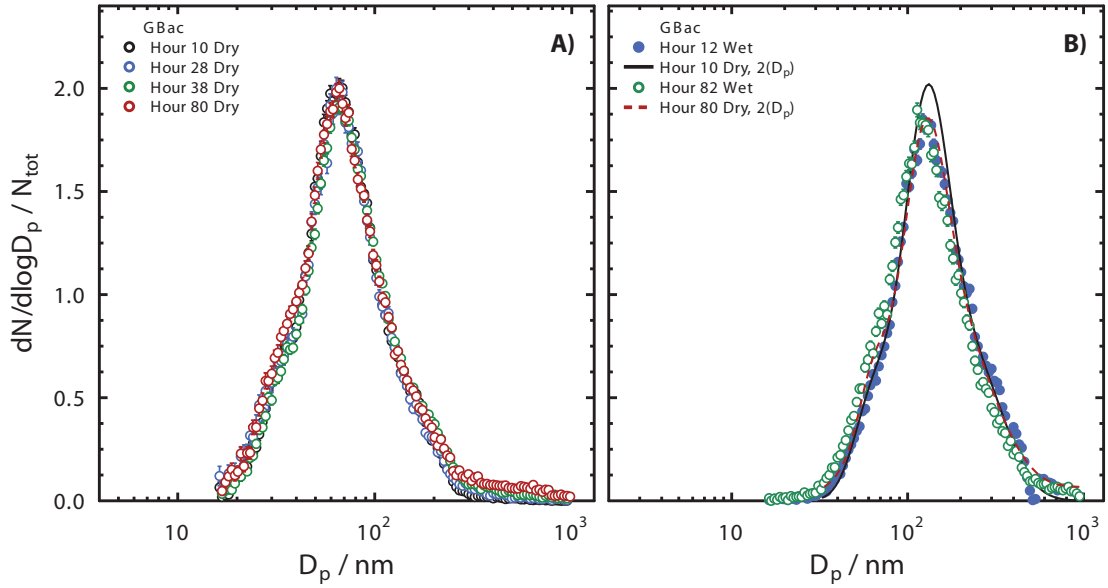

Figure 4.7: Changes over 84 hours in the normalized aerosol particle size distributions in mesocosm experiment GBac produced by aeration through glass frits in artificial seawater inoculated with a mixed bacteria culture from Great South Bay and added nutrients. Dry aerosol spectra are shown in A and humidified spectra in B. Solid lines in panel B correspond to the dry spectra fitted to a multimodal lognormal distribution with twice the dry particle diameter. The hours after inoculation of the mesocosm are indicated.

4.4.3 Water composition

The bacteria concentrations for GBac (Fig. 4.8) show a rapid increase in numbers from an initial concentration of 10^5 mL^{-1}. After about 20 hours, bacterial concentrations were already at 1×10^8 mL^{-1} and peaked at 7×10^8 mL^{-1}. Subsequently the bacterial concentration dropped an order of magnitude and remained constant likely due to the depletion of the nutrient supply. The rapid depletion of nutrient and increase

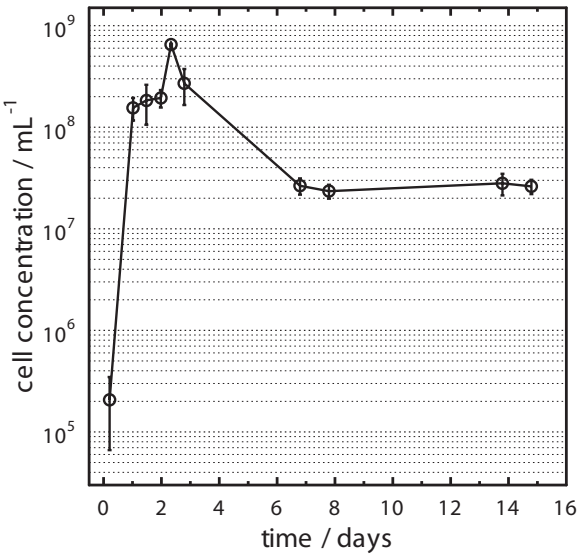

Figure 4.8: Bacteria cell concentrations in artificial seawater as a function of seawater age in the mesocosm experiment GBac.

in bacterial concentrations likely explains the change in the jet generated particle size distributions during the first 16 hours of the GBac experiment as shown in Fig. 4.6. Despite the changing water conditions, the shape of the particle distribution for frit generated particles did not change even between 10 and 28 hours. Between the hour 24 and hour 35, the bacteria concentration did not significantly increase. Water samples were not taken between 10 and 24 hours, and so there still remains the possibility that bacteria already reached concentrations of 10^8 mL^{-1} by hour 10. The GBac mesocosm continued for 13 days during which time the bacterial concentrations fell to about 2×10^7 mL^{-1} then maintained a stationary phase growth where the growth rate is equal to the death rate. During this time the particle size distributions were continually measured.

4.4.4 Week 2: Jet generated particles

On the second week of the GBac mesocosm experiment, changes in the aerosol size distribution were detected days after the continuous 84 sampling time previously discussed. Figure 4.9 shows that jet generated aerosol particle size spectra evolved over time characterized by a noticeable shift of the dominant mode from 52.6 nm to 22.8 nm. On day 7 total particle production fell slightly $N_{\text{tot}} = 826$ mL^{-1} and rose again so that on the day 13, $N_{\text{tot}} = 1014$ mL^{-1}. Within the scatter of the data, the humidified spectra coincided with the theoretical growth factor of pure sea salt.

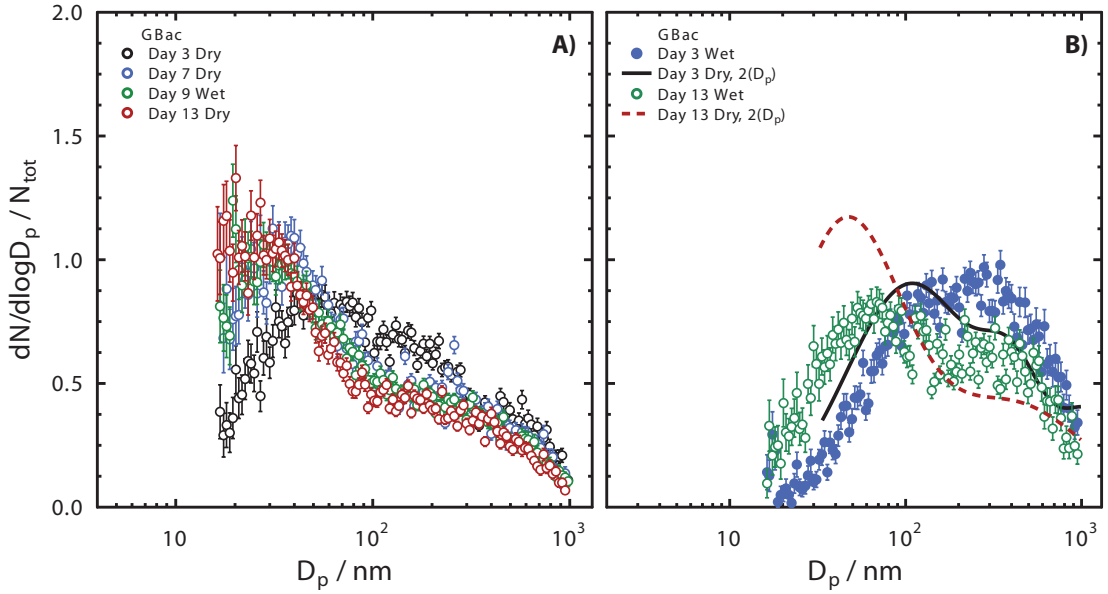

Figure 4.9: Changes in the normalized aerosol particle size distributions in mesocosm experiment GBac produced by plunging water jets in artificial seawater inoculated with a mixed bacteria culture from Great South Bay and added nutrients. Day 3 corresponds to hour 72 in Fig. 4.6. Dry aerosol spectra are shown in A and humidified spectra in B. Solid lines in panel B correspond to dry spectra fitted to a multimodal lognormal distribution with twice the dry particle diameter. The days after inoculation of the mesocosm are indicated.

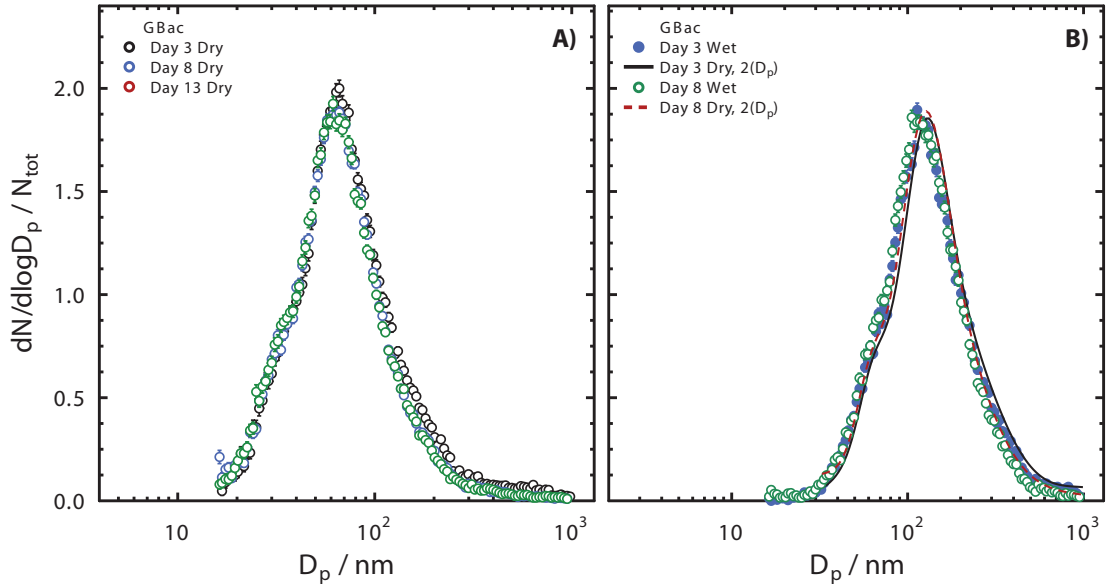

Figure 4.10: Changes in the normalized aerosol particle size distributions in mesocosm experiment GBac produced by aeration through frits in artificial seawater inoculated with a mixed bacteria culture from Great South Bay and added nutrients. Day 3 corresponds to hour 80 in Fig. 4.6. Dry aerosol spectra are shown in A and humidified spectra in B. Solid lines in panel B correspond to dry spectra fitted to a multimodal lognormal distribution with twice the dry particle diameter. The days after inoculation of the mesocosm are indicated.

4.4.5 Week 2: Frit generated particles

Figure 4.7A and B shows that the shape of dry frit generated particle spectra and the humidified spectra did not change over time. N_{tot} did decrease to 1.4×10^4 cm^{-3}, between day 3 and 7. A consistent behavior to that of the jet for both dry and humidified particles.

4.4.6 Summary of experiment GBac

The size distributions obtained from the GBac mesocosms clearly illustrate a changing aerosol particle flux as a function of bacterial growth for the jet and frit generated particles. When bacterial concentrations increased 4 orders of magnitude, the flux of particles increased 2 fold for the jet and at most by a factor of 1.4 for the frit. Surprisingly, when bacterial concentrations remained stationary and the seawater was allowed to age, aerosolization of particles having $D_p < 100$ nm tending to increase, while significantly contributing to total particle production for both the frit and jet. Table 3 gives the fitting parameters of a trimodal lognormal fit to the GBac and LowBac spectra. Additional, key points in time during experiments LowBac and GBac are plotted shown in Fig. 4.9 to emphasize that both bacterial concentration in seawater and seawater age have significant influences on changing the particle size distribution.

Figure 4.11 shows that after 2 weeks of growth and with 10^6 cells per mL for the LowBac experiment, aerosol spectra changed from their initial state. All three modes (see table 3) shifted to smaller diameters and were more pronounced. In the GBac experiment after only 3 days and bacterial concentrations of 10^8 mL, particle production was already greater than observed in the LowBac experiment after 2 weeks. Compared to LowBac day 1, the GBac day 3 spectrum had three very pronounced modes and shifted

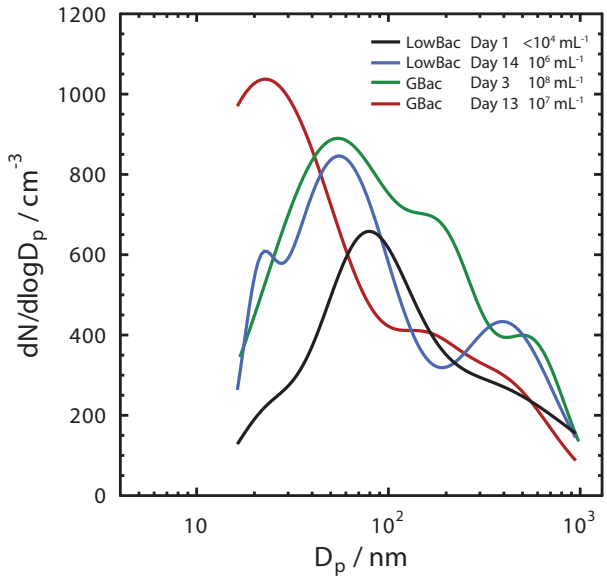

Figure 4.11: Summary of dry aerosol size spectra of jet generated particles as a function of bacteria growth from LowBac and GBac. Approximate bacterial concentrations and days since mesocosm inception are indicated. The distributions are fitted to 3 lognormal modes for clarity.

toward smaller D_p. When bacteria concentrations fell and the seawater was allowed to age for another week (GBac, day 13), the corresponding particle spectra shifted even more towards smaller D_p and particle production was greater, although secondary and ternary modes were less significant compared to GBac Day 3. Even though the concentration of bacteria fell and then remained constant over time, clearly there was a change in the size distribution and number of the aerosolized particles. This effect suggests a change in the composition/nature of particles in the water. Although the standing crop of bacteria did not change, there was likely continual turnover of cells, lysis of dead cells, and modification of the dissolved and particulate organic matter (DOM and POM). Increased production of smaller size particles in aerosol is consistent with these biological processes.

It is important to consider that even though particle production was altered significantly due to bacterial activities, under humidified conditions, the aerosolized particles behave like sea salt in all cases. In the study by Prather *et al.*[99], particles aerosolized from their flume after growth of bacteria for 4 days in natural

Table 3: Summary of lognormal fitting parameters for the GBac experiment as a function of time. For the i^{th} mode, D^i_{pg} nm, σ^i, and N^i_{tot} cm^{-3}, are the median diameter, standard deviation, and total particle contribution, respectively. $\overline{N}_{\text{tot}}$ cm^{-3} is the total particle concentration.

Day	D^1_{pg}	σ^1_g	N^1_{tot}	D^2_{pg}	σ^2_g	N^2_{tot}	D^3_{pg}	σ^3_g	N^3_{tot}	$\overline{N}_{\text{tot}}$
2	48.2	0.74	508	171.6	0.51	256	604.0	0.39	124	888
3	52.6	0.83	807	212	0.44	199	586.5	0.38	142	1150
7	32.5	0.81	610	259.5	0.68	211	703.3	16.8	17	838
9	25.6	0.66	454	80.9	1.20	490	383.1	0.68	112	1056
13	22.8	0.92	1035	156.8	0.42	98	392.0	0.58	174	1307

seawater also were determined to have hygroscopicities similarly to sea salt and did not change over time, in agreement with the results presented here.

Measurements of the humidified particle size distributions can be used to set limits on the average organic volume fraction and organic hygroscopicity using the Zdanovskii-Stokes-Robinson mixing rule[125]. It is determined that the growth factor for all humidified spectra indicate the behavior of pure sea salt, $g_{\text{inorg}} = 2.0$, within our uncertainty in inferring g of ± 0.2, a detection boundary for the growth factor of organic material, g_{org}, as a function of ϵ can be calculated from

$$g_{\text{org}}^3 = \frac{1}{\epsilon}(g^3 - g_{\text{inorg}}^3) + g_{\text{inorg}}^3. \tag{19}$$

In other words, by plugging in a conservative estimate for $g = 1.8 \pm 0.2$, bounds of ϵ and g_{org} can be derived.

Figure 4.12 gives the bounds of uncertainty for any combination of g_{org} and ϵ. Using the conservative uncertainty estimate in the average growth factor for a particle population, $\Delta g = \pm 0.2$, any point lying to the left of the $g = 1.6$ curve could describe the aerosolized particles from the mesocosm experiments LowBac and GBac. If only the error in RH were used, corresponding to $\Delta g = \pm 0.1$ from the theoretical growth factor of NaCl particles, then the range of values can be narrowed. Measurements of dry particle size spectra determined here show that particles having $D_p < 100$ nm contribute the majority of total aerosolized particles from seawater in which high biological activity occurs. Using the results from Prather *et al.*[99], we can assume that $70 - 80\%$ of particles aerosolized from our mesocosm are purely organic and from Fig. 4.12, it is easily seen that g_{org} must be greater than about 1.4. This may imply a presence of soluble and insoluble organic material in the aerosolized particles for the jet and frit and explain why no change in size distribution

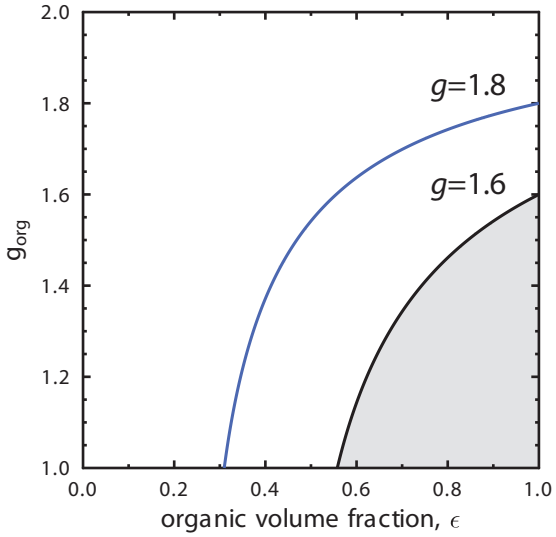

Figure 4.12: Bounds of possible organic volume fractions, ϵ, and the growth factor of organic material, g_{org}, for aerosolized particles from mesocosm experiments. The black line indicates the conservative uncertainty measurement in the growth factor of $\Delta g = \pm 0.2$, implying that g must be in the range of 1.6 and 2.0. If only the uncertainty in controlling RH ($\pm 4\%$) is considered then, $\Delta g = \pm 0.1$ then a range of g between 1.8 and 2.0 is considered. The gray area indicates where combinations of g_{org} and ϵ are in disagreement with the observed humidified particle size distributions.

at RH = 80% is observed.

The humidified spectra presented in this dissertation agree with the growth factors measured by Prather *et al.*[99]. We additionally observe however, that biological activity due to bacteria can significantly increase the flux of particles over time while cell concentrations remain stationary, likely due to bacterial growth and degradation of organic matter. These findings have implications for cloud microphysics and climate, where the determination of the flux of aerosol particles and CCN is crucial[118,119]. Bacterial growth and death continually occur in the oceans where bacteria have access to organic material including phytoplankton exudates, transparent exopolymer particles (TEP), marine microgels, and other carbon sources. Of course in the ocean, microbial community structures and their nutrient sources are complex and variable. However, our results suggest that marine bacteria under conditions of high nutrient loading may play a role in the aerosolization of marine biogenic particles.

4.5 Mesocosm experiments: *Thalassiosira pseudonana* (Tpseu)

In this next experiment, a more realistic microbial community was employed in mesocosm experiments Tpseu, where phytoplankton were grown simultaneously with bacteria. Changes in the particles size distribution were determined due to the biological activity in the seawater containing bacteria and a single diatom *Thalassiosira pseudonana* with a cell wall armored with amorphous hydrated silica glass, $SiO_2 \cdot nH_2O$. *T. pseudonana* is cosmopolitan in the world's oceans[193] and diatoms in general, are the dominant phytoplankton group in Polar regions[192]. The diatom *T. pseudonana* is known to produce and release into seawater, a significant quantity of exudates which support bacterial growth and are a source for microgel and TEP production. Although no bacteria were added with the phytoplankton cultures, background concentrations associated with the Instant Ocean or introduced from the room air at the beginning of the experiment were sufficient that growth occurred. The initial introduction of nutrients and the continual production of exudates by the algae during the course of the experiments supported a rising bacteria population.

4.5.1 Jet generated particles

Figure 4.13 shows changes in the jet generated aerosol particle size distribution as a function of time from following inoculation of *T. pseudonana* in the experiment Tpseu. The distribution in Fig. 4.13A is not normalized to N_{tot} as previously done. It is apparent that the presence of diatoms significantly impacted the aerosolization of particles. Particle production was minimal after 1 day of diatom growth ($N_{\text{tot}} = 222$ cm^{-3}) and increased significantly to just under 1600 cm^{-3} especially for particles having $D_p < 100$ nm. The humidified spectra shown in Fig. 4.13B from particles aerosolized using the jet show that in general, $g \sim 2.0$ given the experimental uncertainty and the scatter in the data.

4.5.2 Frit generated particles

The frit generated particle size spectra for the Tpseu experiment is given in Fig. 4.14. For the first days of growth, particle production was similar. After the first week, particle production rose slightly as it did

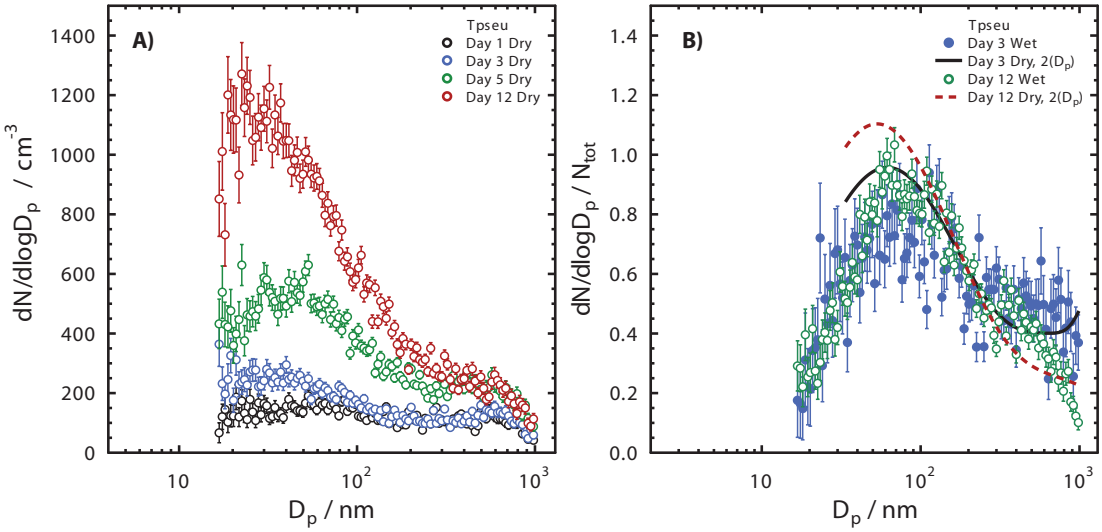

Figure 4.13: Changes in the aerosol particle size distributions in mesocosm experiment Tpseu produced by plunging water jets in artificial seawater inoculated with *Thalassiosira pseudonana* and added nutrients. Dry aerosol spectra are shown in A and humidified spectra in B. Solid lines in panel B correspond to dry spectra with twice the dry particle diameter. The days after inoculation of the mesocosm are indicated.

for frit generated particles for the LowBac and GBac experiments. Hygroscopicity of particles aerosolized using the frit could not be distinguished from sea salt (Fig. 4.14B).

4.5.3 Water composition

The changing aerosol particle size spectra can possibly be explained by changes in water composition. Figure 4.15 details the concentrations of *T. pseudonana* and bacteria, dissolved organic carbon (DOC), and

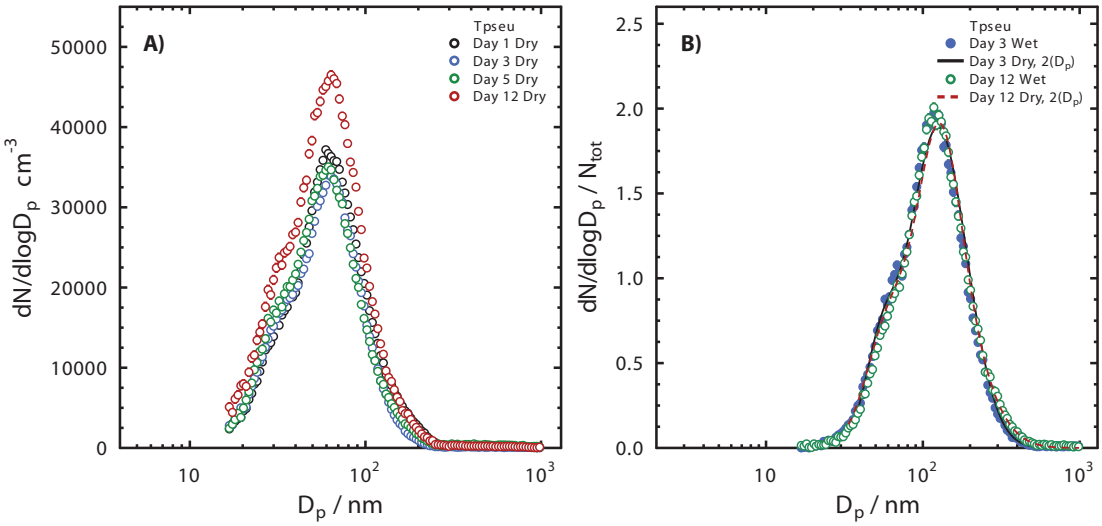

Figure 4.14: Changes in the aerosol particle size distributions in mesocosm experiment Tpseu produced by aeration through glass frits in artificial seawater inoculated with a culture of *Thalassiosira pseudonana* and added nutrients. Dry aerosol spectra are shown in A and humidified spectra in B. Solid lines in panel B correspond to dry spectra with twice the dry particle diameter. The days after inoculation of the mesocosm are indicated.

particulate carbon (PC). Phytoplankton numbers increased from 8×10^4 cells mL^{-1} to 3×10^5 mL^{-1} within 24 hours following inoculation and remained at that concentration through day 5. Over the next 3 days, concentrations leveled off at 3×10^6 mL^{-1} for the remainder of the second week. The bacterial concentrations grew and remained just over an order or magnitude more in numbers matching the increasing phytoplankton concentrations over time. Measurements of PC also tracked the increase in concentrations of bacteria and phytoplankton. DOC concentrations increased with time throughout the course of the experiment from the continual release of exudates by the diatoms.

4.5.4 Summary of experiment Tpseu

The aerosol size distribution of jet generated particles changed significantly over time in the experiment Tpseu. When bacteria and diatoms grew, total production increased for the jet and frit generated particles. Aerosolization of particles using the jet were more sensitive to biological activity than the frit, underscoring importance of different bubble generation and aerosolization methods. Furthermore, it is determined from jet generated particles that when bacteria and phytoplankton concentrations remain constant over time (Fig. 4.13A between day 1 and 5), the amount of aerosolized particles also increase. Also for the jet, the contribution to the increase in total particle production is primary due to particles with $D_p < 100$ nm. This is similar to the spectral effect determined in the GBac experiment. In conclusion, the release of exudates by diatoms resulting in the simultaneous growth of bacteria and in addition to the bacterial decay of organic matter and the possible presence of cell fragments, can impact the aerosolized particle flux from seawater.

4.6 Mesocosm experiments: *Emiliania huxleyi* (Ehux)

The phytoplankton coccolithophorid species *Emiliania huxleyi* has a cell wall composed of calcium carbonate platelets. This species forms massive blooms in polar and temperate coastal oceans, turning the water visibly white due to high concentration of cells. A mesocosm experiment Ehux, was initiated by inoculating ASW with an axenic uni-algal *E. huxleyi* culture and adding nutrients. *E. huxleyi* is known to produce exudates, however at lower concentrations than produced by diatoms at similar cell concentrations[215,216].

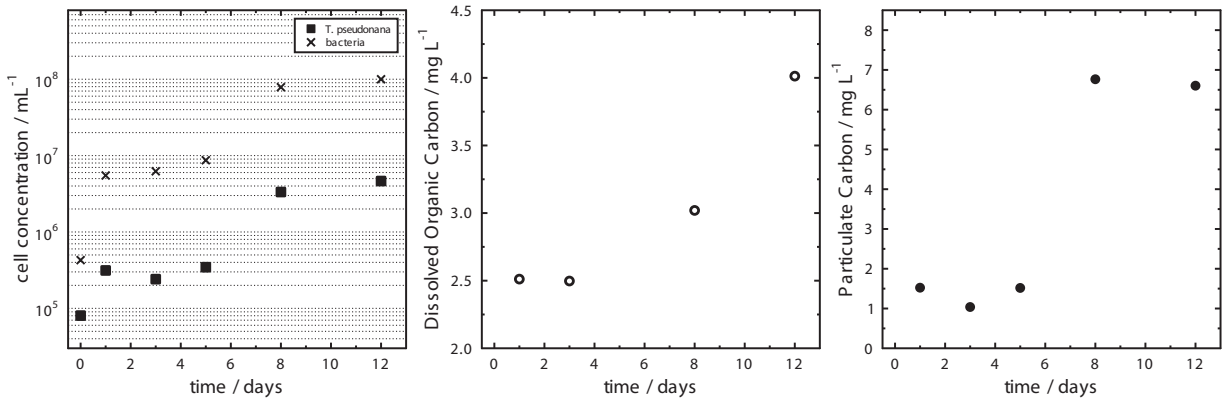

Figure 4.15: Seawater composition as a function of time in the mesocosm experiment Tpseu. Left panel: Concentrations of *Thalassiosira pseudonana* and bacterial cells in artificial seawater. Middle panel: Dissolved organic carbon concentration. Right panel: particulate carbon concentration.

It was therefore expected, that bacteria concentrations would not be stimulated to the same degree as they were in the Tpseu mesocosm.

4.6.1 Jet generated particles

The jet generated aerosol particle spectra are shown in Fig. 4.16. Similar to the Tpseu experiments, particle production increased significantly over time from $N_{\text{tot}} = 775$ on day 1 to 2426 cm^{-3} on day 12. The largest increase was due almost entirely to particles having $D_p < 100$ nm as seen in Fig. 4.16A under dry conditions. The dominant mode initially at 85.8 nm mode clearly shifted toward the smaller diameters down to 30.7 nm, on day 12. The humidified spectra shown in Fig. 4.16B indicates that $g = 2.0$ in general.

4.6.2 Frit generated particles

The frit generated particle size spectra for the Ehux experiment is given in Fig. 4.17. Clearly, aerosolized particles from the frit increased dramatically as a function of seawater age in the Ehux mesocosm (Fig. 4.17A). During 12 days of growth, particle production exactly tripled from $\sim 2 \times 10^4$ to 6×10^4 cm^{-3}. This increase in total particles was more than detected for the mesocosm experiments Tpseu, LowBac, and GBac previously discussed, and therefore may be an effect specifically unique to *E. huxleyi*. Despite the significant change in N_{tot}, the shape of the distribution remained exactly the same. Additionally, hygroscopicity of the frit generated particles shown in Fig. 4.17B remained the same for the entire experimental time period presumably reflecting, once again, the behavior of sea salt.

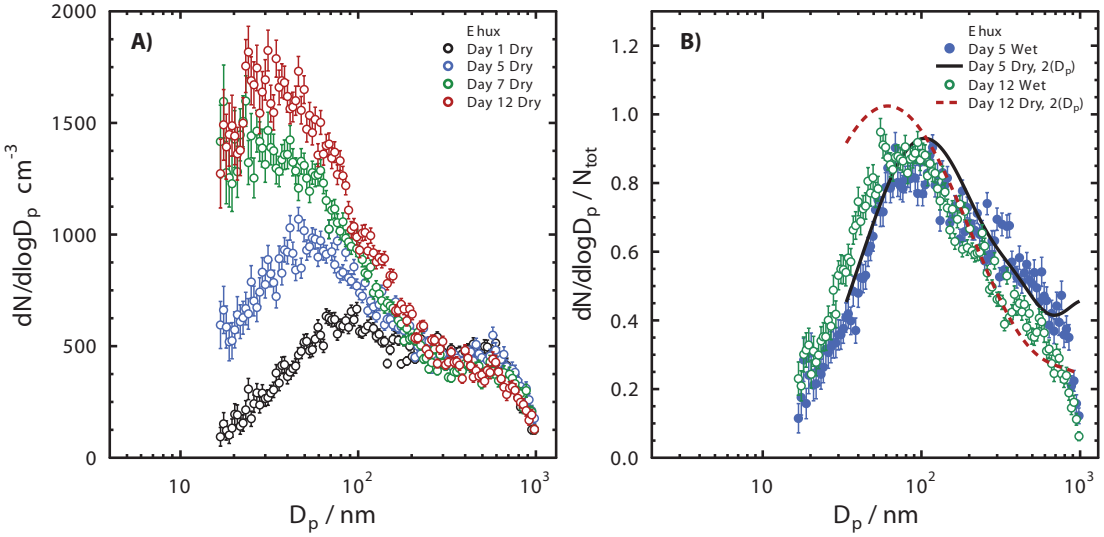

Figure 4.16: Changes in the aerosol particle size distributions produced by plunging water jets in mesocosm experiment Ehux in artificial seawater inoculated with *Emiliania huxleyi* and added nutrients. Dry aerosol spectra are shown in A and humidified spectra in B. Solid lines in panel B correspond to dry spectra with twice the dry particle diameter. The days after inoculation of the mesocosm are indicated.

4.6.3 Water composition

Cell concentrations of *E. huxleyi* and bacteria, in addition to DOC and PC concentrations in seawater are shown in Fig. 4.18. The concentration of phytoplankton cells steadily increased from an initial concentration of 2×10^5 mL^{-1} reaching a maximum of 7×10^6 mL^{-1} on day 11. Concentrations of bacteria did not closely follow phytoplankton concentrations in contrast to the Tpseu experiment but instead, rose rapidly to 4×10^6 in the matter of 1 day, a doubling time of about 8 hours. The bacterial concentrations then remained stationary through day 7, in spite of the fact that the concentration of phytoplankton rose steadily with a doubling time of about 48 hours. The concentration of DOC shown in the middle panel of Fig. 4.18 is consistent with the elevated numbers of bacteria. It is likely that for a bacterial community, consumption of DOC was greater than the exudate production by the phytoplankton which was reflected in the drop during the first 5 days of the experiment in the concentration of DOC. Only until *E. huxleyi* cell concentrations rose above 10^6 mL^{-1} did the DOC concentration begin to increase. The concentration of PC corresponded to the abundance of phytoplankton. High concentration of PC were observed in the Ehux mesocosm experiment reaching $\sim$ 10 mg carbon L^{-1}. This PC production which was greater than found with any of the other phytoplankton may well be due to the continual production of cell wall calcium carbonate platelets by *E. huxleyi*.

4.6.4 Summary of experiment Ehux

The Ehux mesocosm experiment resulted in the aerosolization of particles significantly impacted for both the jet and frit generated particles. Total particle production was tripled from its initial state coinciding with the growth of phytoplankton and bacteria. However, particle aerosolization for the jet and frit were different, as previously observed. Clearly, the shape of the frit generated particle size distribution was insensitive to

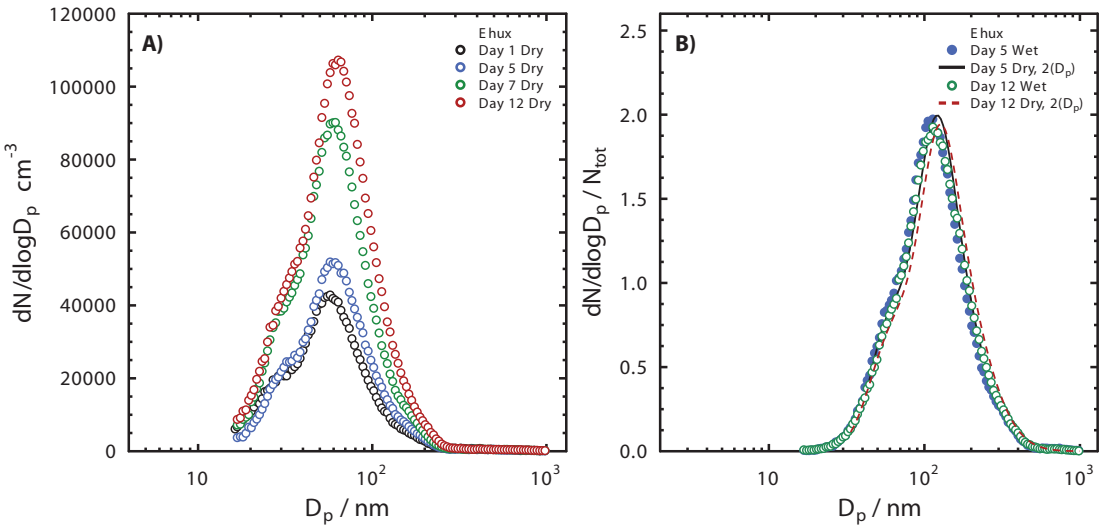

Figure 4.17: Changes in the aerosol particle size distributions in mesocosm experiment Ehux produced by aeration through glass frits in artificial seawater inoculated with *Emiliania huxleyi* and added nutrients. Dry aerosol spectra are shown in A and humidified spectra in B. Solid lines in panel B correspond to dry spectra with twice the dry particle diameter. The days after inoculation of the mesocosm are indicated.

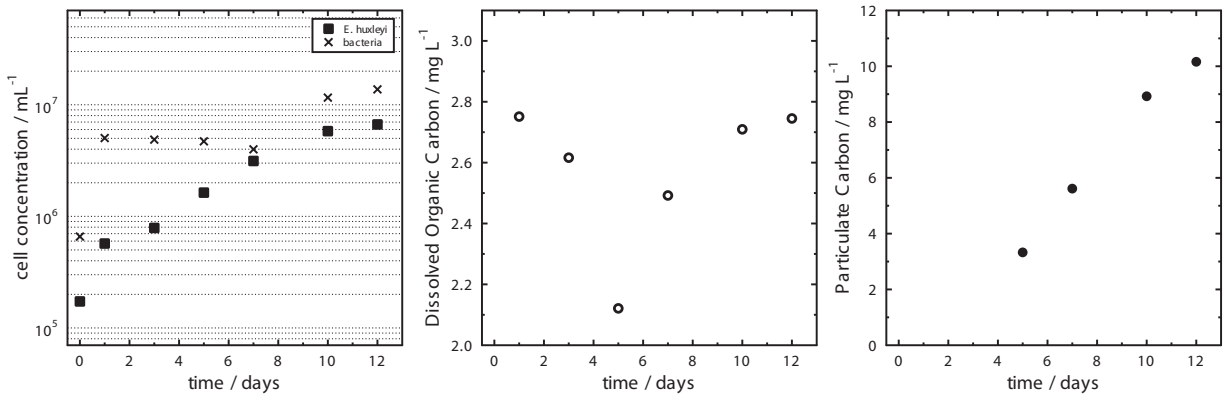

Figure 4.18: Seawater composition as a function of time in the mesocosm experiment Ehux. Left panel: Concentrations of *Emiliania huxleyi* and bacterial cells in artificial seawater. Middle panel: Dissolved organic carbon concentration. Right panel: particulate carbon concentration.

phytoplankton or bacterial growth, in contrast to the jet which changes shape significantly. As previously discussed for jet generated particles, the most significant increase in particle production is due to particles generally having $D_p < 100$ nm, thus the resulting size distribution shape is shifted from larger to smaller D_p. The spectral changes for Ehux for the frits or jets were more sensitive to biological activity in general than for LowBac, GBac, and Tpseu experiments, respective to each aerosolization method. This may imply that the growth of *E. huxleyi* and bacteria simultaneously had a greater effect on aerosolization when compared with bacterial growth alone.

4.7 Mesocosm experiments: *Nannochloris atomus* (Natom)

Nannochloris atomus is representative of smaller phytoplankton with a cell wall composed of cellulose. This phytoplankton is a dominant species in North Atlantic waters where it forms massive blooms during the fall[201]. Although exudate production from *N. atomus* was expected to be less than that of *T. pseudonana*.

4.7.1 Jet generated particles

Changes in jet generated aerosol particle size distributions during the Natom experiment are shown in Fig. 4.19. Over time, dry particle spectra (Fig. 4.19A) were observed to change, however, $N_{\text{tot}} = 1.1 \times 10^3 - 1.3 \times 10^3$ cm^{-3}, and remained essentially the same throughout the whole experiment. The shape of the particle size distribution, however, changed similar to previous mesocosm experiments, shifting toward small particle diameters for increased bacterial and phytoplankton concentrations. From the humidified spectra seen in Fig. 4.19B, particle hygroscopicity did not change over time within the scatter of the data.

4.7.2 Frit generated particles

Changes in the frit generated particle size spectra were detected in the Natom experiment shown in Fig. 4.20. Aerosolized particles from the frit for dry conditions increased as a function of seawater age (Fig. 4.20A). Over the course of 12 days, particle production almost doubled from about 2.1×10^4 to 3.9×10^4 cm^{-3}.

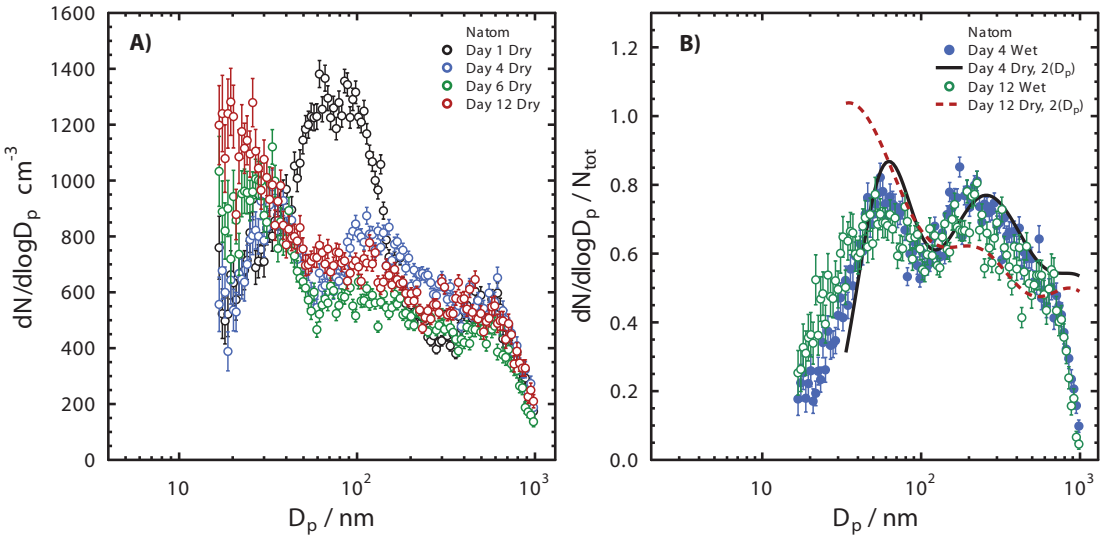

Figure 4.19: Changes in the aerosol particle size distributions in mesocosm experiment Ehux produced by plunging water jets in artificial seawater inoculated with *Nannochloris atomus* and added nutrients. Dry aerosol spectra are shown in A and humidified spectra in B. Solid lines in panel B correspond to dry spectra with twice the dry particle diameter. The days after inoculation of the mesocosm are indicated.

The shape remained exactly the same, a feature similar to all other mesocosm experiments. The humidified spectra shown in Fig. 4.20B appeared to be slightly shifted to the left of what would be considered $g = 2.0$. Based off the peak position of the dry (60.9 nm) and humidified ($\sim$ 103.9 nm) spectra from fitting to lognormal distributions, $g = 1.7$ on average for all humidified frit generated particle size spectra throughout the experimental time period. This values lies above our threshold for detecting significant changes in hygroscopicity compared with pure sea salt (see Fig. 4.12).

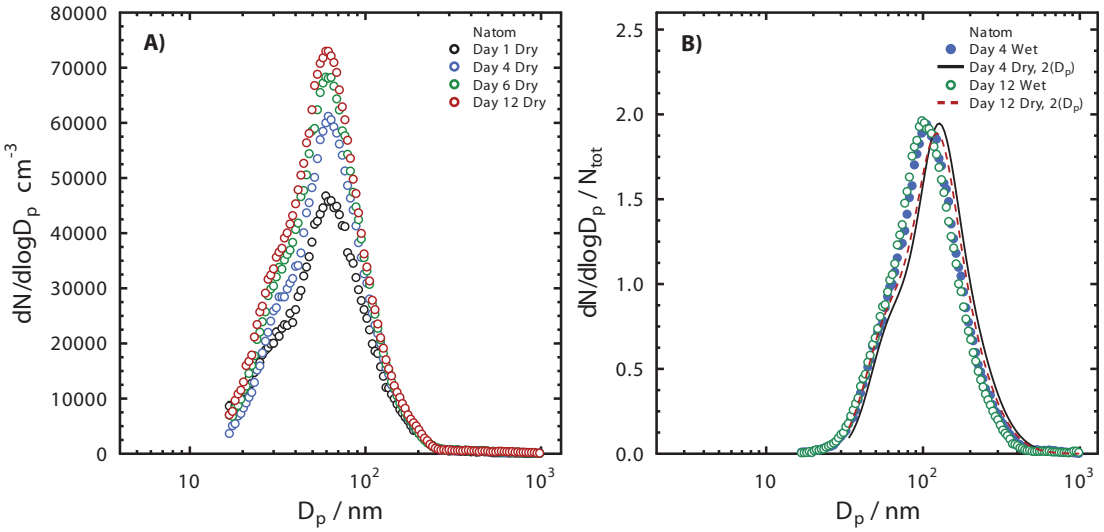

Figure 4.20: Changes in the aerosol particle size distributions in mesocosm experiment Natom produced by aeration through glass frits in artificial seawater inoculated with a *Nannochloris atomus* and added nutrients. Dry aerosol spectra are shown in A and humidified spectra in B. Solid lines in panel B correspond to dry spectra with twice the dry particle diameter. The days after inoculation of the mesocosm are indicated.

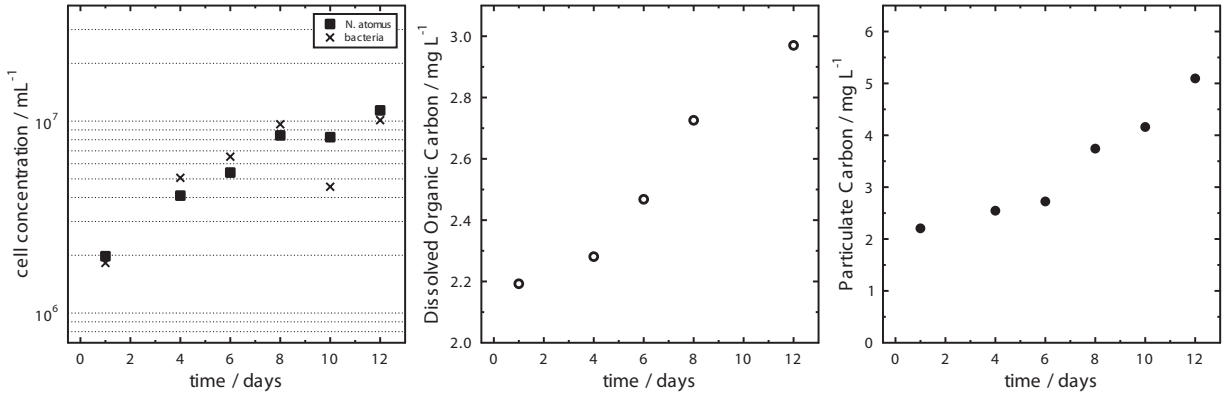

Figure 4.21: Seawater composition as a function of time in the mesocosm experiment Natom. Left panel: Concentrations of *Nannochloris atomus* and bacterial cells in artificial seawater. Middle panel: Dissolved organic carbon concentration. Right panel: particulate carbon concentration.

4.7.3 Water composition

Concentrations of *N. atomus* cells shown in Fig. 4.21 increased steadily over time, but with the slowest doubling time for any of the experiments with phytoplankton, at just under 4.5 days. Bacterial, DOC, and PC concentrations tracked phytoplankton cell concentrations closely. Figure 4.21 shows that the bacterial concentrations dropped significantly after day 8, while the concentration of *N. atomus* remained stabilized. Bacterial numbers increased again after day 10, however, the temporary drop was not noticeable from DOC or PC concentrations. Te exact dynamics within the alga/bacterial community occurring on days 9-11 are unclear, however, it did not affect the particle size spectra on day 8 and 10 (not shown) which fell between values on day 6 and 12.

4.7.4 Summary of experiment Natom

The dry and humidified particle size distributions for jets and frits are clearly dependent on phytoplankton and bacterial growth in the Natom mesocosm experiment. The shapes of the dry jet generated particle size spectra shifted toward smaller D_p although no increase in N_{tot} was detected. For frit generated particles, N_{tot} increased over time, however, the shapes of the particle size distributions were not altered. Humidified particle size spectra from jets and frits were indistinguishable from that expected for pure sea salt particles within our experimental uncertainty.

4.8 Mesocosm experiments: Natural phytoplankton and bacterial community (NatSW)

A mesocosm seawater experiment was conducted for the purpose to quantify the changing aerosol size distribution as a function of biological activity for a natural community of phytoplankton and bacteria growing simultaneously. Natural seawater was collected during incoming tide at Shinnecock Inlet of the Great South Bay on the south shore coast of Long Island, NY and transported back the laboratory to be used for the mesocosm experiment NatSW. The seawater passed through a mesh screen to keep out large

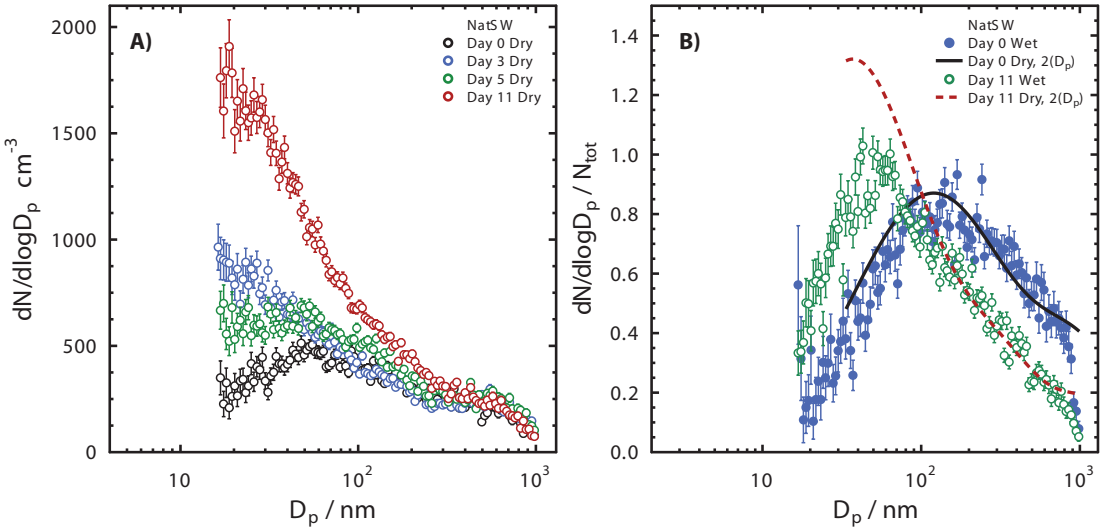

Figure 4.22: Changes in the aerosol particle size distributions in the mesocosm experiment NatSW produced by plunging water jets in natural seawater without inoculation of phytoplankton or bacteria. The days after the start of the mesocosm are indicated. Day 0 was the initial state of the natural seawater without added nutrients. After day 0, nutrients were added to stimulate phytoplankton growth. Dry aerosol spectra are shown in A and humidified spectra in B. Solid lines in panel B correspond to dry spectra with twice the dry particle diameter.

particles about 1 mm in size. Once the mesocosm was filled, the bacteria and phytoplankton concentrations in the seawater were quantified. Particle size spectra were also measured from the natural seawater at day 0 corresponding to the start of the experiment. After completing the initial measurements, nutrients were added to stimulate phytoplankton growth.

4.8.1 Jet generated particles

Figure 4.22 shows the changes in the jet generated aerosol particle size distribution as a function of time in natural seawater from its initial state at day 0 and 11 days of growth after nutrient addition. For jets, N_{tot} increased over time from an initial value of 569 cm^{-3} essentially doubling to $N_{\mathrm{tot}} = 1329$ cm^{-3} 11 days after nutrient addition. The increase in N_{tot} was mostly due to particles having $D_p < 100$ nm, as can be seen in Fig. 4.22A from the shifting particle size spectra. The humidified spectra in Fig. 4.22B indicated that there was little change in particle hygroscopicity over the experimental time as g was similar to that of sea salt.

4.8.2 Frit generated particles

Dry particle size distributions generated using frits are shown in Fig. 4.23. Again, similar spectral features are observed when compared with previous mesocosm experiments. Aerosolized particles increased as a function of seawater age over the course of 5 days of growth and doubled from 3.7×10^4 cm^{-3} initially to 7.0×10^4 cm^{-3} on day 5. On day 11, particle production from the frit fell significantly, however, on this day it was observed that phytoplankton cells settled out of the bulk water and coated the surface of the frits. It is likely, that a different bubble production occurred as a result and therefore, this data is not used. The

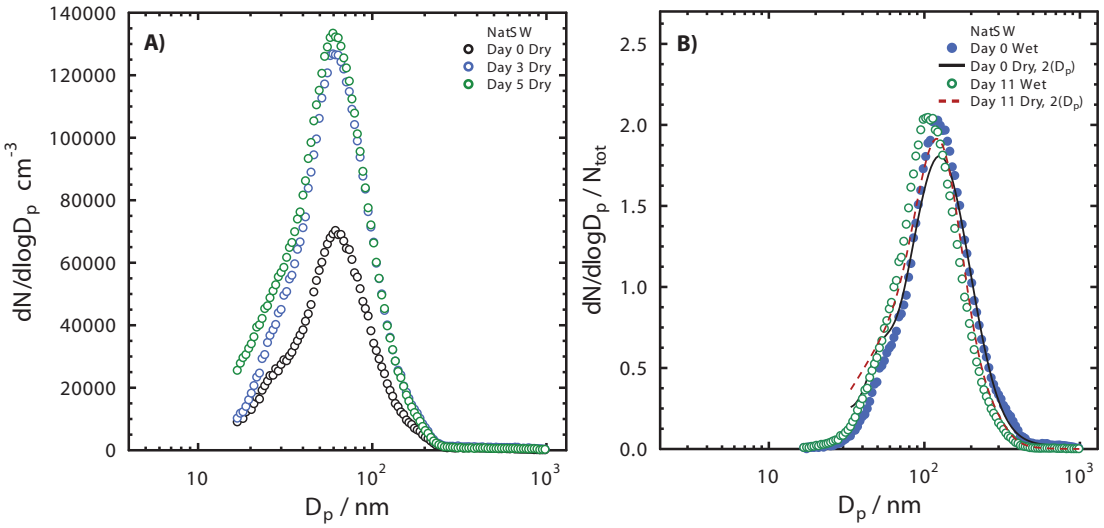

Figure 4.23: Changes in the aerosol particle size distributions in the mesocosm experiment NatSW produced by aeration through glass frits in natural seawater without inoculation of phytoplankton or bacteria. The days after the start of the mesocosm are indicated. Day 0 was the initial state of the natural seawater without added nutrients. After day 0, nutrients were added to stimulate phytoplankton growth. Dry aerosol spectra are shown in A and humidified spectra in B. Solid lines in panel B correspond to dry spectra with twice the dry particle diameter.

humidified spectra are shown in Fig. 4.23B indicates the particle hygroscopicity did not deviate significantly than that observed for pure sea salt within our experimental detection limits.

4.8.3 Water composition

The phytoplankton and bacterial cell concentrations are shown in Fig. 4.24. Initially there were $\sim 10^4$ mL^{-1} phytoplankton cells for the first 5 days, a low but common concentration found throughout the oceans. On the first day, the biological community had to adjust to the new mesocosm environment and consequently phytoplankton concentrations did not increase until after day 1. During day 1 to 5, the phytoplankton population doubled every 18 hours. On day 5, it was determined that diatoms dominated the phytoplankton population reaching concentrations of just under 3×10^5 mL^{-1}. By day 11, phytoplankton numbers had dropped below initial levels. This was likely due to settling out of the cells which were clearly visible on the bottom of the mesocosm. The bacterial population grew quickly, doubling in the first day reaching a maximum concentration of 5.5×10^6 mL^{-1} on day 3. From day 3 to 11, bacterial concentrations declined to 1.0×10^6 mL^{-1}. Bacterial activity on the bottom of the tank was expected to be high due to the substantial biomass from the sedimented phytoplankton. Resuspension of metabolites in the bulk water could have played a role in changing the water composition, however this was unquantifiable.

4.8.4 Summary of experiment NatSW

The changing phytoplankton and bacterial populations influenced the aerosolization of particles for jets and frits, determined from measuring the particle size spectra over time. Jet and frit generated particles both increased by a factor of two over 11 days of phytoplankton and bacterial growth. The increase in particle

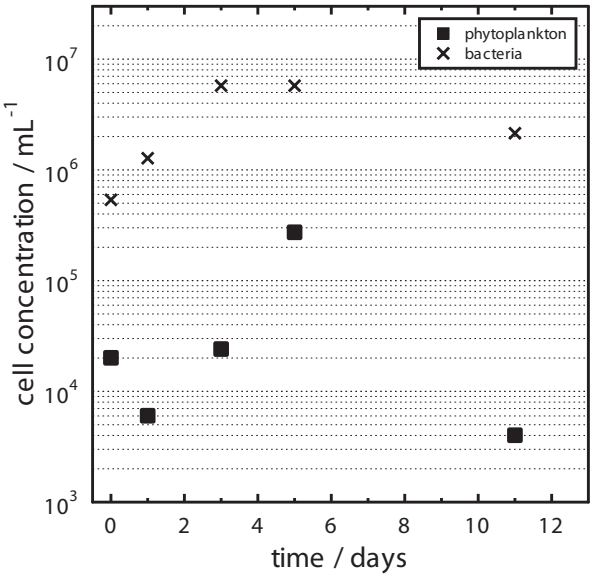

Figure 4.24: Phytoplankton and bacteria cell concentrations in natural seawater as a function of time in the mesocosm experiment NatSW. Day 0 is the initial seawater state before adding nutrient to grow phytoplankton. Day 1 refers to the time after the nutrient was added.

aerosolization between day 0 and 3 coincided with bacterial growth, despite the fact that the phytoplankton population was still low. The shapes of the jet generated particle size spectra shifted dramatically toward smaller particles, which contributed most to the increase in particle flux. The frit generated particle size spectra remained similar, just as in previous mesocosm experiments. From the humidified particle size spectra aerosolized particles had similar hygroscopicities to that of sea salt.

4.8.5 Discussion of mesocosm experimental results

In the mesocosm experiments Tpseu, Ehux, Natom, and NatSW, every effort was made to mimic natural marine biological activity with phytoplankton and bacteria growing simultaneously. Results showed that for each experiment, changes in the particle size distributions occurred with increasing biological activity over time where the common variable was the presence of a bacterial population. When bacterial concentrations increased, aerosolized particles tended to increase in total number for the jet and frit. When bacterial concentrations were stable over time, particle aerosolization was also determined to increase. When bacterial concentrations declined over time, particle aerosolization was also determined to increase, implying that the age of the microbial community also plays an important role in particle aerosolization. Jet and frit generated particle size spectra were very different from each other in terms of particle distribution shape and total particle numbers. However, the shapes of jet generated spectra were sensitive to changes in water composition while the frit retained its shape for all mesocosm experiments. Jet generated particle size spectra tended to always shift toward smaller sized particles, as the seawater in each mesocosm aged as can be seen from all particle size distributions and from table 4 which gives a summary of fit parameters in a trimodal lognormal fit for dry jet generated particle spectra for experiments Tpseu, Ehux, Natom, and NatSW. For continual biological activity, aerosolization of particles with $D_p < 100$ nm were greatly enhanced for jet generated

Table 4: Summary of lognormal fitting parameters as a function of time for the mesocosm experiments Tpseu, Ehux, Natom, and NatSW. For the i^{th} mode, D^i_{pg} nm, σ^i, and N^i_{tot} cm^{-3}, are the median diameter, standard deviation, and total particle contribution, respectively. $\overline{N}_{\text{tot}}$ cm^{-3} is the total particle concentration.

	Day	D^1_{pg}	σ^1_g	N^1_{tot}	D^2_{pg}	σ^2_g	N^2_{tot}	D^3_{pg}	σ^3_g	N^3_{tot}	$\overline{N}_{\text{tot}}$
Tpseu	1	21.2	0.20	12	58.2	0.92	157	504.7	0.67	72.2	241
	3	30.8	1.20	332	468.5	0.67	59	630.1	0.21	13	404
	5	39.9	1.13	654	530.9	0.55	112	-	-	-	766
	8	30.8	0.95	1292	165.4	1.07	301	-	-	-	1593
	12	26.6	1.19	1441	498.2	0.68	127	-	-	-	1568
Ehux	1	85.8	0.84	556	297.4	0.33	75	592.1	0.34	144	775
	3	77.3	0.94	944	460.7	0.42	197	713.4	0.24	52	1193
	5	52.3	0.95	980	223.9	0.39	77.9	583.7	0.43	192	1251
	7	26.6	1.40	2182	531.0	0.40	89	757.2	0.18	21	2291
	10	33.6	1.14	1696	486.3	0.60	143	-	-	-	1839
	12	30.7	1.28	2288	552.1	0.52	138	-	-	-	2426
Natom	1	20.2	0.35	159	75.8	0.70	1002	523.4	0.44	248	1409
	4	29.1	0.40	340	127.6	0.75	648	574.2	0.47	217	1205
	6	24.3	0.45	365	126.1	1.23	765	576.9	0.27	55	1185
	8	19.2	0.78	890	158.9	0.71	424	626.0	0.42	187	1501
	10	22.2	0.57	523	118.5	0.71	436	530.3	0.50	225	1184
	12	17.3	0.88	1117	125.8	0.62	392	502.3	0.54	293	1803
NatSW	0	58.0	1.10	544.7	467.2	0.65	92	689.5	0.13	7	644
	3	19.8	0.69	413	72.5	1.15	504	620.9	0.42	72	989
	5	37.2	1.47	1004	127.3	0.21	8.7	602.9	0.40	62	1075
	11	18.5	1.02	1878	166.3	0.69	243	584.4	0.40	69	2190

particles.

Jet generated aerosol particle size distributions changed significantly over time as phytoplankton and bacteria grew in seawater. Kuhnhenn-Dauben *et al.*[217] report that when using a water impingement method in natural seawater, resulting bubbles exhibit lifetimes that increase by a factor of two when chlorophyll concentrations exceed $\sim$ 20 mg L^{-1}, corresponding to a natural phytoplankton and bacterial population growing 4-5 days due to added nutrients. If bubble residence times increased in the mesocosm tank over time, then total bubble concentrations would increase and may influence aerosol production. Additionally, bubbles that were millimeters in size could be seen at the water surface in the mesocosm experiments reported here. These bubbles burst quickly, but also changed size significantly due to the coalescence of neighboring bubbles, thus they were impossible to quantify. The influence of bubbles having diameters larger than 1 mm on aerosolization is currently unknown and it cannot be stated that they did not have an effect.

Despite the changes in total particle production, the shape of the frit generated particle size distribution did not change for any mesocosm experiment nor for any difference in bacterial or phytoplankton cell concentration. The reason for this may be that bubble numbers were dominated in all instances for diameters

around 100 μm. Thus, a more uniform bubble spectra as observed in Fig. 4.1 for frits may represent more uniform aerosol production.

In general, the most striking feature of all experiments was an increasing particle flux with increasing biological activity due primarily to the enhanced aerosolization of small particles from mesocosms where the common microorganisms were bacteria. Bacterial growth and degradation of organic material thus may change the nature of the organic composition in seawater that affect the aerosolized particle particle flux. This occurs during bacterial growth as well as when bacterial concentrations remain stationary. Prather *et al.*[99] did not observe any change in particle spectra over a 5 day bacterial growth period with concentrations spanning less than an order of magnitude. In this study, continually changing aerosol particle size distributions are observed for bacterial concentration ranging from $< 1 \times 10^4$ to 7×10^8 mL and over the course of 14 days. The observed effects of biological activity on particle aerosolization as seen in mesocosm experiments suggest that similar effects may occur in the ocean.

Finally, the measurements of the humidified particle size spectra generated using jets or frits implied that particle hygroscopicity was similar to sea salt within our experimental detection limits. This allowed for bounds to placed on the values of average particle organic volume fraction (ϵ) and growth factor of organic material (g_{org}) due the fact that the total particle growth factor had to lie within a range of $g = 1.6 - 2.0$ to be consistent with the observations here (see Fig. 4.12).

4.9 Marine particle flux

The flux of marine aerosol particles from the ocean surface is important for estimating climatic impacts on clouds and radiative forcing[24,66,95,118,119,124]. The measured aerosol particle size distributions can be used to calculate the flux of particles from the mesocosms in each experiment according to the equation

$$\frac{dF}{d\log dD_p} = \frac{Q}{A_b}\frac{dN}{d\log D_p}W, \tag{20}$$

$dF/d\log dD_p$ is the flux normalized to the diameter bin width, $Q \sim 10$ L min^{-1} is the cross flow in the headspace of the mesocosm tank and A_b is the bubble surface area coverage in water. This type of flux calculation is termed the "white cap method". The white cap coverage, W, as observed from aerial photographs and observations of ocean surface light scattering by remote sensing of ocean white area is parameterized with simultaneous wind speed at 10 m above the sea surface, U_{10}, in height in a exhaustive data set by Monahan and Ó Muircheartaigh[96] as

$$W = 3.84 \times 10^{-6} U_{10}^{3.41}. \tag{21}$$

Other parameterizations of W exist, however, Eq. 21 is used to compare with previous flux parameterizations who use the same equation for W derived by Monahan and Ó Muircheartaigh[96]. Previous laboratory studies have calculated A_b by integrating the bubble size distribution beneath the water surface taking into account the cross sectional surface area of bubbles rising past a plane surface[27,97]. The uncertainty in calculations of A_b from underwater measurements are found to be high translating to at least ± 2 orders of magnitude

in the flux calculation[24,95]. It is also unclear if tank geometry plays a role in under or overestimating A_b or in changing the bubble bursting process altogether, considering the artificial constraints of the tank itself on the size of the bubble swarm that rises to the surface. Furthermore, it is unclear as to whether or not the white cap fraction measured in the open ocean by optical imagery or remote sensing is the same "white-ness" as appears at the air-water interface in the laboratory[95].

In the following analysis, the flux of marine particles is presented with careful consideration to the uncertainties inherent in its calculation. The purpose here is to provide a means for comparison with previous measurements and parameterizations. It is important to note that the tank utilized in this study can accommodate penetration depths of 55 cm and has a seawater surface area of 0.75 m^2 allowing ample bubble surface travel area and lifetime with minimal interaction with the walls of the tank. Upon visual inspection, the white area observed from surface bubbles covered $\sim 10\%$ of the seawater surface in the tank which translates to $A_b = 0.075$ m^2.

The calculated fluxes on different days of the NatSW mesocosm using the jets or frits are shown in Fig. 4.25 adapted from de Leeuw *et al.*[95]. Previous laboratory[25–27] and field[24,28] measurements are shown for comparison. It is clear that the flux calculations for jet generated particles derived here are about 2-3 orders of magnitude lower than for most other studies extending into the sub-micrometer size range. This may due in part to the method of obtaining A_b which as previously stated, translates to an error of about 2 orders of magnitude. On the other hand, flux measurements are in good agreement with Lewis and Schwartz[24] for

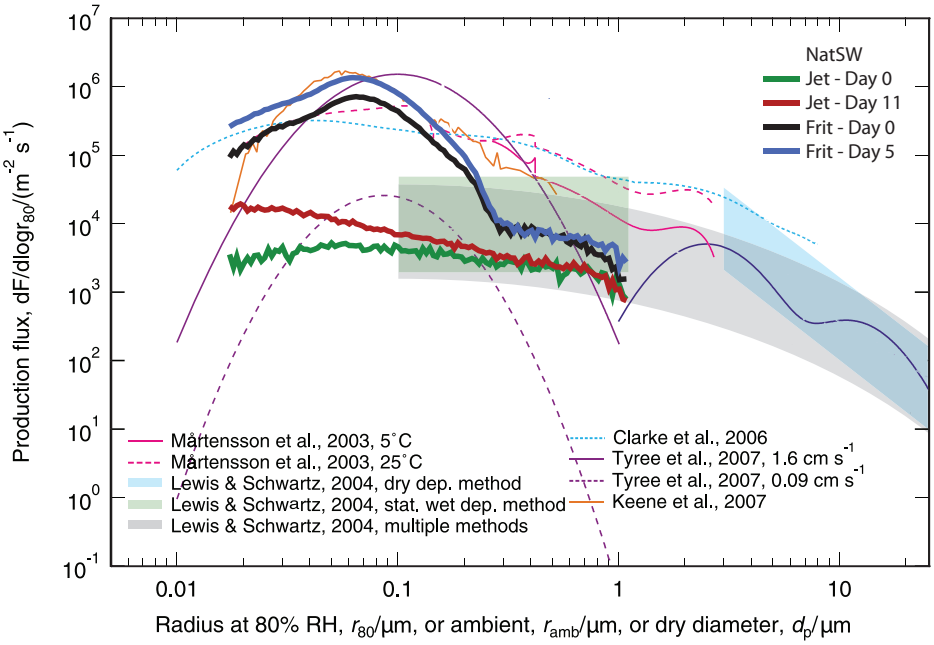

Figure 4.25: Size distribution of marine biogenic particle flux from the NatSW mesocosm experiment in comparison to previous literature parameterizations evaluated for a wind speed of $U_{10} = 8$ m s^{-1}. Estimates of Lewis and Schwartz[24] are based on statistical wet deposition methods (green shading), steady state dry depositional methods (green), and a combination of the two methods (blue shading). Bubbling chambers were used in Mårtensson *et al.*[25], Tyree *et al.*[26], and Keene *et al.*[27]. Surf zone fluxes parameterized by Clarke *et al.*[28] were formulated using size distribution measurements taken at different heights from a 20 m tall tower located $20 - 30$ m from the shoreline.

particle sizes between 0.1 and 1.0 μm using dry and wet deposition methods designed on the basis of modeling aerosol particle transport, to match observations of particle concentrations and accounting for gravitational settling, turbulence, Brownian motion, water condensation, and loss to the sea surface[24]. Calculations of frit generated particle flux are in agreement with previous laboratory studies employing an aeration as the bubble generation method[25–27] and a field study of surf zone flux[28].

We find that the flux spectra of particles $D_p < 0.1$ μm varied by as much as an order of magnitude between periods of low and high biological activity occurring in the experiment NatSW for both the jet and frit. On Day 0 of NatSW, the total flux of aerosolized particles was $F = 5.8 \times 10^3$ cm^{-3} (air) m^{-2} s using the jet. After 11 days of increasing bacterial and phytoplankton concentrations, $F = 1.2 \times 10^4$ cm^{-3} (air) m^{-2} s, an increase by a factor of 2. For frit generated particles F increased from 3.7×10^5 to 7.3×10^5 m^{-2} s. Previous literature has shown that variations in ambient particle size distributions should be used to reproduce observed CCN concentrations and thus, estimate cloud radiative forcing[118,119]. The results from the NatSW mesocosm shown in Fig. 4.25 and the changes in the size spectra for the other mesocosm experiments indicate a strong relationship to biological activity. If these changing fluxes occurred in the ocean during times of elevated primary productivity in surface waters, then they could have a significant impact on predicted CCN concentrations.

4.10 Heterogeneous ice nucleation

Mesocosm experiments described here indicate that biological activity occurring in seawater influences aerosolization of marine particles. Submicron sized marine particles collected from the overlying air can have significant concentrations of associated organic material[3,82,110], and are small enough to potentially be lofted to altitudes where temperature favor ice formation. To better understand the ice nucleating potential of marine biogenic particles, experiments were performed to determine the temperature, T, and relative humidity with respect to ice, $\mathrm{RH_{ice}}$ at which ice nucleation occurs and to discriminate between ice nucleation modes. Ice onset is a term used to describe the first freezing event observed in a single ice nucleation experiment. Onset conditions for deposition freezing (vapor-to-ice transition) and condensation freezing (vapor-to-liquid-to-ice transition) are shown in Fig. 4.26 for the mesocosm experiments NatSW, Natom, and Ehux. The jet and frit generated particles are compared to determine if ice nucleation is dependent on aerosolization method.

Ice nucleation onset conditions of T and $\mathrm{RH_{ice}}$ are shown in Fig. 4.26. Relative humidity with respect to water, RH, is also given. The results from different mesocosm experiments and aerosolization methods on different days are shown. Deposition freezing occured for all particles below a temperature of 215 K between $\mathrm{RH_{ice}} = 109\%$ and 132%. Water condensation was determined between $220 - 230$ K occurring at $\mathrm{RH_{ice}} \simeq 118\%$ or RH = 75%. Immersion freezing was observed subsequent to water uptake at 5% and 25% lower in $\mathrm{RH_{ice}}$ than the homogeneous freezing limit. At temperatures around 240 K water uptake is again observed at RH = 75% followed by immersion freezing. At the warmest investigated temperature (245 K), immersion freezing was observed close to 10 K warmer than expected to occur for homogeneous ice nucleation. It is clear from these data that marine biogenic aerosol particles have the capability to nucleate

ice efficiently in the deposition and immersion mode regardless of the community of organisms in a specific mesocosm, mesocosm growth times, and the particle generation method used. The results are compared to ice nucleation data obtained by Wise *et al.*[8] on pure NaCl and NaCl dyhydrate ($NaCl{\cdot}2H_2O$) particles. These authors observe deposition ice nucleation for NaCl at or below its deliquescence relative humidity for $T = 220 - 240$ K. At these temperatures deposition freezing is not observed for aerosolized marine particles from mesocosm experiments. Wise *et al.*[181] observed that sea salt may be able to take up very small amounts of water around RH = 40% due to salts other than NaCl. This most likely explains why water uptake and immersion freezing occurs for sea salt particles while deposition freezing occurs for pure NaCl.

Deposition freezing occurred with IN concentrations between $\sim 0.2 - 0.3$ L^{-1} (air). IN concentrations were estimated from the flow rate and sampling time used for impaction ~ 9 L min^{-1} for 30 s for the jet and 20 s for the frit. Particle concentrations at $D_p > 250$ nm (the 50% cutoff diameter of the final impactor stage) roughly estimated at 300 cm^{-3}, give rise to IN fractions of the total particle population on the order of 2×10^{-4}. It is important to note that most particles with $D_p > 1000$ nm were removed on impaction by

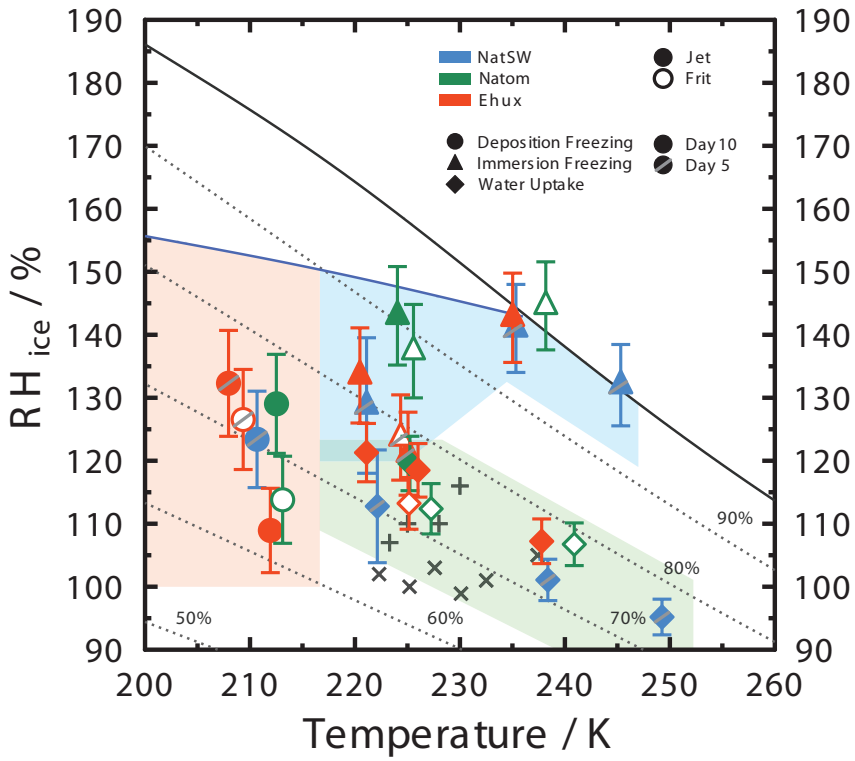

Figure 4.26: Mean onset conditions for ice nucleation for immersion (triangles) and deposition (circles) freezing as a function of temperature, T, and RH_{ice}. Deposition freezing, immersion freezing, and water uptake are also indicated by the light red, light blue and light green shading, respectively. Error bars represent either the experiment uncertainty or the standard deviation of the measurements, whichever is larger. Plus and cross symbols are deposition ice nucleation onsets for NaCl and $NaCl{\cdot}2H_2O$, respectively[8]. Water saturation is indicated by the black solid line. Dotted lines show lines of constant relative humidity with respect to water. The blue line indicates homogeneous ice nucleation of micrometer size aqueous solution droplets[14,15].

Table 5: Summary of deposition ice nucleation results. The total number of particles on each sample, N_p, the number of ice nuclei, IN, per liter of air, the fraction of total particles that nucleated ice, f, the total available surface area on each sample, S_p, temperature, T, relative humidity with respect to ice, $\mathrm{RH_{ice}}$, the heterogeneous ice nucleation rate, J_{het}, and the contact angle, α, are indicated.

	N_p	IN / $\mathrm{L^{-1}}$	f	S_p / $\mathrm{cm^2}$	T / K	$\mathrm{RH_{ice}}$	J_{het} / $\mathrm{cm^{-2}\ s^{-1}}$	α/ °
NatSW - Day 5, Jet	1.44×10^4	0.2	7.1×10^{-5}	1.3×10^{-4}	210.7	123.4	6.6×10^2	19.9
Natom - Day 10, Jet	2.57×10^4	0.2	3.9×10^{-5}	2.2×10^{-4}	212.5	129.0	3.7×10^2	22.2
Natom - Day 10, Frit	2.13×10^4	0.3	4.7×10^{-5}	1.5×10^{-4}	213.1	113.8	5.5×10^2	15.7
Ehux - Day 5, Jet	2.51×10^4	0.2	4.0×10^{-5}	2.3×10^{-4}	208.0	132.3	3.7×10^2	22.8
Ehux - Day 5, Frit	1.96×10^4	0.3	5.1×10^{-5}	1.5×10^{-4}	209.4	126.6	5.7×10^2	21.0
Ehux - Day 10, Jet	1.77×10^4	0.2	5.7×10^{-5}	1.4×10^{-4}	221.1	121.3	5.8×10^2	19.8

subsequent stages in the cascade impactor. The total available surface area for ice nucleation is calculated by integrating the surface area distribution from the particle size spectra, and scaling with the sampling time and impaction area resulting in a total particle surface area, S_p, on the order of 1×10^{-4} $\mathrm{cm^2}$. Table 5 gives details on deposition freezing experiments, the results of which are shown in Fig. 4.26. Heterogeneous ice nucleation rate coefficients, J_{het}, on average for a single sample can be estimated as a function of T and $\mathrm{RH_{ice}}$ using the following equation

$$J_{\mathrm{het}}(T, \mathrm{RH_{ice}}) = \frac{N_{\mathrm{ice}}}{S_p \Delta t}, \tag{22}$$

where N_{ice} is the total number of ice nucleation events at the onset and $\Delta t = 12$ s is the time interval between each picture. Using CNT, the contact angle, α, is calculated and shown in table 5.

Water uptake on marine biogenic particles determined at RH = 75% is consistent with the deliquescence relative humidity of NaCl and sea salt. This confirms previous measurements of humidified size distributions, suggesting that the aerosolized particles are hygroscopic. In subsaturated conditions with respect to water (RH < 100%) immersion freezing occurred. Even though concentrated aqueous solutions are expected at these conditions, there must have been solid material additionally present which triggered ice nucleation. At RH = 80%, an aqueous particle in equilibrium with water vapor would have $a_{\mathrm{w}} = 0.80$ corresponding to an aqueous NaCl solution of about 24wt%. This would imply that marine biogenic particles are highly efficient IN with the ability to nucleate ice up to 30 K warmer than homogeneous freezing of supercooled aqueous solution droplets at the same concentration.

At temperatures between $215 - 220$ K the observed ice nucleation mode changes from deposition to immersion. The explanation for this behavior may be related to the formation of a glassy phase state. A glassy state of organic material is amorphous, non-crystalline with an extremely high viscosity making it physically behave like a solid and limiting the diffusion of water molecules which could otherwise dissolve the material[218]. Previous studies have shown that organic aerosol particles generated in the laboratory[204] as well as collected in the field[37,202,203] nucleate ice in the deposition and immersion modes below and above the glass transition temperature, respectively. The immersion and deposition freezing points shown in Fig.

4.26 could be explained with a glass transition temperature between $215-220$ K of marine biogenic material.

In summary, all aerosolized marine particles from the mesocosms experiments have the ability to nucleate ice in both immersion and deposition ice nucleation modes. Water uptake measurements confirm that these particles are highly hygroscopic, however, immersion freezing at 245 K and RH = 100% must be due to insoluble material in these particles. Due to the fact that all the sea salt is expected to deliquesce by this point suggests the presence of insoluble organic material which is aerosolized from mesocosm experiments with the ability to nucleate ice. Water insoluble organic material has been determined in aerosol particles collected from an ocean source[3,82] and the results of ice nucleation experiments here suggest that this aerosolized insoluble organic material may participate in ice formation processes in mixed-phase and cirrus clouds.

4.11 Population chemical characterization and individual ice nucleating particle compositions

The chemical composition of particles aerosolized from mesocosm experiments were investigated using computer controlled scanning electron microscopy and energy dispersive X-ray analysis (CCSEM/EDX). The purpose of this investigation was to chemically define a particle population in relation to biological activity as described by concentrations of microorganisms and additionally, particle size. Using electron images, individual particle morphology provided qualitative information on particle mixing state for organic and inorganic material. CCSEM/EDX provided EDX spectra of thousands of particles which were grouped in terms of average elemental composition. These data are extremely valuable because they can provide statistically significant chemical information on particle populations. Finally, scanning transmission X-ray microscopy coupled with near-edge X-ray absorption fine structure spectroscopy (STXM/NEXAFS) gave individual ice nucleating particle chemical composition, i. e. unambiguous determination of carbon bonding present in single ice forming particles. Composition, size, and morphology of ice forming particles are compared with the particle population to formulate an ice nucleating particle signature fundamental in understanding underlying ice nucleation processes and allow for parameterization of composition dependent ice nucleation in models.

4.11.1 SEM images

Particles from the Tpseu mesocosm experiment were imaged with an electron microscope using a scanning transmission electron microscopy (STEM) detector at Pacific Northwest National Lab. Figure 4.27 shows images of representative particles aerosolized from the mesocosm on different days and for different particle generation methods (jets and frits). Sea salts are observed at the core of each particle shown in Fig. 4.27 and surrounded by amorphous material. Results from STXM/NEXAFS reported below confirm that this material is organic in nature. The organic material is spread out over the particle due to high velocity impaction which formed a impact pool that completely encompass the inorganic core.

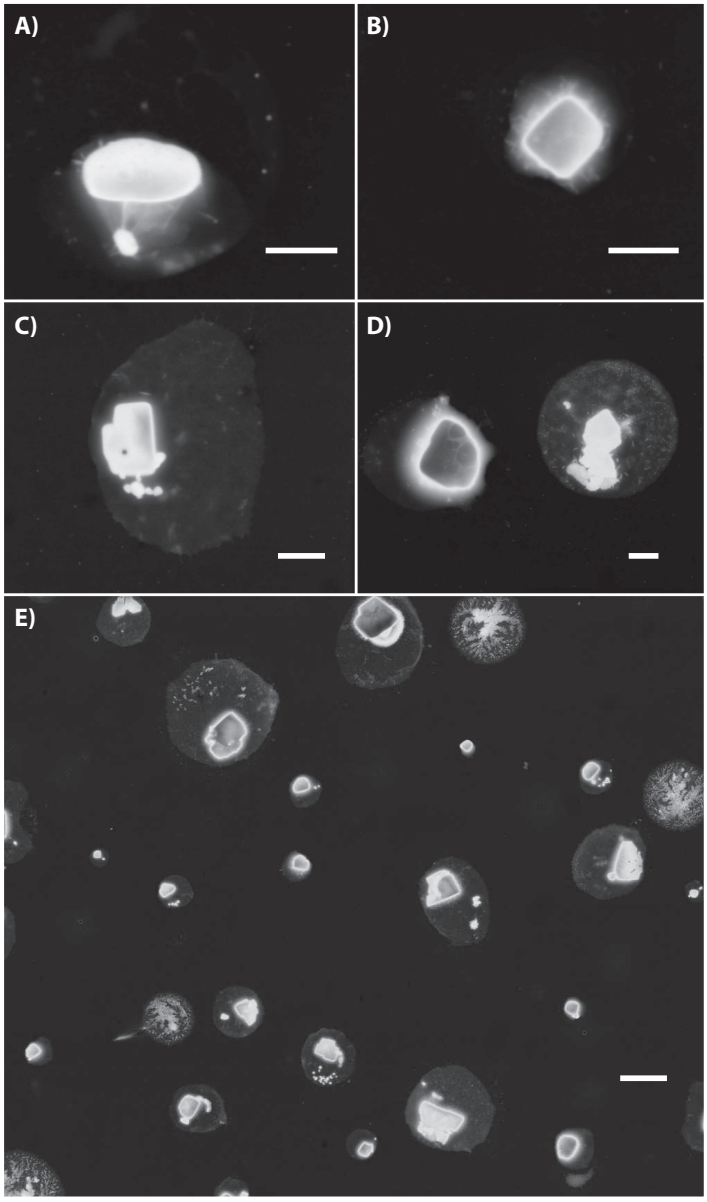

Figure 4.27: Electron microscope images using a scanning transmission electron microscope (STEM) detector of particles aerosolized using jets or frits collected during the experiment Tpseu. For each panel, the day, aerosolization method and length scale are as follows, A) day 1 - jet, 0.5 μm, B) day 5 - frit, 0.5 μm, C) day 12 - jet, 0.5 μm, D) day 12 - frit, 0.5 μm, E) day 12 - jet, 5.0 μm

4.11.2 CCSEM/EDX

The elemental ratios of thousands of particles were determined using CCSEM/EDX and corresponding atomic ratios were calculated using Genesis EDAX software. Particles were grouped into 4 different categories using the clustering algorithm, k-means and the MATLAB statistics toolbox. The k-means algorithm (k=4 in this case), in brief, detects common particle atomic ratios and converges when each particle is assigned to 4 specific classifications, each having a single mean elemental spectra. It is important to note that the number of clusters (or k "means") is somewhat arbitrary. The value of 4 chosen in this study to discriminate differences in atomic ratios and class assignments as a function of size. Also, particles were collected on copper grids with a $15-25$ nm thick carbon film and so background photon counts corresponding to C and O will always exist therefore, only relative values of atomic ratios can be made for these elements.

Figure 4.28 shows the k-means cluster analysis for 4 particle samples from the Tpseu experiment collected during days 3 and 5 using jets and days 5 and 12 using the frits. Relative fractions of each particle cluster are indicated in the top two panels of Fig. 4.28 as the total contribution in a single sample, or as a function of size for all 4 samples combined. Sea salt dominates the majority of the particle population having been a significant fraction for clusters 1-3. This falls in line with measurements of humidified particle size distributions and water uptake. Cluster 3 is the most common particle type characterized as having the most NaCl. Cluster 2 is the second most common which also contains NaCl, but a greater amount of carbon relative to Na or Cl than for cluster 3. Cluster 1 is characterized as having NaCl and high atomic ratios of

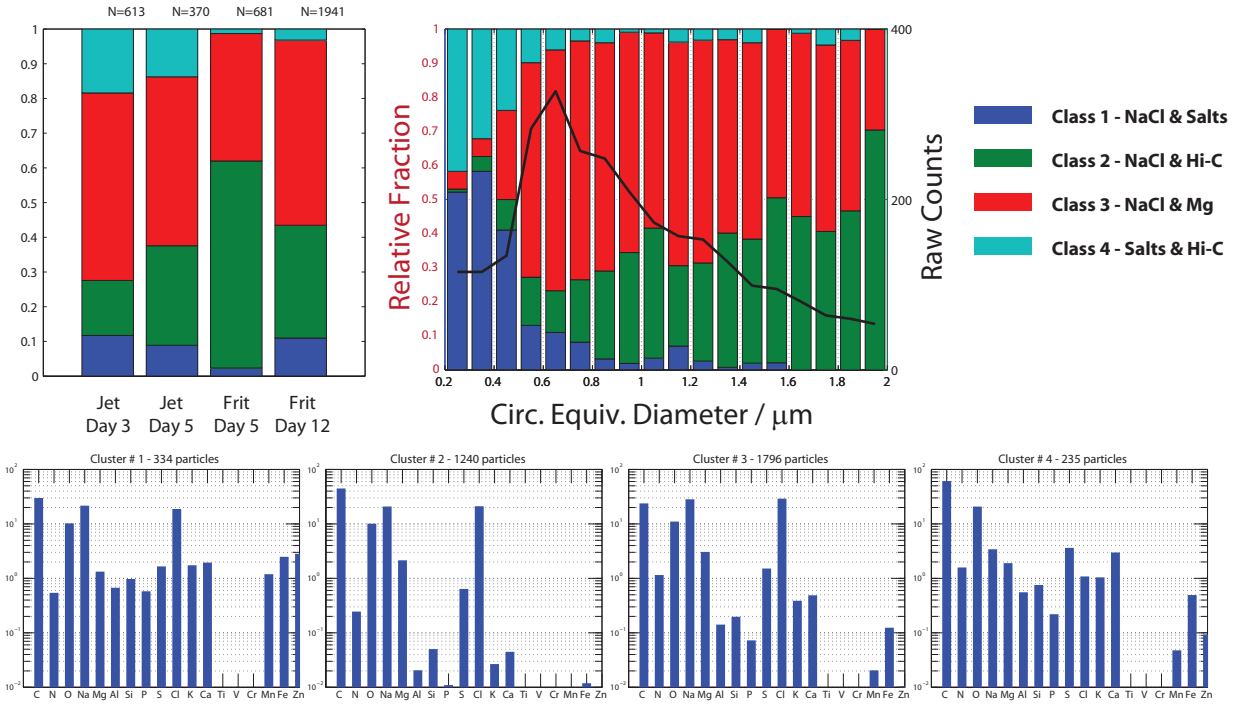

Figure 4.28: Cluster analysis for the Tpseu mesocosm experiment using k-means. The contribution of the 4 clusters to each particle sample is indicated in the top left panel. The center panel gives the cluster contributions as a function of particle circle equivalent diameter for all samples collectively. Average atomic percentages for the 4 clusters are shown in the bottom 4 panels.

other elements. Cluster 4 is unique in that it does not have significant amounts of NaCl but instead, has a greater carbon content relative to other elements than for any other cluster.

In summary, NaCl is the dominant elemental composition for all particles making up the majority of clusters 1-3. This is found for both the jet and the frit. Cluster 4 having high C and low NaCl, is unique and determined to contribute to particles with smaller sizes. This is consistent with previous studies which observed an enrichment of organic material in marine particles in the submicrometer size range[3,82,110].

4.12 Single particle analysis of ice nuclei: STXM/NEXAFS

The chemical composition, mixing state and unique carbon bonding information of individual ice nucleating particles (INP's) was determined using STXM/NEXAFS. This powerful technique unambiguously identified and mapped the presence of carbon functional groups (Fig. 4.29-4.31). Aerosolized particles using either water jet impingement or aeration through glass frits from the mesocosm experiments Ehux and Natom which nucleated ice, were all characterized as having organic material coatings and an inorganic core at about 1 μm in diameter. Carbon bonding was determined to be dominated by the carboxyl functional group (COOH). Particles that did not nucleate ice were also found to be associated with organic material characterized by the presence of COOH. The fact that INP's had a composition similar to many non-INP's

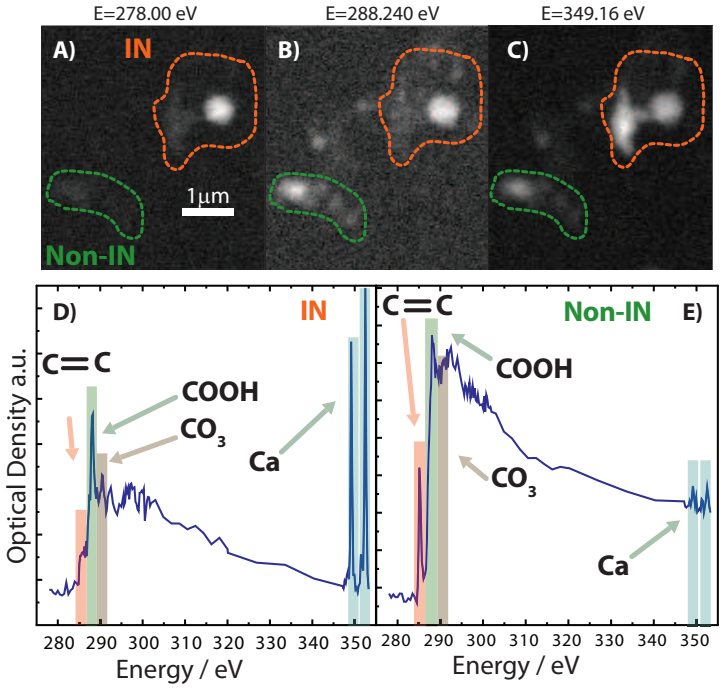

Figure 4.29: Images taken with STXM and carbon spectra using NEXAFS of an ice nucleating particle outlined in the orange dashed line and a non-ice nucleating particle outlined in the green dashed line. Optical density images at X-ray energies, E = 278.00, 288.24, and 349.16 eV in panel A, B, and C, indicate absorption at the carbon pre-edge, carboxyl functional group and calcium, respectively. Panel D shows the full carbon spectrum of the ice nucleating particle with absorption peaks indicated. Panel E shows the spectrum for the non-ice nucleating particle. Abbreviations in D and E are as follows: C=C for carbon double bonding, COOH for the carboxyl functional group, CO3 for carbonate and Ca for calcium.

is consistent with the stochastic nature of ice nucleation, i. e. that the most abundant particle type having the greatest available surface area is responsible for ice nucleation.

STXM images of a representative INP and one adjacent non-INP at three different X-ray energies and their corresponding NEXAFS spectra are shown in Fig. 4.29. These particles were aerosolized using water jet impingement from the Ehux mesocosm on day 10. At an X-ray energy of 278 eV, absorption occurs significantly in the core of the ice nucleus which is likely sea salt. The corresponding spectrum for the ice nucleus (Fig. 4.29D) indicates the highest absorption peak occurs for COOH around 288.5 eV. The area around the INP core absorbed more photons which translates to a higher OD as seen by the white shading in Fig. 4.29B and outlined by the orange dashed line. Another feature common to ice nucleating particles is the presence of calcium indicated in the raw OD image of the ice nucleus (Fig. 4.29C). While the non-INP shown in Fig. 4.29 is also found to be dominated by COOH (Fig. 4.29E), a strongly absorbing core or the presence of calcium is not observed as clearly as it is for the ice nucleating particle.

Another representative INP is shown in Fig. 4.30. The carbon spectrum shows once again that COOH dominates the carbon composition. Other minor peaks are sometimes present in some INP's like the hydroxyl functional group (C-OH) shown in Fig. 4.30, however, this is not always the case. Calcium is clearly identified in the INP as indicated in the absorption spectrum. Using a mapping analysis tool[29] the COOH functional

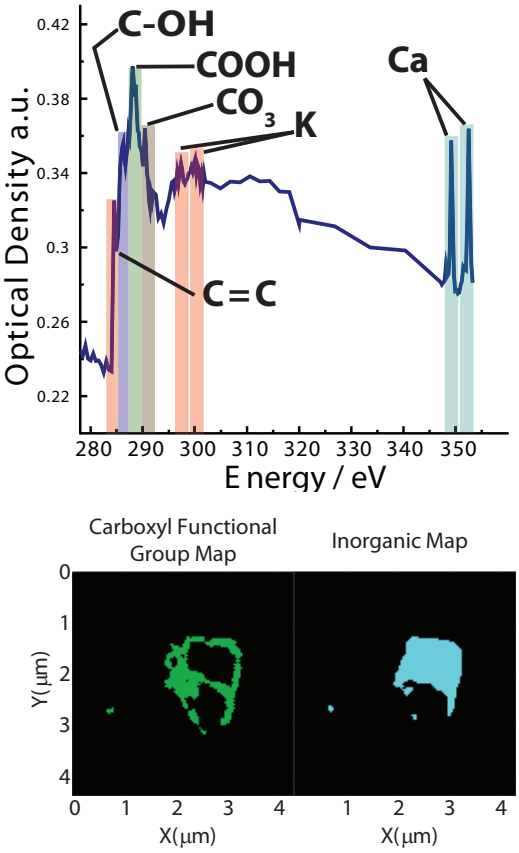

Figure 4.30: A representative NEXAFS spectrum of an ice nucleating particle and corresponding maps of carboxyl function groups and inorganic material. Absorption peaks are indicated.

group is determined to coat the INP's inorganic core. In total, 12 INP's were probed with STXM/NEXAFS and all were coated with organic material dominated in composition by COOH. For the experiment Natom on day 10 using water jets, 3 INP's were identified and all were dominated by COOH, inorganic material and calcium. In the experiment Ehux on day 10, 5 INP's were identified with STXM/NEXAFS using water jet impingement. Four particles that nucleated ice were identified from the same experiment when using glass frits, all of which has similar carbon spectra and morphology.

Many ice nucleating particles also had other peaks as shown in Fig. 4.29 and 4.30 indicating that even though COOH is the dominant carbon bond, there existed variability in the nature of the organic material. To discriminate between those regions of particles in which organic material, inorganic material, and calcium are dominant, these components are mapped using singular value decomposition (SVD)[30] and the carbon spectra corresponding to each colored region on the particle is averaged using a methodology adapted from Moffet *et al.*[18]. Figure 4.31 shows the resulting SVD and spectral analysis. It is clear that the COOH functional group is surrounding each particle and dominates the carbon spectra. It is also clear that even where inorganic material or calcium dominates, the COOH group is present. The morphology of the INP's is similar to that of the rest of the particle population. The fact that most particles that did nucleate ice, had a COOH coating around an inorganic core implies that while there are common characteristics of ice nucleating particles, these may also shared by the majority of the particle population.

In conclusion, the composition of ice nucleating particles were all found to have an inorganic core surrounded by an organic coating dominated by the carboxyl functional group. The similar organic chemical

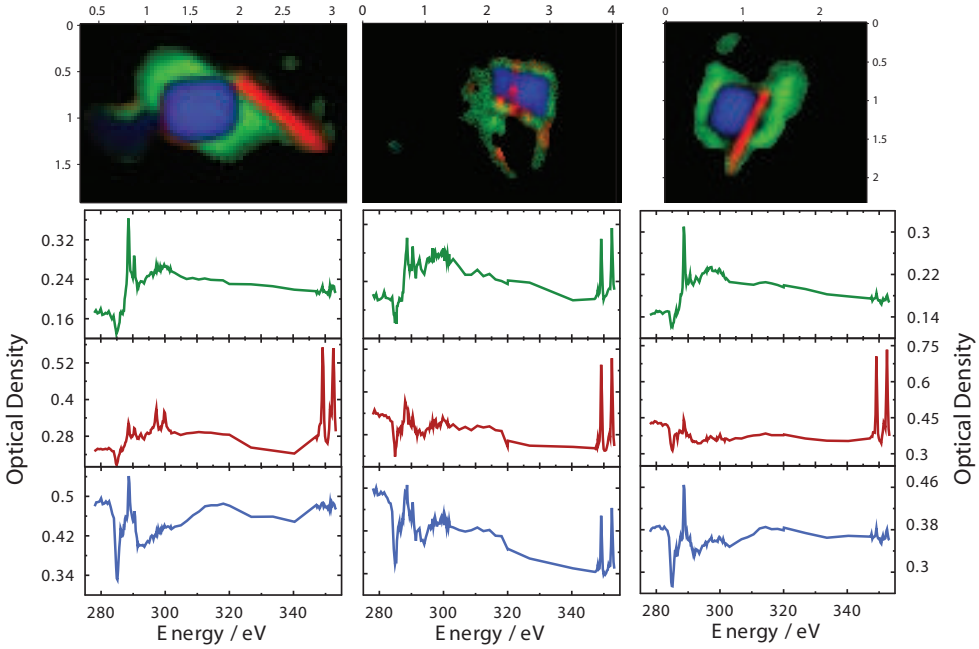

Figure 4.31: Carbon K-edge maps of three ice nucleating particles using singular value decomposition[18,29,30]. Green, blue, and red colors indicate locations dominated by the carboxyl functional group, inorganic material, and calcium, respectively. Carbon spectra corresponding to these colored regions are indicated below each particle, where the green, blue, and red spectra correspond to the same colored regions mapped on each respective particle.

composition and organic coating may explain why the ice nucleation efficiency of the particles was similar as shown in Fig. 4.26 for deposition freezing. It is likely that some of the organic material was water insoluble, and that the various particle samples had similar organic composition which would explain the similar ice nucleation efficiency in the immersion mode. Another similarity was that the core of all ice nucleating particles averages ~ 1 μm in diameter with the smallest diameter being about 0.5 μm. Ice nucleating particles were also similar in composition to the dominant particle cluster determined by CCSEM/EDX which was sea salt and carbonaceous material.

4.13 Summary and conclusions

The effect of biological activity in seawater on the nature and dynamics of particles aerosolized from the sea surface due to bubble bursting was investigated in terms of the bubble generation method, total aerosol particle production and the size distribution, hygroscopicity, ice nucleation potential, and chemical composition of the particles. Experiments were conducted in a mesocosm tank filled with artificial and natural seawater using impinging water jets and aerating glass frits to generate bubbles. Aerosolized particles were produced as a result of bubble bursting and their particle size distributions were measured in dry and humidified air, at relative humidities of $< 20\%$ and 80 $\pm 4\%$, respectively, to determine changes in aerosolization and particle hygroscopicity as a function of biological activity. Bacteria and phytoplankton cell concentrations, and in some cases dissolved organic and particulate carbon were determined in the tank seawater to asses the degree to which community composition and activities affected aerosolization and particle characteristics. In two experiments marine particles were aerosolized from artificial seawater with undetectable bacteria concentrations to verify that particle size spectra were reproducible. A third experiment used artificial seawater aged for 2 weeks to investigate the effect of background bacterial concentrations on aerosolization. In a fourth experiment, a mixed bacterial culture obtained by enrichment of Great South Bay seawater was used to inoculate artificial seawater to which nutrient was added to determine the effect of bacterial growth on aerosolization. To mimic microbial communities in seawater where phytoplankton and bacteria grow simultaneously, three different experiments using artificial seawater were inoculated with single species of phytoplankton, either *T. pseudonana*, *E. huxleyi*, or *N. atomus*, and nutrients were added to stimulate growth. In a final experiment, natural seawater collected off the south eastern shore of Long Island, NY at the Shinnecock inlet to which nutrients were added to stimulate phytoplankton growth, was used to determine the affect of a growing natural microbial community on particle aerosolization.

The size distribution of bubbles produced by two bubble generation methods, water impingement and aeration by glass frits was measured. Both the shape of the bubble size distributions and total production were dissimilar. A water jet produced a wide distribution of bubble diameters between 16 μm and 1000 μm, while the frit generated bubble size distribution produced a factor of 10 times more bubbles for diameters ~ 100 μm. In experiments using only artificial seawater, aerosol particle size distributions for the jets peaked in production for aerosol particles diameters around 100 nm. The distributions tended to be broad with total particle production on the order of 1000 cm^{-3}. The frit generated particle size distributions also peaked around 100 nm, however the shape of the distribution was much more narrow and 10-30 times more particles

were produced than were by the jets. This could be attributed to the higher bubble production for the frits compared to the jets.

In mesocosm experiments where bacteria were grown over time, aerosol particle size distributions for both jet and frit generated bubbles changed in various ways. As bacterial concentrations increased over 4 orders of magnitude ($< 10^4$ to $> 10^8$ cells mL^{-1} for the 2 week mesocosm experiments LowBac and GBac) the number of aerosolized particles using the jet increased by a factor of about 2.2. Additionally, the increased presence of bacteria coincided with a change in the shape of the size distribution shifting it toward smaller sized particles. Consistently, higher bacterial numbers in seawater resulted in particle production gradually increasing and eventually dominating for diameters around $\sim$ 20 nm. The total number of aerosolized particles from the frit increased by a factor up to 1.6, but despite the changing water composition, the shape of the aerosol particle size distribution generated by frits remained largely unchanged. This may be explained by the greater bubble production in a narrow size range for the frits which was not observed for the jets. Measurements of humidified aerosol particle size distributions for all experiments at 80% relative humidity indicated that particle growth factors were on average $1.6 - 2.0$ for the entire diameter range for both the frit and the jet.

When growing either *T. pseudonana*, *E. huxleyi*, or *N. atomus* in seawater mixed with bacteria, similar changes in aerosolization with respect to jets or frits were observed compared with the experiments in which only bacteria were present. The total number of particles aerosolized using the jet increased by a factor of about 3.6 averaged for all phytoplankton species with cell concentrations ranging between $10^5 - 10^7$ mL^{-1} and bacterial concentrations between $10^5 - 10^8$ mL^{-1}. Changes in the shapes of the jet generated particle size distributions when phytoplankton and bacteria were grown simultaneously, were similar to when bacteria were grown alone and characterized by a shift toward particle diameters of $\sim$ 25 nm which eventually dominated entire size spectra. Frit generated particle size distributions were again, unchanged as a function of biological activity, however, total particle production increased for all three phytoplankton species by on average ~ 2 fold. Particle growth factors for humidified aerosol particle size distributions again fell between $1.6 - 2.0$ on average and did not change as a function of microbial growth.

In natural seawater as the in situ community of phytoplankton and bacterial community grew, aerosolized particles increased in number by a factor of about 3.4 and 1.9 with us of water jet impingement and aeration through glass frits, respectively. Jet generated particle size distributions shifted to smaller diameters. Aerosol particles having diameters < 100 nm made up the majority of their total numbers as dominant production shifted to 20 nm in diameter by the end of the experiment. The shape of frit generated particle size distributions did not change. Particles from the natural seawater mesocosm experiment had growth factors at 80% relative humidity between $1.6 - 2.0$ on average and did not change as a function of biological activity.

Compared to previous laboratory studies by other investigators, estimates of particle flux were 2-3 orders of magnitude lower when using the jets, although they agreed with previous flux calculation by Lewis and Schwartz[24]. Flux calculations for frit generated particles, on the other hand, were in better agreement with previous laboratory studies using similar bubble generation methods. The most significant difference in flux between the jet and frit generated particles is the total particles produced.

The ice nucleation ability of aerosolized particles was probed as a function of biological activity for both

jets and frits for mesocosms containing *E. huxleyi*, *N. atomus*, and natural sea water. All aerosolized marine particles had the ability to nucleate ice in immersion and deposition modes with a similar efficiency under atmospheric conditions of temperature and relative humidity with respect to ice. The fact that deposition ice nucleation occurs less efficiently than pure NaCl and that insoluble or solid particles must have been present for immersion freezing to occur, implies that marine particles posses material other than inorganic sea salt associated. Water uptake was observed to occur at the sea salt deliquescence relative humidity, as expected. Ice nucleating particles aerosolized from the mesocosms likely contained sea salt and insoluble organic material as inferred from the results presented here.

The chemical composition was obtained for aerosolized particle populations using computer controlled scanning electron microscopy and energy dispersive X-ray analysis. These examinations confirmed that the majority of aerosol particles consisted of organic coated sea salt. Using the k-means cluster analysis, it was determined that carbon had a variable concentration in all sea salt containing particles. A unique particle type which contains a high amount of carbon as well as other salts was found to be enhanced for particle diameters as low as 0.2 μm.

Individual ice nucleating particles aerosolized from each mesocosm experiment were investigated using scanning transmission X-ray microscopy coupled with near edge X-ray absorption fine structure spectroscopy to determine their chemical composition in comparison to the rest of the particle population. Every ice nucleating particle was confirmed to have an inorganic core with an organic coating, validating the result that the ice nucleation efficiencies were the same for particle samples from different mesocosms. This was verified by mapping the carboxyl function group which was the dominant feature in carbon absorption spectra and entirely encompassed the particles. The majority of non-ice nucleating particles were observed to have a similar composition to ice nucleating particles. Three key findings can be made from this analysis. The first is that only organic coated particles were found to act as ice nuclei, the second is that ice nucleating particles were part of the dominant particle type found in the particle population, and the third is that ice nucleating particles were relatively large averaging ~ 1 μm in diameter.

The results suggest that the growth of microorganisms including phytoplankton and bacteria and the release of organic matter into seawater can have an effect on particle aerosolization by increasing total particle numbers. However the great majority of aerosolized particles have similar hygroscopicities, ice nucleation efficiencies, and are composed of sea salt coated with organic material. Therefore particle aerosolization, composition and ice nucleation potential of particles aerosolized to the atmosphere from the world's oceans may be linked to biological activity occurring in seawater. These findings impact predictions of the sea to air fluxes of sea salt and organic material as a function of biological activity and suggest the appropriateness of including aerosolized marine particles in modeling water cloud and ice cloud formation with subsequent climatic implications.

5 Results: Ice nucleation from aqueous NaCl droplets with and without marine diatoms

The sections from 5.1 to 5.5 are the reproduction of the publication of "Ice nucleation from aqueous NaCl droplets with and without marine diatoms" by P. Alpert, J. Y. Aller, and D. A. Knopf published in Atmospheric Chemistry and Physics, Vol. 11, 5539-5555, 2011, with permission from Copernicus Publications on behalf of the European Geosciences Union. The layout of the article as well as the section figures and table numberings have been adapted to match with the thesis structure.

Ice nucleation from aqueous NaCl droplets with and without marine diatoms

Peter A. Alpert[1], Josephine Y. Aller[2], and Daniel A. Knopf[1*]

[1]Institute for Terrestrial and Planetary Atmospheres/School of Marine and Atmospheric Sciences, Stony Brook University, Stony Brook, NY 11794-5000, USA
[2]School of Marine and Atmospheric Sciences, Stony Brook University, Stony Brook, NY 11794-5000, USA

[*]To whom correspondence should be addressed. Email:Daniel.Knopf@stonybrook.edu

Published in Atmospheric Chemistry and Physics, Vol. 11, 5539-5555, 2011, with permission from Copernicus Publications on behalf of the European Geosciences Union, copyright 2011.

5.1 Abstract

Ice formation in the atmosphere by homogeneous and heterogeneous nucleation is one of the least understood processes in cloud microphysics and climate. Here we describe our investigation of the marine environment as a potential source of atmospheric IN by experimentally observing homogeneous ice nucleation from aqueous NaCl droplets and comparing against heterogeneous ice nucleation from aqueous NaCl droplets containing intact and fragmented diatoms. Homogeneous and heterogeneous ice nucleation are studied as a function of temperature and water activity, a_{w}. Additional analyses are presented on the dependence of diatom surface area and aqueous volume on heterogeneous freezing temperatures, ice nucleation rates, ω_{het}, ice nucleation rate coefficients, J_{het}, and differential and cumulative ice nuclei spectra, $k(T)$ and $K(T)$, respectively. Homogeneous freezing temperatures and corresponding nucleation rate coefficients are in agreement with the water activity based homogeneous ice nucleation theory within experimental and predictive uncertainties. Our results confirm, as predicted by classical nucleation theory, that a stochastic interpretation can be used to describe the homogeneous ice nucleation process. Heterogeneous ice nucleation initiated by intact and fragmented diatoms can be adequately represented by a modified water activity based ice nucleation theory. A horizontal shift in water activity, $\Delta a_{\mathrm{w,het}} = 0.2303$, of the ice melting curve can describe median heterogeneous freezing temperatures. Individual freezing temperatures showed no dependence on available diatom surface area and aqueous volume. Determined at median diatom freezing temperatures for a_{w} from 0.8 to 0.99, $\omega_{\mathrm{het}} \simeq 0.11^{+0.06}_{-0.05}\,\mathrm{s}^{-1}$, $J_{\mathrm{het}} \simeq 1.0^{+1.16}_{-0.61} \times 10^4\,\mathrm{cm}^{-2}\,\mathrm{s}^{-1}$, and $K \simeq 6.2^{+3.5}_{-4.1} \times 10^4\,\mathrm{cm}^{-2}$. The experimentally derived ice nucleation rates and nuclei spectra allow us to estimate ice particle production which we subsequently use for a comparison with observed ice crystal concentrations typically found in cirrus and polar marine mixed-phase clouds. Differences in application of time-dependent and time-independent analyses to predict ice particle production are discussed.

5.2 Introduction

Aerosol particles play an important role in the radiative balance of our Earth's climate by directly scattering and absorbing short wave and long wave radiation[65–69]. They can also act as cloud condensation nuclei (CCN) and ice nuclei (IN) further impacting climate by changing the radiative properties of clouds[1,70–72,219–221]. Ice crystals in particular impact atmospheric processes in other ways including the initiation of precipitation with subsequent consequences for the hydrological cycle[74]. Ice can nucleate homogeneously from an aqueous supercooled aerosol particle or heterogeneously by four modes: deposition (the IN nucleates ice directly from the supersaturated vapour phase), immersion (the IN nucleates ice in a supercooled aqueous aerosol particle), condensation (water is taken up by the IN and freezes subsequently), and contact (the impact of an IN with a supercooled aqueous particle nucleates ice)[42,45]. While it is impossible to directly observe ice nucleation in situ[46], heterogeneous ice nucleation is regarded as a possible formation mechanism for cirrus[47–49,51] and mixed-phase clouds[50,62,63].

Sea salt particles emitted from oceans constitute the most globally abundant aerosol type by mass. They are important for climate, principally due to their role in the atmosphere as a source for highly reactive halogen species in gas phase, liquid phase, and heterogeneous reactions[222–225]. Sea salt aerosol particles can

also act as CCN at low supersaturations with respect to liquid water compared with sulfate particles according to Köehler theory and thus, compete for water vapour in warm clouds despite their relatively low particle concentrations in air[226–228]. Freezing of aqueous sea salt aerosol particles has implications for heterogeneous halogen chemistry and mixed-phase and cirrus cloud formation processes particularly in colder, high-latitude climates. Sea salt residue in cirrus ice crystals were consistently observed from aircraft measurements over the Florida coastline at altitudes around 13 km and indicate the lofting of marine particles by convective systems[52]. Freezing temperatures of micrometer sized aqueous sea salt and NaCl aerosol particles occurs homogeneously below 235 K and follows the water activity based homogeneous ice nucleation theory[7,14]. We extend these previous studies to also determine nucleation dependency on a_w, ice nucleation rate coefficients, and the stochastic behavior of the nucleation process. These combined experimental data serve to validate the water activity based ice nucleation theory and aid in explaining in situ observations and model studies of cirrus clouds impacted by marine aerosol particles.

Only a few studies have hinted that marine biogenic particles, i.e. phytoplankton and bacteria, may have the potential to nucleate ice at warmer temperatures than observed for homogeneous freezing[113–115]. Schnell[113], for example, found efficient IN in laboratory cultures of phytoplankton, however, could not determine if the IN was actually the phytoplankton, their excretory products, associated marine or terrestrial bacteria, or some other nucleating agent. Schnell and Vali[114] showed that surface sea water contained IN associated with phytoplankton however, they also could not conclusively identify the IN. Fall and Schnell[115] investigated biogenic ice nucleation using a culture of a marine dinoflagellate species *Heterocapsa niei* which contained a mix of terrestrial and marine bacterial species. A specific bacterium of terrestrial origin found in this mixed culture was isolated and determined to possess an ice active gene, however, they could not identify the actual ice nuclei in the culture[115]. A study in which the ice nucleating ability of Arctic aerosol particles collected on filter samples was measured, suggested an ocean source of organic ice nuclei, however, no conclusive evidence was provided to specifically identify the organic ice nucleating agent[116]. Finally in a very recent study, several representative Arctic and Antarctic sea-ice bacterial isolates and a polar virus were shown to be very poor IN, nucleating ice at expected homogeneous freezing temperatures[229].

A study by Knopf *et al.*[202] demonstrated the capability of *Thalassiosira pseudonana*, a marine planktonic diatom with a siliceous cell wall and an organic coating, to act as efficient IN in the immersion mode under typical tropospheric conditions. Here we provide new detailed analysis and discussion on the findings by Knopf *et al.*[202] and present new data on homogeneous freezing of aqueous NaCl droplets void of diatoms. In this and the recent Knopf *et al.*[202] publication, we focus on diatoms for two reasons. First, they are a diverse group of unicellular marine and freshwater phototrophic organisms which are cosmopolitan in distribution in surface waters and extremely abundant and productive[230]. Second, they have been described from atmospheric samples just above sea level and at high altitudes[231–234]. Bigg and Leck[104] and references therein provide numerous examples of aerosolized diatoms originating from the sea surface microlayer (SML). As a result of aeolian transport, marine diatoms have been found on mountaintops in the Antarctic[235,236] and as contaminates in snow located in Canada reached by Asian and Arctic air masses[237]. Diatom fragments identified as amorphous silica at concentrations of 20–28 L^{-1} (air) were collected from ground based sampling at ∼65 m on Amsterdam Island, an isolated volcanic island in the Southern Indian Ocean[238]. Furthermore,

airborne diatom frustules and diatom fragments are ubiquitous in marine Antarctic regions[239]. Diatom fragments have even been shown to accompany African dust plumes in the atmosphere[240], and aircraft measurements at altitudes of over one kilometer have recorded diatoms over continental land masses[232].

The fact that diatoms are present in the atmosphere suggests that they may participate in cloud formation processes. While not specifically reporting on the IN efficiency of diatoms, Schnell[113] and Schnell and Vali[114] in fact found that regions of greatest atmospheric IN concentrations measured by Bigg[112] were above major oceanic water mass convergence zones, i.e. the subtropical convergence zone and the Antarctic convergence zone. Characterized by upwelling of nutrient laden bottom waters, overturning, and mixing, these highly productive waters are dominated by diatoms[192].

Periods of high biological activity associated with phytoplankton blooms can produce organic-rich aerosol particles as a result of bubble bursting and wave breaking processes[3,109,241,242]. Although most of these studies do not specifically identify aerosolized material, it is well known that a variety of primary biological components including diatoms and other phytoplankters, bacteria, viruses, transparent exopolymers, and colloidal gels are present in the SML and can be aerosolized[81,92,102,104,243,244]. These biogenic particles may constitute a significant part of the atmospheric aerosol mass fraction in the submicron size range[3]. A very recent study by Ovadnevaite *et al.*[109] reports detection of high contributions of primary organic matter in marine aerosol of $3.8\,\mu g\,m^{-3}$, far greater than organic mass concentrations of on average $1.75\,\mu g\,m^{-3}$ observed in polluted European air masses advected out over the N.E. Atlantic[109,245]. The high organic mass detected by Ovadnevaite *et al.*[109] was associated with elevated chlorophyll concentrations in oceanic surface waters, consistent with phytoplankton bloom conditions. A seasonal variability of IN concentrations over the oceans has been observed from filter measurements with the highest concentrations observed in mid-summer and lowest concentrations observed during winter months[246–249]. The mixed-phase Arctic cloud experiment (M-PACE) reports a mean IN concentration of $\simeq 0.8\,L^{-1}$ (air) in fall using a continuous flow diffusion chamber (CFDC)[61,62]. Springtime IN concentrations in the Arctic measured during the NASA FIRE Arctic Cloud Experiment (ACE) and Surface Heat Budget of the Arctic (SHEBA) program[250] were enhanced by a factor of 5 ($\sim 4\,L^{-1}$ (air)) over those measured during fall months[61]. Using similar IN measurement techniques and air mass trajectory analysis, periods of elevated primary production in surface waters could be related to observed IN concentrations[61,249,250].

Here we present a comparative analysis of homogeneous and heterogeneous freezing of aqueous NaCl droplets with and without intact and fragmented marine diatoms, for the remainder of the manuscript referred to as aqueous NaCl/diatom droplets and aqueous NaCl droplets, respectively. We investigated homogeneous freezing of aqueous NaCl droplets with respect to the water activity based homogeneous ice nucleation theory[14]. We use optical microscopy to individually observe thousands of aqueous NaCl droplet freezing temperatures[144,153,251]. Optical microscopy also allows for direct measurements of individual droplet volume, and thus experimental determination of homogeneous ice nucleation rate coefficients of micrometer sized aqueous NaCl droplets. We examined heterogeneous freezing of diatoms via the immersion mode with respect to the modified water activity based ice nucleation theory[15,252]. We also determined diatom surface area and aqueous volume dependence on heterogeneous freezing temperatures. Additionally, we quantify heterogeneous ice nucleation from intact and fragmented diatoms immersed in droplets in terms of time-

dependent and time-independent approaches. A time-dependent analysis is used to derive heterogeneous ice nucleation rates and a time-independent analysis to derive ice active surface site densities, both of which allow for estimations of atmospheric ice particle production. The atmospheric implications of our findings are discussed.

5.3 Results and discussion

5.3.1 Homogeneous freezing of aqueous NaCl droplets

Figure 5.1 summarizes melting and homogeneous freezing of about 2500 aqueous NaCl droplets as a function of temperature, T, and wt % and a_w determined at particle preparation conditions. The corresponding raw data is shown in Fig. 5.2 and will be discussed below. Direct measurements of a_w for aqueous NaCl droplets in the supercooled temperature regime do not exist[33], and thermodynamic models for aqueous

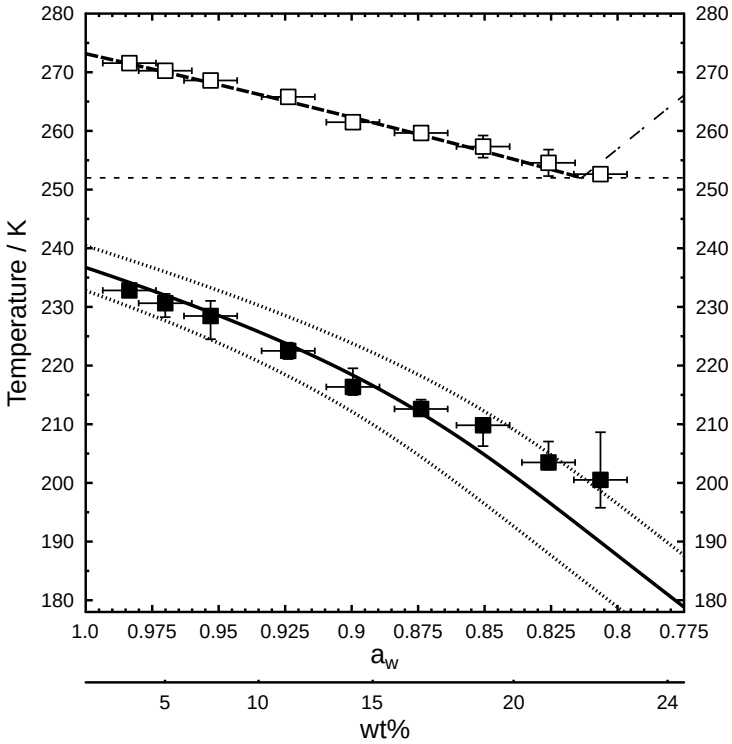

Figure 5.1: Median homogeneous freezing temperatures and corresponding mean melting temperatures for aqueous NaCl droplets are shown as filled and open squares, respectively, as a function of a_w and wt %. The error bars for the freezing temperatures indicate the 10^{th} and 90^{th} percentile and error bars for the melting temperatures indicate one standard deviation. Uncertainty in a_w is ± 0.01. The narrow dashed line represents the ice melting curve[15]. The wide dashed line and the dash-dotted lines indicate the eutectic temperature and the solid-liquid equilibrium curve of $NaCl \cdot 2H_2O$, respectively[31,32]. The solid line represents the predicted homogeneous freezing curve[15]. The two dotted lines represent an uncertainty of the homogeneous freezing curve due to an uncertainty in a_w of ± 0.025[33]. It is assumed that a_w of the aqueous droplets does not change with temperature[7,14].

NaCl only provide a_w for a range of concentrations at 298.15 K[6], thus we assume that aqueous droplet a_w determined at the preparation conditions does not change with decreasing T[7,14]. The ice melting curve, $a_w^{ice}(T)$, is the activity of water in solution in equilibrium with ice[14,15]. Within our experimental uncertainty, Fig. 5.1 indicates good agreement of our experimentally determined mean melting temperatures, T_m^{NaCl}, with $a_w^{ice}(T)$[5,14,15]. Within experimental and theoretical uncertainties, our experimentally derived median homogenous freezing temperatures, T_f^{NaCl}, are in good agreement with predicted freezing temperatures. The predicted homogeneous freezing curve was adjusted for the droplet diameters employed in our experiments[14,15]. T_f^{NaCl} for a_w of 0.806 shows slightly warmer temperatures than predictions. This may be explained by the formation of $NaCl{\cdot}2H_2O$[7] which may have affected the freezing process. The melting of all crystalline particles prepared at $a_w = 0.806$ was visually different to the melting of crystalline particles prepared at higher a_w. The observed melting temperature at $a_w = 0.806$ may indicate the melting of the eutectic mixture at the temperature of 252 K[7]. Another explanation for the slight deviations of T_f^{NaCl} from the homogeneous freezing curve at low a_w may be that a_w does change in the supercooled region, particularly for highly concentrated NaCl solutions. Freezing and melting temperatures shown in Fig. 5.1 for the investigated a_w are given in Table 6, in addition to corresponding ice saturation ratios evaluated at $S_{ice}(T_f^{NaCl})$ and predicted freezing temperatures, $T_f^{Koop}(a_w)$. The data displayed in Fig. 5.1 indicates that the variations in the melting temperatures are smaller than for the corresponding freezing temperatures. This is primarily due to the stochastic nature of the ice nucleation process, although, the presence of different droplet sizes and possible events of heterogeneous ice nucleation could contribute to the difference[144,153,251].

Figure 5.2 summarizes all observed ice nucleation events from aqueous NaCl droplets, where each panel corresponds to a different a_w value at particle preparation conditions. The frozen fraction of droplets, f, was calculated from observations by $f = N_{ice}/N_{tot}$, where N_{ice} is the number of frozen particles as a function of T, and N_{tot} is the total number of analyzed droplets. These data points manifest a cumulative distribution as a function of T. The uncertainty of f indicates the range within a temperature increment of 0.2 K. The probability density histogram (PDH) binned in 1.0 K increments was normalized to N_{tot} with the increment size chosen to better visualize the distribution of freezing frequencies.

We applied a normal distribution to describe the stochastic nature of homogeneous ice nucleation and thus f[42,127]. As discussed previously in detail, the probability of observing n nucleation events from the binomial distribution is approximated by the Poisson distribution using Stirling's formula under typical conditions for homogeneous nucleation of aqueous aerosol particles[127]. If a large number of nucleation events are observed, $n > 100$, then the binomial distribution reduces to a normal distribution[127,253].

The red solid curve in Fig. 5.2 is a fit of f to a normal cumulative distribution function (CDF) according to

$$f_{fit} = \frac{1}{2}\left[1 - \mathrm{erf}\left(\frac{T-\mu}{\sqrt{2}\sigma}\right)\right] \tag{23}$$

where μ and σ are the mean and standard deviation fitting parameters that describe the distribution. Figure 5.2 indicates that our observed freezing events are in very good agreement with Eq. (23). Deviations of observed ice nucleation distributions from f_{fit} were mostly found at higher temperatures due to possible heterogeneous freezing events. However, the number of heterogeneous ice nucleation events were too few

Table 6: Summary of ice nucleation parameters evaluated at median freezing temperatures for homogeneous and heterogeneous ice nucleation given in the top and bottom panel, respectively. Median heterogeneous freezing and mean melting temperatures of intact and fragmented diatoms were taken from Knopf *et al.*[34]. All other values were obtained from this study.

a_{w}	0.984	0.970	0.953	0.924	0.900	0.874	0.851	0.826	0.806
$T_{\mathrm{f}}^{\mathrm{NaCl}}\,\mathrm{K}^{-1}$	232.8	230.6	228.5	222.5	216.4	212.6	209.8	203.5	200.5
$T_{\mathrm{f}}^{\mathrm{Koop}}(a_{\mathrm{w}})\,\mathrm{K}^{-1}$	233.9	231.6	228.7	223.2	217.9	211.3	204.3	195.9	188.9
$T_{\mathrm{m}}^{\mathrm{NaCl}}\,\mathrm{K}^{-1}$	271.6	270.3	268.6	265.8	261.5	259.6	257.3	254.6	252.6
$S_{\mathrm{ice}}(T_{\mathrm{f}}^{\mathrm{NaCl}})$	1.45	1.46	1.46	1.50	1.51	1.51	1.50	1.51	1.50
$J_{\mathrm{hom}}(T_{\mathrm{f}}^{\mathrm{NaCl}}) \times 10^6\,\mathrm{cm}^{-3}\,\mathrm{s}^{-1}$	3.52	2.07	1.00	1.66	1.40	2.56	1.26	3.31	0.44
a_{w}	0.984	0.969	0.951	0.926	0.902	0.873	0.850	0.826	0.800
$T_{\mathrm{f}}^{\mathrm{dia}}\,\mathrm{K}^{-1}$	242.3	241.1	238.6	234.0	232.0	224.9	224.7	220.7	216.6
$T_{\mathrm{m}}^{\mathrm{dia}}\,\mathrm{K}^{-1}$	271.6	270.5	268.7	265.7	263.5	259.3	257.3	254.5	253.9
$S_{\mathrm{ice}}(T_{\mathrm{f}}^{\mathrm{dia}})$	1.33	1.32	1.33	1.35	1.34	1.38	1.35	1.35	1.35
$\omega_{\mathrm{het}}(T_{\mathrm{f}}^{\mathrm{dia}})\,\mathrm{s}^{-1}$	0.13	0.17	0.13	0.11	0.11	0.06	0.13	0.07	0.08
$J_{\mathrm{het}}(T_{\mathrm{f}}^{\mathrm{dia}}) \times 10^4\,\mathrm{cm}^{-2}\,\mathrm{s}^{-1}$	1.51	0.44	1.50	0.39	0.70	0.64	2.16	0.75	1.14
$k(T_{\mathrm{f}}^{\mathrm{dia}}) \times 10^4\,\mathrm{cm}^{-2}\,\mathrm{K}^{-1}$	7.5	2.3	8.7	2.6	2.2	2.0	6.0	5.1	9.5
$K(T_{\mathrm{f}}^{\mathrm{dia}}) \times 10^4\,\mathrm{cm}^{-2}$	9.1	2.1	6.4	2.9	3.0	7.7	8.3	7.0	9.7

compared with N_{tot} to provide any significant weighting to the fit. Deviations of observed ice nucleation distributions from the fits for lower temperatures occur for aqueous NaCl droplets with lowest a_{w} of $0.806 - 0.851$. This is likely due to our experimental uncertainty a_{w}. In an analysis (not shown here) in which only the data within the 10th and 90th percentiles were employed to obtain f_{fit}, corresponding values for μ and σ were found not to be affected significantly. Again this was due to the larger number of homogeneous ice nucleation events that occurred compared to the few heterogeneous ice nucleation events.

Here, we derive homogeneous ice nucleation rate coefficients, J_{hom}, for aqueous NaCl droplets with varying initial a_{w}. The analytical approach and corresponding interpretation of J_{hom} has been explained in detail previously[127,128]. In a chosen temperature interval, ΔT, different numbers of freezing events will occur. We derived $J_{\mathrm{hom}}(T^i)$ as the average homogeneous ice nucleation rate coefficient at the mean temperature, T^i, of the i-th temperature interval. This derivation employed all experimental data, including the data points outside of the 10th and 90th percentiles, using the following formula,

$$J_{\mathrm{hom}}(T^i) = \frac{n_{\mathrm{nuc}}^i}{t_{\mathrm{tot}}^i \cdot V^i}\,, \tag{24}$$

where n_{nuc}^i is the number of nucleation events that occur within the i-th temperature interval, t_{tot}^i is the

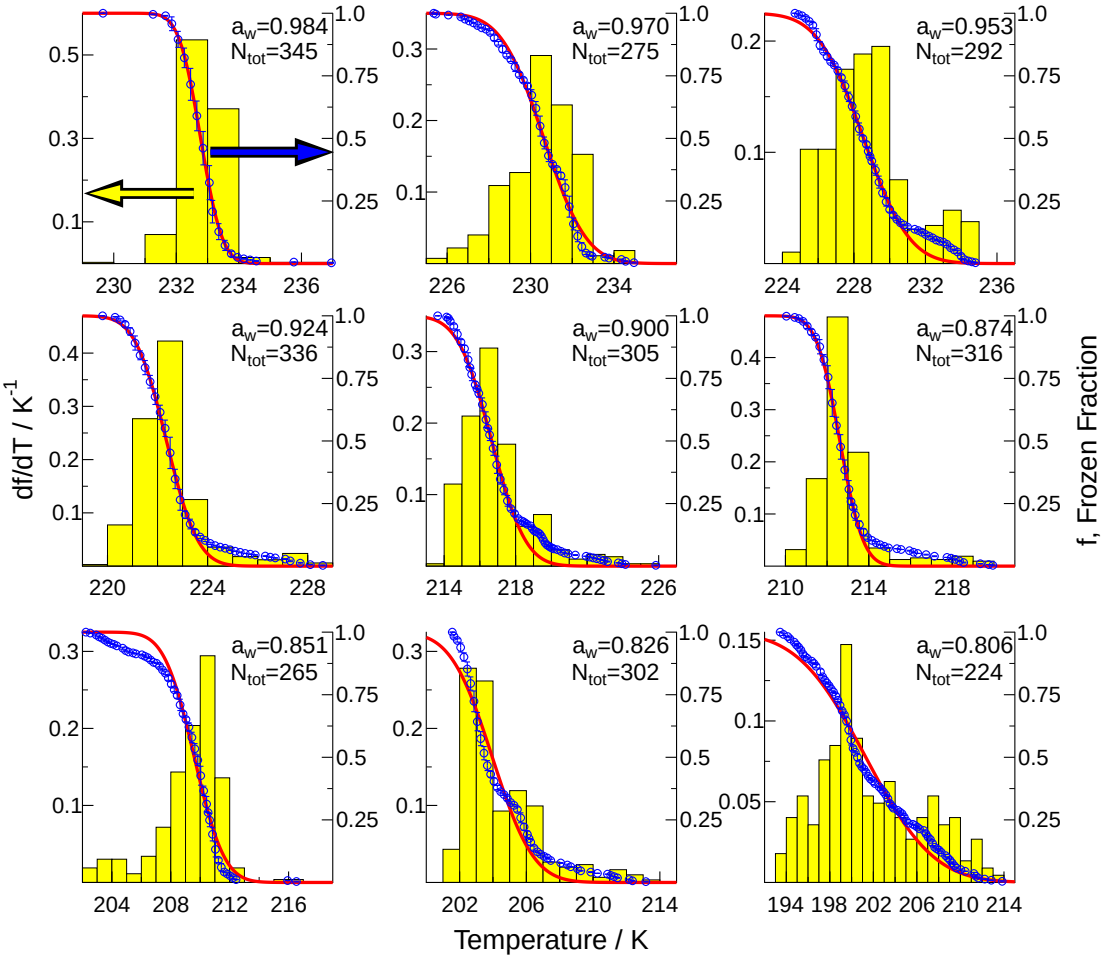

Figure 5.2: Summary of all observed homogeneous ice nucleation events as a function of a_w and T. The frozen fraction, f, of droplets in 0.2 K temperature increments is represented by blue circles. Error bars indicate the range of f in a temperature increment of 0.2 K. Yellow bars show the probability density histogram (PDH) binned in 1.0 K increments. For each panel, a_w and the total number of analyzed droplets, N_tot, are given. The values for the PDH are given on the left y-axis and f on the right y-axis.

total observation time in the i-th temperature interval, and V^i accounts for the individual droplet volumes available at the start of the temperature interval, T^i_st, those of which remain liquid throughout the i-th interval and those which freeze within this interval. The product $t^i_\mathrm{tot} \cdot V^i$ is given by the sum of the contribution from the droplets that remain liquid and those that freeze according to

$$t^i_\mathrm{tot} \cdot V^i = \frac{\Delta T}{r} V^i_\mathrm{liq} + \sum_{j=1}^{n^i_\mathrm{nuc}} \frac{1}{r} \left(T^i_\mathrm{st} - T^i_{\mathrm{nuc},j} \right) V^i_{\mathrm{liq},j} \,, \tag{25}$$

where r is the experimental cooling rate, V^i_liq is the total volume that remains liquid until the end of

the temperature interval, and $T^i_{\mathrm{nuc},j}$ and $V^i_{\mathrm{liq},j}$ are the freezing temperature and corresponding volume, respectively, of the j-th droplet nucleating ice within the i-th interval. Derivations of $J_{\mathrm{hom}}(T^i)$ employ $\Delta T = 0.2\,\mathrm{K}$ corresponding to our total experimental error in determining the temperature. As discussed above, experimental heterogeneous ice nucleation events cannot be avoided when studying homogeneous nucleation[153], however, this effect is not critical for deriving J_{hom} as a function of T due to the goodness of the fit in Fig. 5.2 and the insignificant number of heterogeneous compared to homogeneous freezing events as previously discussed.

Figure 5.3 shows experimentally derived J_{hom} as a function of T and initial a_{w}. J_{hom} values for given a_{w} which extend to higher temperatures and do not show a strong increase with decreasing temperature, are most likely affected by heterogeneous freezing events. For example, the freezing data for aqueous NaCl droplets with $a_{\mathrm{w}} = 0.900$ in Fig. 3 does not show a strong increase in J_{hom} for temperatures between $220 - 226$ K, and remain almost constant at values below 10^5 cm^{-3} s^{-1}. However, J_{hom} values increase significantly from 220 K to 214 K as the homogeneous freezing limit is approached. Also shown in Fig. 5.3 are theoretical predictions of J_{hom} applying the water-activity based homogeneous ice nucleation theory, $J^{\mathrm{Koop}}_{\mathrm{hom}}$, for each initial a_{w}[14,15]. Within the theoretical uncertainty, $J^{\mathrm{Koop}}_{\mathrm{hom}}$ agrees with the experimental data. A potential exception are J_{hom} values obtained for $a_{\mathrm{w}} = 0.806$ for which $J^{\mathrm{Koop}}_{\mathrm{hom}}$ under predicts our

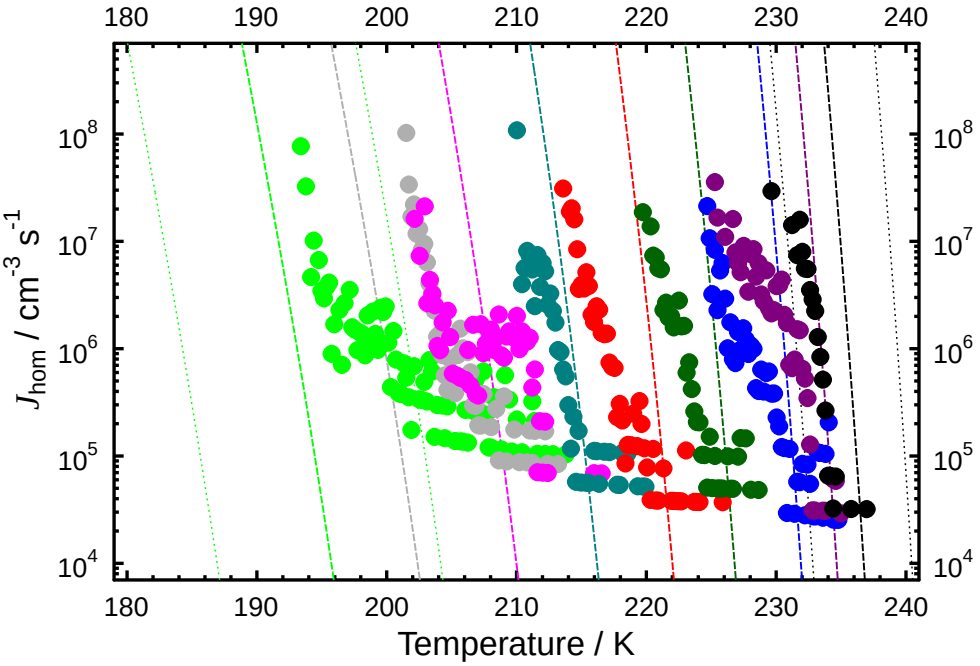

Figure 5.3: Experimentally derived homogeneous ice nucleation rate coefficients, J_{hom} (circles), and theoretically predicted J_{hom} values (dashed lines)[14] shown as a function of T and a_{w}. Black, purple, blue, green, red, teal, magenta, gray, and lime colors correspond to aqueous NaCl droplets with initial a_{w} of 0.984, 0.970, 0.953, 0.924, 0.900, 0.874, 0.851, 0.826, 0.806. The uncertainty for predicted J_{hom} due to an uncertainty in a_{w} of ± 0.025 is indicated as dotted lines for a_{w} of 0.984 and 0.806.

observations. This may be due to the occurrence of heterogeneous ice nucleation events and/or the unknown behavior of supercooled aqueous NaCl solutions, especially at this low a_w value. It should be noted that the uncertainty of the a_w based homogeneous ice nucleation theory for $a_w = 0.800$, is given as ± 0.05 in a_w which translates to ± 12 orders of magnitude uncertainty in predictions of J_{hom} [33]. J_{hom} evaluated at T_f^{NaCl} given in Table 6 remains the same to within one order of magnitude. This translates into a corresponding constant shift in water activity, Δa_w, as suggested by the water-activity based homogeneous ice nucleation theory [14]. Deviations between the observed and predicted J_{hom} values for aqueous NaCl droplets may be attributed to the unknown behavior of a_w in the supercooled temperature regime [144]. The J_{hom} presented here can be employed to further constrain the water-activity based homogeneous ice nucleation theory [14,144,153].

5.3.2 Heterogeneous freezing of aqueous NaCl droplets containing diatoms

Median heterogeneous freezing temperatures of aqueous NaCl droplets containing diatoms *T. pseudonana*, T_f^{dia}, and corresponding mean melting temperatures, T_m^{dia}, are shown in Fig. 5.4 as a function of a_w and droplet composition [202]. The droplet composition was calculated using the E-AIM model [6] and assuming that

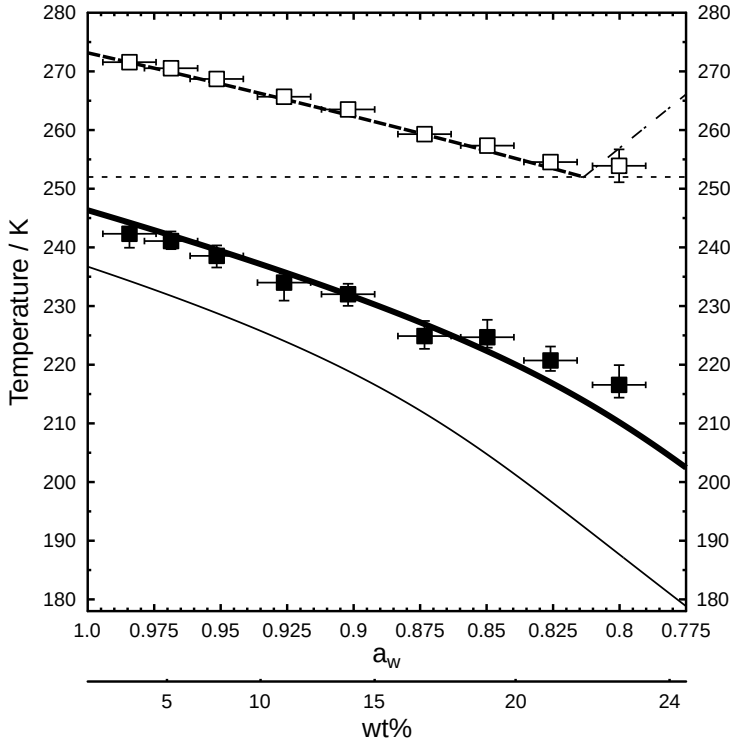

Figure 5.4: Median freezing temperatures and mean melting temperatures of aqueous NaCl/diatom droplets are shown as filled and open squares, respectively as a function of a_w and wt %. The uncertainty for the freezing temperatures are given by the 10th and 90th percentiles and the uncertainty in the melting temperature represents one standard deviation. The error in a_w is ± 0.01. The thick solid line represents the ice melting curve shifted by $\Delta a_{w,het} = 0.2303$, and the thin solid line is the homogeneous freezing curve [15]. Other lines are the same as in Fig. 5.1.

a_w remains constant with temperature. Within the experimental uncertainty T_m^{dia} are in good agreement with $a_w^{ice}(T)$ [14,15]. The homogeneous freezing curve [14,15] is plotted for comparison. Clearly, freezing occurs at much higher temperatures for aqueous NaCl/diatom droplets [202] compared to predicted homogeneous ice nucleation temperatures. At high a_w, corresponding to more dilute solutions, ice nucleation temperatures are enhanced by ~10 K compared to the homogeneous freezing temperatures. At low a_w, ice nucleation proceeds at temperatures ~30 K above predicted homogeneous freezing temperatures. T_m^{dia} and T_f^{dia} shown in Fig. 5.4 for the investigated a_w are given in Table 6, in addition to $S_{ice}(T_f^{dia})$.

The experiments above were repeated using the same aqueous diatom solution, but filtered using a 0.1 μm filter to remove diatoms and possible fragments. This procedure resulted only in homogeneous ice nucleation indicating that the diatoms cause heterogeneous ice nucleation in the immersion mode at elevated temperatures and not dissolved organic material associated with the diatom.

Previous work suggests that heterogeneous immersion mode nucleation can be described by a horizontal shift of the ice melting curve, $\Delta a_{w,het}$, similar to the derivation of homogeneous ice nucleation temperatures [14,15]. Following this approach, we derive a heterogeneous freezing curve given by

$$a_w^{f,het}(T) = a_w^{ice}(T) + \Delta a_{w,het} \,. \tag{26}$$

The new freezing curve, $a_w^{f,het}(T)$, was constructed by fitting T_f^{dia} to Eq. (26) leaving $\Delta a_{w,het}$ as the only free parameter. The best fit yields $\Delta a_{w,het} = 0.2303$ to describe T_f^{dia}. The data presented in Fig. 5.4 indicates that T_f^{dia} is in good agreement with the modified water-activity based ice nucleation theory for predictions of heterogeneous immersion freezing if similar uncertainties as made for predictions of homogeneous freezing are assumed [33]. For $a_w < 0.85$, T_f^{dia} show a slight trend to higher freezing temperatures compared to the predictions. Nevertheless, the overall good agreement of T_f^{dia} with $a_w^{f,het}(T)$ described by $\Delta a_{w,het}$ indicates that heterogeneous ice nucleation induced by intact and fragmented diatoms can be adequately described by thermodynamic quantities [15,252].

Figure 5.5 shows all observed heterogeneous freezing temperatures from Fig. 5.4 as a function of aqueous NaCl/diatom droplet volume and a_w. A linear fit to the data in Fig. 5.5 indicates for the most part no or very weak correlations between observed freezing temperatures and droplet volume as determined from given R^2 coefficients ($R^2 < 0.2$) except for $a_w = 0.984$ and 0.902. Over the experimentally accessed range of volumes and a_w the freezing temperatures do not depend significantly on the volume of the droplet.

Figure 5.6 shows the heterogeneous freezing temperatures of aqueous NaCl/diatom droplets as a function of estimated diatom surface area for all investigated a_w. Similar to Fig. 5.5, linear fits to the data and corresponding R^2 coefficients were determined. The R^2 coefficients indicate that there is no correlation between diatom surface area and freezing temperature except very weak correlation for droplets with initial a_w of 0.926. In summary, the surface area dependence was less than the scatter in the data which was approximately 4–6 K.

Figure 5.7 summarizes approximately 2500 observed heterogeneous ice nucleation events as a function of T and a_w. The cumulative distribution and f in addition to the PDH for heterogeneous freezing, were determined as described above for homogeneous ice nucleation of aqueous NaCl droplets. The PDH and

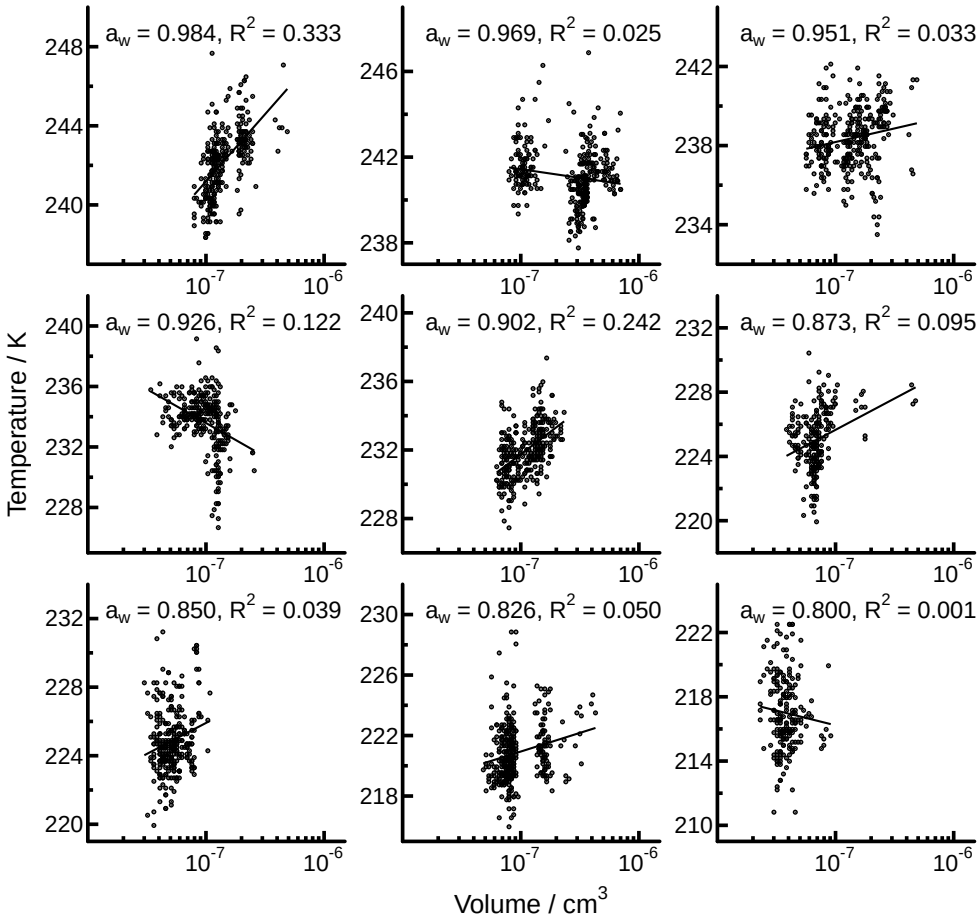

Figure 5.5: Heterogeneous freezing temperatures of aqueous NaCl/diatom droplets shown as dots are plotted as a function of droplet volume for each investigated water activity. The solid lines represent best fits to the data. The coefficient of determination, R^2, indicates the quality of the corresponding fits.

cumulative distributions for heterogeneous ice nucleation due to diatoms immersed in aqueous NaCl droplets show striking similarities to the ones derived from homogeneous nucleation of aqueous NaCl droplets without diatoms shown in Fig. 5.2.

To quantify the heterogeneous freezing behavior of diatoms via the immersion mode, we consider two analytical approaches, a time-dependent [254] and a time-independent [255]. The time-dependent approach follows classical nucleation theory which maintains that heterogeneous ice nucleation, like homogeneous ice nucleation, is dominated by molecular kinetics. Water molecules in an aqueous phase randomly cluster and break apart on the surface of an IN, and each cluster that forms has a probability of growing large enough in time to become the center of a critical ice embryo and subsequently trigger bulk phase ice nucleation (see e.g. Pruppacher and Klett, 1997). The time-independent approach maintains that the dominant influence of heterogeneous nucleation is the presence of surface inhomogeneities which act as preferred sites, or "active

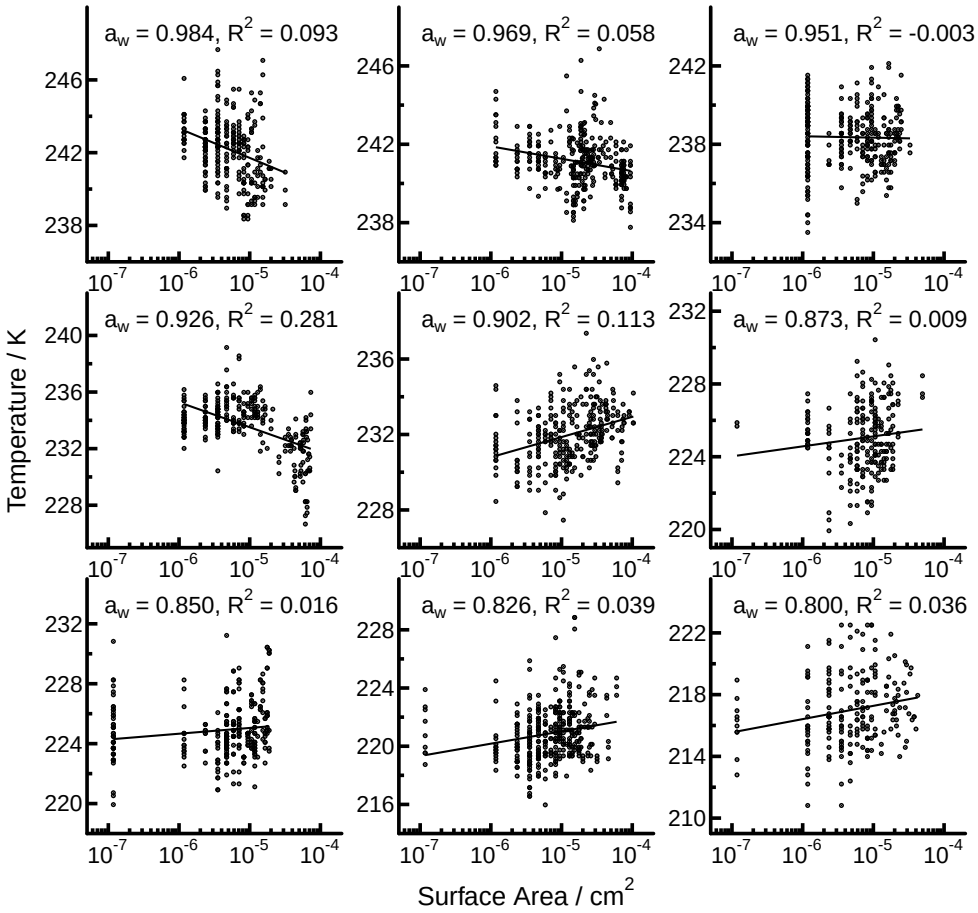

Figure 5.6: Heterogeneous freezing temperatures of aqueous NaCl/diatom droplets shown as dots are plotted as a function of diatom surface area for each investigated water activity. The solid lines represent best fits to the data. The coefficient of determination, R^2, indicates the quality of the corresponding fits.

sites", of critical ice embryo formation and thus, ice nucleation[42,137,256]. These active sites are then destined to become IN at site-specific characteristic temperatures. Thus, ice nucleation is triggered by the appearance of active sites as a function of temperature on the surface of particles immersed in aqueous droplets[137].

5.3.2.1 Time-dependent analysis Here, we quantify heterogeneous ice nucleation due to intact and fragmented diatoms employing a time-dependent approach. As indicated in Fig. 5.6, heterogeneous freezing temperature dependence on diatom surface area was less than the scatter in the data. We therefore derive heterogeneous ice nucleation rates independent of diatom surface area as a function of T and a_{w}. However, in the case where ice nucleation is found to depend on diatom surface area outside the range probed in our experiments and/or diatom surface areas are available from field samples, we additionally provide surface dependent heterogeneous ice nucleation rate coefficients as a function of T and a_{w}.

We follow a previously described analysis[127,128] to calculate the time-dependent heterogeneous ice nucleation rate given as

$$\omega_{\mathrm{het}}(T^i) = \frac{n^i_{\mathrm{nuc}}}{t^i_{\mathrm{tot}}}\,, \tag{27}$$

and t^i_{tot} is given by

$$t^i_{\mathrm{tot}} = \frac{\Delta T}{r}\left(n^i_{\mathrm{tot}} - n^i_{\mathrm{nuc}}\right) + \sum_{j=1}^{n^i_{\mathrm{nuc}}} \frac{1}{r}\left(T^i_{\mathrm{st}} - T^i_{\mathrm{nuc},j}\right)\,, \tag{28}$$

where n^i_{tot} is the total number of liquid droplets at the start of the i-th temperature interval. The remaining variables are the same as in Eq. (25).

Measurements of diatom surface area and observations of heterogeneous freezing events allowed us to derive heterogeneous ice nucleation rate coefficients, J_{het}. Following a previously described analysis[127,128],

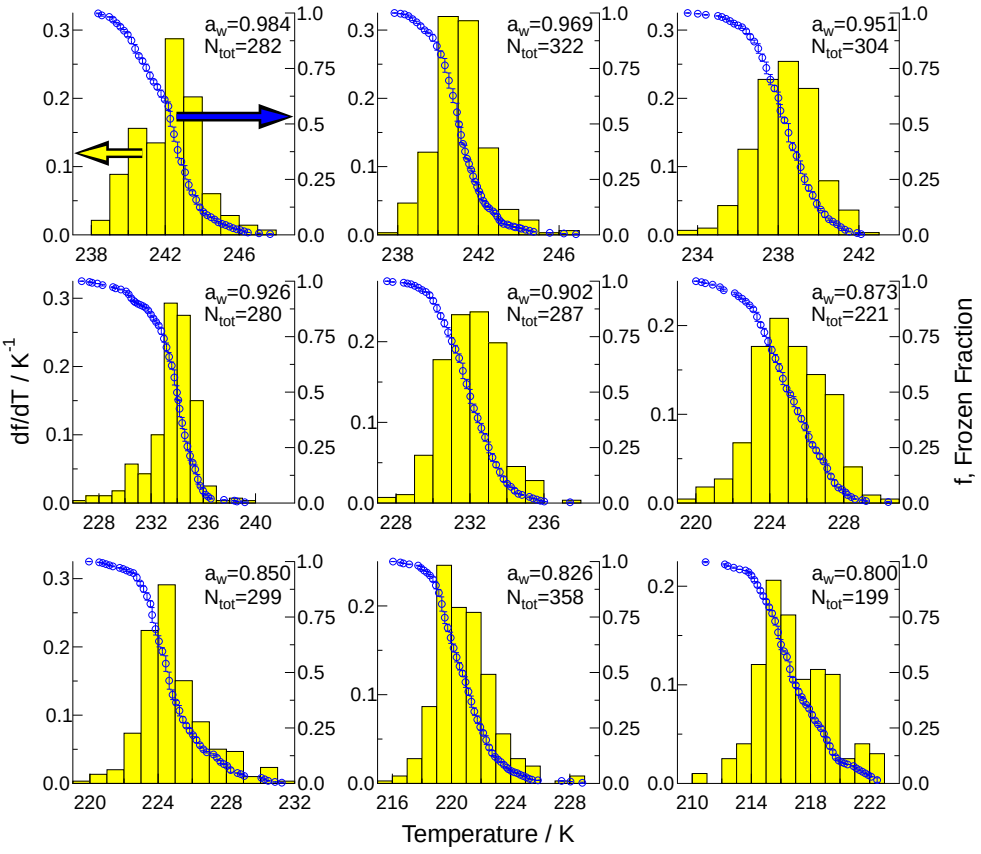

Figure 5.7: Summary of all observed heterogeneous ice nucleation events as a function of a_{w} and T. The frozen fraction, f, of droplets in 0.2 K temperature increments is represented by blue circles. Error bars indicate the range of f in a temperature increment of 0.2 K. Yellow bars show the probability density histogram (PDH) binned in 1.0 K increments. For each panel, a_{w} and the total number of analyzed droplets, N_{tot}, are given. The values for the PDH are given on the left y-axis and f on the right y-axis.

$J_{\mathrm{het}}(T^i)$ is the average heterogeneous ice nucleation rate coefficient for a given temperature interval which can be described as

$$J_{\mathrm{het}}(T^i) = \frac{n^i_{\mathrm{nuc}}}{t^i_{\mathrm{tot}} \cdot A^i} \,. \tag{29}$$

The product $t^i_{\mathrm{tot}} \cdot A^i$ is derived according to

$$t^i_{\mathrm{tot}} \cdot A^i = \frac{\Delta T}{r} A^i_{\mathrm{liq}} + \sum_{j=1}^{n^i_{\mathrm{nuc}}} \frac{1}{r} \left(T^i_{\mathrm{st}} - T^i_{\mathrm{nuc},j}\right) A^i_{\mathrm{liq},j} \,. \tag{30}$$

A^i_{liq} is the total diatom surface area in the droplets that remains liquid until the end of the temperature interval and $A^i_{\mathrm{liq},j}$ is the diatom surface area of the j-th droplet that nucleates ice within the i-th temperature interval. Other variables are the same as in Eqs. (25) and (28). For calculation of $\omega_{\mathrm{het}}(T)$ and $J_{\mathrm{het}}(T)$, $\Delta T = 0.2\,\mathrm{K}$ reflects the experimental temperature uncertainty.

Figure 5.8a,b presents ω_{het} and J_{het}, respectively, for the individually analyzed ice nucleation events presented in Fig. 5.7 as a function of T and a_{w}. Figure 5.8 demonstrates that ω_{het} and J_{het} increase exponentially with decreasing T. In some instances, values of ω_{het} and J_{het} for different a_{w} overlap each other. This behavior may be due to a temperature dependence of or uncertainty in a_{w}. According to classical nucleation theory, ω_{het} and J_{het} reflects an exponential dependence on temperature[42] suggesting that heterogeneous ice nucleation due to intact and fragmented diatoms follows a time-dependent freezing process, in line with classical nucleation theory.

5.3.2.2 Time-independent analysis A time-independent approach[137] can also be used to quantify heterogeneous ice nucleation due to intact and fragmented diatoms. This mechanistic explanation commonly referred to as the singular approach, maintains that the freezing process is dominated by an active site on the surface of a particle which triggers ice nucleation at a specific characteristic temperature.

Following a previously described analysis by Vali[137], we derive differential and cumulative nuclei spectra to quantify a time-independent approach for explaining heterogeneous ice nucleation due to diatoms. The differential nuclei spectra for the i-th temperature interval, $k(T^i)$, is defined as the ice active surface site density for a unit surface area of a sample

$$k(T^i) = \frac{1}{A^i_{\mathrm{tot}}} \frac{n^i_{\mathrm{nuc}}}{\Delta T} \,, \tag{31}$$

where A^i_{tot} is the total diatom surface area in the droplets that remains liquid at the start of the i-th temperature interval[137]. A cumulative nucleus spectrum as a function of temperature, $K(T^i)$, can be evaluated from experimental data by numerically integrating Eq. (31) from $T^{\mathrm{dia}}_{\mathrm{m}}$ to T^i yielding

$$K(T^i) = \sum_{T^{\mathrm{dia}}_{\mathrm{m}}}^{T_i} \frac{n^i_{\mathrm{nuc}}}{A^i_{\mathrm{tot}}} \,, \tag{32}$$

where $K(T^i)$ includes the sites which had become ice active for temperatures warmer than T^i. Derivations

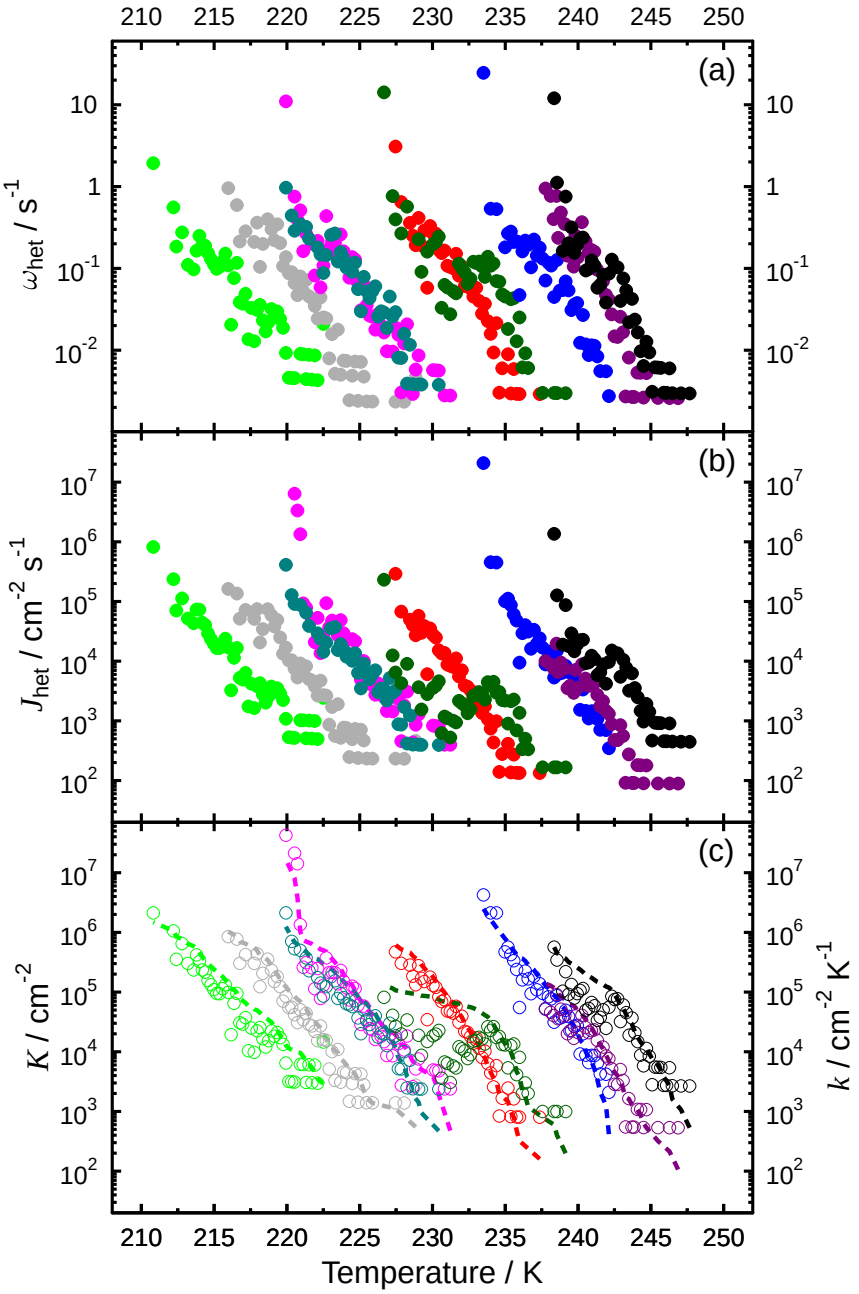

Figure 5.8: Experimentally derived **(a)** heterogeneous ice nucleation rates, ω_{het}, **(b)** heterogeneous ice nucleation rate coefficients, J_{het}, and **(c)** differential and cumulative nuclei spectra, $k(T)$ and $K(T)$, respectively, for aqueous NaCl/diatom droplets shown as a function of T and a_w. In **(c)**, the $k(T)$ and $K(T)$ are given as open circles and dotted lines, respectively. Black, purple, blue, green, red, teal, magenta, gray, and lime colors correspond to aqueous NaCl droplets containing diatoms with initial a_w of 0.984, 0.969, 0.951, 0.926, 0.902, 0.873, 0.850, 0.826 and 0.800.

of $k(T)$ and $K(T)$ employ $\Delta T = 0.2\,\mathrm{K}$.

Figure 5.8c presents $k(T)$ and $K(T)$ for the individually analyzed ice nucleation events presented in Fig. 5.7 as a function of T and a_w. Figure 5.8c demonstrates that $k(T)$ for most data increases exponentially with decreasing T. As previously described, $k(T)$ is the differential spectrum for $K(T)$ and thus it follows from Eqs. (31) and (32) that $k(T) = dK(T)/dT$. Since $k(T)$ shows an exponential behavior, $K(T)$ also increases exponentially with deceasing temperature for ice nucleation events at specific a_w. In some instances, values of $k(T)$ and $K(T)$ for different a_w overlap each other. Similar to the time-dependent approach, this behavior may be due to a temperature dependence of or uncertainty in a_w.

5.3.3 Water activity and heterogeneous ice nucleation

Figure 5.4 indicates that the water activity criterion can also be used to predict median freezing temperatures of heterogeneous ice nucleation[15]. Table 6 gives ω_het, J_het, and $K(T)$ evaluated at the median freezing temperatures shown in Fig. 5.4. On average and over the range of investigated a_w values, $\omega_\mathrm{het}(T_\mathrm{f}^\mathrm{dia}) = 0.11^{+0.06}_{-0.05}\,\mathrm{s}^{-1}$, $J_\mathrm{het}(T_\mathrm{f}^\mathrm{dia}) = 1.0^{+1.16}_{-0.61} \times 10^4\,\mathrm{cm}^{-2}\,\mathrm{s}^{-1}$, and $K(T_\mathrm{f}^\mathrm{dia}) = 6.2^{+3.5}_{-4.1} \times 10^4\,\mathrm{cm}^{-2}$ for aqueous NaCl/diatom droplets, where the plus and minus errors indicate the range in values. The narrow range of ω_het, J_het, and $K(T)$ along the freezing line indicates that the shifted $a_\mathrm{w}^\mathrm{ice}$ curve shown in Fig. 5.4 is representative of these freezing rates and nuclei spectra. This further supports the contention that immersion mode freezing can be parameterized by $\Delta a_\mathrm{w,het}$. Here, we report that a shift of $\Delta a_\mathrm{w,het} = 0.2303$ describes heterogeneous ice nucleation temperatures for immersion freezing where $\omega_\mathrm{het}(T_\mathrm{f}^\mathrm{dia}) = 0.11\,\mathrm{s}^{-1}$, $J_\mathrm{het}(T_\mathrm{f}^\mathrm{dia}) = 1.0 \times 10^4\,\mathrm{cm}^{-2}\,\mathrm{s}^{-1}$, and $K(T_\mathrm{f}^\mathrm{dia}) = 6.2 \times 10^4\,\mathrm{cm}^{-2}$. Further studies are necessary to investigate whether ω_het, J_het, and $K(T)$ can be similarly parameterized as a function of a_w as for the case of homogeneous ice nucleation[14].

5.4 Atmospheric implications

5.4.1 Homogeneous ice nucleation

The results of the homogeneous freezing experiments reported here allow for a better constraint of predicted J_hom from aqueous NaCl droplets and can be used to narrow the uncertainty in the theoretical predictions of the water activity based homogeneous ice nucleation theory[14,15,33,144]. This is significant because an uncertainty of 0.025 in a_w can lead to changes in J_hom of up to 6 orders of magnitude or 8 K in temperature[33,144,153]. In addition, the derivation of J_hom allows for estimation of ice particle production rates from derived homogeneous nucleation according to $P_\mathrm{hom}^\mathrm{ice} = J_\mathrm{hom} \cdot V_\mathrm{particle}$, where V_particle is the amount of total liquid volume of aerosol per cm^3 of air. We assume sea salt concentrations, estimated here from field observations of aerosol particle concentrations in the free troposphere as $10\,\mathrm{cm}^{-3}$ [52,257], with mean dry diameter of 200 nm and a wet diameter of 480 nm at 90% RH[258,259], and applying $J_\mathrm{hom} = 10^6\,\mathrm{cm}^{-3}\,\mathrm{s}^{-1}$ at a temperature of 215 K (Fig. 5.3), $P_\mathrm{hom}^\mathrm{ice}$ could reach 0.035 ice particles L^{-1} (air) min^{-1}. Ice crystal concentrations in cirrus clouds usually fall between 10 and $100\,\mathrm{L}^{-1}$ (air)[48,260–262]. Thus, after 30 min at these atmospheric conditions, approximately 1 ice crystal per liter of air could form.

5.4.2 Heterogeneous ice nucleation

As far as we are aware, neither spatial and temporal concentrations nor corresponding determination of surface areas of aerosolized diatoms are available. In fact, we are only aware of two studies which have reported airborne diatom concentrations. A study by Tormo *et al.*[263] observed airborne diatoms in excess of $0.07\,\mathrm{L}^{-1}$ (air) in summer outside the city of Badajoz, SW Spain, about 100 m away from the Gevora River. We would expect that airborne concentrations of diatoms would be greater over marine waters where wave action can result in greater generation of sea spray and bubble bursting aerosols when compared with rivers. In fact, a study in which filter samples were collected from a 9 m high tower on a 55 m high cliff off the coast on Amsterdam Island (a tiny remote volcanic island in the Southern Indian Ocean some 3000 km from any continent) found concentrations of marine biogenic particles characterized as amorphous silica diatom fragments, ranging from ∼20–28 L^{-1} of air[238]. While not specifically reporting size distributions, ambient insoluble particles from their air samples had mean diameters of $\simeq (0.8 \pm 0.7)\,\mu\mathrm{m}$[238]. Brown *et al.*[232] found a diversity of viable airborne algal species in concentrations as high as $4\,\mathrm{L}^{-1}$ (air), suggesting that this number would be greater if nonviable algae were additionally counted. Concentrations of marine bacteria in air originating from ocean waters is estimated to be on the order of $10\,\mathrm{L}^{-1}$ (air)[264], which can provide an upper limit on airborne diatom concentrations assuming similar processes that lead to aerosolization of diatoms. If, however, diatom fragments are aerosolized or whole diatoms are fragmented in the atmosphere, i.e. during dust transport[240], then concentrations can actually exceed those of bacteria, given that one whole diatom would be broken into smaller and more numerous fragments. IN concentration at −15 °C taken in air over the Arctic Ocean show a positive correlation with particle sizes between 50 nm and 120 nm[265], smaller than sizes of viable airborne bacteria that are typically ∼4 μm[266,267]. Diatom fragments would be expected to fall within this size range which could explain the correlation with IN concentrations measured by Bigg[265]. Lastly, a very recent study found a unique organic marine aerosol mass concentration of up to $3.8\,\mu\mathrm{g\,m}^{-3}$ in an aerosol plume passing over highly productive surface waters in the North Atlantic off Mace Head[109].

From the above discussion, we estimate a conservative lower limit of airborne diatom fragment concentrations of $0.1\,\mathrm{L}^{-1}$ (air). In cases of high biological production and strong wave activity, this number may be 2 orders of magnitude higher. The major contribution of primary organic matter to sea spray aerosol have been found to be in the submicrometer size range[3,109] and thus, we assume a maximum size of a diatom fragment to be 1 μm. This provides an upper estimate for the corresponding surface dependent ice particle production. We expect that these estimates will vary with additional field collected data.

In the case that ice nucleation induced by intact or fragmented diatoms is assumed to be independent of surface area, we can derive ice particle production rates as a function of T and RH, $P_{\mathrm{het}}^{\mathrm{ice}}(T, \mathrm{RH})$, as

$$P_{\mathrm{het}}^{\mathrm{ice}}(T, \mathrm{RH}) = \omega_{\mathrm{het}}(T, \mathrm{RH}) \cdot N_{\mathrm{particle}}\,, \tag{33}$$

where N_{particle} is the total diatom concentration per unit volume of air and ω_{het} is determined from Fig. 5.8a for given T and RH.

If available diatom surface area is accounted for in the description of heterogeneous ice nucleation then,

$$P_{\rm het}^{\rm ice}(T, {\rm RH}) = J_{\rm het}(T, {\rm RH}) \cdot S_{\rm particle}\,, \tag{34}$$

and

$$P_{\rm het}^{\rm ice}(T) = K(T, {\rm RH}) \cdot S_{\rm particle}\,. \tag{35}$$

$J_{\rm het}(T, {\rm RH})$ and $K(T, {\rm RH})$ are determined from Fig. 5.8b,c. $S_{\rm particle}$ is the total diatom surface area per unit volume of air. Following the arguments presented above, we assume that the diatom fragments are a square plate with side length of 1 μm resulting in a surface area of 2 $\mu{\rm m}^2$ per diatom particle and therefore, $2 \times 10^{-9}\,{\rm cm}^2\,{\rm L}^{-1}$ of air given diatom concentrations of $0.1\,{\rm L}^{-1}$ (air). Equations (33) and (34) describe time-dependent ice particle production whereas Eq. (35) yields ice particle production as a function of temperature reflecting the fundamental differences in the description of the ice nucleation process.

We now estimate ice particle production for the two following scenarios: i) Ice formation at conditions typical for Arctic mixed-phase clouds. ii) Ice formation at typical cirrus cloud temperatures of about 220 K.

Assuming diatom concentrations of $0.1\,{\rm L}^{-1}$ (air) and RH = 95%, we derive for $T = 240\,{\rm K}$ and corresponding $\omega_{\rm het} = 0.11\,{\rm s}^{-1}$, $P_{\rm het}^{\rm ice} = 0.7$ ice particles ${\rm L}^{-1}$ (air) ${\rm min}^{-1}$. This indicates that all available diatoms would nucleate ice within seconds. Assuming the ice nucleation process to be surface dependent and applying $J_{\rm het} = 1.0 \times 10^4\,{\rm cm}^{-2}\,{\rm s}^{-1}$ and K=6.2×10^4 ${\rm cm}^{-2}$, the corresponding $P_{\rm het}^{\rm ice}$ is equal to $0.001\,{\rm L}^{-1}$ (air) ${\rm min}^{-1}$ and $0.0001\,{\rm L}^{-1}$ (air), respectively. From this example, it follows that the time-dependent analysis will always yield higher ice particle numbers with time at fixed temperatures (or small updraft velocities) compared to analysis using the time-independent approach. Typical ice crystal concentrations observed in Arctic mixed-phase clouds are $\sim$0.1–$10\,{\rm L}^{-1}$ (air)[62,268,269]. Thus, if a minor fraction of background sea salt particles contains diatoms or fragments of diatoms, then a significant amount of ice crystal production could be attributable to diatoms if ice nucleation follows a time-dependent mechanism. IN concentrations in polar regions can be greater in summer than those in winter and fall months[61,63,249,268], and can coincide with phytoplankton blooms in the surface waters below[112–114]. This seasonality may be attributable to aerosolized diatoms acting as IN.

At $T = 220\,{\rm K}$ and RH = 85%[48,262] applying the same diatom concentration for cirrus cloud formation assuming ice nucleation does not depend on surface area, we derive $\omega_{\rm het} = 0.51\,{\rm s}^{-1}$ and $P_{\rm het}^{\rm ice} = 3.06$ ice particles ${\rm L}^{-1}$ (air) ${\rm min}^{-1}$. This indicates that all available diatoms would nucleate ice within seconds. Accounting for the surface dependence of the ice nucleation process, we can employ $J_{\rm het} = 1.8 \times 10^5\,{\rm cm}^{-2}\,{\rm s}^{-1}$ and $K = 1.1 \times 10^6\,{\rm cm}^{-2}$ which yield corresponding $P_{\rm het}^{\rm ice} = 0.022\,{\rm L}^{-1}$ (air) ${\rm min}^{-1}$ and $P_{\rm het}^{\rm ice} = 0.0022\,{\rm L}^{-1}$ (air), respectively. As in the previous example, for a fixed or slowly decreasing temperature, the time-dependent nucleation description will always result in higher ice crystal concentrations. Thus, predictions of ice crystal production are sensitive to the choice of either a time-dependent or time-independent approach.

Typical ice crystal concentrations observed in cirrus clouds due to heterogeneous ice nucleation can be expected to be greatly affected by depletion of water vapour subsequent to ice crystal formation according to the Bergeron-Wegener-Findeisen process[270–272], rapid ice particle production through riming according to the Hallett-Mossop effect[273,274], and the presence of other IN. Thus, ice crystal concentrations in cirrus

clouds impacted by heterogeneous ice nucleation are ill defined and remain largely uncertain[73]. As previously mentioned, cirrus clouds typically have ice crystal concentrations of 10–100 L^{-1} (air). Our calculations indicate that a time-dependent approach will result in rapid ice crystal production rates so that after approximately 5 to 10 min at a constant or slowly changing temperature, diatoms could significantly impact cirrus cloud formation. On the other hand, this does not apply when employing a time-independent approach for ice particle production resulting in ice crystal numbers lower than typical observations.

From these estimates, it remains unclear whether it is more appropriate to apply either a time-dependent or time-independent approach for determination of ice crystal production or if a combination of the two would be more appropriate[42,142,275]. For a given temperature, the difference between the two theoretical approaches is about 2 orders of magnitude. While this seems small compared to typical uncertainties in ice nucleation rate predictions, the cloud microphysical evolution would proceed in significantly different directions depending on which nucleation mechanism is assumed to be taking place. Of course this discussion serves only as an example and is simplified compared to the actual progression within the cloud formation process. We therefore recommend taking advantage of cloud system resolving models with a high time resolution[174,276] to evaluate the sensitivity of time-dependent and time-independent ice crystal production utilizing the results presented here for heterogeneous ice nucleation due to marine biogenic particles as represented by diatoms.

5.5 Summary

Homogeneous and heterogeneous freezing of ice from micrometer-sized aqueous NaCl droplets with and without diatoms have been analyzed in the temperature range of 180 to 260 K and for water activities of 0.8 to 0.99. The freezing of about 5000 individual droplets has been investigated in this study.

The median homogeneous freezing temperatures agreed, within experimental and theoretical uncertainties, with predictions of the water-activity based homogeneous ice nucleation theory. The experimentally derived homogeneous ice nucleation rate coefficients were in agreement with predictions of the water-activity based theory and can be employed to further constrain that theory. Corresponding ice particle production rates were derived from experimentally obtained homogeneous ice nucleation rate coefficients.

The median heterogeneous freezing temperatures due to intact and fragmented diatoms were well represented by the modified water-activity based theory, where a horizontal shift by $\Delta a_{\mathrm{w,het}} = 0.2303$ in the corresponding ice melting curve described the experimentally derived freezing data. Diatom surface area and aqueous volume was determined for every droplet investigated. Under our experimental conditions, heterogeneous freezing temperatures neither depended on the droplet volume nor on the available diatom surface area. The heterogeneous ice nucleation rate evaluated at median freezing temperatures, represented by the shifted melting curve, is $0.11^{+0.06}_{-0.05}\,s^{-1}$. Assuming that ice nucleation depends on surface area we derive heterogeneous ice nucleation rate coefficients and time-independent cumulative nuclei spectra as $1.0^{+1.16}_{-0.61} \times 10^4\,cm^{-2}\,s^{-1}$ and $6.2^{+3.5}_{-4.1} \times 10^4\,cm^{-2}$, respectively. Assuming diatom concentrations of 0.1 L^{-1}, corresponding ice particle production rates indicate that intact and fragments of diatoms can efficiently form ice crystals under typical tropospheric conditions. Ice particle production assuming a time-dependent nucleation mechanism is always greater at slow updrafts or slowly changing temperatures when compared with a time-independent nucleation

process. High resolution cloud system resolving models can be used to evaluate the sensitivity of ice particle production in response to intact and fragmented diatoms by either time-dependent or time-independent analyses.

6 Results: Initiation of the ice phase by marine biogenic surfaces in supersaturated gas and supercooled aqueous phases

The sections from 6.1 to 6.4 are the reproduction of the publication of "Initiation of the ice phase by marine biogenic surfaces in supersaturated gas and supercooled aqueous phases" by P. Alpert, J. Y. Aller, and D. A. Knopf published in Physical Chemistry Chemical Physics, Vol. 13, 19882-19894, 2011, with permission from Royal Society of Chemistry Publishing. The layout of the article as well as the section figures and table numberings have been adapted to match with the thesis structure.

Initiation of the ice phase by marine biogenic surfaces in supersaturated gas and supercooled aqueous phases

Peter A. Alpert[1], Josephine Y. Aller[2], and Daniel A. Knopf[1*]

[1]Institute for Terrestrial and Planetary Atmospheres/School of Marine and Atmospheric Sciences, Stony Brook University, Stony Brook, NY 11794-5000, USA
[2]School of Marine and Atmospheric Sciences, Stony Brook University, Stony Brook, NY 11794-5000, USA

[*]To whom correspondence should be addressed. Email:Daniel.Knopf@stonybrook.edu

Published in Physical Chemistry Chemical Physics, Vol. 13, 19882-19894, 2011, with permission from Royal Society of Chemistry Publishing, copyright 2011.

6.1 Abstract

Biogenic particles have the potential to affect the formation of ice crystals in the atmosphere with subsequent consequences for the hydrological cycle and climate. We present laboratory observations of heterogeneous ice nucleation in immersion and deposition modes under atmospherically relevant conditions initiated by *Nannochloris atomus* and *Emiliania huxleyi*, marine phytoplankton with structurally and chemically distinct cell walls. Temperatures at which freezing, melting, and water uptake occur, are observed using optical microscopy. The intact and fragmented unarmoured cells of *N. atomus* in aqueous NaCl droplets enhance ice nucleation by $10 - 20$ K over the homogeneous freezing limit and can be described by a modified water activity based ice nucleation approach. *E. huxleyi* cells covered by calcite plates do not enhance droplet freezing temperatures. Both species nucleate ice in the deposition mode at an ice saturation ratio, S_{ice}, as low as ~ 1.2 and below 240 K, however, for each, different nucleation modes occur at warmer temperatures. These observations show that markedly different biogenic surfaces have both comparable and contrasting effects on ice nucleation behaviour depending on the presence of the aqueous phase and the extent of supercooling and water vapour supersaturation. We derive heterogeneous ice nucleation rate coefficients, J_{het}, and cumulative ice nuclei spectra, K, for quantification and analysis using time-dependent and time-independent approaches, respectively. Contact angles, α, derived from J_{het} via immersion freezing depend on T, a_{w}, and S_{ice}. For deposition freezing, α can be described as a function of S_{ice} only. The different approaches yield different predictions of atmospheric ice crystal numbers primarily due to the time evolution allowed for the time-dependent approach with implications for the evolution of mixed-phase and ice clouds.

6.2 Introduction

Aerosol particles are ubiquitous in the atmosphere and have the ability to affect the earth and climate by directly scattering and absorbing solar and terrestrial radiation.[65–69] They can act also as cloud condensation nuclei and ice nuclei (IN) which can further affect the global radiative budget and impact precipitation initiation.[1,70–72,74,219–221] Ice in mixed phase clouds, for example, can alter radiative forcing due to sedimentation and water vapour scavenging which can impact cloud lifetime and albedo.[75] Atmospheric ice formation is recognized as important, however, it remains one of the largest uncertainties in models predicting future climate.[1]

Ice nucleation of micrometer sized cloud droplets can occur homogeneously for supercooled temperatures, T, lower than 235 K and supersaturation with respect to ice, S_{ice}, higher than 1.4.[14,42–44] Heterogeneous ice nucleation can occur via various modes (i) an ice nucleus immersed in a supercooled aqueous droplet (immersion), (ii) deposition of ice on the ice nucleus directly from the supersaturated water vapour phase (deposition), (iii) condensation of liquid water from the supersaturated water vapour phase on the ice nucleus followed by ice formation (condensation), and (iv) contact of an ice nucleus with a supercooled aqueous droplet (contact).[42,45] Microorganisms and particles of biological origin have been found to act as efficient IN for conditions relevant to the atmosphere in the immersion and condensation freezing mode.[34,35,57,277,277–280] Certain plant pathogenic bacteria are known in fact, to be some of the most efficient IN due their capability to form ice by immersion freezing close to the melting point.[113,114,281–283] Bacteria can shed pieces of their

cell membrane which form ice in water droplets[284] and freeze-dried and pulverized bacteria can act as IN via immersion and contact freezing,[285] which indicate that even fragments of biological membranes are capable of forming ice. Pollen grains are efficient IN when in contact with liquid water, i. e. in the immersion, contact, and condensation freezing modes,[286–288] however, are not efficient IN via deposition freezing.[286] These studies suggest that water present in surface groves and capillaries extending into the pollen interior may enhance the liquid to ice phase transition.[286–288] Fungal spores,[289,290] and lichens[291–293] can also nucleate ice, however, the freezing potential of these biological particle types has only been investigated via immersion freezing. The freezing ability of bacterial ice nucleators can be deactivated when their phospholipids content is altered, which implies that a membrane structure is required for the ice nucleating proteins to arrange water molecules into an ice lattice.[294–301] It has been suggested that numerous proteins with high levels of symmetry and high repetitions of amino acids anchor to a phospholipid membrane.[297,299–301] The N-terminal ends then may arrange in a tertiary structure to form an ice nucleus by manipulating the hydrogen bonding network of surrounding water.[297] Previous studies have shown that some organic amphiphilic molecules can form a surfactant monolayer coating on the surface of water drops which trigger ice nucleation.[128,144,302–305] These studies showed that the two dimensional monolayer crystal structure, and thus, the arrangement of the carboxyl or hydroxyl groups at the water-air interface represent a close match to a hexagonal ice lattice.[302] Various grooves, cracks and capillaries may act to form relatively hydrophobic and hydrophilic patches than compared with a smooth homogeneous surface.[42] These defects would make it favorable for a water molecule to join a disordered water cluster facilitating the formation of ice, in contrast to the addition of a water molecule to oriented layers of water molecules which may not as readily nucleate ice.[42] Considering the vast diversity of microorganisms, the potential for biogenic ice nucleation is great.[301]

Among the above mentioned studies which focus on immersion freezing in pure water droplets, relatively few have considered the effects of aqueous solutions on the ice nucleation capabilities of biogenic particles.[15,34,35] This is due to limitations and difficulties in observing highly supercooled aqueous solution droplets and simultaneously stabilizing droplet composition, i. e. minimizing vapour mass transport following initial ice nucleation events through the Bergeron-Wegner-Findeisen process.[270–272] Laboratory observations of biogenic particles acting as IN via condensation and contact freezing have only been investigated for temperatures down to 260 K and have necessitated costly experimental designs.[279,285] Deposition freezing is relatively more difficult to observe due to the necessity for precisely measuring relatively small water vapour pressures at low temperatures, which has only been determined for pollen grains down to 240 K.[287] Here, we present the results of an investigation into the ice nucleation potential of two unique marine biogenic particle types for temperatures as low as 200 K via immersion mode as a function of NaCl composition up to $\sim$ 23 wt% and water activity, a_{w}, down to 0.80. We also present experimental results of deposition and condensation freezing, or water condensation followed by immersion mode freezing, as a function of the ice saturation ratio, S_{ice}, from 1.00 up to water saturation.

Biogenic particles can originate from the marine or terrestrial biosphere, and as described above those that act as efficient IN have been of continental origin. Marine biogenic particles also have the potential to nucleate ice at warmer temperatures than observed for homogeneous freezing.[34,35,113–115] Although, a study by Junge and Swanson[229] reported that several representative polar sea ice bacteria and a virus were not

efficient IN via immersion mode.[229] Only recently an efficient marine biogenic IN has been unambiguously identified.[34,35] This is surprising given that oceans cover $\sim 70\%$ of the Earth's surface and particles, including phytoplankton, bacteria, viruses, transparent exopolymers, and colloidal gels, have clearly been shown to become aerosolized from the sea surface microlayer.[3,81,102,104,243,244,306] While these various particles originate from oceans along with other sea salt aerosol particles, studies have clearly demonstrated that they can also be aerosolized without any sea salt attached.[104,306–310] A study by Knopf *et al.*[34] observed that intact and fragments of the diatom *Thalassiosira pseudonana* can at atmospherically relevant conditions act as efficient IN in both the immersion and deposition mode and with and without association of NaCl.

In recent literature, three different approaches have been proposed for describing heterogeneous ice nucleation: classical nucleation theory, CNT, (a time-dependent description), singular hypothesis approach, SH, (a time-independent description), and the modified a_{w} based ice nucleation theory.[35,144,173,256,275,311] Our experiments are designed to obtain a quantitative understanding of the parameters used in these three approaches as a function of temperature, T, S_{ice}, and a_{w}.

CNT derives ice nucleation kinetics in terms of the heterogeneous ice nucleation rate coefficient, J_{het}, in units of $\mathrm{cm}^{-2}\ \mathrm{s}^{-1}$, which describes the rate of ice nucleation and scales with the surface area of the ice nucleating particle.[42] J_{het} is related to the formation and growth of water molecule clusters on the surface of an IN as a function of time to become the center of a critical ice embryo and subsequently trigger bulk phase ice nucleation.[42] CNT can provide a physical understanding of the underlying kinetics of the ice nucleation mechanism and information about thermodynamic variables involved in the formation of the solid phase such as water diffusivity and the interfacial energy between ice and the initial parent phase. The IN surface is related to J_{het} by the contact angle, α, which holds information on the interfacial energy between the IN, the ice embryo, and the surrounding parent phase which can be an aqueous solution or supersaturated water vapour.[42,133] The application of CNT for heterogeneous nucleation can be more challenging compared to the description of homogeneous freezing not only due the lack of thermodynamic data, but because of the unknown relationship between the IN surface and aqueous solution.

The singular hypothesis approach (SH), a time-independent description, can also be used to describe heterogeneous ice nucleation.[137] SH maintains that the heterogeneous ice nucleation processes characterized only by temperature, is controlled by the presence of surface inhomogeneities which act as preferred sites, or "active sites", for ice formation.[42,137,256] These can be cracks and deformations located on an otherwise relatively homogeneous surface, for example, or finite surface patches which exhibit crystalline or chemical properties favorable for ice formation.[42] SH derives cumulative IN spectra, K, in units of cm^{-2}.[137] At a single temperature, K indicates the total number of ice embryos which activate at all warmer temperatures. Thus, only a specific number of IN will nucleate ice at constant temperature according to SH. This interpretation applies equally to both the immersion or deposition modes and thus, provides an overall phenomenological explanation of the heterogeneous ice nucleation process.

A modified a_{w} based homogeneous ice nucleation approach has been suggested to describe immersion freezing.[14,15] Homogeneous ice nucleation temperatures of aqueous solutions expressed as a function of a_{w} collapses to a single line, the homogeneous freezing line, as does ice melting temperatures for various solutes.[14,15] The homogeneous freezing line, independent of the nature of the solute in solution, is constructed

by imposing a horizontal shift of water activity, $\Delta a_{\mathrm{w,hom}}$, of the ice melting curve.[14] Furthermore, $\Delta a_{\mathrm{w,hom}}$ has been used to parameterize the homogeneous ice nucleation rate coefficient and thus, allowing the homogeneous ice nucleation process to be described by $\Delta a_{\mathrm{w,hom}}$ independent of the nature of the solute.[14]

Previous literature has reported that heterogeneous ice nucleation in the immersion mode can be adequately described by an IN-specific horizontal shift in a_{w} of the melting curve, $\Delta a_{\mathrm{w,het}}$, for a variety of solutes and very different types of IN.[15,35,144,166–169,305] It is important to note that prediction of heterogeneous freezing temperatures can be obtained without knowledge of thermodynamic parameters and contact angles. The application of the modified a_{w} based ice nucleation approach may imply that $\Delta a_{\mathrm{w,het}}$ holds information about the interaction of the IN surface with its surrounding aqueous environment.

In fact, a relationship between J_{het} and a_{w},[35,144] in addition to K and a_{w},[35] has been investigated. Alpert *et al.*[35] provided detailed analysis of immersion freezing due to marine diatomaceous phytoplankton cells, which have biological surfaces composed of hydrated amorphous glass, $SiO_2 \cdot nH_2O$, coated by organic material.[193,312] This study showed that intact and fragments of *T. pseudonana* immersed in aqueous NaCl droplets can be described by the modified a_{w} based heterogeneous ice nucleation approach.[15] Furthermore, a fixed $\Delta a_{\mathrm{w,het}}$ yields a constant J_{het} and K value valid for a wide range of a_{w}.[35] Additionally, Knopf and Forrester[144] observed heterogeneous ice nucleation of aqueous NaCl droplets coated by 1-nonadecanol monolayers and were able to reproduce experimentally derived J_{het} as a function of a_{w} without knowledge of solute concentration and contact angles similar to the a_{w} based homogeneous ice nucleation approach.[144]

Here, we provide analysis and quantification of the ability of two distinctly different marine microorganisms to initiate ice formation at conditions relevant to the troposphere. The differences and similarities of ice nucleation efficiencies in heterogeneous freezing involving two phytoplankton species with very different cell structures and chemical composition are presented. The first species is the marine microalga *Nannochloris atomus* which has a cell wall composed of an underlying supportive layer comprised of a network of cellulose fibrils and a gelatinous outer layer with pectin embedded in the polysaccharide matrix.[313] The second is the collolithophorid *Emiliania huxleyi*, which possess a polysaccharide-rich cell wall covered by calcified plates or coccoliths.[194,314] Heterogeneous ice nucleation in both the immersion and deposition freezing modes is determined as a function of T, wt% of NaCl, a_{w}, relative humidity (RH), and S_{ice}. A modified a_{w} based ice nucleation approach is used to describe immersion freezing temperatures. Both CNT and SH are used to derive J_{het} and K, respectively, in both the immersion and deposition mode. CNT is further employed to determine contact angles from experimental data. Estimates of ice particle production are given for both freezing modes employing the two approaches. Finally, the atmospheric implications of our findings are discussed.

6.3 Results and Discussion

6.3.1 Immersion Freezing

Median freezing temperatures of aqueous NaCl droplets containing the eukaryotic cells *N. atomus*, $T_{\mathrm{f}}^{\mathrm{ato}}$, and the coccolithophorid *E. huxleyi*, $T_{\mathrm{f}}^{\mathrm{hux}}$, are shown in Fig. 6.1 as a function of a_{w} and wt% determined at droplet preparation conditions. The droplet composition was calculated using the E-AIM model[6] and it was

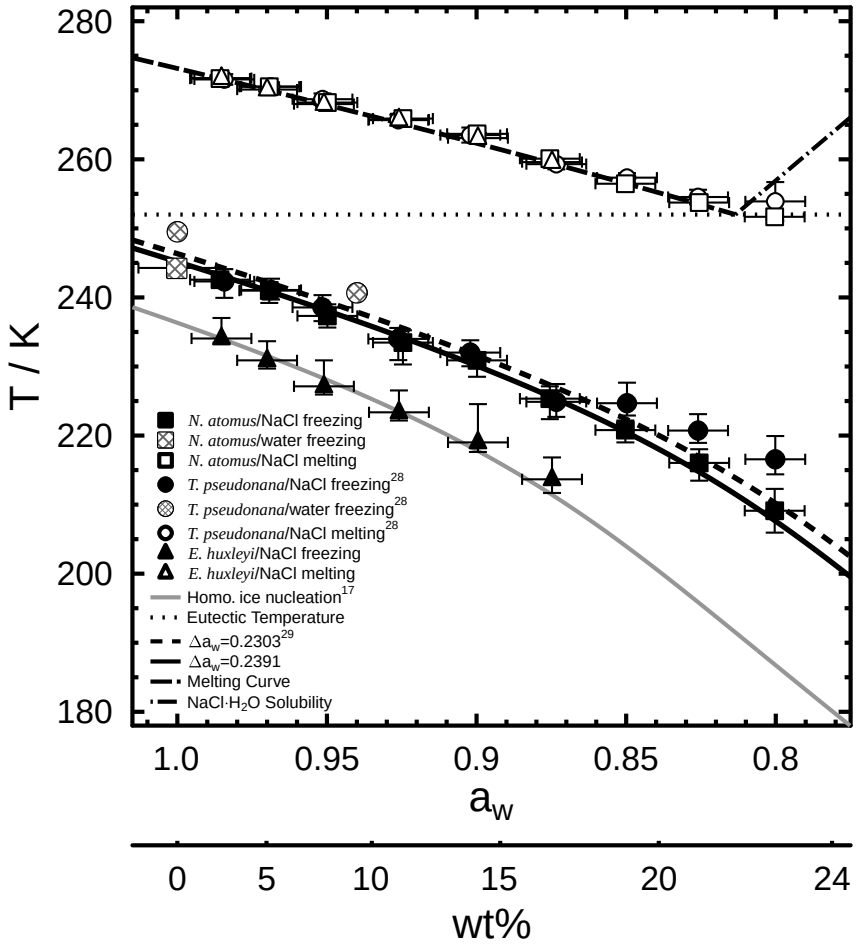

Figure 6.1: Median heterogeneous freezing temperatures and corresponding mean melting temperatures for phytoplankton cells immersed in aqueous NaCl droplets are shown as solid and open symbols, respectively, as a function of a_{w} and wt%. *N. atomus* and *E. huxleyi* are indicated by squares and triangles, respectively. Median freezing temperatures of *T. pseudonana* are shown as circles for comparison.[34,35] Hashed symbols indicate immersion freezing from Fig. 6.6. The error bars for the freezing temperatures indicate the 10^{th} and 90^{th} percentile and error bars for the melting temperatures indicate one standard deviation. Uncertainty in a_{w} is ± 0.01. The narrow dashed line represents the predicted ice melting curve.[15] The dotted and the dash-dotted lines indicate the eutectic temperature and the solid-liquid equilibrium curve of $\mathrm{NaCl} \cdot 2\mathrm{H_2O}$, respectively.[31,32] The grey line represents the predicted homogeneous freezing curve.[15] The solid and wide dotted lines represent a shift of the melting curve by $\Delta a_{\mathrm{w,het}} = 0.2391$ and 0.2303. It is assumed that a_{w} of the aqueous droplets does not change with temperature.[7,14]

assumed that a_{w} determined at the preparation conditions remains constant with decreasing T.[7,14,35] Within the experimental uncertainty, melting temperatures of aqueous NaCl droplets containing *N. atomus* and *E. huxleyi*, $T_{\mathrm{m}}^{\mathrm{ato}}$ and $T_{\mathrm{m}}^{\mathrm{hux}}$, respectively, are in good agreement with the predicted melting curve, $a_{\mathrm{w}}^{\mathrm{ice}}$.[14,15] $T_{\mathrm{f}}^{\mathrm{ato}}$ are 10 K to 25 K warmer than the homogeneous freezing curve shown in Fig. 6.1,[14] indicating that *N. atomus* can trigger heterogeneous freezing in the immersion mode. In contrast, $T_{\mathrm{f}}^{\mathrm{hux}}$ are similar to the homogeneous freezing limit which indicate that *E. huxleyi* are not efficient IN. $T_{\mathrm{m}}^{\mathrm{ato}}$, $T_{\mathrm{f}}^{\mathrm{ato}}$, $T_{\mathrm{m}}^{\mathrm{hux}}$, and $T_{\mathrm{f}}^{\mathrm{hux}}$ are given in Table 7, in addition to corresponding S_{ice}.

In addition to cell preparations for immersion freezing experiments, droplet samples were prepared using

suspensions from the same phytoplankton cultures filtered through a 0.1 μ m nuclepore filter to remove any intact or fragmented cells. Homogeneous ice nucleation occurred for all filtered droplet samples indicating that the phytoplankton acted as ice nuclei and not any other dissolved organic material associated with the cells.

Previous studies suggest that heterogeneous immersion freezing can be described by a horizontal shift of the ice melting curve as a function of water activity, $\Delta a_{\mathrm{w,het}}$.[14,15] The freezing curve, $a_{\mathrm{w}}^{\mathrm{f,het}}$, indicated in Fig. 6.1, is constructed by fitting $T_{\mathrm{f}}^{\mathrm{ato}}$ to the following equation,

$$a_{\mathrm{w}}^{\mathrm{f,het}}(T) = a_{\mathrm{w}}^{\mathrm{ice}}(T) + \Delta a_{\mathrm{w,het}} \tag{36}$$

where $\Delta a_{\mathrm{w,het}}$ is the only free parameter. The best fit yields $\Delta a_{\mathrm{w,het}}^{\mathrm{ato}} = 0.2391$ and shows good agreement with $T_{\mathrm{f}}^{\mathrm{ato}}$. Heterogeneous freezing points of the diatom *T. pseudonana*, $T_{\mathrm{f}}^{\mathrm{pse}}$, are shown in Fig. 6.1 for comparison.[34] Similar to *N. atomus*, $T_{\mathrm{f}}^{\mathrm{pse}}$ can also be described by the single parameter $\Delta a_{\mathrm{w,het}}^{\mathrm{pse}} = 0.2303$ indicated in Fig. 6.1. The deviations of $T_{\mathrm{f}}^{\mathrm{pse}}$ from predictions may be due to changes in a_{w} in the supercooled temperature region.[34,35] This effect may be enhanced at high NaCl concentrations, but also due to the presence of insoluble biogenic organic material.[34,35] These finding support a modified a_{w} approach[15] to describe and predict immersion freezing temperatures due to the presence of marine biogenic surfaces from different phytoplankton cells which have organic and siliceous-organic cell walls.

Observation of individual heterogeneous freezing events allows us to acquire data to generate immersion freezing event probability density histograms and cumulative distributions (see Fig. 6.2). We find that the freezing event distributions for *N. atomus* closely resemble those of heterogeneous and homogeneous freezing of micrometer sized aqueous NaCl droplets with and without diatoms.[35]

Table 7: Summary of immersion freezing parameters derived at median freezing temperatures for *N. atomus*, *E. huxleyi*, and *T. pseudonana*.

a_{w}	0.98	0.97	0.95	0.93	0.90	0.87	0.85	0.83	0.80
$T_{\mathrm{f}}^{\mathrm{pse}}$ / K	242.3	241.1	238.6	234.0	232.0	224.9	224.7	220.7	216.6
$T_{\mathrm{m}}^{\mathrm{pse}}$ / K	271.6	270.5	268.7	265.7	263.5	259.3	257.3	254.5	253.9
$S_{\mathrm{ice}}(T_{\mathrm{f}}^{\mathrm{pse}})$	1.33	1.32	1.33	1.35	1.34	1.38	1.35	1.35	1.35
$J_{\mathrm{het}}(T_{\mathrm{f}}^{\mathrm{pse}}) \cdot 10^4/\mathrm{cm}^{-2}\mathrm{s}^{-1}$	1.5	0.4	1.5	0.4	0.7	0.6	2.2	0.8	1.1
$K(T_{\mathrm{f}}^{\mathrm{pse}}) \cdot 10^4/\mathrm{cm}^{-2}$	9.1	2.1	6.4	2.9	3.0	7.7	8.3	7.0	9.7
a_{w}	0.99	0.97	0.95	0.93	0.90	0.88	0.85	0.83	0.80
$T_{\mathrm{f}}^{\mathrm{ato}}$ / K	242.6	241.0	237.2	233.5	230.5	225.3	220.8	216.0	209.1
$T_{\mathrm{m}}^{\mathrm{ato}}$ / K	271.7	270.5	268.2	265.9	263.6	260.1	256.5	253.7	251.7
$S_{\mathrm{ice}}(T_{\mathrm{f}}^{\mathrm{ato}})$	1.33	1.33	1.35	1.36	1.36	1.38	1.39	1.40	1.42
$J_{\mathrm{het}}(T_{\mathrm{f}}^{\mathrm{ato}}) \cdot 10^4/\mathrm{cm}^{-2}\ \mathrm{s}^{-1}$	1.1	0.3	1.3	0.3	1.1	0.4	0.5	0.15	0.7
$K(T_{\mathrm{f}}^{\mathrm{ato}}) \cdot 10^4/\mathrm{cm}^{-2}$	4.1	2.6	6.9	4.8	3.5	2.4	2.4	2.5	7.7
a_{w}	0.99	0.97	0.95	0.93	0.90	0.88			
$T_{\mathrm{f}}^{\mathrm{hux}}$ / K	234.1	230.9	227.1	223.4	219.0	213.7			
$T_{\mathrm{m}}^{\mathrm{hux}}$ / K	271.8	270.1	268.0	265.8	263.1	259.6			
$S_{\mathrm{ice}}(T_{\mathrm{f}}^{\mathrm{hux}})$	1.44	1.46	1.48	1.48	1.49	1.50			

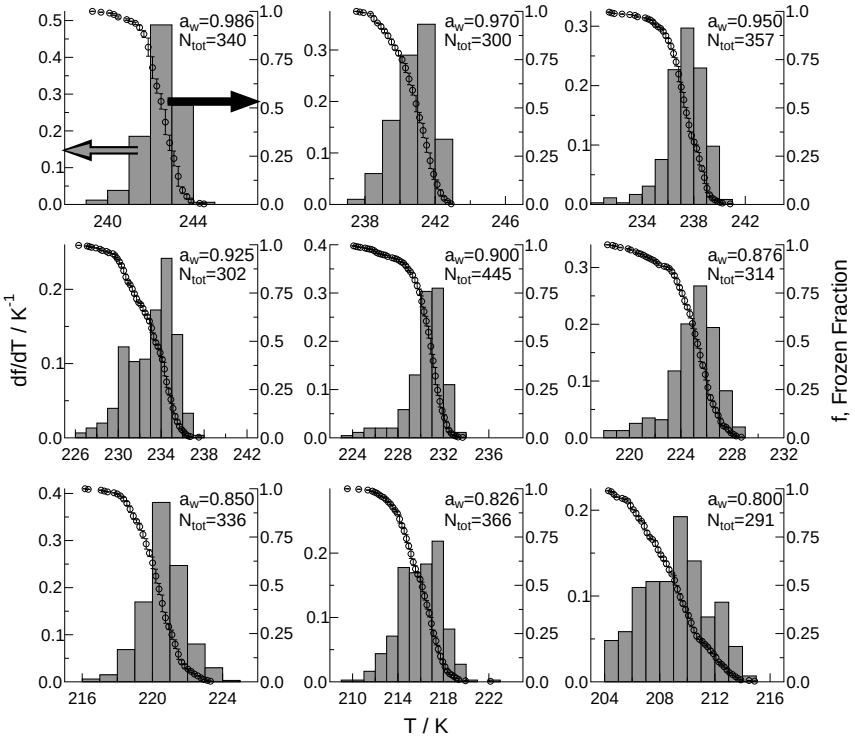

Figure 6.2: Summary of all observed immersion freezing events due to *N. atomus* cells as a function of a_{w} and T. The frozen fraction, f, of droplets in 0.2 K temperature increments is represented by black circles. Error bars indicate the range of f in a temperature increment of 0.2 K. Grey bars show the probability density histogram (PDH) binned in 1.0 K increments. For each panel, a_{w} and the total number of analysed droplets, N_{tot}, are given. The values for the PDH are given on the left y-axis and f on the right y-axis.

We quantify the heterogeneous freezing behaviour of these two particle types using two different analytical approaches. The first based on CNT, a time-dependent description of freezing events maintains that freezing events will continue to take place over time at a constant T if aqueous droplets containing IN are present.[42] The second, based on SH a time-independent description of events alternately maintains that heterogeneous ice nucleation is controlled by temperature, with a specific number of active sites which will become IN at site-specific characteristic temperatures.[42,137,256]

Time-Dependent Description

Measurements of *N. atomus* surface area and temperatures at which ice nucleation occurs allow us to derive J_{het}. The analytical approach and corresponding interpretation of J_{het} has been explained in detail previously.[35,44,127,128] Within a specific temperature interval, ΔT, different numbers of freezing events will occur. We derived $J_{\mathrm{het}}(T^i)$ as the average heterogeneous ice nucleation rate coefficient at the mean temperature, T^i, of the i^{th} temperature interval. This derivation takes advantage of all experimental data, including the data points outside of the 10^{th} and 90^{th} percentiles, using the following formula,

$$J_{\mathrm{het}}\left(T^i\right) = \frac{n^i_{\mathrm{nuc}}}{t^i_{\mathrm{tot}} \cdot A^i}. \tag{37}$$

where n^i_{nuc} and $t^i_{\mathrm{tot}} \cdot A^i$ are the number of freezing events and the product of the total observation time and

the available *N. atomus* surface area, respectively, in the i^{th} temperature interval. The product $t^i_{\text{tot}} \cdot A^i$ is the sum of the contribution from the droplets that remain liquid and those that freeze according to

$$t^i_{\text{tot}} \cdot A^i = \frac{\Delta T}{r} A^i_{\text{rm}} + \sum_{j=1}^{n^i_{\text{nuc}}} \frac{1}{r} \left(T^i_{\text{st}} - T^i_{\text{nuc},j} \right) A^i_j, \tag{38}$$

where r is the experimental cooling rate, A^i_{rm} is the total surface area remaining until the end of the temperature interval, T^i_{st} is the start of the temperature interval, and $T^i_{\text{nuc},j}$ and A^i_j are the freezing temperature and corresponding cell surface area, respectively, of the j^{th} droplet nucleating ice within the i^{th} interval. Derivations of $J_{\text{het}}(T^i)$ employ $\Delta T = 0.2$ K (representing a time interval of 1.2 s employing $r = 10$ K min^{-1}) corresponding to our total experimental error in determining the temperature. The time required for a single nucleation event to occur within the i^{th} interval is given by $(T^i_{\text{st}} - T^i_{\text{nuc},j})/r$, where $(T^i_{\text{st}} - T^i_{\text{nuc},j}) \leq T$.

Figure 6.3a shows experimentally derived J_{het} for *N. atomus* immersed in aqueous NaCl droplets as a function of T and initial a_{w}. J_{het} has a strong dependence on T and a_{w}. At a constant a_{w} value, J_{het} increases by approximately 4 orders of magnitude over a range of 10 and 20 K for dilute and concentrated aqueous NaCl solution droplets containing *N. atomus*, respectively. At a constant T, J_{het} increases about 4 orders of magnitude over a change in a_{w} of 0.075 at higher T and 0.05 at lower T. A summary of J_{het} evaluated at $T^{\text{ato}}_{\text{f}}$ are given in Table 7. $J_{\text{het}}(T^{\text{ato}}_{\text{f}})$ averages $6.44^{+6.67}_{-4.92} \cdot 10^3$ cm^{-2} s^{-1}, where the plus and minus errors indicate the range. The range in $J_{\text{het}}(T^{\text{ato}}_{\text{f}})$ is narrow which indicates that the shifted $a^{\text{ice}}_{\text{w}}$ curve shown in Fig. 6.1 is representative of our averaged J_{het} value. A shift of $\Delta a^{\text{ato}}_{\text{w,het}} = 0.2391$ can therefore describe heterogeneous ice nucleation temperatures of *N. atomus* via immersion freezing and be assigned a value of $J_{\text{het}} = 6.44 \cdot 10^3$ cm^{-2} s^{-1}.

CNT uses the contact angle, α, to describe heterogeneous ice nucleation. α is a parameter that characterizes the interfacial energies between the IN, aqueous solution, and the ice embryo. The compatibility factor, f_{het}, depends on α and describes the reduction in the free energy of formation for an ice embryo according to $f_{\text{het}}(m) = (m^3 - 3m + 2)/4$, where $m = \cos(\alpha)$ and assuming that the curvature of the IN surface is much larger than that of the ice embryo.[42,133,134,315] f_{het} can be calculated from experimental data from

$$J_{\text{het}}(T) = \frac{k_{\text{b}} T}{h} \exp\left(-\frac{\Delta F(T)}{k_{\text{b}} T} \right) n_{\text{s}} \exp\left(-\frac{\Delta G(T)}{k_{\text{b}} T} f_{\text{het}} \right), \tag{39}$$

where k_{b} is the Boltzmann constant, h is Planck's constant and n_{s} is the number density of water molecules at the IN-water interface.[42] $\Delta F(T)$ and $\Delta G(T)$ are the diffusion activation energy and Gibb's free energy of formation, respectively, of an ice embryo for homogeneous ice nucleation. The fractional reduction in $\Delta G(T)$ due to an IN is described by f_{het}, where $0 < f_{\text{het}} < 1$.

Derivations of ΔF in eqn (39) depend on the diffusivity of water in aqueous solution, $D_{\text{H}_2\text{O}}$. For the temperature range and aqueous NaCl concentration investigated here for immersion freezing of *N. atomus*, $D(T)^{\text{NaCl}}_{\text{H}_2\text{O}}$ is unavailable. We therefore utilize the results of the molecular dynamics study by Kim and Yethiraj[36] who derive the ratio $f_{\text{D}} = D^{\text{NaCl}}_{\text{H}_2\text{O}} / D^{\circ}_{\text{H}_2\text{O}}$ for various NaCl concentrations as low as 260 K.[36] The diffusivity of pure water as a function of T, $D(T)^{\circ}_{\text{H}_2\text{O}}$, is taken from Smith and Kay[130] and for a fixed

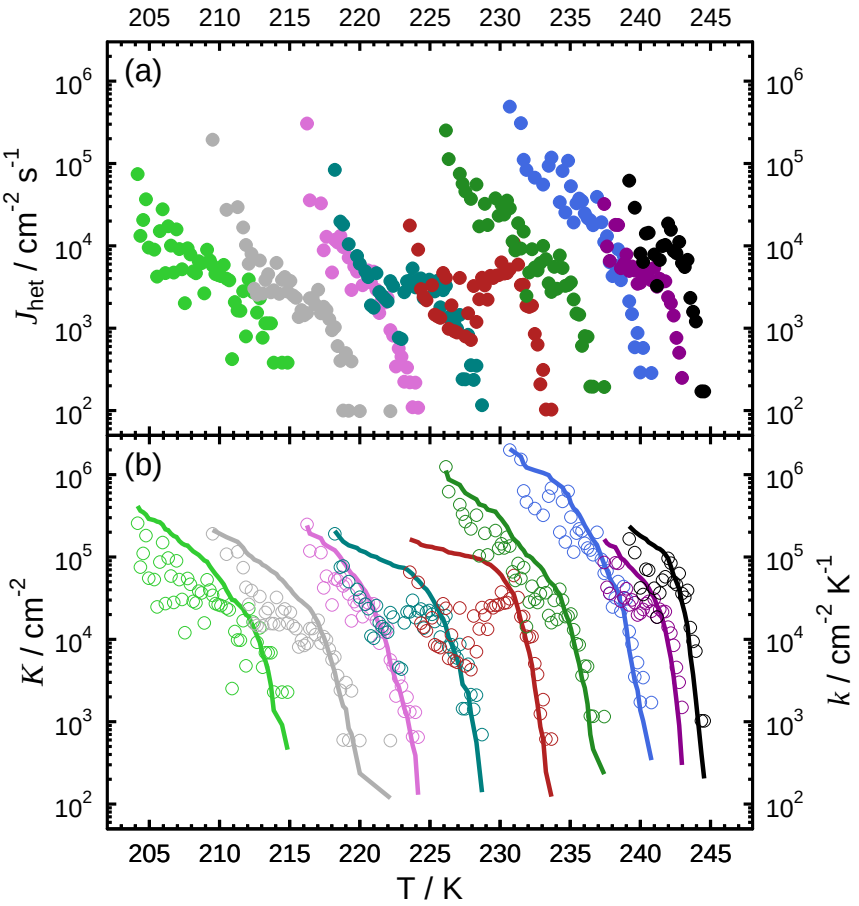

Figure 6.3: Experimentally derived (a) heterogeneous ice nucleation rate coefficients, J_{het}, and (b) differential and cumulative ice nuclei spectra, k and K, respectively, for *N. atomus* immersed in aqueous NaCl droplets shown as a function of T and a_w. In (b), k and K are given as open circles and lines, respectively. Black, purple, blue, green, red, teal, magenta, grey, and lime colors correspond to a a_w of 0.986, 0.970, 0.950, 0.925, 0.900, 0.876, 0.850, 0.826, and 0.800.

aqueous NaCl concentration, we fit f_D to a quadratic function in T.[144] In Fig. 6.4, we provide $D(T)^{NaCl}_{H_2O}$ for the range of freezing temperatures for aqueous NaCl droplets with and without *N. atomus*. $\Delta F(T)$ based on a previous derivation,[316] can then be calculated according to

$$\Delta F(T) = \frac{d\ln\left[D^{\circ}_{H_2O}(T) f_D\right]}{dT} k_b T, \tag{40}$$

and used in eqn (39) for the calculation of α. It should be noted that the extrapolation to lower temperatures may introduce uncertainties when applied to CNT because of the unknown behaviour of $D(T)^{NaCl}_{H_2O}$ at greater supercoolings than previously investigated.[36] However, this is expected to be negligible because the contribution of the error from further scaling the derivative of a monotonically decreasing function, as is the natural logarithm of $D(T)^{NaCl}_{H_2O}$ in eqn (40), is insignificant compared to our experimental uncertainty in a_w.

Derivations of $\Delta G(T)$ in eqn (39) depend on the interfacial energy between the ice embryo and aqueous

solution, $\sigma_{\mathrm{i/l}}$. According to CNT,[42,133]

$$\Delta G(T) = \frac{16\pi}{3} \frac{\nu^2(T)\sigma^3_{\mathrm{i/l}}(T)}{[k_{\mathrm{b}}T \ln S_{\mathrm{ice}}(T)]^2}, \tag{41}$$

where $\nu(T)$ is the volume of a water molecule in ice.[128] We calculate $\sigma_{\mathrm{i/l}}(T, a_{\mathrm{w}})$ by setting $f_{\mathrm{het}} = 1$ in eqn (39), using homogeneous ice nucleation rate coefficients, $J_{\mathrm{hom}}(T, a_{\mathrm{w}})$, from the a_{w} based homogeneous ice nucleation approach,[14,15] employing $D^{\mathrm{NaCl}}_{\mathrm{H_2O}}$ as described above[36], and replacing n_{s} for n_{v} which describes the volume number density of water molecules in liquid water. The resulting σ values are applied to calculate α for heterogeneous ice nucleation. In eqn (39), n_{s} and n_{v} have been corrected for NaCl concentration in solution and vary between $1.0 \cdot 10^{15} - 9.7 \cdot 10^{14}$ cm^{-2} and $3.3 \cdot 10^{22} - 3.0 \cdot 10^{22}$ cm^{-3}, respectively, calculated using the E-AIM model at 298.15 K.[6] Figure 6.3 gives $\sigma_{\mathrm{i/l}}$ in the range of T and a_{w} for homogeneous and heterogeneous freezing.

We derive α from experimentally derived J_{het} from Fig. 6.3a and using eqn (39)-(41). α as a function of T and S_{ice} for all experimentally observed freezing temperatures due to *N. atomus* is given in Fig. 6.5a and b, respectively. Also included in Fig. 6.5 are α for marine diatoms acting as IN in the immersion mode calculated from data taken from Knopf *et al.*[34] and Alpert *et al.*[35] The error on the contact angles derived here range from $\pm 2.1°$ and $\pm 4.3°$ for a range of S_{ice} of $1.25 - 1.45$. The error in α is predominantly due to an error of

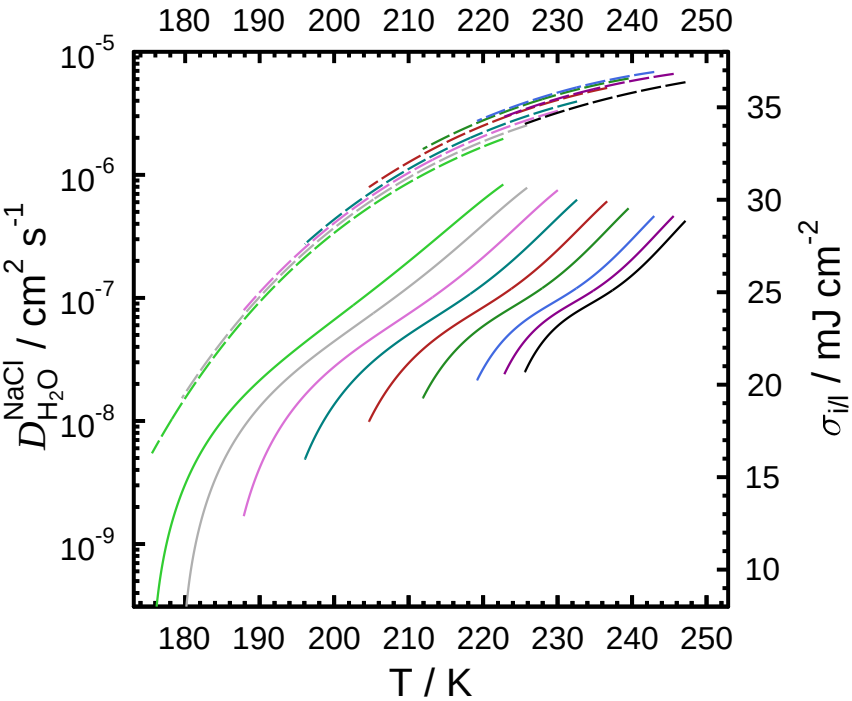

Figure 6.4: Thermodynamic variables employed in calculations of contact angles. In aqueous NaCl solution, the water diffusion coefficient, $D^{\mathrm{NaCl}}_{\mathrm{H_2O}}$, is given as dashed lines and the interfacial energy of ice, $\sigma_{\mathrm{i/l}}$, is given by solid lines as a function of T and a_{w}. $D^{\mathrm{NaCl}}_{\mathrm{H_2O}}$ is derived from Kim and Yethiraj[36] and extrapolated to lower T. $\sigma^{\mathrm{NaCl}}_{\mathrm{i/l}}$ is derived from theoretical homogeneous ice nucleation rate coefficients[14] and employs $D^{\mathrm{NaCl}}_{\mathrm{H_2O}}$. Black, purple, blue, green, red, teal, magenta, grey, and lime colors correspond to a a_{w} of 0.986, 0.970, 0.950, 0.925, 0.900, 0.876, 0.850, 0.826, and 0.800.

± 0.01 in a_w and to a lesser extent due to the uncertainty in J_{het}. At a constant a_w, α for *T. pseudonana* and *N. atomus* increases with decreasing T in Fig. 6.5a and increasing S_{ice} in Fig. 6.5b. At constant T or S_{ice}, α increases with increasing a_w. Thus, α is strongly dependent on both T and a_w. For $a_w > 0.85$, α largely overlaps for both *T. pseudonana* and *N. atomus*. For $a_w \leq 0.85$, however, differences in α are significant between the two phytoplankton species which reflects the differences in ice nucleation temperatures and J_{het}. The dependence of α on a_w, S_{ice}, and T is not surprising when looking at the definition of α according to Young's equation, which indicates that α depends on the interfacial surface energies between the ice nucleus and ice, ice nucleus and aqueous solution, and ice and aqueous solution.[42] Decreasing the temperature of a liquid, usually results in an increase in surface tension[317] as well as the addition of salts such as NaCl,[144] here expressed as a_w. Thus, α must change with changes in thermodynamic conditions expressed as a_w, S_{ice}, or T.

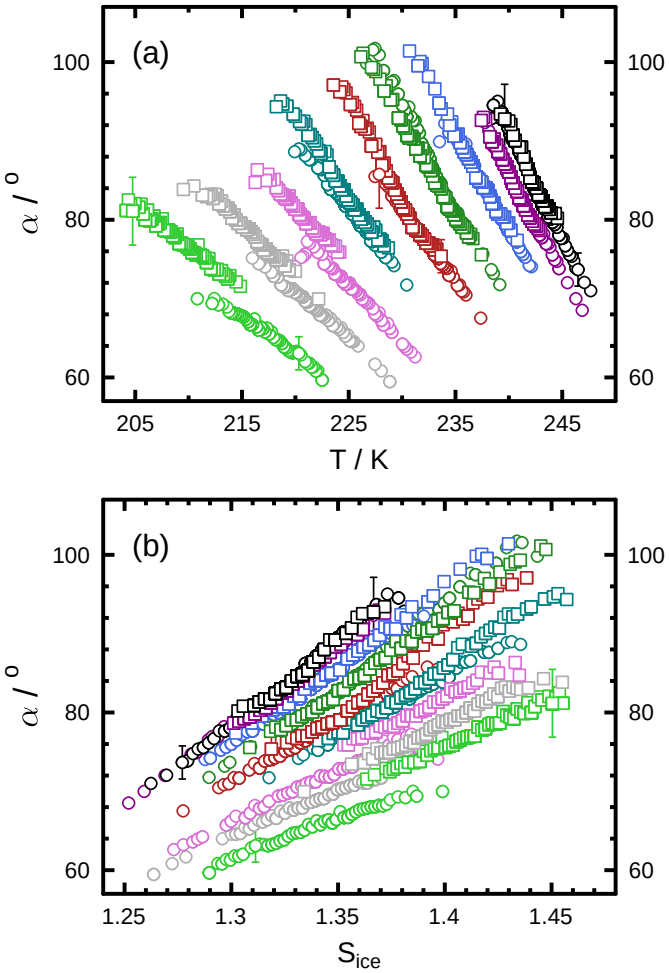

Figure 6.5: Contact angles, α, calculated from experimentally derived J_{het} (a) as a function of T and (b) as a function of S_{ice}. Squares represent α for *N. atomus* immersed in aqueous NaCl droplets. α for *T. pseudonana* are plotted as circles calculated for droplet freezing data taken from Knopf *et al.*[34] and Alpert *et al.*[35] Black, purple, blue, green, red, teal, magenta, grey, and lime colors correspond to a a_w of 0.986, 0.970, 0.950, 0.925, 0.900, 0.876, 0.850, 0.826, and 0.800.

Time-Independent Approach

We derive differential and cumulative ice nuclei spectra to quantify a time-independent description for explaining heterogeneous ice nucleation due to *N. atomus*. The differential ice nuclei spectra for the i^{th} temperature interval, $k(T^i)$, is defined as the ice active surface site density for a unit surface area according to

$$k(T^i) = \frac{1}{A^i_{\text{tot}}} \frac{n^i_{\text{nuc}}}{\Delta T}, \tag{42}$$

where A^i_{tot} is the total *N. atomus* surface area in the droplets that remains liquid at the start of the i^{th} temperature interval, and n^i_{nuc} is the number of freezing events in the i^{th} temperature interval.[137] A cumulative ice nuclei spectrum as a function of temperature, $K(T^i)$, is derived from experimental data by numerically integrating eqn (42) from $T^{\text{ato}}_{\text{m}}$ to T^i yielding

$$K(T^i) = \sum_{T^{\text{pse}}_{\text{m}}}^{T_i} \frac{n^i_{\text{nuc}}}{A^i_{\text{tot}}}, \tag{43}$$

where $K(T^i)$ includes the sites which had become ice active for temperatures warmer than T^i. Derivations of k and K employ $\Delta T = 0.2$ K.

Figure 6.3b presents k and K for all individually analysed ice nucleation events as a function of T and a_{w}. Figure 6.3b demonstrates that k for most data increases exponentially with decreasing T. As previously described, k is the differential spectrum for K and thus it follows from eqn (42) and (43) that $k = dK/dT$. k shows a general exponential dependence and therefore, K should also exponentially depend on T for ice nucleation events. At all a_{w} values, however, K additionally experiences a decrease in slope with decreasing temperature. This could be due to different characteristics of sites that become active more gradually with decreasing temperature. At constant a_{w}, K increases by 4 orders of magnitude for a change in T of about 10 and 15 K at more dilute and concentrated solutions, respectively. At constant T, K changes by 4 orders of magnitude for a change in a_{w} by about $0.05 - 0.075$. A summary of K evaluated at $T^{\text{ato}}_{\text{f}}$ is given in Table 7 for all a_{w} values. The average value of $K(T^{\text{ato}}_{\text{f}}) = 4.10^{+3.62}_{-1.74} \cdot 10^4$ cm^{-2} where the plus and minus errors indicate the range of the data. The range in $K(T^{\text{ato}}_{\text{f}})$ is narrow and indicates that the shifted a^{i}_{w} curve shown in Fig. 6.1 is representative of this K value and can be assigned to $\Delta a^{\text{ato}}_{\text{w,het}} = 0.2391$. This implies that K may also be parameterized by $\Delta a^{\text{ato}}_{\text{w,het}}$.

6.3.2 Deposition Freezing

Figure 6.6 shows onset deposition freezing conditions for intact and fragmented *N. atomus* and *E. huxleyi* cells as a function of T and S_{ice}. Deposition freezing involving the diatom *T. pseudonana* is shown for comparison.[34] Average values of onset S_{ice} and RH are also indicated in Fig. 6.6 and provided in Table 8. *N. atomus* can initiate the ice phase via deposition mode below 240 K at $S_{\text{ice}} > 1.21$. At 245 K, *N. atomus* take up water slightly below water saturation and subsequently freeze via immersion mode. Immersion freezing from Fig. 6.6 is indicated in Fig. 6.1. Water uptake without subsequent immersion freezing can occur below

water saturation for *N. atomus* for temperatures higher than $T = 250$ K and RH $> 85.8\%$. *E. huxleyi* are able to nucleate ice in the deposition mode with similar efficiency to *N. atomus*, in stark contrast with their poor ice nucleation ability in the immersion mode. Deposition freezing onsets for *E. huxleyi* occurred at $S_{\mathrm{ice}} > 1.19$ for $T < 250$ K. The IN activated fraction of *N. atomus*, *E. huxleyi*, and *T. pseudonana*, range from $(0.05 - 0.44)\%$, $(0.04 - 0.13)\%$, and $(0.02 - 0.31)\%$, respectively, and are determined from the minimum and maximum value of the ratio between the number of ice nucleation events and the number of deposited particles per sample. Heterogeneous freezing of *N. atomus* and *E. huxleyi* largely overlap observations of heterogeneous freezing of *T. pseudonana*[34] for $T < 240$ K indicating similar ice nucleation behaviour in the deposition mode. Average onset S_{ice} for deposition freezing decreases with increasing T for all three phytoplankton species. Above 240 K, differences in ice nucleation behaviour appears between the phytoplankton species. Water uptake and immersion freezing occurs for *N. atomus* at 245 K, and for higher T, only water uptake was observed. *T. pseudonana* are able to act as an IN via immersion freezing until 250 K, and for higher T, only water uptake is observed. *E. huxleyi* does not nucleate ice via immersion

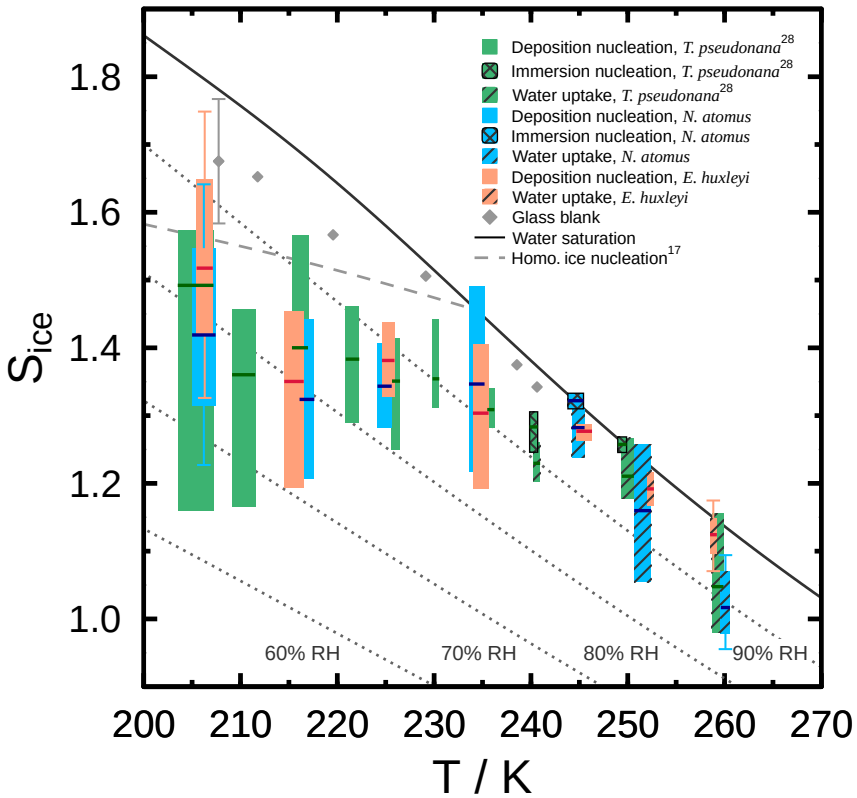

Figure 6.6: Deposition and immersion ice nucleation and water uptake of *N. atomus* and *E. huxleyi* as a function of T and S_{ice}. Blue and orange bars represent *N. atomus* and *E. huxleyi*, respectively. *T. pseudonana* freezing and water uptake data taken from Knopf *et al.*[34] is plotted in green for comparison. The range in ice nucleation onset conditions for deposition, water uptake, and immersion freezing is indicated by solid, single-hashed, and double-hashed bars, respectively. Horizontal lines within the bars indicate average ice nucleation onset conditions with respect S_{ice}. Ice formation on blank hydrophobic sample substrates are indicated by grey diamonds. The solid black line indicates water saturation, and dotted lines indicate lines of constant RH. The grey dashed line indicates the homogeneous freezing limit corresponding to a homogeneous ice nucleation rate coefficient of about $5 \cdot 10^9$ cm^{-3} s^{-1}.

Table 8: Summary of average ice nucleation onset conditions for *N. atomus*, *E. huxleyi*, and *T. pseudonana*.

	Deposition Freezing			**Immersion Freezing**			**Water Uptake**		
Phytoplankton Type	T/K	S_{ice}	RH/%	T/K	S_{ice}	RH/%	T/K	S_{ice}	RH/%
N. atomus	206.7	141.9	79.2	244.3	133.4	100.3	244.9	128.2	97.4
	215.7	132.4	78.1				251.0	116.0	93.4
	225.3	134.3	85.2				260.1	101.7	89.6
	234.9	134.7	92.0						
E. huxleyi	206.4	151.8	84.5	N/A	N/A	N/A	252.2	119.2	97.2
	215.3	135.0	79.5				258.9	112.4	97.8
	225.3	138.1	79.5						
	235.0	130.4	90.0						
	245.1	134.7	92.9						
T. pseudonana	204.5	149.2	82.1	240.7	128.3	93.6	241.1	123.0	90.0
	210.9	136.0	77.8	249.7	127.9	101.7	250.3	121.1	96.8
	216.0	140.0	82.8				259.5	104.8	91.6
	221.4	138.8	85.1						
	226.0	135.1	86.2						
	230.5	135.4	88.2						
	236.0	130.9	91.2						

freezing, but nucleates ice via deposition ice nucleation at 245 K, and for higher T only water uptake is observed. These results indicate that markedly different biological surfaces have both comparable and contrasting effects on ice nucleation behaviour depending on the presence of the aqueous phase, and the extent of supercooling and water vapour supersaturation.

Deposition freezing due to *N. atomus* and *E. huxleyi* can be quantified following CNT and SH described above. However, for deposition freezing, the ice embryo that forms on the IN surface is surrounded by a supersaturated water vapour parent phase and not an aqueous solution like for immersion freezing. The rationale for the two approaches is otherwise the same.

Time-Dependent Description

Measurements of the surface areas of *N. atomus* and *E. huxleyi* allow us to derive J_{het} as a function of T. The approach and interpretation of J_{het} is the same with the exception of the product $t^i_{\mathrm{tot}} \cdot A^i$ given by eqn (38) is the sum of the contributions from the dry cells that did not nucleate ice and those that did, where $T^i_{\mathrm{nuc},j}$ and A^i_j are the freezing temperature and corresponding surface area, respectively, of the j^{th} sample to nucleate ice within the i^{th} interval. Derivations of $J_{\mathrm{het}}(T^i)$ via deposition freezing employ $\Delta T = 0.02$ K (representing a time interval of 12 s employing $r = 0.1$ K min^{-1}) corresponding to the temperature difference between two consecutive recorded images during cooling of the sample.

Figure 6.7a shows experimentally derived J_{het} for *N. atomus*, *E. huxleyi*, and *T. pseudonana*[34] as a function of T for deposition ice nucleation at a constant T_{dew}. J_{het} has a strong dependence on T, i. e. J_{het} increases by about 3 orders of magnitude over 2 K range in T. Figure 6.7a indicates that J_{het} is similar for all three phytoplankton species, despite their vastly different cell walls on which ice nucleates. This reflects their similar deposition ice nucleation efficiency shown in Fig. 6.6. The range of J_{het} for some

phytoplankton groups at a common T appear larger or smaller than for other species due to the surface area between particle samples. The surface area of *N. atomus*, *E. huxleyi*, and *T. pseudonana* samples range from $(0.25 - 2.66) \cdot 10^{-3}$ cm^2, $(0.50 - 2.31) \cdot 10^{-3}$ cm^2, and $(0.03 - 6.10) \cdot 10^{-3}$ cm^2, respectively.

The experimental derivations of J_{het} allow for the calculation of α following CNT. In the deposition mode, α characterizes the interfacial energies between the IN, the ice embryo, and the supersaturated water vapour phase. As a result, the equation used to derive α in the immersion mode must be modified. α is still derived from f_{het}, however, J_{het} for deposition freezing is given by

$$J_{\text{het}}(T) = A \cdot \exp\left(-\frac{\Delta G(T)}{k_{\text{b}} T} f_{\text{het}}\right), \tag{44}$$

where A is the kinetic coefficient defined as the rate at which a critical ice embryo gains one molecule from the vapour phase.[134,136] $\Delta G(T)$ for deposition freezing depends on the interfacial energy between the ice

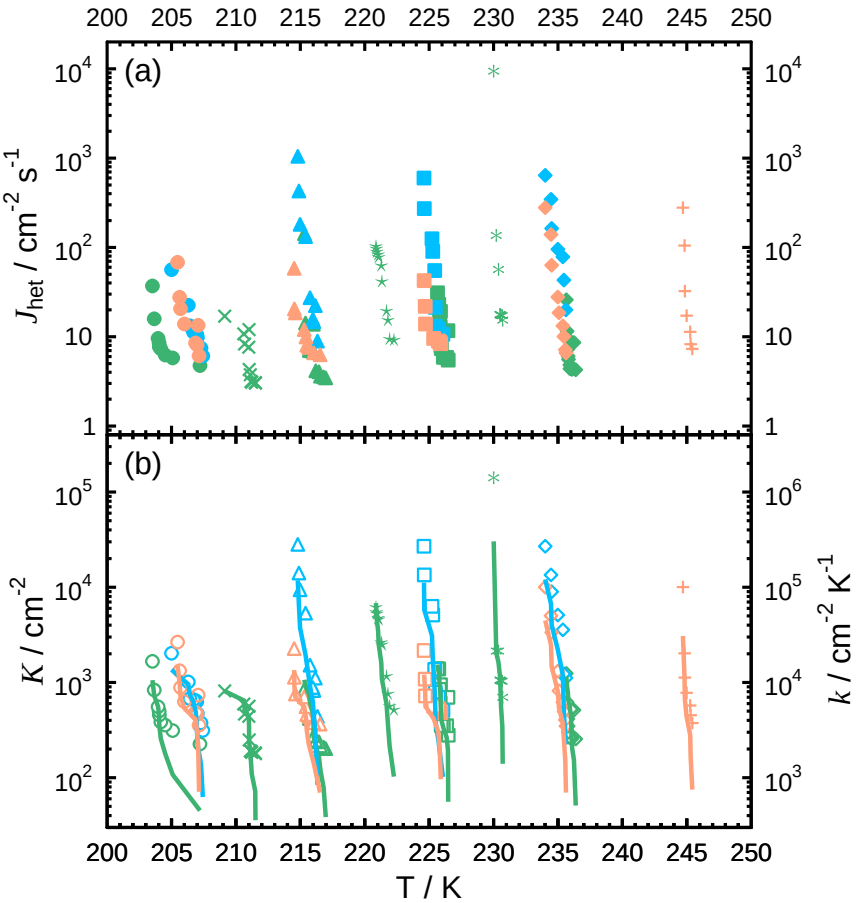

Figure 6.7: Experimentally derived (a) heterogeneous ice nucleation rate coefficients, J_{het}, and (b) differential and cumulative ice nuclei spectra, k and K, respectively, for *N. atomus*, *E. huxleyi*, and *T. pseudonana* in the deposition mode shown as a function of T. Blue, orange, and green colors represent *N. atomus*, *E. huxleyi*, and *T. pseudonana*, respectively. In (b), k and K are given as symbols and lines, respectively. Ice nucleation experiments conducted at a constant dew point are indicated by the same symbol.

embryo and supersaturated water vapour phase, $\sigma_{i/v}$. As a result, $\sigma_{i/v}$ is substituted for $\sigma_{i/l}$ in eqn (41). α can be calculated from experimentally derived J_{het} assuming constant values $A = 10^{25}$ cm^{-2} s^{-1},[134,135] and $\sigma_{i/v} = 106$ mJ m^{-2}.[42,136]

Figure 6.8 shows α as a function of T and S_{ice} for all experimentally observed onsets for deposition freezing due to *N. atomus* and *E. huxleyi*. α for *T. pseudonana* acting as IN in the deposition mode are also given in Fig. 6.8 obtained from Knopf *et al.*[34] The uncertainty in α is primarily due to the uncertainty in S_{ice} and conservatively estimated to be between $\pm 2°$ to $\pm 3°$ depending on the onset conditions of T and S_{ice}.[37] Figure 6.8a indicates that α varies greatly with T, due to the range of ice onset conditions. For

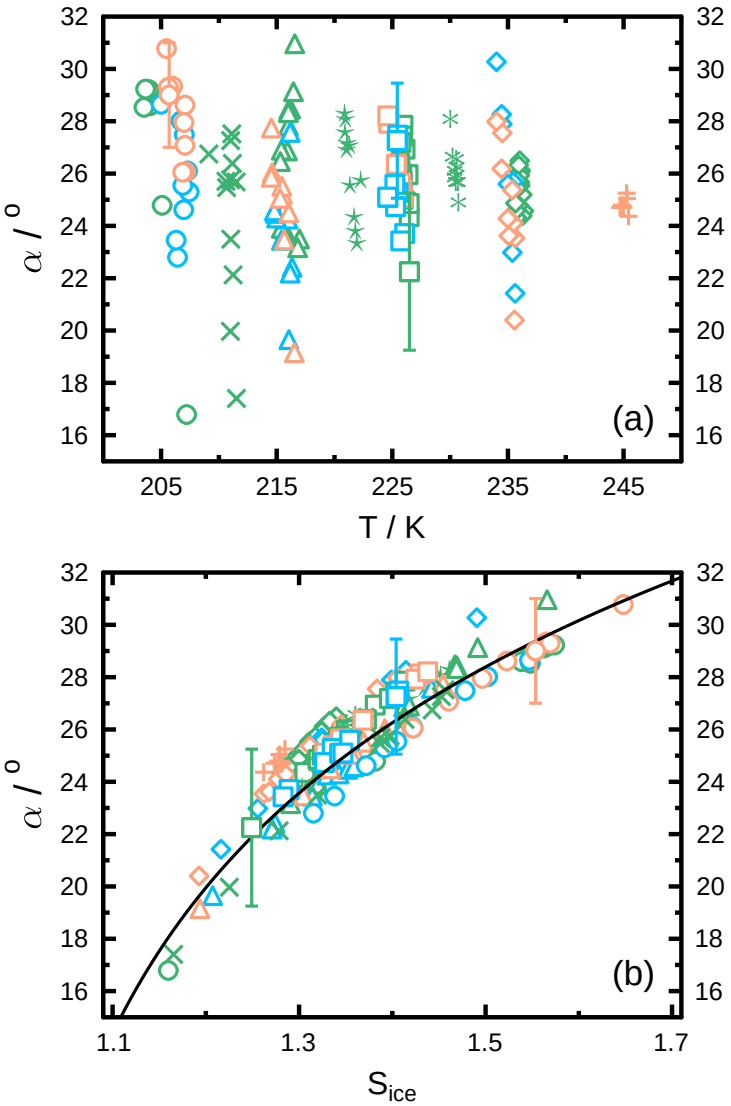

Figure 6.8: Contact angles, α, calculated from experimentally derived J_{het} for deposition freezing as a function of T in (a) and as a function of S_{ice} in (b). Blue, orange, and green colors represent *N. atomus*, *E. huxleyi*, and *T. pseudonana*, respectively. Ice nucleation experiments conducted at a constant dew point are indicated by the same symbol. The solid line in (b) represents the parameterization of Wang and Knopf[37].

constant T_{dew}, α increases as T decreases. When plotted as a function of S_{ice}, however, α becomes a compact distribution of points with a clear trend as shown in Fig. 6.8b. For all phytoplankton species, α tends to increase with increasing S_{ice}. Wang and Knopf[37] proposed a parameterization of α as a function of S_{ice} valid for a wide range of insoluble organic and inorganic particle types. This parameterization is depicted in Fig. 6.8b and is, within our uncertainty, in agreement with α calculated for the three phytoplankton types. The fact that α calculated from many different particle types fit to a single curve is remarkable, however, further studies are required to investigate and explain the thermodynamic dependence on α.[37]

Time-Independent Description

The approach and interpretation of k and K for deposition freezing are the same as described above for immersion freezing. We derive k and K according to eqn (42) and (43), where A^i_{tot} here is the total available dry cell surface area. These derivations for deposition freezing employ $\Delta T = 0.02$ K.

Figure 6.7b presents k and K for all individually analysed ice nucleation events as a function of T observed at different experimental T_{dew}. Figure 6.3b demonstrates that k and K have a strong dependence on temperature. K increases by about 2 orders of magnitude over a 2 K range in T. For *N. atomus*, *E. huxleyi*, and *T. pseudonana*, K is similar indicating that active sites on any of the three phytoplankters occurs at similar temperatures and for similar surface area densities. Derivations of k and K following SH may indicate an exponential dependence on the appearance of ice active sites as T decreases. The range in K observed is different for different cell types, which is due to different particle surface areas in each sample.

6.4 Conclusions

6.4.1 Dependence of Heterogeneous Ice Nucleation on Thermodynamic Parameters

Our results on the efficient ice nucleation ability of two phytoplankton species, *N. atomus* and *E. huxleyi* via immersion and deposition freezing, has been analysed according to the modified a_{w} based ice nucleation theory, CNT, and SH approach. Although the experiments were not designed to test the time dependency of the underlying nucleation process, our analysis of the freezing data covering a large number of freezing events and ranges in a_{w} or S_{ice} yields insight with regard to the applied approaches. The potential for thermodynamic variables, T, a_{w}, and S_{ice} to describe the ice nucleation efficiencies of investigated phytoplankton by these three approaches has been quantified. Immersion freezing temperatures can be well described by a_{w} similar to previous studies.[15,34,35,166–168,252] Following CNT, we show that for immersion freezing, T and a_{w} both lead to alterations in α. For deposition freezing we observe a similar effect, although, we note that α can be adequately described by S_{ice}. This behaviour could be expected since α depends on the surface tensions of the three involved phases according to Young's equation[42] which in turn depend on either solution composition (a_{w}) or water vapour (S_{ice}) and T. According to the SH approach, derived $K(T)$ for immersion freezing from aqueous solutions with constant a_{w} shows two distinct exponential slopes indicating two different kinds of ice active sites on particle surfaces becoming active at different temperatures. In addition, these sites become ice active at very different temperatures when a_{w} of the aqueous phase is varied, thus further indicating that thermodynamic variables are the governing factor for the underlying ice nucleation mechanism. For deposition freezing, a similar conclusion is reached in that the number of ice active sites

strongly depends on T and S_{ice}. These dependencies cannot be resolved by the SH approach since the characteristics of ice active sites are not fundamentally defined, in contrast to CNT employing the concept of a contact angle. Recent publications suggest that freezing distributions can be modelled by imposing a IN population with each IN possessing ice nucleation efficiencies sampled from a statistical distribution of active sites.[142,146,311] These studies, however, do not account for any dependence of active sites on thermodynamic variables as shown in Figs. 6.3 and 6.7. Further studies are required to develop empirical parameterization of active site distributions which dependent on T, a_{w} and S_{ice} to characterize the heterogeneous ice nucleation process.

6.4.2 Marine Biogenic Ice Nucleation

Thalassiosira pseudonana and *N. atomus* have similar ice nucleating efficiencies in the immersion mode (Fig. 6.1). This is in spite of the fact that these two organisms have vastly different cell wall structures. The biomineral cell wall of the diatom is composed of organic coated hydrated amorphous silica, $SiO_2{\cdot}nH_2O$[193,312] supplemented with proteins and polysaccharides which together provide for a rigid structure.[313] *Nannochloris atomus* in contrast, has only an organic layered cell wall comprised of cellulose and other polysaccharides.[313] The enhanced freezing temperatures due to *T. pseudonana* and *N. atomus* implies that organic material associated with a range of phytoplankton groups may likely efficiently nucleate ice in the immersion mode. *E. huxleyi*, which do not enhance ice nucleation above the homogenous freezing limit in the immersion mode, have a polysaccharide rich cell wall, but no organic material associated with their outer layer of calcitic coccoliths or plates.[194,314] Although we studied biogenic calcite, a previous study also demonstrated that the mineral calcite did not enhance freezing temperatures in the immersion mode.[318] The lack of organic material associated with the external coccoliths in spite of the underlying organic cell wall, combined with the fact that calcite is inefficient in nucleating ice, may explain why *E. huxleyi* are not efficient IN via immersion freezing. In contrast to the good ice nucleation efficiency of diatoms and chlorophytes investigated here, various polar sea ice diatoms depress ice nucleation[319] and sea ice bacteria and viruses were observed not to enhance ice nucleation temperatures above the homogeneous freezing limit.[229] It is possible that ice nucleating proteins which limit the amount of supercooling and anti-freeze proteins which suppress ice nucleation present in some, but not all marine microorganisms, may be responsible for different ice nucleation abilities observed for the phytoplankton investigated here and in previous studies.[34,35] Organic amphiphilic molecules structured in monolayers provide a two dimensional match of their hydrophilic functional groups with a hexagonal ice lattice facilitating the hydrogen bonding of water molecules to form ice.[302] It may also be possible that a similar effect may occur for phytoplankton cellular membranes.[34,35]

As far as we are aware, there are no studies which identify ice nucleating proteins in marine phytoplankton or any other ice nucleating agent associated with phytoplanktonic derived organic material. However, cellular proteins are in general thought to be responsible for enhancing ice nucleation,[297,299,301] for example, for various plant pathogenic bacteria.[298,320,321] For marine algae, however, the genome map of the diatom *T. pseudonana*,[193] examined by Janech *et al.*[319] did not reveal any known ice bonding proteins capable of altering or suppressing ice crystallization.[193,319]

There are striking differences in the ice nucleation efficiency between immersion and deposition freezing by the two phytoplankton species investigated here and *T. pseudonana* previously studied.[34,35] Our results clearly demonstrate that biogenic calcite can trigger ice formation in the deposition mode and not in the immersion mode, although the explanation for this is not understood. Our observations of the ice nucleating efficiency of *E. huxleyi* via deposition freezing are consistent with those of Eastwood *et al.*[145] who showed that mineral calcite can also act as IN via deposition freezing. It is possible, that because calcite has a rhombohedral crystal structure,[322] it may be unfavorable for water molecules to form a hexagonal lattice typical of ice. In the immersion mode, an IN which has a similar lattice structure to that of ice may play an important role for orientation of the water molecules,[144,302] however, for deposition freezing, ice nucleation may be also dependent on other factors such as cavities, cracks, or irregularities at the IN interface.[42]

6.4.3 Atmospheric Implications

The time-dependent and time-independent descriptions used to quantify heterogeneous ice nucleation are fundamentally different, and as a result their application for atmospheric models to predict ice particle concentrations per unit volume of air, N_{ice}, may yield different results. The experimentally derived J_{het} from Figs. 6.3a and 6.7a are used to calculate ice particle production rates, P_{ice}, from the following equation,

$$P_{\mathrm{ice}}(T, \mathrm{RH}) = J_{\mathrm{het}}(T, \mathrm{RH}) \cdot A_{\mathrm{particle}}, \tag{45}$$

where A_{particle} is the particle surface area per unit volume of air. P_{ice} is a function of T, and RH, or $\mathrm{RH}_{\mathrm{ice}}$ for immersion or deposition freezing, respectively. N_{ice} can then be determined by integrating eqn (45) with respect to time. According to SH, N_{ice} can be directly calculated from K values obtained from Figs. 6.3b and 6.7b from the following equation,

$$N_{\mathrm{ice}}(T, \mathrm{RH}) = K(T, \mathrm{RH}) \cdot A_{\mathrm{particle}}. \tag{46}$$

Note that for immersion freezing, $a_{\mathrm{w}} = \mathrm{RH}$ when the vapour pressure of an aqueous droplet is in equilibrium with the environmental water partial pressure,[14,15] and for deposition freezing, the relative humidity with respect to ice is equal to S_{ice}. The following calculations provide a first order estimate for N_{ice} due to marine phytoplankton and are presented in order to initiate discussion of the application of the two approaches in cloud system resolving models. The actual ice particle concentration in the atmosphere at any given time will necessarily be affected by depletion of water vapour subsequent to ice crystal formation according to the Bergeron-Wegener-Findeisen process,[270–272] ice crystal sedimentation,[166,323–325] and ice multiplication through riming as described by the Hallett-Mossop effect,[273,274] which are not considered in these estimates. Other particle types acting as IN are not considered for the following calculations, although we recognize that in the atmosphere other particles can be present which compete with marine biogenic particles as IN.

Concentrations of airborne phytoplankton particles are assumed to be on the order 0.1 L^{-1} (air) generalised from Alpert *et al.*[35] It should be noted that there are very few quantitative reports of airborne phytoplankton particle concentrations, and the assumed value is representative of a conservative low es-

timate based on the available literature.[232,238,263,326,327] We assume that the fragments of *N. atomus* are spherical in shape and those from *E. huxleyi*, to be flat and discoidal, both having diameters of 1 μm. The corresponding surface areas are then $3 \cdot 10^{-8}$ cm^2 and $1.6 \cdot 10^{-8}$ cm^2, respectively, or $3 \cdot 10^{-9}$ cm^2 L^{-1} (air) and $1.6 \cdot 10^{-9}$ cm^2 L^{-1} (air), respectively.

We provide example calculations of N_{ice} for two different cloud types employing both time-dependent, $N_{\text{ice}}^{\text{CNT}}$, and time-independent, $N_{\text{ice}}^{\text{SH}}$, approaches. First, we calculate N_{ice} from *N. atomus* acting as IN for mixed-phase clouds due to immersion freezing at $T = 240$ and RH = 97%. Second, we calculate N_{ice} from *E. huxleyi* acting as IN in the deposition mode for cirrus clouds at $T = 215$ K and $S_{\text{ice}} = 1.30$.

Employing a time-dependent approach at $T = 240$ K and RH = 97%, $J_{\text{het}} = 5 \cdot 10^3$ cm^{-2} s^{-1} taken from Fig. 6.3a yields $P_{\text{ice}} = 4.5 \cdot 10^{-4}$ L^{-1} (air) min^{-1} thus, after 20 min of ice particle production due to *N. atomus* acting as IN in the immersion mode at these conditions, $N_{\text{ice}}^{\text{CNT}} = 0.02$ ice crystals L^{-1} (air). Using a time-independent approach, $K = 6 \cdot 10^4$ cm^{-2} taken from Fig. 6.3b yields $N_{\text{ice}}^{\text{SH}} = 1.8 \cdot 10^{-4}$ ice crystals L^{-1} (air) corresponding to only a small fraction of particles which have active sites to form ice crystals.

Ice crystals which form from *E. huxleyi* via deposition freezing for cirrus conditions are first derived employing a time-dependent approach at $T = 215$ K and $S_{\text{ice}} = 1.30$, where $J_{\text{het}} = 20$ cm^{-2} s^{-1} taken from Fig. 6.6a which yields $P_{\text{ice}} = 1.9 \cdot 10^{-6}$ L^{-1} (air) min^{-1}. After 20 min, $N_{\text{ice}}^{\text{CNT}} = 3.8 \cdot 10^{-5}$ ice crystals L^{-1} (air). Using a time-independent approach, $K = 7 \cdot 10^2$ cm^{-2} taken from Fig. 6.3b yields $N_{\text{ice}}^{\text{SH}} = 1.1 \cdot 10^{-6}$ ice crystals L^{-1} (air).

Clearly, the different approaches yield different ice crystal numbers primarily due to the time evolution allowed for the time-dependent approach. It remains unclear, however, which of two approaches is more correct to use in predicting potential ice particles in clouds. Over the course of 20 minutes, which corresponds to an approximate time to go from $\text{RH}_{\text{ice}} = 100\%$ to the homogeneous freezing limit at typical cirrus updrafts, there is about a 2 order of magnitude difference in ice particle production between time-dependent and time-independent approaches. Use of these two ice nucleation approaches in cloud system resolving models could provide insight to identify which approach is most atmospherically relevant. One would conduct sensitivity studies in which all other relevant parameters including updraft velocity and IN concentrations are kept the same and monitoring subsequent changes in mixed-phase and ice cloud evolution. Differences between CNT or SH models may lead to differences in mixed-phase and ice cloud evolution, which may alter cloud properties such as albedo and radiative forcing.

7 Conclusions and Outlook

The main focus of the research presented in this thesis is the investigation of the impact of biological activity, such as occurs in the ocean, on particle aerosolization and the potential for marine biogenic particles to nucleate ice, an essential process in the formation of ice clouds. This thesis presents a laboratory investigation of the link between the presence of bacteria, phytoplankton and biological activity in seawater, and the aerosolization of particles and the subsequent heterogeneous ice nucleation in immersion and deposition modes. Experiments were carried out using a custom-built mesocosm coupled to a scanning mobility particle sizer spectrometer in which particles which were aerosolized from seawater and their sizes quantified with nanometer resolution under dry and humidified conditions. Cryogenic cold-cell chambers in which biogenic particles were exposed to temperature and relative humidity experienced in the atmosphere were subsequently used for observation of heterogeneous ice nucleation. Additionally, phytoplankton cells and cell fragments in aqueous NaCl solution droplets were used as proxies of marine biogenic particles for use in heterogeneous ice nucleation experiments. State-of-the art electron and X-ray spectromicroscopic techniques complemented these experiments to provide single particle chemical analysis. The main conclusions are summarized below.

7.1 Conclusions

Aerosolization of marine biogenic particles and particle hygroscopicity, ice nucleation efficiency, and chemical composition as a function of biological activity in seawater

This study investigated the effect of biological activity in seawater on aerosolization of marine particles by quantifying total particle production and size distributions, particle growth due to water condensation at RH = 80%, the ice nucleation potential of marine particles, particle chemical compositions and individual ice particle carbon bonding composition. Aerosolization took place in mesocosms filled with artificial or natural seawater in which bacteria and phytoplankton grew over time. Using impinging water jets and aeration through glass frits to generate bubbles, aerosolized particles were produced and the corresponding size distribution and total production was determined. Results showed that for over 4 orders of magnitude increases in bacterial concentrations, particle production increased 2-3 fold. This increase was observed when bacteria were grown alone, together with a single phytoplankton species, or in natural seawater with a complex microbial community. As populations of microorganisms increased, production of particles $20-30$ nm in diameter were enhanced using jets and in many cases, particles in this size range dominated total aerosol production. In contrast, the shape of particle size distributions generated with the frit never changed despite the changing biological community and associated water conditions. The frits generated an order of magnitude more bubbles than the jets and produced bubbles in a more narrow size range, which may explain the difference in particle production between the two methods. The great majority of aerosolized particles from all mesocosm experiments produced by either bubble generation methods were highly hygroscopic. All particles were found to have a similar composition of organic material coating a

sea salt core, and had a similar efficiency to nucleate ice in both the immersion and deposition mode. The composition of individual ice nucleating particles were all similar, with an inorganic core coated by organic material in which the dominant carbon bond was the carboxyl function group. It is most logical to assume that the source of the organic coatings on the ice nucleating particles came from compounds released into the water during the growth of bacteria and phytoplankton which was aerosolized. The results here establishes an unambiguous link between biological activity in seawater and the aerosolization of organic and inorganic matter to potentially participate in ice formation.

Ice nucleation from aqueous NaCl droplets with and without phytoplankton

Heterogeneous ice nucleation of micrometer sized droplets with immersed cells and cell fragments of the diatom *Thalassiosira pseudonana*, the coccolithophorid *Emiliania huxleyi*, and the green alga *Nannochloris atomus* were investigated to determine if representatives of the dominant groups of phytoplankton could all serve as atmospheric ice nuclei, compared with homogeneous ice nucleation from aqueous NaCl droplets. Droplet freezing temperatures and ice nucleation kinetics for homogeneous ice nucleation were found to be in agreement with predictions of the water-activity based homogeneous ice nucleation theory. Diatoms and green algae were found to be efficient heterogeneous ice nuclei in the immersion mode, however *E. huxleyi* was not. Median heterogeneous freezing temperatures of NaCl solution droplets due to intact and fragmented diatoms and green algae can be represented entirely by the modified water activity based ice nucleation theory. In other words, immersion freezing temperatures can be described by shifting the ice melting curve by a value $\Delta a_{\mathrm{w}} = 0.2303$ for diatoms and $\Delta a_{\mathrm{w}} = 0.2391$ for green algae. This demonstrates that the heterogeneous ice nucleation process is controlled by thermodynamic parameters of temperature and water activity.

Ice nucleation from phytoplankton cells or fragments not associated with NaCl

In these experiments, heterogeneous ice nucleation was investigated for phytoplankton cells and cell fragments exposed to low temperatures at supersaturated conditions, without the presence of NaCl. *T. pseudonana*, *E. huxleyi*, and *N. atomus* were determined all to have the ability to efficiently nucleate ice in the deposition mode. Despite distinct differences in cell wall composition between the phytoplankton, all nucleated ice with a similar efficiency around a relative humidity with respect to ice of about 135%. A similar conclusion can be made for deposition freezing of aerosolized marine biogenic particles from mesocosm experiments described above. *T. pseudonana* and *N. atomus* were able to take up water, essentially hydrating, and nucleate ice in the immersion mode in agreement with droplet freezing studies. *E. huxleyi* presented an interesting case due to the fact that it was an efficient ice nucleus for deposition freezing but did not nucleate ice in the immersion mode, nor did it take up water. These results highlight the possible need to consider the nature of the biogenic/organic particles having both comparable and contrasting effects on ice nucleation behavior in different freezing modes.

7.2 Outlook

A link between marine biological activity, aerosolization of marine biogenic particles and the ability of the particles to heterogeneously nucleate ice are presented in this thesis. Nevertheless, in spite of the discoveries presented, significant work is still needed to provide a more complete understanding of oceanic to atmospheric exchange of biogenic particles and the relationship between those particles and processes involved in ice cloud formation. The results presented here raise a number of provocative questions.

- The importance for bubble generation for studying marine particle aerosolization calls for more field measurements with consistent methodology. Key ocean locations for such studies include regions where phytoplankton bloom, coastal waters, and in the open ocean.
- Field studies should also carefully consider the biological activity in seawater and measurements of ambient aerosol particle size distributions for derivation of sub- and super-micron particle fluxes. Additional data to better quantify changing aerosolization effects are needed in different parts of the ocean where phytoplankton and bacteria grow, in addition to various intensities of wind, temperature, ocean waves and different microbial communities.
- Future laboratory studies should focus on addressing the influence of viruses, nanogels, proteinaceous particles, and transparent exopolymer material in seawater on aerosolization. While important and interesting, this is not easy to investigate due to the complex nature of these types of materials. Therefore, careful and detailed studies are required to provide sufficient information to answer this question.
- STXM/NEXAFS and CCSEM/EDX have been successfully used to detail aerosol particle chemical composition and chemical aging in a particle population[4,29]. Also, ice nucleation studies have been carried out in parallel with these powerful spectromicroscopic methods[202,203]. It may be possible to use these techniques for a more accurate and direct calculation of a composition dependent sea spray aerosol flux using for example a micro-orifice uniform-deposit impactor (MOUDI) covering a wide range of particle diameters between 10 nm and 10 μm with 13 impactor stages.
- How would atmospheric models respond to changing marine particle flux as a function of biological activity? The appearance and disappearance of algal blooms in the oceans is widespread, but up to now, general circulation models, such as the CAM5, use sea salt emission rates that are not dependent on biological activity occurring in the ocean and therefore, aerosolized organic material is parameterized as a mass fraction of only the existing sea salt emission[25,328]. Model responses of cloud droplet number, liquid water path and cloud radiative forcing to a changing flux of particles and organic mass fraction simultaneously as a function of ocean biological activity, should be investigated.
- What is the ice nucleating agent in marine biogenic material? Some microorganisms have a freeze tolerant ability in which ice nucleation is purposefully induced outside of the cell as a means of preventing intracellular freezing. These biogenic ice nuclei include certain proteins, carbohydrates and phospholipids. Considering the fact that many phytoplankton thrive in cold environments such as near, on,

or even under Arctic or Antarctic sea ice, further investigation of the ice nucleating biological agents in marine phytoplankton or bacteria are needed to help explain why a phytoplankton cell or organic material derived from biological activity in seawater nucleates ice.

- There is current debate about how best to interpret ice nucleation data generated in the field or the laboratory in terms of a fundamental description for heterogeneous ice nucleation. Some ice nucleation parameterizations are made without any consideration to time or particle surface area as a first order estimate[329] however, this has no basis in any physical theory. In fact, some of the applied observables are not even physical variables such as the activated IN fraction. Other descriptions use statistical modifications of classical nucleation theory to fit and reproduce experimental results, but these are limited in range to nucleation times and surface areas used in the laboratory. As a result of many experiments described in this dissertation we propose that a water activity based ice nucleation theory is entirely suitable and should be the preferred approach for a wholistic description of immersion freezing founded on classical nucleation theory without restrictions on time and surface area. Cloud system resolving models should be designed in such a way to use a water activity based parameterization of heterogeneous ice nucleation in models to predict ice cloud formation compared against other empirical or non-physical descriptions.

References

[1] P. Forster, V. Ramaswamy, P. Artaxo, T. Berntsen, R. Betts, D. W. Fahey, J. Haywood, J. Lean, D. C. Lowe, G. Myhre, J. Nganga, R. Prinn, G. Raga, M. Schulz and R. Van Dorland, in *Climate Change 2007: The Physical Science Basis. Contribution of Working Group I to the Fourth Assessment Report of the Intergovernmental Panel on Climate Change*, Cambridge University Press, Cambridge, United Kingdom and New York, NY, USA, 2007, ch. 2. Changes in Atmospheric Constituents and in Radiative Forcing, pp. 131–234.

[2] P. Verdugo, *Ann. Rev. Mar. Sci.*, 2012, **4**, 375–400.

[3] C. D. O'Dowd, M. C. Facchini, F. Cavalli, D. Ceburnis, M. Mircea, S. Decesari, S. Fuzzi, Y. J. Yoon and J. P. Putaud, *Nature*, 2004, **431**, 676–680.

[4] A. Laskin, R. C. Moffet, M. K. Gilles, J. D. Fast, R. A. Zaveri, B. Wang, P. Nigge and J. Shutthanandan, *J. Geophys. Res.*, 2012, **117**, D15302.

[5] D. M. Murphy and T. Koop, *Q. J. R. Meteorol. Soc.*, 2005, **131**, 1539–1565.

[6] S. L. Clegg, P. Brimblecombe and A. S. Wexler, *J. Phys. Chem. A*, 1998, **102**, 2155–2171.

[7] T. Koop, A. Kapilashrami, L. T. Molina and M. J. Molina, *J. Geophys. Res.*, 2000, **105**, 26393–26402.

[9] I. N. Tang, H. R. Munkelwitz and J. G. Davies, *J. Aerosol Sci.*, 1977, **8**, 149–159.

[10] M. D. Cohen, R. C. Flagan and J. H. Seinfeld, *J. Phys. Chem.*, 1987, **91**, 4563–4574.

[11] D. J. Cziczo, J. B. Nowak, J. H. Hu and J. P. D. Abbatt, *J. Geophs. Res.*, 1997, **102**, 18843–18850.

[12] D. D. Weis and G. E. Ewing, *J. Geophs. Res.*, 1999, **104**, 21275–21285.

[13] D. J. Cziczo and J. P. D. Abbatt, *J. Phys. Chem. A*, 2000, **104**, 2038–2047.

[8] M. E. Wise, K. J. Baustian, T. Koop, M. A. Freedman, E. J. Jensen and M. A. Tolbert, *Atmos. Chem. Phys.*, 2012, **12**, 1121–1134.

[14] T. Koop, B. P. Luo, A. Tsias and T. Peter, *Nature*, 2000, **406**, 611–614.

[15] T. Koop and B. Zobrist, *Phys. Chem. Chem. Phys.*, 2009, **11**, 10839–10850.

[16] W. D. Nesse, *Introduction to Mineralogy*, Oxford University Press, Oxford, 2000.

[17] D. A. Knopf and P. A. Alpert, *Farad. Discuss.*, 2013, Accepted Manuscript.

[18] R. C. Moffet, T. Henn, A. Laskin and M. K. Gilles, *Anal. Chem.*, 2010, **82**, 7906–7914.

[19] K. Sellegri, C. D. O'Dowd, Y. J. Yoon, S. G. Jennings and G. de Leeuw, *J. Geophys. Res.*, 2007, **111**, D22215.

[20] P. A. Bowyer, *J. Geophys. Res.*, 2001, **106**, 14179–14190.

[21] G. B. Deane and M. D. Stokes, *Nature*, 2002, 839–844.

[22] H. Medwin and N. D. Breitz, *J. Geophys. Res.*, 1989, **94**, 12751–12759.

[23] S. Baldy, *J. Geophys. Res.*, 1988, **93**, 8239–8248.

[24] E. R. Lewis and S. E. Schwartz, *Sea Salt Aerosol Production: Mechanisms, Methods, Measurements, and Models*, American Geophysical Union, 2000 Florida Ave., N.W., Washington, DC 20009, 2004.

[25] E. M. Mårtensson, E. D. Nilsson, G. de Leeuw, L. H. Cohen and H.-C. Hansson, *J. Geophys. Res.*, 2003, **108**, D9, 4297.

[26] C. A. Tyree, V. M. Hellion, O. A. Alexandrova and J. O. Allen, *J. Geophys. Res.*, 2007, **112**, D12204.

[27] W. C. Keene, H. Maring, J. R. Maben, D. J. Kieber, A. A. P. Pszenny, E. E. Dahl, M. A. Izaguirre, A. J. Davis, M. S. Long, X. L. Zhou, L. Smoydzin and R. Sander, *J. Geophys. Res.*, 2007, **112**, 2657–2665.

[28] A. D. Clarke, S. R. Owens and J. C. Zhou, *J. Geophys. Res.*, 2006, **111**, D06202.

[29] R. C. Moffet, T. R. Henn, A. V. Tivanski, R. J. Hopkins, Y. Desyaterik, A. L. D. Kilcoyne, T. Tyliszczak, J. Fast, J. Barnard, V. Shutthanandan, S. S. Cliff, K. D. Perry, A. Laskin and M. K. Gilles, *Atmos. Chem. Phys.*, 2010, **10**, 961–976.

[30] I. N. Koprinarov, A. P. Hitchcock, C. T. McCrory and R. F. Childs, *J. Phys. Chem. B*, 2002, **106**, 5358–5364.

[31] W. F. Linke, *Solubilities of Inorganic and Metal Organic Compounds*, Am. Chem. Soc., Washington D. C., 1965.

[32] E. C. W. Clarke and D. N. Glew, *J. Phys. Chem. Ref. Data*, 1985, **14**, 489–610.

[33] T. Koop, *Z. Phys. Chemie-Int. J.*, 2004, **218**, 1231–1258.

[34] D. A. Knopf, P. A. Alpert, B. Wang and J. Y. Aller, *Nat. Geosci.*, 2011, **4**, 88–90.

[35] P. A. Alpert, J. Y. Aller and D. K. Knopf, *Atmos. Chem. Phys.*, 2011, **11**, 55395555.

[36] J. S. Kim and A. Yethiraj, *J. Phys. Chem. B*, 2008, **112**, 1729–1735.

[37] B. Wang and D. A. Knopf, *J. Geophys. Res.*, 2011, **116**, D03205.

[40] B. L. Henke, E. M. Gullikson and J. C. Davis, *Atom. Data Nucl. Data*, 1993, **54**, 181–342.

[39] D. Solomon, J. Lehmann, J. Kinyangi, B. Liang, K. Heymann, L. Dathe, K. Hanley, S. Wirick and C. Jacobsen, *Soil Sci. Soc. Am. J.*, 2009, **73**, 1817–1830.

[38] R. C. Moffet, A. V. Tivanski and M. K. Gilles, in *Fundamentals and Applications in Aerosol Spectroscopy*, ed. R. Signorell and J. P. Reid, Taylor and Francis Group, LLC, Boca Raton, FL, 2011, ch. 17. Scanning Transmission X-ray Microscopy: Applications in Atmospheric Aerosol Research, pp. 419–462.

[41] J. H. Seinfeld and S. N. Pandis, *Atmospheric Chemistry and Physics - From Air Pollution to Climate Change*, John Wiley & Sons., Hoboken, NJ, 2nd edn, 2006.

[42] R. Pruppacher, H. and J. D. Klett, *Microphysics of Clouds and Precipitation*, Kluwer Academic Publishers, Netherlands, 1997.

[43] C. A. Angell, *Annu. Rev. Phys. Chem.*, 1983, **34**, 593–630.

[44] D. A. Knopf and Y. J. Rigg, *J. Phys. Chem. A*, 2010, **115**, 762773.

[45] G. Vali, *J. Aerosol Sci.*, 1985, **16**, 575–576.

[46] D. A. Hegg and M. B. Baker, *Rep. Prog. Phys.*, 2009, **72**, 056801.

[47] A. J. Heymsfield, L. M. Miloshevich, C. Twohy, G. Sachse and S. Oltmans, *Geophys. Res. Lett.*, 1998, **25**, 1343–1350.

[48] W. Haag, B. Kärcher, J. Ström, A. Minikin, U. Lohmann, J. Ovarlez and A. Stohl, *Atmos. Chem. Phys.*, 2003, **3**, 1791–1806.

[49] M. Seifert, J. Ström, R. Krejci, A. Minikin, A. Petzold, J.-F. Gayet, U. Schumann and J. Ovarlez, *Atmos. Chem. Phys.*, 2003, **3**, 1037–1049.

[50] P. J. DeMott, K. Sassen, M. R. Poellot, D. Baumgardner, D. C. Rogers, S. D. Brooks, A. J. Prenni and S. M. Kreidenweis, *Geophys. Res. Lett.*, 2003, **30**, 14, 1732.

[51] P. J. DeMott, D. C. Rogers, S. M. Kreidenweis, Y. Chen, C. H. Twohy, D. Baumgardner, A. J. Heymsfield and K. R. Chan, *Geophys. Res. Lett.*, 1998, **25**, 1387–1390.

[52] D. J. Cziczo, D. M. Murphy, P. K. Hudson and D. S. Thomson, *J. Geophys. Res.*, 2004, **109**, D04201.

[53] V. I. Khvorostyanov, H. Morrison, J. A. Curry, D. Baumgardner and P. Lawson, *J. Geophys. Res.*, 2006, **111**, D02201.

[54] J. Ovarlez, J.-F. Gayet, K. Gierens, J. Ström, H. Ovarlez, F. Auriol, R. Busen and U. Schumann, *Geophys. Res. Lett.*, 2002, **29**, 601–604.

[55] E. Jensen, L. Pfister, T. Bui, A. Weinheimer, E. Weinstock, J. Smith, J. Pittman, D. Baumgardner, P. Lawson and M. J. McGill, *J. Geophys. Res.*, 2005, **110**, D03208.

[56] M. P. Meyers, P. J. DeMott and W. R. Cotton, *J. Appl. Meteorol.*, 1992, **31**, 708–721.

[57] P. J. DeMott and A. J. Prenni, *Atmos. Environ.*, 2010, **44**, 1944–1945.

[58] M. Kamphus, M. Ettner-Mahl, T. Klimach, F. Drewnick, L. Keller, D. J. Cziczo, S. Mertes, S. Borrmann and J. Curtius, *Atmos. Chem. Phys.*, 2010, **10**, 8077–8095.

[59] G. de Boer, H. Morrison, M. D. Shupe and R. Hildner, *Geophys. Res. Lett.*, 2011, **38**, L01803.

[60] P. R. Field, A. J. Heymsfield, B. J. Shipway, P. J. DeMott, K. A. Pratt, D. C. Rogers, J. Stith and K. A. Prather, *J. Atmos. Sci.*, 2012, **69**, 1066–1079.

[61] A. J. Prenni, P. J. Demott, D. C. Rogers, S. M. Kreidenweis, G. M. McFarquhar, G. Zhang and M. R. Poellot, *Tellus B*, 2009, **61**, 436–448.

[62] J. Verlinde, J. Y. Harrington, G. M. McFarquhar, V. T. Yannuzzi, A. Avramov, S. Greenberg, N. Johnson, G. Zhang, M. R. Poellot, J. H. Mather, D. D. Turner, E. W. Eloranta, B. D. Zak, A. J. Prenni, J. S. Daniel, G. L. Kok, D. C. Tobin, R. Holz, K. Sassen, D. Spangenberg, P. Minnis, T. P. Tooman, M. D. Ivey, S. J. Richardson, C. P. Bahrmann, M. Shupe, P. J. DeMott, A. J. Heymsfield and R. Schofield, *Bull. Amer. Meteor. Soc.*, 2007, **42**, 248–252.

[63] D. C. Rogers, P. J. DeMott, S. M. Kreidenweis and Y. L. Chen, *J. Atmos. Ocean. Technol.*, 2001, **18**, 725–741.

[64] G. W. Petty, *A First Course in Atmospheric Radiation*, Sundog Publishing, Madison, WI, 2nd edn, 2006.

[65] R. J. Charlson, S. E. Schwartz, J. M. Hales, R. D. Cess, J. A. Coakley, J. E. Hansen and D. J. Hofmann, *Science*, 1992, **255**, 423–430.

[66] M. O. Andreae and P. J. Crutzen, *Science*, 1997, **276**, 1052–1058.

[67] V. Ramanathan, P. J. Crutzen, J. T. Kiehl and D. Rosenfeld, *Science*, 2001, **294**, 2119–2124.

[68] T. L. Anderson, R. J. Charlson, S. E. Schwartz, R. Knutti, O. Boucher, H. Rodhe and J. Heintzenberg, *Science*, 2003, **300**, 1103–1104.

[69] A. McComiskey, S. E. Schwartz, B. Schmid, H. Guan, E. R. Lewis, P. Ricchiazzi and J. A. Ogren, *J. Geophys. Res.*, 2008, **113**, D09202.

[70] S. Twomey, *Atmos. Environ. A*, 1991, **25**, 2435–2442.

[71] M. B. Baker, *Science*, 1997, **276**, 1072–1078.

[72] Y. J. Kaufman, D. Tanrá and O. Boucher, *Nature*, 2002, **419**, 215–223.

[73] W. Cantrell and A. Heymsfield, *B. Am. Meteorol. Soc.*, 2005, **86**, 795–807.

[74] U. Lohmann and J. Feichter, *Atmos. Chem. Phys.*, 2005, **5**, 715–737.

[75] T. Storelvmo, C. Hoose and P. Eriksson, *J. Geophys. Res.*, 2011, **116**, D05207.

[76] T. Chen, W. B. Rossow and Y. C. Zhang, *Tellus A*, 2000, **50**, 259–264.

[77] P. M. Cox, R. A. Betts, C. D. Jones, S. A. Spall and I. J. Totterdell, *Nature*, 2000, **408**, 184–187.

[78] V. B. Žutić, E. Ćosović, E. Marčenko and N. Bihari, *Mar. Chem.*, 1981, **10**, 505–520.

[79] U. Passow and A. L. Alldredge, *Mar Ecol. Prog. Ser.*, 1994, **113**, 185198.

[80] P. Verdugo, A. L. Alldredge, F. Azam, D. L. Kirchman, U. Passow and P. H. Santschi, *Mar. Chem.*, 2004, **92**, 67–85.

[81] J. Y. Aller, M. R. Kuznetsova, C. J. Jahns and P. Kemp, *J. Aerosol. Sci.*, 2005, **36**, 801–812.

[82] M. C. Facchini, M. Rinaldi, S. Decesari, C. Carbone, E. Finessi, M. Mircea, S. Fuzzi, D. Ceburnis, R. Flanagan, E. D. Nilsson, G. de Leeuw, M. Martino, J. Woeltjen and C. D. O'Dowd, *Geophys. Res. Lett.*, 2008, **35**, L17814.

[83] P. Verdugo and P. H. Santschi, *Deep Sea Res. II*, 2010, **57**, 1486–1493.

[84] P. Verdugo, *Adv. Polym. Sci.*, 1994, **110**, 145156.

[85] W. C. Chin, M. V. Orellana and P. Verdugo, *Nature*, 1998, **391**, 568–572.

[86] *The Sea Surface and Global Change*, ed. P. S. Liss and R. A. Duce, Cambridge University Press, Cambridge, UK, 1st edn, 1997.

[87] M. I. Gladyshev, *Biophysics of the Surface Microlayer of Aquatic Systems*, IWA Publishing, London, UK, 1st edn, 2002.

[88] J. M. N. Sieburth, *Limnol. Oceanogr.*, 1963, **8**, 489–492.

[89] H. F. Bezdek and A. F. Carlucci, *Limnol. Oceanogr.*, 1972, **17**, 566–570.

[90] M. R. Kuznetsova and C. Lee, *Mar. Chem.*, 2001, **73**, 319–322.

[91] M. Kuznetsova, C. Lee, J. Aller and N. Frew, *Limnol. Oceanogr.*, 2004, **49**, 1605–1619.

[92] O. Wurl and M. Holmes, *Mar. Chem.*, 2008, **110**, 89–97.

[93] D. C. Blanchard, *Prog. Oceanogr.*, 1963, **7**, 113–202.

[94] S. A. Thorpe, *Q. J. R. Meteorol. Soc.*, 1992, **118**, 1–22.

[95] G. de Leeuw, E. L. Andreas, M. D. Anguelova, C. W. Fairall, E. R. Lewis, C. D. O'Dowd, M. Schulz and S. E. Schwartz, *Rev. Geophys.*, 2011, **49**, RG2001.

[96] E. C. Monahan and I. G. Ó Muircheartaigh, *Science*, 1980, **10**, 20942099.

[97] E. Fuentes, H. Coe, G. Green, D. de Leeuw and G. McFiggans, *Atmos. Chem. Phys.*, 2010, **10**, 141–162.

[98] K. A. H. Hultin, E. D. Nilsson, R. Krejci, E. M. Mårtensson, M. Ehn, r. Hagström and G. de Leeuw, *J. Geophys. Res.*, 2010, **115**, D06201.

[99] K. A. Prather, T. H. Bertram, V. H. Grassian, G. B. Deane, M. D. Stokes, P. J. DeMott, L. I. Aluwihare, B. P. Palenik, F. Azam, J. H. Seinfeld, R. C. Moffet, M. J. Molina, C. D. Cappa, F. M. Geiger, G. C. Roberts, L. M. Russell, A. P. Ault, J. Baltrusaitis, D. B. Collins, C. E. Corrigan, L. A. Cuadra-Rodriguez, C. J. Ebben, S. D. Forestieri, T. L. Guasco, S. P. Hersey, M. J. Kim, W. F. Lambert, R. L. Modini, W. Mui, B. E. Pedler, M. J. Ruppel, O. S. Ryder, N. G. Schoepp, R. C. Sullivan and D. Zhao, *P. Natl. Acad. Sci.*, 2013, **110**, 7550–7555.

[100] P. A. Bowyer, D. K. Woolf and E. C. Monahan, *J. Geophys. Res.*, 1990, **95**, 5313–5319.

[101] J. Zábori, R. Krejci, A. M. L. Ekman2, E. M. Mårtensson, J. Ström, G. de Leeuw and E. D. Nilsson, *Atmos. Chem. Phys.*, 2012, **12**, 10405–10421.

[102] D. C. Blanchard and L. Syzdek, *Science*, 1970, **170**, 626–628.

[103] J. Zábori, M. Matisāns, R. Krejci, E. D. Nilsson and J. Ström, *Atmos. Chem. Phys.*, 2012, **12**, 1070910724.

[104] E. K. Bigg and C. Leck, *J. Geophys. Res.*, 2008, **113**, D11209.

[105] E. K. Bigg, *Atmos. Chem. Phys. Discuss.*, 2011, **11**, C967C969.

[106] E. Fuentes, H. Coe, D. Green and G. McFiggans, *Atmos. Chem. Phys.*, 2011, **11**, 2585–2602.

[107] E. Fuentes, H. Coe, D. Green, G. de Leeuw and G. McFiggans, *Atmos. Chem. Phys.*, 2010, **10**, 9295–9317.

[108] M. V. Orellana, P. A. Matrai, C. Leck, C. D. Rauschenberg, A. M. Lee and E. Coz, *P. Natl. Acad. Sci.*, 2011, **108**, 13612–13617.

[109] J. Ovadnevaite, C. O'dowd, M. Dall'Osto, D. Ceburnis, D. R. Worsnop and H. Berresheim, *J. Geophys. Res.*, 2011, **38**, L02807.

[110] L. M. Russell, L. N. Hawkins, A. A. Frossard, P. K. Quinn and T. S. Bates, *P. Natl. Acad. Sci.*, 2010, **107**, 6652–6657.

[111] D. J. Cziczo, K. D. Froyd, C. Hoose, E. J. Jensen, M. Diao, M. A. Zondlo, J. B. Smith, C. H. Twohy and D. M. Murphy, *Science*, 2013, **340**, 1320–1324.

[112] E. K. Bigg, *J. Atmos. Sci.*, 1973, **30**, 1153–1157.

[113] R. C. Schnell, *Geophys. Res. Lett.*, 1975, **2**, 500–502.

[114] R. C. Schnell and G. Vali, *J. Atmos. Sci.*, 1976, **33**, 1554–1564.

[115] R. Fall and R. C. Schnell, *J. Mar. Res.*, 1985, **43**, 257–265.

[116] J. Rosinski, P. L. Haagenson, C. T. Nagamoto and F. Parungo, *J. Aerosol. Sci.*, 1986, **17**, 23–46.

[117] P. A. Alpert, D. A. Knopf and J. Y. Aller, *Phys. Chem. Chem. Phys.*, 2011, **13**, 19882–19894.

[118] J. Wang, *J. Geophys. Res.*, 2007, **112**, D16201.

[119] J. Wang, Y.-N. Lee, P. H. Daum, J. Jayne and M. L. Alexander, *Atmos. Chem. Phys.*, 2008, **8**, 6325–6339.

[120] S. M. Burrows, C. Hoose, U. Pöschl and M. G. Lawrence, *Atmos. Chem. Phys.*, 2013, **13**, 245–267.

[121] S. T. Martin, *Chemical Reviews*, 2000, **100**, 3403–3453.

[122] F. Cavalli, M. C. Facchini, S. Decesari, M. Mircea, L. Emblico, S. Fuzzi, D. Ceburnis, Y. J. Yoon, C. D. O'Dowd, J. P. Putaud and A. Dell'Acqua, *J. Geophys. Res.*, 2004, **109**, 256–259.

[123] G. McFiggans, P. Artaxo, U. Baltensperger, H. Coe, M. C. Facchini, G. Feingold, S. Fuzzi, M. Gysel, A. Laaksonen, U. Lohmann, T. F. Mentel, D. M. Murphy, C. D. O'Dowd, J. R. Snider and E. Weingartner, *Atmos. Chem. Phys.*, 2006, **6**, 2593–2649.

[124] M. O. Andreae and D. Rosenfeld, *Earth-Sci. Rev.*, 2008, **89**, 13–41.

[125] R. H. Stokes and R. A. Robinson, *J. Phys. Chem.*, 1966, **70**, 2126–2130.

[126] R. H. Moore, E. D. Ingall, A. Sorooshian and A. Nenes, *Geophys. Res. Lett.*, 2008, **35**, L07801.

[127] T. Koop, B. P. Luo, U. M. Biermann, P. J. Crutzen and T. Peter, *J. Phys. Chem. A*, 1997, **101**, 1117–1133.

[128] B. Zobrist, T. Koop, B. P. Luo, C. Marcolli and T. Peter, *J. Phys. Chem. A*, 2007, **111**, 2149–2155.

[129] P. W. Atkins and J. de Paula, *Physical Chemistry*, W. H. Freeman and Company, 41 Madison Ave., New York, NY, 10010, 8th edn, 2006, pp. 791–829.

[130] R. S. Smith and B. D. Kay, *Nature*, 1999, **398**, 788–791.

[131] D. R. H. Jones and G. A. Chadwick, *J. Cryst. Growth*, 1971, **11**, 260–264.

[132] J. S. Kim, Z. Wu, A. R. Morrow, A. Yethiraj and A. Yethiraj, *J. Phys. Chem. B.*, 2012, **116**, 12007–12013.

[133] J. H. Seinfeld and S. N. Pandis, *Atmospheric Chemistry and Physics*, John Wiley & Sons, New York, 1998.

[134] N. Fletcher, *J. Chem. Phys.*, 1958, **29**, 572–576.

[135] N. H. Fletcher, *J. Meterol.*, 1959, **16**, 173–180.

[136] P. V. Hobbs, in *Ice Physics*, Oxford University Press, London, 1999, ch. 6. Surface Properties, pp. 392–460.

[137] G. Vali, *J. Atmos. Sci.*, 1971, **29**, 402–409.

[138] M. J. Wheeler and A. K. Bertram, *Atmos. Chem. Phys.*, 2012, **12**, 1189–1201.

[139] F. Lüönd, O. Stetzer, A. Welti and U. Lohmann, *J. Geophys. Res.*, 2010, **115**, D14201.

[140] A. Welti, F. Lüönd, Z. A. Kanji, O. Stetzer and U. Lohmann, *Atmos. Chem. Phys.*, 2012, **12**, 9893–9907.

[141] Y. J. Rigg, P. A. Alpert and D. A. Knopf, *Atmos. Chem. Phys.*, 2013, **13**,.

[142] C. Marcolli, S. Gedamke, T. Peter and B. Zobrist, *Atmos. Chem. Phys.*, 2007, **7**, 5081–5091.

[143] B. Ervens and G. Feingold, *Atmos. Chem. Phys.*, 2012, **12**, 5807–5826.

[144] D. A. Knopf and S. Forrester, *J. Phys. Chem. A*, 2011, **115**, 5579–5591.

[145] M. L. Eastwood, S. Cremel, C. Gehrke, E. Girard and A. K. Bertram, *J. Geophys. Res.*, 2008, **113**, D22203.

[146] A. Welti, F. O. Lüönd, Stetzer and U. Lohmann, *Atmos. Chem. Phys.*, 2009, **9**, 67056715.

[147] G. Kulkarni and S. Dobbie, *Atmos. Chem. Phys.*, 2010, **10**, 95–105.

[148] Z. A. Kanji and J. P. D. Abbatt, *J. Phys. Chem. A*, 2010, **114**, 935–941.

[149] R. W. Saunders, O. Möhler, M. Schnaiter, S. Benz, R. Wagner, H. Saathoff, P. J. Connolly, R. Burgess, B. J. Murray, M. Gallagher, R. Wills and J. M. C. Plane, *Atmos. Chem. Phys.*, 2010, **10**, 12271247.

[150] G. P. Schill and M. A. Tolbert, *J. Phys. Chem. A*, 2012, **116**, 6817–6822.

[151] B. Riechers, F. Wittbracht, A. Hutten and T. Koop, *Phys. Chem. Chem. Phys.*, 2013, **15**, 5873–5887.

[152] B. Zobrist, U. Weers and T. Koop, *J. Chem. Phys.*, 2003, **118**, 10254–10261.

[153] D. A. Knopf and M. D. Lopez, *Phys. Chem. Chem. Phys.*, 2009, **11**, 8056–8068.

[154] D. A. Knopf and Y. J. Rigg, *J. Phys. Chem. A*, 2011, **115**, 762–773.

[155] B. Kärcher and U. Lohmann, *J. Geophys. Res.*, 2002, **107**, D2.

[156] B. Kärcher and U. Lohmann, *J. Geophys. Res.*, 2002, **107**, (D23) 4698.

[157] B. Kärcher, J. Hendricks and U. Lohmann, *J. Geophys. Res.*, 2006, **111**, D01205.

[158] J. Hendricks, B. Kärcher and U. Lohmann, *J. Geophys. Res.*, 2011, **116**, D18206.

[159] S.-M. Fan, J. P. Schwarz, J. Liu, D. W. Fahey, P. Ginoux, L. W. Horowitz, H. Levy, Y. Ming and J. R. Spackman, *J. Geophys. Res.*, 2012, **117**, D23205.

[160] D. A. Knopf, B. P. Luo, U. K. Krieger and T. Koop, *J. Phys. Chem. A*, 2003, **107**, 4322–4332.

[161] D. A. Knopf, B. P. Luo, U. K. Krieger and T. Koop, *J. Phys. Chem. A*, 2005, **109**, 2707–2709.

[162] K. S. Carslaw, S. L. Clegg and P. Brimblecombe, *J. Phys. Chem.*, 1995, **99**, 11557–11574.

[163] M. Massucci, S. L. Clegg and P. Brimblecombe, *J. Phys. Chem. A*, 1999, **103A**, 4209–4226.

[164] S. L. Clegg and P. Brimblecombe, *J. Phys. Chem. A*, 2005, **109**, 2703–2706.

[165] S. L. Clegg, P. Brimblecombe and A. S. Wexler, *J. Phys. Chem. A*, 1998, **102**, 2137–2154.

[166] B. Zobrist, C. Marcolli, T. Koop, B. P. Luo, D. M. Murphy, U. Lohmann, A. A. Zardini, U. K. Krieger, T. Corti, D. J. Cziczo, S. Fueglistaler, P. K. Hudson, D. S. Thomson and T. Peter, *Atmos. Chem. Phys.*, 2006, **6**, 3115–3129.

[167] B. Zuberi, A. Bertram, C. A. Cassa, L. T. Molina and M. J. Molina, *Geophys. Res. Lett.*, 2002, **29**, 10, 1504.

[168] C. M. Archuleta, P. J. DeMott and S. M. Kreidenweis, *Atmos. Chem. Phys.*, 2005, **5**, 2617–2634.

[169] B. Zobrist, C. Marcolli, T. Peter and T. Koop, *J. Phys. Chem. A*, 2008, **112**, 3965–3975.

[170] R. Iannone, D. I. Chernoff, A. Pringle, S. T. Martin and A. K. Bertram, *Atmos. Chem. Phys.*, 2011, **11**, 1191–1201.

[171] S. L. Broadley, B. J. Murray, R. J. Herbert, J. D. Atkinson, S. Dobbie, T. L. Malkin, E. Condliffe and L. Neve, *Atmos. Chem. Phys.*, 2012, **12**, 287–307.

[172] V. Pinti, C. Marcolli, B. Zobrist, C. R. Hoyle and T. Peter, *Atmos. Chem. Phys.*, 2012, **12**, 5859–5878.

[173] B. J. Murray, S. L. Broadley, T. W. Wilson, J. D. Atkinson and R. H. Wills, *Atmos. Chem. Phys.*, 2011, **11**, 4191–4207.

[174] B. Kärcher and U. Lohmann, *J. Geophys. Res.*, 2003, **108**, D14, 4402.

[175] R. J. Cipriano and D. C. Blanchard, *J. Geophys. Res.*, 1981, **86**, 8085–8092.

[176] E. Lamarre and W. K. Melville, *Nature*, 1991, **351**, 469472.

[177] P. A. Hwang and W. J. Teague, *J. Atmos. Ocean Tech.*, 2000, **17**, 847–853.

[178] H. Chanson, S. Aoki and A. Hoque, *Chem. Eng. Sci.*, 2004, **59**, 747–758.

[179] I. Leifer, G. Caulliez and G. de Leeuw, *J. Mar. Sys.*, 2007, **66**, 61 – 70.

[180] J. Cloke, W. A. Mckay and P. S. Liss, *Mar. Chem.*, 1991, **34**, 77–95.

[181] M. E. Wise, E. J. Freney, C. A. Tyree, J. O. Allen, S. T. Martin, L. M. Russell and P. R. Buseck, *J. Geophys. Res.*, 2009, **114**, D03201.

[182] G. K. Batchelor, *An Introduction to Fluid Dynamics*, Cambridge University Press, Cambridge, England, 1967.

[183] C. P. Ribeiro Jr. and D. Mewes, *Chem. Eng. Sci.*, 2007, **62**, 4501–4509.

[184] M. Simonnet, C. Gentric, E. Olmos and N. Midoux, *Chem. Eng. Sci.*, 2007, **62**, 858 – 866.

[185] R. Krishna, J. Ellenberger and C. Maretto, *Int. Comm. Heat Mass Transfer*, 1999, **26**, 467–475.

[186] R. Krishna, M. I. Urseanu and A. J. Dreher, *Chem. Eng. Procces.*, 2000, **39**, 371–378.

[187] J. F. Richardson and W. N. Zaki, *Trans. Instn. Chem. Engrs.*, 1954, **32**, S82–S100.

[188] H. Chanson and R. Manasseh, *J. Fluids Eng.*, 2003, **125**, 910–921.

[189] H. Chanson, S. Aoki and M. Maruyama, *Coast. Eng.*, 2002, **46**, 139–157.

[190] E. Lamarre and M. W. K., *J. Acoust. Soc. Am.*, 1994, **96**, 3605–3616.

[191] K. G. Porter and Y. S. Feig, *Limnol. Oceanogr.*, 1980, **25**, 943–948.

[192] S. Alvain, C. Moulin, Y. Dandonneau and H. Loisel, *Global Biogeochem. Cycles*, 2008, **22**, GB3001.

[193] E. V. Armbrust, *Nature*, 2009, **495**, 185–192.

[194] J. R. Young, J. M. Didymus, P. R. Bown, B. Prins and S. Mann, *Nature*, 1992, **356**, 516–518.

[195] W. Balch, D. Drapeau, B. Bowler and E. Booth, *Deep-Sea Res. Part II*, 2007, **54**, 478–495.

[196] C. W. Brown and J. A. Yoder, *J. Geophys. Res.*, 1994, **99**, 7467–7482.

[197] J. Giraudeau and G. W. Bailey, *Cont. Shelf Res.*, 1995, **15**, 1825–1852.

[198] A. Winter, R. W. Jordan and P. H. Roth, in *Coccolithophores*, ed. A. Winter and W. G. Siesser, Cambridge University Press, Cambridge, 1994, ch. Biogeography of living coccolithophores in oceanic waters, pp. 161–178.

[199] G. Berge, *Sarsia*, 1962, **6**, 27–40.

[200] J. B. Waterbury, S. W. Watson, F. W. Valois and D. G. Franks, *Can. B. Fish. Aquat. Sci.*, 1986, **214**, 71–120.

[201] H. G. Marshall and M. S. Cohn, *Seasonal phytoplankton assemblages in northeastern coastal waters of the United States*, NOAA Technical Memorandum NMFS-F /NEC- 15, Woods Hole, MA, 1982, pp. 1–31.

[202] D. A. Knopf, B. Wang, A. Laskin, R. C. Moffet and M. K. Gilles, *J. Geophys. Res.*, 2010, **37**, L11803.

[203] B. Wang, A. Laskin, T. Roedel, M. K. Gilles, R. C. Moffet, A. V. Tivanski and D. A. Knopf, *J. Geophys. Res.*, 2012, **117**, D00V19.

[204] B. Wang, A. T. Lambe, P. Massoli, T. B. Onasch, P. Davidovits, D. R. Worsnop and D. A. Knopf, *J. Geophys. Res.*, 2012, **117**, D16209.

[205] D. A. Knopf and T. Koop, *J. Geophys. Res.*, 2006, **111**, 1376–1377.

[206] D. A. Knopf, *J. Phys. Chem. A*, 2006, **110**, 5745–5750.

[207] M. Dymarska, B. J. Murray, L. M. Sun, M. L. Eastwood, D. A. Knopf and A. K. Bertram, *J. Geophys. Res.*, 2006, **111**, D04204.

[208] M. T. Parsons, D. A. Knopf and A. K. Bertram, *J. Phys. Chem. A*, 2004, **108**, 11600–11608.

[209] A. Laskin, M. J. Iedema and J. P. Cowin, *Aerosol Science and Technology*, 2003, **37**, 246–260.

[210] A. L. Kilcoyne, T. Tyliszczak, W. F. Steele, S. Fakra, P. Hitchcock, K. Franck, E. Anderson, B. Harteneck, E. G. Rightor, G. E. Mitchell, A. P. Hitchcock, L. Yang, T. Warwick and H. Ade, *J. Synchrotron Rad.*, 2003, **10**, 125136.

[211] R. R. L. Guillard, in *Culture of marine invertebrate animals*, ed. W. L. Smith and M. H. Chanley, Plenum Press, New York, NY, 1975, ch. Culture of phytoplankton for feeding marine invertebrates, pp. 29–66.

[212] R. L. Modini, B. Harris and Z. D. Ristovski, *Atmos. Chem. Phys.*, 2010, **10**, 2867–2877.

[213] W. R. Arnold, J. S. Cotsifas, A. R. Winter, J. S. Klinck, D. S. Smith and R. C. Playle, *Environ. Toxicol. Chem.*, 2007, **26**, 935–943.

[214] H. Ogawa and E. Tanoue, *J. Oceanogr.*, 2003, **59**, 129–147.

[215] L. I. Aluwihare and D. J. Repeta, *Mar. Ecol. Prog. Ser.*, 1999, **186**, 105–117.

[216] U. Passow, *Prog. Oceanogr.*, 2002, **55**, 287–333.

[217] V. Kuhnhenn-Dauben, D. A. Purdie, U. Knispel, H. Voss and U. Horstmann, *J. Geophys. Res.*, 2008, **113**, C06009.

[218] T. Koop, J. Bookhold, M. Shiraiwa and U. Pöschl, *Phys. Chem. Chem. Phys.*, 2011, **13**, 19238–19255.

[219] S. Twomey, *Atmos. Environ.*, 1974, **8**, 1251–1256.

[220] B. A. Albrecht, *Science*, 1989, **245**, 1227–1230.

[221] M. B. Baker and T. Peter, *Nature*, 2008, **451**, 299–300.

[222] R. Vogt, P. J. Crutzen and R. Sander, *Nature*, 1996, **383**, 327–330.

[223] D. O. De Haan, T. Brauers, K. Oum, J. Stutz, T. Nordmeyer and B. J. Finlayson-Pitts, *Int. Rev. Phys. Chem.*, 1999, **18**, 343–385.

[224] B. J. Finlayson-Pitts, *Chem. Rev.*, 2003, **103**, 4801–4822.

[225] R. Sander, W. C. Keene, A. A. P. Pszenny, R. Arimoto, G. P. Ayers, E. Baboukas, J. M. Cainey, P. J. Crutzen, R. A. Duce, G. Honninger, B. J. Huebert, W. Maenhaut, N. Mihalopoulos, V. C. Turekian and R. Van Dingenen, *Atmos. Chem. Phys.*, 2003, **3**, 1301–1336.

[226] S. J. Ghan, G. Guzman and H. Abdul-Razzak, *J. Atmos. Sci.*, 1998, **55**, 3340–3347.

[227] C. D. O'Dowd, J. A. Lowe and M. H. Smith, *Geophys. Res. Lett.*, 1999, **26**, 1311–1314.

[228] C. H. Twohy and J. R. Anderson, *Environ. Res. Lett.*, 2008, **3**, 045002.

[229] K. Junge and B. D. Swanson, *Biogeosciences*, 2008, **5**, 865–873.

[230] *The diatoms: Applications for the Environmental and Earth Sciences*, ed. E. F. Stoermer and J. P. Smol, Cambridge University Press, Cambridge, 1999.

[231] C. Darwin, *Q. J. Geo. Soc.*, 1846, **2**, 26–30.

[232] R. M. Brown, D. A. Larson and H. C. Bold, *Science*, 1964, **143**, 583–585.

[233] S. Kawai, *Int. Aerobio. Newsletter*, 1981, **15**, 6–10.

[234] H. Hakansson and T. Nihlen, *Archiv Für Protistenkunde*, 1990, **138**, 313–322.

[235] D. E. Kellogg and T. B. Kellogg, *Geology*, 1996, **24**, 115–118.

[236] R. M. McKay, P. J. Barrett, M. A. Harper and M. J. Hannah, *Palaeogeo. Palaeocli. Palaeoeco.*, 2008, **260**, 168–183.

[237] H. E. Welch, D. C. G. Muir, B. N. Billeck, W. L. Lockhart, G. J. Brunskill, H. J. Kling, M. P. Olson and R. M. Lemoine, *Env. Sci. Tech.*, 1991, **25**, 280–286.

[238] A. Gaudichet, R. Lefévre, A. Gaudry, B. Ardouin, G. Lambert and J. M. Miller, *Tellus*, 1989, **41B**, 344–352.

[239] M. O. Chalmers, M. A. Harper and W. A. Marshall, *An Illustrated Catalogue of Airborne Microbiota from the Maritime Antarctic.*, British Antarctic Survey, National Environment Research Council, Cambridge, 1996.

[240] M. A. Harper, in *The Diatoms: Applications for the Environmental and Earth Sciences*, Cambridge University Press, Cambridge, 1999, ch. 22. Diatoms as markers of atmospheric transport, pp. 429–435.

[241] J. Sciare, O. Favez, R. Sarda-Esteve, K. Oikonomou, H. Cachier and V. Kazan, *J. Geophys. Res.*, 2009, **114**, D15302.

[242] A. Sorooshian, L. T. Padro, A. Nenes, G. Feingold, A. McComiskey, S. P. Hersey, H. Gates, H. H. Jonsson, S. D. Miller, G. L. Stephens, R. C. Flagan and J. H. Seinfeld, *Global Biogeochem. Cyc.*, 2009, **23**, GB4007.

[243] D. C. Blanchard, *Adv. Chem. Series*, 1975, **145**, 360–387.

[244] M. Kuznetsova, C. Lee and J. Aller, *Mar. Chem.*, 2005, **96**, 359–377.

[245] M. Dall'Osto, D. Ceburnis, G. Martucci, J. Bialek, R. Dupuy, S. G. Jennings, H. Berresheim, J. Wenger, R. Healy, M. C. Facchini, M. Rinaldi, L. Giulianelli, E. Finessi, D. Worsnop, M. Ehn, J. Mikkilä, M. Kulmala and C. D. O'Dowd, *Atmos. Chem. Phys.*, 2010, **10**, 8413–8435.

[246] L. F. Radke, P. V. Hobbs and J. E. Pinnons, *J. Appl. Meteorol.*, 1976, **15**, 982–995.

[247] H. Flyger and N. Z. Heidam, *J. Aerosol Sci.*, 1978, **9**, 157–168.

[248] R. D. Borys, *PhD thesis*, Dept. Atmos. Sci. Colorado State Univ., Ft. Collins, USA, 1983.

[249] E. K. Bigg, *Tellus B*, 1996, **48**, 223–233.

[250] D. C. Rogers, P. J. DeMott and S. M. Kreidenweis, *J. Geophys. Res.*, 2001, **16**, 15053–15063.

[251] T. Koop, H. P. Ng, L. T. Molina and M. J. Molina, *J. Phys. Chem. A*, 1998, **102**, 8924–8931.

[252] B. Zobrist, C. Marcolli, T. Peter and T. Koop, *J. Phys. Chem. A*, 2008, **112**, 3965–3975.

[253] S. M. Ross, *Stochastic Processes: Second Edition*, Wiley Series in Probability and Mathematical Statistics, Canada, 1996.

[254] E. K. Bigg, *Proc. Phys. Soc. B*, 1953, **66**, 688–694.

[255] N. E. Dorsey, *T. Am. Philos. Soc.*, 1948, **38**, 247–328.

[256] G. Vali, *J. Atmos. Sci.*, 1994, **51**, 1843–1856.

[257] M. Ikegami, K. Okada, Y. Zaizen and Y. Makino, *Tellus Ser. B-Chem. Phys. Meteorol.*, 1994, **46**, 142–151.

[258] K. M. Zhang, E. M. Knipping, A. S. Wexler, P. V. Bhave and G. S. Tonnesen, *Atmos. Environ.*, 2005, **39**, 3373–3379.

[259] E. R. Lewis and S. E. Schwartz, *Atmos. Environ.*, 2006, **40**, 588–590.

[260] D. R. Dowling and L. F. Radke, *J. Appl. Meteorol.*, 1990, **29**, 970–978.

[261] A. J. Heymsfield and G. M. McFarquhar, *Mid-latitude and Tropical Cirrus: Microphysical Properties*, Oxford University Press, 198 Madison Avenue, New York, New York 10016, 2002, pp. 78–101.

[262] J. Ström, M. Seifert, B. Kärcher, J. Ovarlez, A. Minikin, J. F. Gayet, R. Krejci, A. Petzold, F. Auriol, W. Haag, R. Busen, U. Schumann and H. C. Hansson, *Atmos. Chem. Phys.*, 2003, **3**, 1807–1816.

[263] R. Tormo, D. Recio, I. Silva and A. F. Munoz, *Euro. J. Phycol.*, 2001, **42**, 248–252.

[264] S. M. Burrows, W. Elbert, M. G. Lawrence and U. Pöschl, *Atmos. Chem. Phys.*, 2009, **9**, 9263–9280.

[265] E. K. Bigg, *Tellus Ser. B-Chem. Phys. Meteorol.*, 2001, **53**, 510–519.

[266] B. T. Shaffer and B. Lighthart, *Microbial Ecol.*, 1997, **34**, 167–177.

[267] S. M. Burrows, T. Butler, P. Jöckel, H. Tost, A. Kerkweg, U. Pö, schl and M. G. Lawrence, *Atmos. Chem. Phys.*, 2009, **9**, 9281–9297.

[268] G. M. McFarquhar, G. Zhang, M. R. Poellot, G. L. Kok, R. McCoy, T. Tooman, A. Fridlind and A. J. Heymsfield, *J. Geophys. Res.*, 2007, **112**, D24201.

[269] A. M. Fridlind, A. S. Ackerman, G. McFarquhar, G. Zhang, M. R. Poellot, P. J. DeMott, A. J. Prenni and A. J. Heymsfield, *J. Geophys. Res.*, 2007, **112**, D24202.

[270] T. Bergeron, *Proc. 5th Assembly U.G.G.I., Lisbon*, 1935, **2**, 156.

[271] A. Wegener, *Thermodynamik Der Atmosphäre*, Johann Ambrosius Barth, Leipzig, 1911.

[272] W. Findeisen, *Meteorol. Z.*, 1938, **55**, 121–133.

[273] J. Hallett and S. C. Mossop, *Nature*, 1974, **249**, 26–28.

[274] S. C. Mossop and J. Hallett, *Science*, 1974, **186**, 632–633.

[275] G. Vali, *Atmos. Chem. Phys.*, 2008, **8**, 5017–5031.

[276] V. T. J. Phillips, C. Andronache, B. Christner, C. E. Morris, D. C. Sands, A. Bansemer, A. Lauer, C. McNaughton and C. Seman, *Biogeosci.*, 2009, **6**, 987–1014.

[277] P. A. Ariya, J. Sun, N. A. Eltouny, E. D. Hudson, C. T. Hayes and G. Kos, *Int. Rev. Phys. Chem.*, 2009, **28**, 1–32.

[278] O. Möhler, P. J. DeMott, G. Vali and Z. Levin, *Biogeosci.*, 2007, **4**, 1059–1071.

[279] O. Möhler, D. G. Georgakopoulos, C. E. Morris, S. Benz, V. Ebert, S. Hunsmann, H. Saathoff, M. Schnaiter and R. Wagner, *Biogeosci.*, 2008, **5**, 1425–1435.

[280] D. G. Georgakopoulos, V. Després, J. Fröhlich-Nowoisky, R. Psenner, P. A. Ariya, M. Pósfai, H. E. Ahern, B. F. Moffett and T. C. J. Hill, *Biogeosci.*, 2009, **6**, 721–737.

[281] L. R. Maki, E. L. Galyan, M. M. Changchi and D. R. Caldwell, *J. Aerosol. Sci.*, 1974, **28**, 456–459.

[282] G. Vali, M. Christensen, R. W. Fresh, E. L. Galyan, L. R. Maki and R. C. Schnell, *J. Atmos. Sci.*, 1976, **33**, 1565–1570.

[283] S. A. Yankofsky, Z. Levin, T. Bertold and N. Sandlerman, *J. Appl. Meteorl.*, 1981, **20**, 1013–1019.

[284] P. Phelps, T. H. Giddings, M. Prochoda and R. Fall, *J. Bacteriol*, 1986, **167**, 496–502.

[285] Z. Levin and S. A. Yankofsky, *J. Clim Appl. Meteorol.*, 1983, **22**, 1964–1966.

[286] K. Diehl, C. Quick, S. Matthias-Maser, S. K. Mitra and R. Jaenicke, *Atmos. Res.*, 2001, **58**, 75–87.

[287] K. Diehl, S. Matthias-Maser, R. Jaenicke and S. K. Mitra, *Atmos. Res.*, 2002, **61**, 125–133.

[288] N. von Blohn, S. K. Mitra, K. Diehl and S. Borrmann, *Atmos. Res.*, 2005, **78**, 182–189.

[289] S. Pouleur, C. Richard, J. G. Martin and H. Antoun, *Appl. Environ. Microbiol.*, 1992, **58**, 2960–2964.

[290] R. Iannone, D. I. Chernoff, A. Pringle, S. T. Martin and A. K. Bertram, *Atmos. Chem. Phys.*, 2011, **11**, 1191–1201.

[291] T. L. Kieft and T. Ruscetti, *Appl. Environ. Microbiol.*, 1988, **54**, 1678–1681.

[292] T. L. Kieft and T. Ruscetti, *J. Bacteriol.*, 1990, **172**, 3519–3523.

[293] S. K. Henderson-Begg, T. Hill, R. Thyrhaug, M. Khan and B. F. Moffett, *Atmos. Sci. Lett.*, 2009, **10**, 215–219.

[294] P. Mazur, *Am. J. Physiol.*, 1984, **247**, C125–C142.

[295] A. G. Govindarajan and S. E. Lindow, *J. Bio. Chem.*, 1988, **263**, 9333–9338.

[296] A. G. Govindarajan and S. E. Lindow, *P. Natl. Acad. Sci.*, 1988, **85**, 1334–1338.

[297] C. L. Hew and Y. D. S. C., *Eur. J. Biochem.*, 1992, **203**, 33–42.

[298] *Biological Ice Nucleation and its Applications*, ed. J. R. E. Lee, G. J. Warren and L. V. Gusta, American Phytopathological Society, St. Paul, MN, USA, 1995.

[299] K. E. Zachariassen and E. Kristiansen, *Cryobiology*, 2008, **319**, 1214.

[300] D. J. Bowles, P. J. Lillford, D. A. Rees and I. A. Shanks, *Philosophical Transactions: Biological Sciences*, 2002, **357**, 829–955.

[301] B. C. Christner, *Appl. Microbiol. Biotechnol.*, 2010, **85**, 481–489.

[302] M. Gavish, R. Popovitz-Biro, M. Lahav and L. Leiserowitz, *Science*, 1990, **250**, 973–975.

[303] R. Popovitz-Biro, J. L. Wang, J. Majewski, E. Shavit, L. Leiserowitz and M. Lahav, *J. Am. Chem. Soc.*, 1994, **116**, 1179–1191.

[304] L. H. Seeley and G. T. Seidler, *J. Chem. Phys.*, 2001, **114**, 10464–10470.

[305] W. Cantrell and C. Robinson, *Geophys. Res. Lett.*, 2006, **33**, L07802.

[306] C. Leck and E. K. Bigg, *Tellus B*, 2005, **57**, 305–316.

[307] C. Leck, M. Norman, E. K. Bigg and R. Hillamo, *J. Geophys. Res.*, 2002, **107**, 131–141.

[308] M. Posfai, J. Li, J. R. Anderson and P. R. Buseck, *Atmos. Res.*, 2003, **66**, 231–240.

[309] C. Leck and E. K. Bigg, *Geophys. Res. Lett.*, 2005, **32**, L19803.

[310] K. E. Bigg, *Eviron. Chem.*, 2007, **4**, 155–161.

[311] D. Niedermeier, S. Hartmann, R. A. Shaw, D. Covert, T. F. Mentel, J. Schneider, L. Poulain, P. Reitz, C. Spindler, T. Clauss, A. Kiselev, E. Hallbauer, H. Wex, K. Mildenberger and F. Stratmann, *Atmos. Chem. Phys.*, 2010, **10**, 3601–3614.

[312] M. Sumper and E. Brunner, *Chembiochem*, 2008, **9**, 1187–1194.

[313] M. T. Madigan, J. M. Martinko and J. Parker, *Biology of Microorganisms*, Prentice Hall Pearson Education, Inc., Upper Saddle River, NJ, USA, 10th edn, 2003.

[314] J. R. Young and K. Henriksen, *Rev. Mineral. Geochem.*, 2003, **54**, 189–215.

[315] J.-P. Chen, A. Hazra and Z. Levin, *Atmos. Chem. Phys.*, 2008, **8**, 174317449.

[316] P. W. Atkins, *Physical Chemistry*, Freeman and Company, New York, 9th edn, 2010.

[317] G. L. Gaines, *Insoluble Monolayers at Liquid-Gas Interfaces*, Interscience Publishers, New York, 1966.

[318] J. E. Manson, *J. Meteorol.*, 1957, **14**, 85–86.

[319] M. G. Janech, A. Krell, T. Mock, J. S. Kang and J. A. Raymond, *J. Phycol.*, 2006, **42**, 410–416.

[320] S. E. Lindow, D. C. Arny and C. D. Upper, *Phytopathol.*, 1978, **68**, 523–527.

[321] S. E. Lindow, D. C. Arny and C. D. Upper, *Plant Physiol.*, 1982, **70**, 1084–1089.

[322] J. W. Wang and U. Becker, *Am. Mineral.*, 2009, **94**, 380–386.

[323] J. P. D. Abbatt, S. Benz, D. J. Cziczo, Z. Kanji, U. Lohmann and O. Möhler, *Science*, 2006, **313**, 1770–1773.

[324] U. Lohmann, P. Spichtinger, S. Jess, T. Peter and H. Smit, *Environ. Res. Lett.*, 2008, **3**, 045022.

[325] D. L. Mitchell, P. Rasch, D. Ivanova, G. McFarquhar and T. Nousiainen, *Geophys. Res. Lett.*, 2008, **35**, L09806.

[326] P. H. Gregory, E. D. Hamilton and T. Sreeramulu, *Nature*, 1955, **176**, 1270.

[327] H. Schlichting, *J. Air Pollut. Con. Assoc.*, 1969, **43**, 615–627.

[328] N. Meskhidze, J. Xu, B. Gantt, Y. Zhang, A. Nenes, S. J. Ghan, X. Liu, R. Easter and R. Zaveri, *Atmos. Chem. Phys.*, 2011, **11**, 11689–11705.

[329] P. J. DeMott, A. J. Prenni, X. Liu, S. M. Kreidenweis, M. D. Petters, C. H. Twohy, M. S. Richardson, T. Eidhammer and D. C. Rogers, *P. Natl. Acad. Sci.*, 2010, **107**, 1121711222.